

PL-TR-95-2037(I)

## CIRRIS 1A POST FLIGHT CALIBRATION

Gail Bingham  
James Peterson  
Steven Brown  
David Morse  
Brent Bartschi  
Allan Steed

Space Dynamics Laboratory/Utah State University  
Logan, Utah 84322

January 1995

Final Report (Volume I)  
3 June 1981 - 31 May 1994

Approved for public release; distribution unlimited


DTIC QUALITY INSPECTED 6

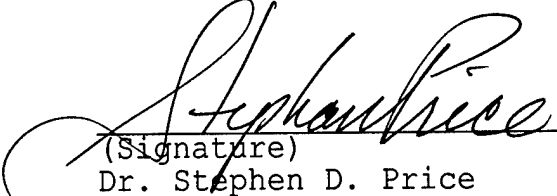


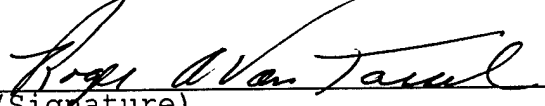
**PHILLIPS LABORATORY**  
**Directorate of Geophysics**  
**AIR FORCE MATERIEL COMMAND**  
**HANSCOM AFB, MA 01731-3010**

19961210 060

"This technical report has been reviewed and is approved for publication"

  
(Signature)  
Richard M. Nadile  
Contract Manager

  
(Signature)  
Dr. Stephen D. Price  
Branch Chief

  
(Signature)  
Dr. Roger A. Van Tassel  
Division Director

This report has been reviewed by the ESC Public Affairs Office (PA) and is releasable to the National Technical Information Service (NTIS).

Qualified requestors may obtain additional copies from the Defense Technical Information Center (DTIC). All others should apply to the National Technical Information Service (NTIS).

If your address has changed, if you wish to be removed from the mailing list, or if the addressee is no longer employed by your organization, please notify PL/IM, 29 Randolph Road, Hanscom AFB, MA 01731-3010. This will assist us in maintaining a current mailing list.

Do not return copies of this report unless contractual obligations or notices on a specific document requires that it be returned.

REPORT DOCUMENTATION PAGE			Form Approved OMB No. 0704-0188	
Public reporting burden for this collection of information is estimated to average 1 hour per response, including the time for reviewing instructions, searching existing data sources, gathering and maintaining the data needed, and completing and reviewing the collection of information. Send comments regarding this burden estimate or any other aspect of this collection of information, including suggestions for reducing this burden, to Washington Headquarters Services, Directorate for Information Operations and Reports, 1215 Jefferson Davis Highway, Suite 1204, Arlington, VA 22202-4302, and to the Office of Management and Budget, Paperwork Reduction Project (0704-0188), Washington, DC 20503.				
1. AGENCY USE ONLY (Leave blank)	2. REPORT DATE January 1995	3. REPORT TYPE AND DATES COVERED Final (3 Jun 1981-31 May 1994)		
4. TITLE AND SUBTITLE CIRRIS 1A Post Flight Calibration			5. FUNDING NUMBERS PE 62101F PR 7670 TA 10 WU AI	
6. AUTHOR(S) Gail Bingham      David Morse James Peterson      Brent Bartschi Steven Brown      Allan Steed			Contract F19628-81-C-0123	
7. PERFORMING ORGANIZATION NAME(S) AND ADDRESS(ES) Space Dynamics Laboratory Utah State University Logan, Utah 84341			8. PERFORMING ORGANIZATION REPORT NUMBER SDL/92-091	
9. SPONSORING/MONITORING AGENCY NAME(S) AND ADDRESS(ES) Phillips Laboratory 29 Randolph Road Hanscom AFB, MA 01731-3010 Contract Manager: Richard Nadile (GPOB)			10. SPONSORING/MONITORING AGENCY REPORT NUMBER PL-TR-95-2037 (I)	
11. SUPPLEMENTARY NOTES				
12a. DISTRIBUTION/AVAILABILITY STATEMENT Approved for public release; distribution unlimited			12b. DISTRIBUTION CODE	
13. ABSTRACT (Maximum 200 words) The Cryogenic Infrared Radiance Instrumentation for Shuttle (CIRRIS 1A) instrument is a state-of-the-art cryogenically cooled instrument designed to observe the infrared spectrum of the earth's atmosphere. The Space Dynamics Laboratory at Utah State University (SDL/USU) participated as the prime contractor in this program. CIRRIS 1A was launched on the shuttle Discovery (STS-39) on 28 April 1991. All of the instruments operated as designed during the mission. Data obtained from this experiment will help refine knowledge of the background radiance and structure of atmospheric infrared emissions, and will be used to update and validate U.S. Air Force atmospheric models used in the design of operational systems. SDL/USU performed a complete ground calibration of the primary and ancillary sensors to verify instrument design and to create algorithms necessary for post flight data reduction. This report represents Volume 1 of the CIRRIS 1A Post Flight Calibration Final Report. Volume 1 describes the calibration approach, discusses the results of the calibration, and provides graphical data for the primary detectors of each sensor. General descriptions of the radiometer and interferometer are also included. Volume 2 contains reduced data for various parameters for all of the detectors.				
14. SUBJECT TERMS CIRRIS 1A, calibration, radiometer, interferometer, infrared, shuttle			15. NUMBER OF PAGES 240	
			16. PRICE CODE	
17. SECURITY CLASSIFICATION OF REPORT Unclassified	18. SECURITY CLASSIFICATION OF THIS PAGE Unclassified	19. SECURITY CLASSIFICATION OF ABSTRACT Unclassified	20. LIMITATION OF ABSTRACT SAR	

# TABLE OF CONTENTS

	<u>page</u>
TABLE OF CONTENTS.....	iii
LIST OF FIGURES .....	vi
LIST OF TABLES .....	xi
FOREWORD .....	xii
EXECUTIVE SUMMARY .....	xiii
1. INTRODUCTION .....	1
1.1 MISSION OBJECTIVES.....	1
1.2 GENERAL INSTRUMENT DESCRIPTION .....	2
1.2.1 CIRRIS 1A Optical System.....	4
1.2.1.1 Telescope.....	5
1.2.1.2 Focal Plane Arrays .....	6
1.2.2 Internal Stimulation Sources .....	6
1.2.3 Supercritical Helium Cooling System .....	7
1.3 FLIGHT SUMMARY.....	8
1.4 FLIGHT DATA VERIFICATION AND ANALYSIS.....	10
2. CALIBRATION METHODS .....	11
2.1 CALIBRATION HISTORY .....	11
2.2 PROCEDURES .....	11
2.3 CALIBRATION APPROACH.....	11
2.4 CALIBRATION SOURCE.....	12
2.5 CALIBRATION DATA ANALYSIS SYSTEM.....	15
3. RADIOMETER CALIBRATION RESULTS .....	17
3.1 INTRODUCTION .....	17
3.1.1 Radiometer Description.....	17
3.1.2 Radiometer Calibration Equation .....	19
3.1.3 Radiometer Radiometric Model .....	19
3.2 RADIOMETER CALIBRATION TESTS AND RESULTS .....	20
3.2.1 Point Source Spatial Response .....	20
3.2.1.1 Detector Positions.....	21
3.2.1.2 Scatter .....	23
3.2.1.3 Crosstalk .....	24
3.2.1.4 Point Source Response Maps .....	24
3.2.1.5 Effective Field-of-View Solid Angles.....	25
3.2.1.6 Modulation Transfer Function.....	30
3.2.2 Jones Cone Response.....	36



3.2.3	Radiometric Response Functions .....	37
3.2.3.1	Electronic Gain Response.....	37
3.2.4	Absolute Responsivity.....	40
3.2.5	Linearity.....	48
3.2.5.1	Jones Source - Aperture Linearity Measurements.....	49
3.2.5.2	Extended Source Linearity Measurements .....	49
3.2.5.3	Point Source - Aperture Linearity Measurements .....	52
3.2.5.4	Small Signal Response Linearity Measurements (ac/dc) .....	52
3.2.6	Relative Spectral Responsivity .....	56
3.2.6.1	In-Band Response.....	57
3.2.6.2	Out-of-Band Rejection .....	62
3.2.7	Measurement Uncertainties .....	69
3.2.7.1	Dark Noise.....	69
3.2.7.2	Dark Offset .....	74
3.2.7.3	Noise versus Flux .....	74
3.2.7.4	Noise Equivalent Radiance (NER).....	77
3.2.7.5	Radiometer Precision.....	80
4.	INTERFEROMETER CALIBRATION RESULTS.....	82
4.1	INTRODUCTION .....	82
4.1.1	Interferometer Description .....	82
4.1.2	Interferometer Calibration Equation.....	84
4.1.3	Calibration Requirements .....	85
4.2	INTERFEROMETER CALIBRATION TESTS AND RESULTS .....	85
4.2.1	Spatial Response Functions .....	85
4.2.1.1	Point Source Response Maps .....	86
4.2.1.2	Effective Field-of-View Solid Angles.....	88
4.2.1.3	Detector Positions.....	89
4.2.1.4	Interferometer and Radiometer Detector Coalignment.....	91
4.2.1.5	Scatter .....	91
4.2.1.6	Crosstalk.....	92
4.2.1.7	Field Stop Location .....	92
4.2.2	Interferometer Radiometric Response .....	94
4.2.2.1	Relative Spectral Responsivity.....	94
4.2.2.2	Absolute Responsivity.....	101
4.2.3	Linearity.....	122
4.2.4	Measurement Uncertainty.....	130
4.2.4.1	Noise Response .....	130
4.2.5	Interferometer Processing Software Verification/Comparison .....	143
4.2.5.1	Frequency (Wavelength) Verification.....	143
4.2.5.2	Spectral Line Shape .....	145

5.	ANCILLARY SENSORS CALIBRATION.....	149
5.1	PHOTOMETERS .....	149
5.1.1	Photometer Radiance Calibration.....	152
5.1.2	Photometer Spectral Sensitivity .....	156
5.1.3	Photometer Temperature Response.....	158
5.2	CELESTIAL ASPECT SENSOR (CAS) .....	160
5.3	HORIZON SENSOR .....	161
5.4	LOW-LIGHT-LEVEL TELEVISION CAMERAS (LLTV).....	161
5.5	TAPE RECORDERS .....	162
5.6	DFE-2 FLIGHT ANOMALY .....	163
6.	CALIBRATION EVALUATION .....	164
6.1	CALIBRATION EVALUATION .....	164
6.1.1	Radiometer Calibration.....	164
6.1.2	Interferometer Calibration .....	165
6.1.2.1	Intersensor Absolute Calibration Difference.....	165
6.1.2.2	Interferometer Spectra versus Blackbody Response .....	172
6.1.3	Radiometer and Interferometer Calibration Accuracy .....	182
6.1.3.1	Radiometer .....	182
6.1.3.2	Interferometer .....	182
6.1.4	Ancillary Sensors.....	183
	REFERENCES .....	187
	APPENDIX 1 - CIRIS 1A PROGRAM SUMMARY .....	189
	APPENDIX 2 - CHARACTERIZATION OF THE CIRIS 1A LLLTV SYSTEMS.....	215

## LIST OF FIGURES

<u>Figure</u>	<u>Page</u>
1 Air Force earthlimb model of atmospheric infrared emissions compared with a theoretical 300 K 1-m <sup>2</sup> blackbody target. ....	2
2 The CIRRIS 1A instrument installed in its shipping container. ....	3
3 Schematic layout of the CIRRIS 1A optical system. ....	4
4 CIRRIS 1A BRDF measurement history. ....	6
5 Schematic of the CIRRIS 1A cryogenic cooling system. ....	8
6 Optical configurations of multifunction infrared calibrator 2 (MIC2). ....	13
7 CIRRIS 1A mated to the multifunction calibrator. ....	14
8 CIRRIS 1A calibration data collection setup. ....	16
9 CIRRIS 1A calibration data distribution setup. ....	16
10 CIRRIS 1A radiometer focal plane array configuration. ....	18
11 Composite detector response contour map of radiometer focal planes 1 and 2. ....	22
12 Point source response maps for radiometer focal planes 1 and 2. ....	26
13 Three-dimensional plots of the point source response maps for radiometer focal plane 1. ....	7
14 Three-dimensional plots of the point source response maps for radiometer focal plane 2. ....	28
15 CIRRIS 1A radiometer Y-axis modulation transfer function (MTF). ....	31
16 CIRRIS 1A radiometer X- and Y-axis modulation transfer function (MTF), Map A (D1-1 to D1-6). ....	32
17 CIRRIS 1A radiometer detector 1-7 modulation transfer function (MTF) (Map F). ....	33
18 CIRRIS 1A radiometer detector 1-8 modulation transfer function (MTF) (Maps B, G, H). ....	33
19 CIRRIS 1A radiometer Y-axis modulation transfer function (MTF), Map A (D2-1 to D2-3). ....	34
20 CIRRIS 1A radiometer detector 2-4 modulation transfer function (MTF) (Maps B, F, G, H). ....	34
21 CIRRIS 1A radiometer detector 2-5 modulation transfer function (MTF) (Maps A, B, C, D). ....	35
22 Simplified diagram of a Jones cone. ....	36
23 Orientation of the entrance aperture for the Jones cone maps. ....	36
24 Jones source maps for radiometer detectors 1-1 and 1-6. ....	38
25 Jones source maps for radiometer detectors 2-2 and 2-3. ....	39
26 A schematic of the calculation of the effective flux ( $\Phi_{\text{eff}}$ ) and the use of $\Phi_{\text{eff}}$ to develop the radiometer response equations. ....	42

27	A comparison of the CIRRIS 1A filter RSR and typical atmospheric spectra in each band. ....	43
28	Development of the band flux ratio used to partially correct the CIRRIS 1A data for the non-ideal RSR. ....	44
29	The effect of constants on fit of coefficients for filter 0, detector 6, response function. ....	46
30	An example of the DRE effect observed in focal plane 1 in high bias above a voltage of about 0.75 V (dc restored). ....	48
31	Extended source linearity calibration for radiometer detector 1-6. ....	50
32	Extended source linearity calibration for radiometer detector 2-3. ....	52
33	Typical amplitude plot for linearity coefficient, detector 1-6. ....	54
34	Typical integrated power spectrum for linearity coefficient, detector 1-6. ....	54
35	AC-DC linearity for radiometer detector 1-1. ....	55
36	AC-DC linearity for radiometer detector 1-3. ....	55
37	Relative spectral response for radiometer detector 1-4. ....	58
38	Relative spectral response for radiometer detector 2-3. ....	60
39	Vender-supplied detector responsivities for radiometer focal plane 1. ....	60
40	Vender-supplied detector responsivities for radiometer focal plane 2. ....	61
41	Radiometer beamsplitter transmission. ....	61
42	Basic measurement setup using external interferometer and auxiliary filter to test filter out-of-band rejection. ....	63
43	Radiometer out-of-band rejection, filter 0. ....	65
44	Radiometer out-of-band rejection, filter 1. ....	66
45	Radiometer out-of-band rejection, filter 2. ....	66
46	Radiometer out-of-band rejection, filter 3. ....	67
47	Radiometer out-of-band rejection, filter 5. ....	67
48	Radiometer out-of-band rejection, filter 7. ....	68
49	Radiometer out-of-band rejection, focal plane 2. ....	68
50	RMS noise history for radiometer detector 1-6. ....	70
51	RMS noise history for radiometer detector 2-3. ....	71
52	Mean amplitude for the relative dark voltages for all radiometer detectors. ....	72
53	Standard deviation for the relative dark voltages for all radiometer detectors. ....	72
54	Mean amplitude under dark conditions for detector 1-6. ....	73
55	Power spectrum under dark conditions for detector 1-6. ....	73
56	Offset history for radiometer detector 1-6. ....	75
57	Offset history for radiometer detector 2-3. ....	76
58	Noise flux versus band pass flux for radiometer detector 1-6, filter 0. ....	78
59	Noise flux versus band pass flux for radiometer detector 2-3. ....	78
60	CIRRIS 1A radiometer focal plane 1 internal source tracking. ....	81

61	CIRRIS 1A radiometer focal plane 2 internal source tracking .....	81
62	CIRRIS 1A interferometer focal plane array configuration. ....	83
63	Point source response map for the interferometer detectors .....	87
64	Three-dimensional plot of the point source response map for the interferometer detectors. ....	88
65	Composite detector response contour map of the CIRRIS 1A interferometer and radiometer focal planes. ....	90
66	Interferometer field stop coordinates (indicating geometric center of the field stop and centroid of the detector). ....	93
67	Interferometer focal plane 3 manufacturer's (SBRC) response curve. ....	95
68	Relative spectral response curves obtained with each of the four sources for detector 3-3, filter 6. ....	96
69	Example of coadding to increase signal-to-noise ratio. ....	97
70	Coadded scans to increase signal-to-noise ratio. ....	98
71	Relative spectral response data for interferometer detector 3-2, filters 0-7, under long scan and medium bias conditions. ....	99
72	The overlay of the measured extended source file at 242 K on the RSR of filter 2 to develop the absolute coefficient. All files for filter 2 were integrated in this same region. ....	102
73	Normalized absolute response data for interferometer detector 3 medium bias -- raw data (filters 0,1,2,3). ....	105
74	Medium and low bias data for detector 3 and the least squares fit coefficients for the equation $y = a \log (bx)$ . The bias gain needed to bring the low bias data on to the same line is also shown. ....	110
75	Filter adjusted long scan curves showing the similar slopes to all the medium bias data for each detector. The low bias data shows no consistent pattern. Coefficients for filters 4, 2, 1, 6, and 0 were multiplied by 150, 30, 10, 3, and 0.5 to bring the values into a similar range for comparison. ....	114
76	Filter adjusted long scan curves as a function of temperature. Coefficients for filters 4, 2, 1, 6, and 0 were multiplied by 150, 30, 10, 3, and 0.5 to bring the values into a similar range for comparison. ....	116
77	Filter gain adjusted curves for detector 5, medium and low bias against dc and temperature. ....	118
78	Absolute response coefficients with the single slope equation and offset developed for each detector. ....	121
79	Block diagram of a typical CIRRIS 1A interferometer signal conditioning electronics channel. ....	123
80	Typical modulated output response for a given dc offset. ....	125
81	Integration band for a typical transformed response. ....	125
82	Linearity results for detector 3-3, low bias (raw data with line fit). ....	126
83	Linearity results for detector 3-3, low bias (linearity correction function). ....	126

84	Relative spectral response interferogram for detector 3-3, filter 5, low bias, before linearization. ....	127
85	Relative spectral response interferogram for detector 3-3, filter 5, low bias, after linearization.....	127
86	Transform of relative spectral response interferogram for detector 3-3, filter 7, low bias, before linearization.....	128
87	Transform of relative spectral response interferogram for detector 3-3, filter 7, low bias, after linearization. Note increase in signal in main peak, reduction in side lobes.....	128
88	Dark noise history for interferometer detector 3.....	132
89	Offset history for interferometer detector 3.....	133
90	Calibrated noise transform and medium curve examples.....	135
91	NESR plots for each detector.....	136
92	Areas of the spectrum used to calculate the standard deviation of the out-of-band noise, detector 3-2, filter 5 data.....	137
93	Standard deviation versus flux for the region indicated in Figure 92 (individual range).....	137
94	Standard deviation versus flux for the region indicated in Figure 92 -- data adjusted for electronic gain.....	138
95	Noise versus flux for all interferometer detectors, medium bias.....	140
96	Noise versus flux for interferometer detectors, low bias.....	140
97	The effect of the MIC2 light leak on the RSR calculation of filter 0.....	142
98	Comparison of the ARC and IDAS software transforming the 3.391 laser line (2948.12 cm <sup>-1</sup> in vacuum).....	144
99	Comparison of CIRRIS absorption cell measurements and FASCOD3 predicted line shape.....	145
100	CIRRIS 1A unapodized line shape and line shape with various Kaiser-Bessel apodizations. Line is from a 3.391 mm laser flooding detector 3-2.....	146
101	Demonstration of the CIRRIS 1A line shape of detector 3-2 using rotational water at 884 cm <sup>-1</sup> collected at a tangent height of 34 km. Model is FASCOD3-HITRAN 92 at 0.05 cm resolution.....	146
102	Wavelength dispersion of a 3.391 laser focused on the center and four corners of interferometer detector 3-2.....	148
103	Spectral line dispersion between the central (detector 3-2) and off-axis detectors of CIRRIS 1A.....	148
104	Photometer stimulator tracking history from initial calibration to launch.....	150
105	CIRRIS 1A photometer response versus lamp current.....	151
106	Stim history during flight and at the post flight calibration (pf).....	152
107	Normalized spectral response for the three CIRRIS 1A photometers measured post flight.....	153
108	Photometer temperatures during flight.....	158

109	Photometer stim temperature response curve. ....	159
110	Temperature response of the photometer PCP3-3 5577Å to internal stim and an external chamber light source. ....	160
111	A photograph taken with the CIRRIS 1A celestial aspect sensor camera. The camera fiducials are the two larger dots on the left edge of the film.....	162
112	The radiometer response to a crossing of Alpha Sco.....	165
113	A comparison of the interferometer and radiometer radiance data for a vertical limb scan from about 15 km to 160 km tangent height. ....	167
114	A comparison of the interferometer and radiometer radiance data for a vertical limb scan from about 15 km to 160 km tangent height. ....	169
115	Verification of interferometer gain linearity as a function of radiometer change in radiance. ....	172
116	Examples of middle level dc calibration spectra for D3-4, medium bias mode, compared with the theoretical spectra.....	173
117	Two examples of comparisons of calibration spectra compared with theoretical spectra for D3-4, filter 7, low bias. ....	177
118	A comparison of calibration spectra and theory for detector 5, medium bias. ....	178
119	The effect of interferometer gain on the radiometer-interferometer relationship.....	178
120	Two examples of the comparison of the calibration spectra with the theoretical shape for low bias. ....	179
121	Two examples of the large differences in the calibration and theoretical spectra generated by OPUS when the nonlinearity correction was tested. ....	180
122	CIRRIS data (filter 7) of ozone profile comparison with climatology.....	181
123	5577 Photometer response to air glow layer at about 85 km in block 10B near the early part of the mission.....	185
124	5577 Photometer response to air glow layer at about 85 km in block 11A near the end of the mission. ....	186

## LIST OF TABLES

<u>Table</u>	<u>Page</u>
1	CIRRIS 1A Radiometer Filter Wheel Characteristics ..... 18
2	Point Source Response Map Parameters ..... 21
3	Summary of Radiometer Detector Centroids ..... 23
4	Summary of Radiometer Detector Scatter ..... 24
5	CIRRIS 1A Radiometer Effective Fields-of-View Solid Angles ..... 29
6	CIRRIS 1A Radiometer Bias Groups ..... 40
7	CIRRIS 1A Radiometer Electronic Gains ..... 40
8	Constants Used in OPUS ..... 46
9	CIRRIS 1A Radiometer Linearity Coefficients (filter 0, bandpass, linear fit) ..... 47
10	Radiometer Noise Equivalent Radiances ..... 79
11	CIRRIS 1A Radiometer Precision ..... 80
12	CIRRIS 1A Interferometer Filter Wheel Characteristics ..... 84
13	Point Source Response Map Configuration ..... 86
14	CIRRIS 1A Interferometer Field-of-View Solid Angles ..... 89
15	Interferometer Detectors' Object-Space Position Coordinates ..... 91
16	Summary of Interferometer Scatter Data ..... 92
17	CIRRIS 1A Field Stop Location ..... 94
18	Mean Absolute Long Scan Coefficients and a Mean Based Bias Gain for the CIRRIS 1A Interferometer ..... 103
19	A Sample of the Absolute Coefficient Tables Generated for Each Interferometer Detector, Filter, and Bias ..... 107
20	The Absolute Coefficients Developed for Detector 3, Filter 3, Medium Bias Using the Integral Method ..... 108
21	Fit Coefficient Data ..... 112
22	Unified Slope Coefficients for Medium Bias Detectors 1, 2, 3, and 4, and Mean Coefficients for Low Bias. A Base Coefficient is Provided for Filter 3 and an Offset Coefficient for the other Filters. No Fit Equation is Provided for Detector 5, Medium Bias ..... 120
23	Linearity Coefficients for CIRRIS 1A Low Bias Correction ..... 130
24	Transform to Transform Variability of 10 Consecutive Interferograms Collected with a 30 K Extended Source ..... 132
25	Relative Response Data at Maximum Light Leak Spectrum ..... 143
26	Maximum Value of the Reference Spectrum ..... 143
27	Calibration Data for Photometer PCP 3-1, Flight Spare with 3911 Å Filter ..... 154
28	Calibration Data for Photometer PCP 3-1, Flight Spare with 5580 Å Filter ..... 154
29	Calibration Data for Photometer PCP 3-2, 3914 Å Filter ..... 155
30	Calibration Data for Photometer PCP 3-3, 5577 Å Filter ..... 155
31	Photometer Sensitivity During Flight Blocks ..... 157
32	Radiometer and Interferometer Comparisons for Filter Pairs ..... 181
33	A Comparison of Photometric Responses to Air Glow Layer (89 km) Crossing Through the Mission. (Measurements with 3914 levels greater than about 2 kR have significant moonshine or auroral contamination.) ..... 184



## FOREWORD

The Cryogenic Infrared Radiance Instrumentation for Shuttle (CIRRIS 1A) program, sponsored by the Strategic Defense Initiative Organization (SDIO) and managed by the Geophysics Directorate of the USAF Phillips Laboratory, is a state-of-the-art cryogenically cooled instrument designed to observe the infrared spectrum of the earth's atmosphere. The Space Dynamics Laboratory at Utah State University (SDL/USU) was awarded contract no. F19628-81-C-0123 to participate as the prime contractor in this program. As part of this program, SDL designed, constructed, calibrated, tested, and integrated primary and support instruments for the CIRRIS 1A experiment. In addition, SDL personnel provided mission support and documentation, including flight crew training. CIRRIS 1A was launched on the space shuttle Discovery on 28 April 1991. All of the instruments operated as designed during the mission.

This report, submitted in compliance with CDRL 160, presents the results of the CIRRIS 1A post flight calibration. This document represents the current understanding of the CIRRIS 1A calibration accuracy and applicability to the data collected during the CIRRIS mission. Several drafts of this report were previously submitted for review; this document is the final submission. The calibration coefficients will continue to be refined as the flight data are further analyzed.

This document represents Volume 1 of the CIRRIS 1A Post Flight Calibration Final Report. Volume 1 describes the calibration approach, discusses the results of the calibration, and provides graphical data for the primary detectors of each sensor. General descriptions of the radiometer and interferometer are also included. Volume 2 contains reduced data for various parameters for all of the detectors.

SDL/USU would like to acknowledge Boston College, Miranda Laboratories, and PhotoMetrics for alignment and pointing data, and coding of OPUS.

## EXECUTIVE SUMMARY

The Cryogenic Infrared Radiance Instrumentation for Shuttle (CIRRIS 1A) instrument was launched on the shuttle Discovery (STS-39) on 28 April 1991 to characterize the phenomenology and dynamics of upper atmospheric processes. The state of the art, cryogenically cooled instrument collected simultaneous high resolution spectral and spatial measurements of the upper atmosphere and space objects. Excellent data were obtained during the STS-39 mission, and data analysis shows that all primary sensors performed well. Data obtained from this experiment will help refine knowledge of the background radiance and structure of atmospheric infrared emissions, and will be used to update and validate U.S. Air Force atmospheric models used in the design of operational systems.

The two primary CIRRIS 1A infrared sensors are a high resolution Michelson interferometer and a dual-channel radiometer, which share the collection optics of a high off-axis-rejection telescope. The telescope and ancillary instruments are mounted on a two-axis gimbal system to provide pointing and scanning capability. During flight, all of the sensor and housekeeping data were redundantly recorded on tape recorders for post flight reduction and analysis.

A complete ground calibration of the primary and ancillary sensors was performed to verify the instrument design and to create algorithms necessary for post flight data reduction. CIRRIS 1A underwent an engineering evaluation before flight and a full calibration after the mission. This report presents the results of the CIRRIS 1A post flight calibration.

The CIRRIS 1A radiometer calibration measured sensor point source response, spectral response, and absolute response. Individual response equations were fit to each detector range. The radiometer absolute calibration was verified by examining star crossing data collected by individual radiometer detectors. The radiometer detectors are sufficiently small and sensitive to see individual stars; therefore, comparisons between CIRRIS 1A and other sensors were possible. CIRRIS 1A viewed three infrared stars, Alpha Bo, Alpha Sco, and Alpha Centary. The CIRRIS measurement of Alpha Bo peaks at  $1.205E-14 \text{ W cm}^{-2}$ , which is within 4.65% of the value reported by IRAS (infrared astronomy satellite) for this star. From this and other CIRRIS 1A celestial observations, SDL/USU concludes that the radiometer absolute calibration is within 5% of the standards used by other space and ground-based celestial observation systems.

The CIRRIS 1A interferometer calibration produced a map of the point source response of each detector, the relative spectral response of each filter passband for each detector, and the absolute response of each detector in each passband. The results show that the CIRRIS interferometer has met all specifications for resolution and spectral accuracy. The positions of the interferometer and radiometer focal planes with respect to each other and to the interferometer field stop were mapped and verified using flight data.

This document represents the current understanding of the CIRRIS 1A calibration accuracy and applicability to the data collected during the mission. The calibration coefficients will continue to be refined as the flight data are further analyzed

## 1. INTRODUCTION

The Cryogenic Infrared Radiance Instrumentation for Shuttle (CIRRIS 1A) instrument, a state-of-the-art, cryogenically cooled instrument designed to observe the infrared spectrum of the Earth's atmosphere, was successfully flown on the shuttle Discovery during STS-39 (28 April - 6 May 1991). The primary objective of the CIRRIS 1A mission was to obtain spectral and spatial measurements of infrared atmospheric emissions under various conditions. Nearly 100% of the mission goals were achieved. Data obtained from this mission are being used to refine knowledge of the background radiance and structure of atmospheric infrared emissions. A summary of the CIRRIS 1A program is provided in Appendix 1.

This report provides the final results of the post flight calibration of the CIRRIS 1A instrument. In addition to the calibration results, the report also describes the instrument and provides general flight results. Lessons learned throughout the program are also discussed. The report is divided into two volumes: Volume I provides the complete text, as well as results for several detectors, and Volume II contains the results for all detectors, where available.

### 1.1 MISSION OBJECTIVES

The primary objective of the CIRRIS 1A mission was to obtain spectral and spatial measurements of infrared atmospheric emissions from earthlimb airglow, auroral enhancements, targets of opportunity (TOO), and contaminants. These measurements were made in the spectral range of 2.5 - 25  $\mu\text{m}$  over an altitude ranging from the Earth's surface to 260 km.

Data obtained from the CIRRIS 1A mission will ultimately be used to refine atmospheric infrared predictive models. Figure 1 shows the current U.S. Air Force radiance model of atmospheric airglow emissions for the infrared region between 2 and 26  $\mu\text{m}$  at a tangent height of 100 km. This figure shows significant emission peaks at 5.3  $\mu\text{m}$  (NO), 10  $\mu\text{m}$  ( $\text{O}_3$ ), and 15  $\mu\text{m}$  ( $\text{CO}_2$ ). Superimposed on this trace is the emission plot of a cold satellite target; clearly, the airglow emissions overwhelm the satellite emissions, except in narrow areas or windows between strong atmospheric bands. In order to detect a satellite or similar target, an infrared sensor must thus be filtered to admit radiation only from those narrow window areas. The CIRRIS 1A experiment was designed to obtain data to precisely define the extent of these spectral windows. The data from the auroral measurements will be used to validate and refine nuclear predictive codes.

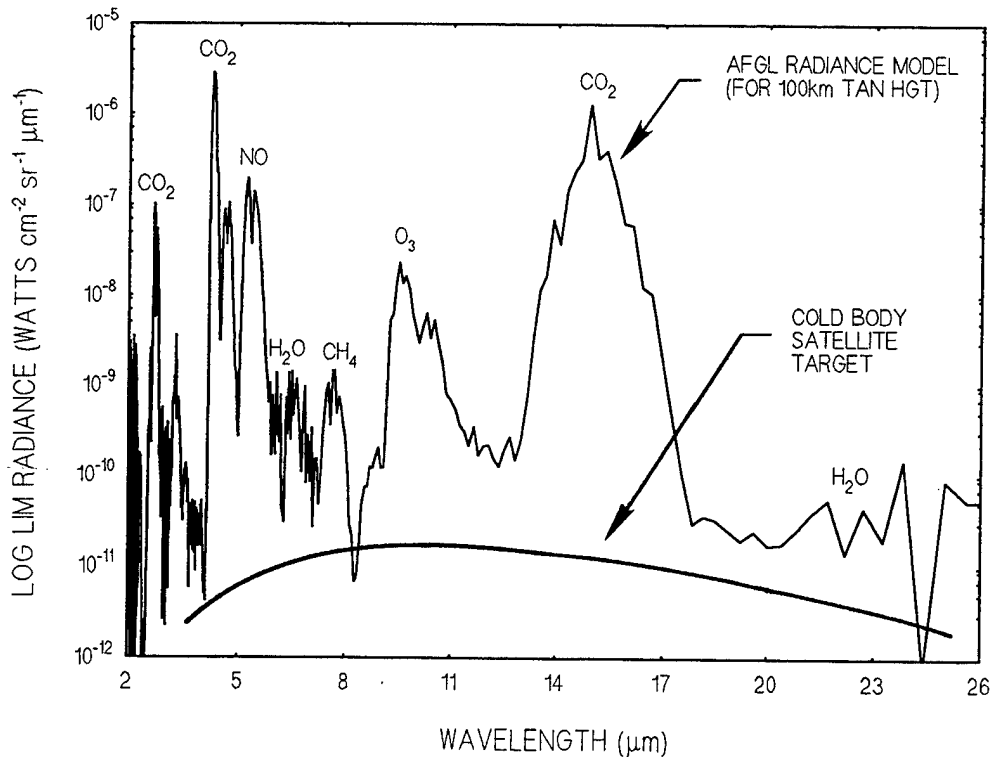


**Figure 1. Air Force earthlimb model of atmospheric infrared emissions compared with a theoretical 300 K 1-m<sup>2</sup> blackbody target.**

## 1.2 GENERAL INSTRUMENT DESCRIPTION

The CIRRIS 1A instrument, designed, constructed, and tested by the Space Dynamics Laboratory at Utah State University (SDL/USU), is a cryogenic instrument featuring two primary sensors; a high-resolution Michelson interferometer and a dual channel radiometer. These sensors share the common collecting optics of a high off-axis rejection 0.3 m telescope. The optics, detectors, and preamplifiers are cooled with helium to temperatures of 12 K to maximize the instrument's sensitivity to faint infrared sources. Coaligned on the outside of the telescope heat exchanger are two photometers, two low-light-level television (LLTV) cameras, a 16-mm film camera celestial aspect sensor (CAS), and an infrared horizon sensor. These ancillary sensors provide position data on the sensor's field of view. The entire assembly is mounted on a two-axis-gimbal system to provide pointing and scanning capability. All of the sensor and house-keeping data are redundantly recorded on tape recorders for post flight reduction and analysis. The entire payload mass is 2045 kg. Figure 2 is a photograph of the CIRRIS 1A instrument in its shipping container.

Detailed descriptions of the radiometer and interferometer are presented in Section 3 and Section 4, respectively. Descriptions of the ancillary instruments are in Section 5.

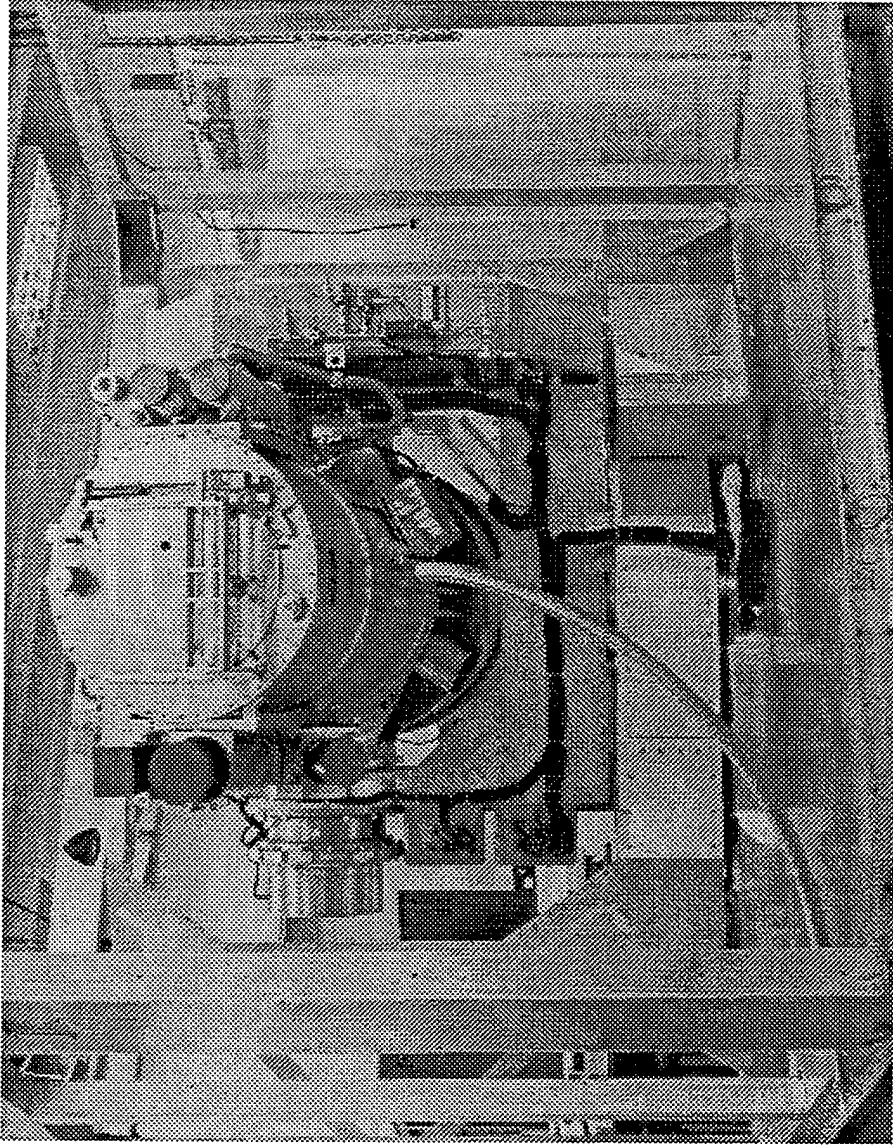


**Figure 2.** The CIRRIS 1A instrument installed in its shipping container.

### 1.2.1 CIRRIS 1A Optical System

The CIRRIS 1A optical system includes the telescope, radiometer, and interferometer. The telescope, which uses low scatter optics, is cryogenically cooled with liquid helium (LHe) from the supply dewar attached behind it. The primary sensors view objects through a quasi-elliptical entrance aperture in the telescope cover, which remains closed except during data taking sessions. The radiometer and interferometer employ 19 detectors that are arranged in three focal planes; the radiometer contains 14 detectors on two focal planes and the interferometer has 5 detectors on one focal plane. The interferometer focal plane and one radiometer focal plane are located behind precision filter wheels.

Figure 3 shows the schematic layout of the CIRRIS 1A optical system including the high off-axis rejection telescope, the two filter wheels, and the three focal planes. It also shows the locations of the internal calibration and stimulation sources used to verify operation during the mission, and discussed in paragraph 1.2.2.

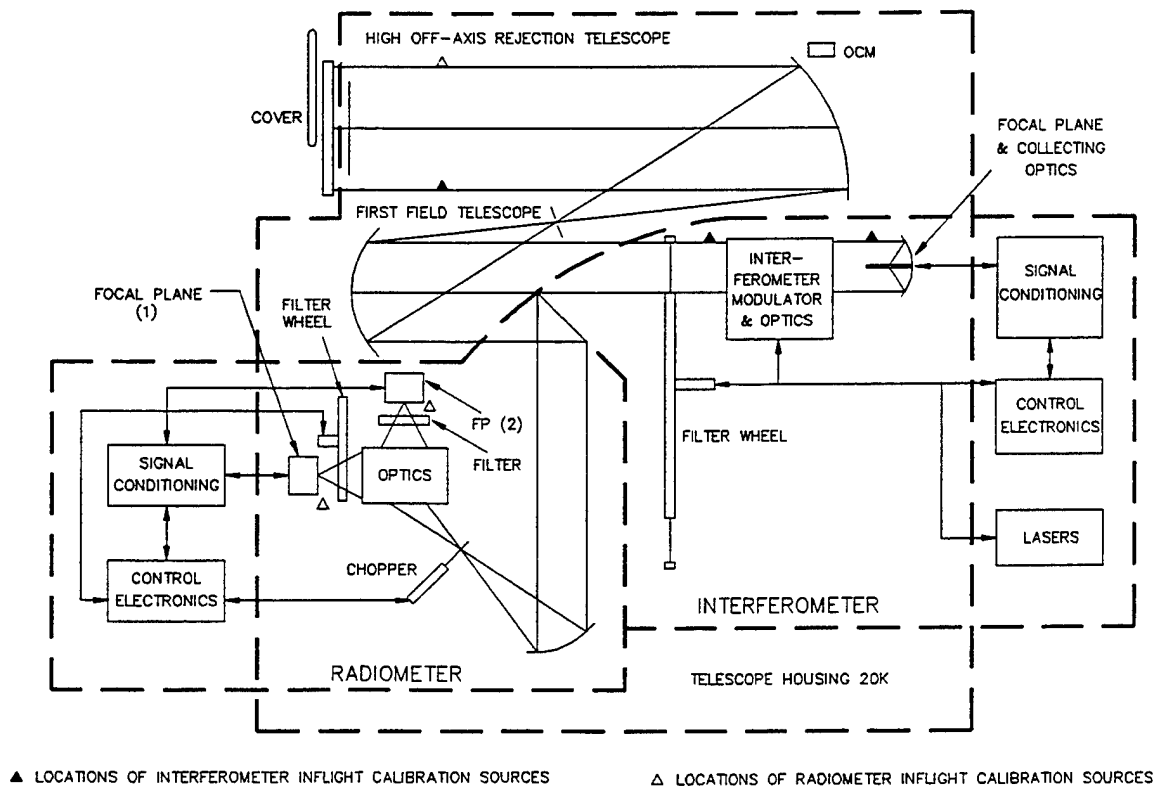


**Figure 3. Schematic layout of the CIRRIS 1A optical system.**

### 1.2.1.1 Telescope

The CIRRIS 1A high off-axis rejection telescope provides a low-scatter optical system to prevent the intense in-band energy emitted by the earth from biasing readings made in the near-earth atmosphere. The telescope has a 30.48-cm diameter, D-shaped aperture with an image quality of 0.5 mr on axis, optical efficiency of 60%, and an out-of-field-of-view rejection of  $1 \times 10^{-10}$  at 2.5 degrees.

The cleanliness of the telescope primary collection mirror is of primary importance to minimize the off-axis scattering of light within the system. To characterize the scatter from the primary mirror, an SDL/USU subcontractor, Sensor Systems Group (SSG), periodically performed Bi-directional Reflectance Distribution Function (BRDF) tests on the mirror. Although BRDF is normally measured with the mirror removed from the telescope, SSG developed an external BRDF station for this program that allowed measurement with the mirror mounted inside the telescope structure. A small region near the top-center of the mirror was tested during each measurement. A visual inspection of the mirror was also made during each test to assess the validity of using the reference spot to represent the entire mirror.

Figure 4 shows the history of the CIRRIS 1A BRDF measurements. The baseline BRDF measurement was made at SSG in January 1988. This test provided the in situ baseline BRDF, and agreed well with the BRDF measurement made with the mirror removed from the telescope. The second measurement, March 1988, occurred after the telescope was delivered to SDL, and showed that no contamination occurred during shipment. Additional measurements were made at the end of the engineering calibration effort (December 1988), and upon arrival at LMSC for integration (March 1989). Results from these tests showed that the mirror condition significantly degraded throughout the measurement period. Because of this degradation, the primary mirror was again cleaned prior to installation of CIRRIS 1A into the experiment support structure (ESS).

After cleaning, the BRDF was again measured (April 1989), showing the mirror condition to be at baseline conditions. Measurements were also made during integration at LMSC (December 1989), and prior to shipment to Kennedy Space Center (July 1990), which was also the final pre-flight BRDF test. Based on the final preflight BRDF measurement, SDL and SSG personnel agreed that the mirror condition was within acceptable limits. The post flight measurement, made in May 1991, showed evidence of particulate contamination and a light film coating on the mirror. SSG estimates that the BRDF of the primary mirror during the mission was in the range of  $8 \times 10^{-4}$  and  $2 \times 10^{-3}$  at  $1^\circ$ . SSG concluded that the degradation in BRDF during the final four in situ measurements (December 1990 to the post launch measurement in May 1991) most likely resulted from normal accumulation of contaminants during the pumping and cooling of the telescope during prelaunch operations. The slope of the line connecting the measurements indicated that only a small amount of contamination was due to accumulation of contamination during the mission when the telescope aperture was open.

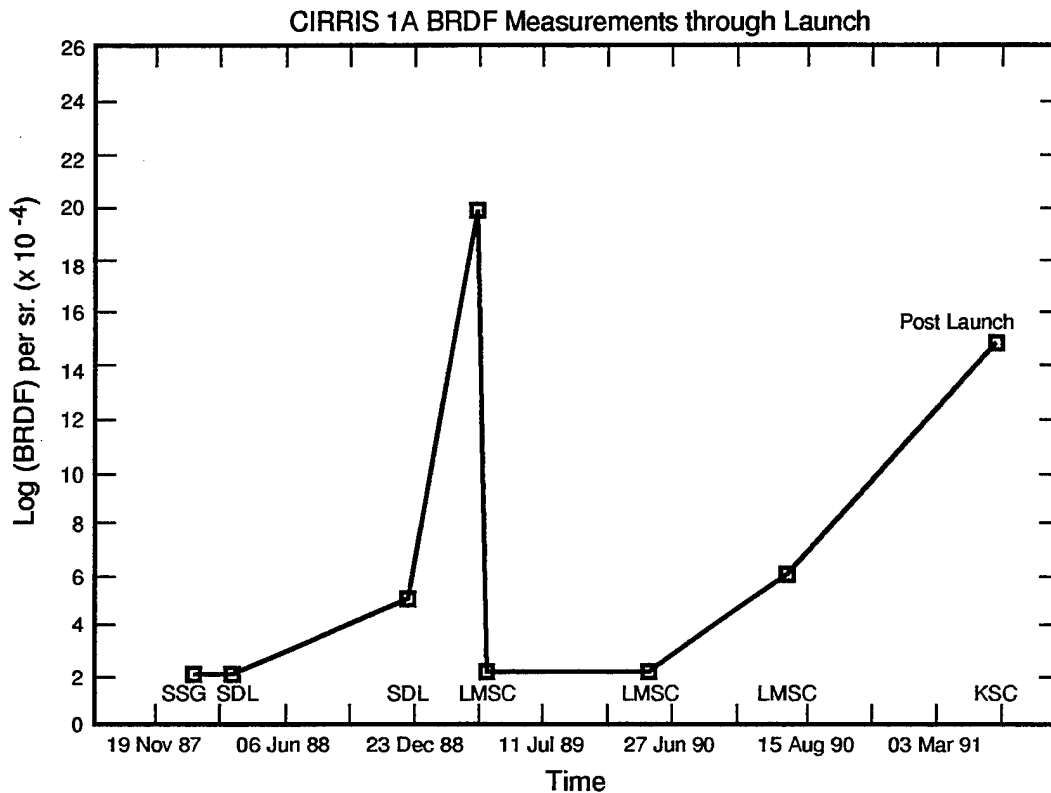


Figure 4. CIRRIS 1A BRDF measurement history.

### 1.2.1.2 Focal Plane Arrays

The radiometer focal plane arrays (FPA) consist of a 9-element focal plane, referred to as focal plane array 1, and a 5-element focal plane, referred to as focal plane 2. The interferometer FPA is a 5-element focal plane. Detailed description of the radiometer and interferometer focal planes are given in Section 3 and 4, respectively.

### 1.2.2 Internal Stimulation Sources

CIRRIS 1A contains internal stimulators for tracking instrument performance. Stimulators wide band 1, wide band 2, and stimulator (STIM) 3 are positioned in the baffle to reflect off the front cover of the telescope, and are visible by both the interferometer and radiometer. An off-axis source positioned to illuminate the primary mirror to monitor the scattering from its surface can also be seen by both instruments. Stimulators 1 and 2 (STIMS 1 and 2) are only visible to the radiometer, and only in the Chopper Off mode. STIM 1 is located at the detector array in focal plane array 1, and STIM 2 is at the detector array in focal plane array 2. A blackbody source and an alignment source are visible to the interferometer. Wide band 2 and STIM 3 were tracked by the radiometer through preflight operations and during flight. Interferometer performance was tracked using wide band 1 and a blackbody source located at the entrance of the interferometer cube.



### 1.2.3 Supercritical Helium Cooling System

The CIRRIS 1A supercritical helium cooling system consists of an upper cylindrical cryogenic heat exchanger section, which houses the telescope, and a lower dewar section, which is bolted to the upper section. The lower dewar system contains about 43 kg of supercritical helium at 5.0 K, 3.0 atm. These two components share a common vacuum environment. The helium is used to maintain the various optical detectors at about 10 K and the optical components, such as the telescope front baffle, at less than 40 K. There are two vapor-cooled shields, one in the dewar section and one in the heat exchanger section. The shields, dewar, and telescope are suspended from the outer vacuum enclosure by means of four G-10 support cylinders.

Figure 5 is a schematic diagram of the cryogenic cooling system. When the temperature of either the radiometer detector heat exchanger or the telescope mounting flange exceeds their operating limits, a control algorithm activates the primary heater to apply up to 5 watts to the helium in the dewar to increase the coolant flow rate. Each of the two focal planes is maintained at 10 K by a 150 mW trim heater.

As shown in Figure 5, after the helium passes through the interferometer detector heat exchanger, (IFR Det HtX), the radiometer detector heat exchanger (RAD Det HTX), and the telescope heat exchanger (Tele HtX), it then flows sequentially through the following heat exchangers: tank section rad shield, telescope section rad shield, and, finally, through the Environment Controlled Enclosure (ECE) heat exchanger, which has a 225 W maximum load. Figure 5 also contains plumbing information about items such as burst disks, valves, the Tylan helium flow meter, and temperature diode locations designated by the C-numbers (C for CIRRIS). The pressure of the helium in the dewar is held constant at 3.0 atm. (44.09 psia) by one of the two Tavco absolute pressure relief valves; the other Tavco valve is for backup. The total mass of the dewar, heat exchanger, and telescope is about 680 kg (1500 lbm).

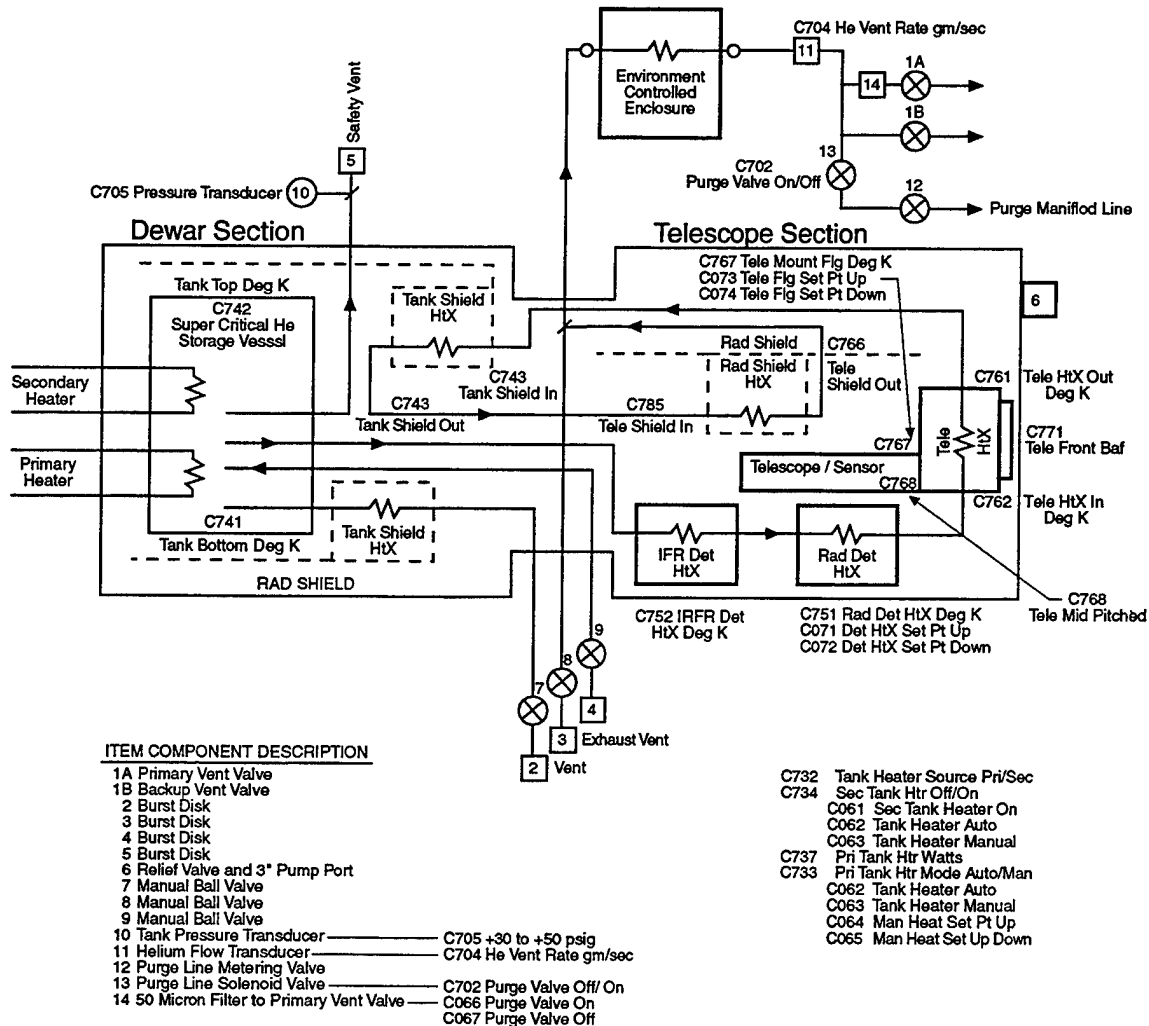


Figure 5. Schematic of the CIRRI 1A cryogenic cooling system.

### 1.3 FLIGHT SUMMARY

CIRRI 1A was launched on 28 April 1991 from Kennedy Space Center (KSC) on board the space shuttle Discovery (STS-39) into a 260-km circular orbit at an inclination of 57 degrees. The shuttle landed at KSC on 6 May 1991 after a successful mission. SDL/USU, Phillips Laboratory, and other essential flight operations personnel were located at the Payload Operations Control Center (POCC) at Johnson Space Center (JSC) to assist the mission specialists. Although no downlink existed to acquire continuous real time data, flight operations personnel at JSC verbally obtained temperature and vacuum trending data, tape recorder hours used, and various other parameters from the mission specialists. This enabled the CIRRI 1A scientists and engineers to closely follow instrument performance.

All of the CIRRI 1A instruments arrived on orbit in a fully functional condition and met or exceeded all specifications and requirements during the mission. The interferometer and radiome-

ter functioned in nearly 140 different operational measurement modes and nearly 20 hours of prime data were collected and stored on the CIRRIS 1A tape recorder units. The interferometer arrived on orbit in proper alignment, indicating that all optical, mechanical, and electrical elements of the interferometer remained in position throughout the launch phase.

The ancillary instruments also operated successfully on orbit. The LLLTVs provided scenes ranging from celestial to hard earth views. The wide field-of-view (WFOV) camera reticle altitude settings correlated to the predicted altitudes of the aurora and air glow. The narrow field-of-view camera sensitivity appeared to be nominal and the autoranging capabilities worked as designed. Coalignment appeared to be closely correlated to the WFOV camera, as expected. The celestial aspect sensor, horizon sensor, and data handling and recording equipment performed as designed during flight. The pointing system also performed as designed, effectively tracking resident space objects (RSOs), the most difficult pointing exercise.

Analysis of the flight data indicates that photometer output decreased in sensitivity during flight, suggesting that the photometers did not perform as expected. Post flight tests indicate that this decreased sensitivity resulted from exposure to very high light levels at various times throughout the flight. This behavior was also observed during ground testing. A second condition observed during post flight testing was an apparent "shut off" during exposure to high light levels. Photometer tubes will saturate at a particular light level, and any further flux increase actually produces a lower count output. It appears that during the intense auroral activity in the early portion of the flight, the photometers were exposed to flux levels higher than they were designed to measure. While the photometers were protected by a sun sensor, this sensor was not sensitive enough to shut down the photometers in the intense aurora. Despite these problems, the photometers still provided several hours of useful data. Post flight testing showed that the photometers were working properly, although at a decreased sensitivity.

A second flight anomaly occurred with the data formatting equipment (DFE). DFE-2 quit operating while the system was powered up via bus A, PDC-1. When this anomaly was detected, the DFE was switched to the redundant bus B, PDC-2 and the mission continued without additional failure. Post flight inspection showed that the +28 volt fuse in PDC-1 had blown. After the fuse was replaced, the DFE operated properly. The ability to switch to a redundant system contributed to the success of the mission. The cause of the fuse failure was not discovered.

The CIRRIS 1A supercritical helium cooling system successfully cooled all telescope components and electronics boxes through the 72-hour data collection period of the flight. While taking data, the focal planes, telescope components, and the front telescope baffle were maintained within design temperature brackets. However, the actual parasitic helium flow rate was nearly double that predicted for flight, and the dewar helium pressure increased after the aperture was opened. This resulted in an earlier-than-predicted cryogen run out, and necessitated re-scheduling the flight operations' timeline to assure that all CIRRIS 1A operations could be accomplished. With the amended timeline, all significant operations were completed. A complete discussion of the flight results are presented in Vendell et al. (1992).

Approximately 18 hours of airglow and auroral data were recorded on the CIRRIS 1A tape recorders during the mission. This includes about 200,000 interferometer spectral scans and 30 gi-

gabytes of multispectral radiometer data. After flight, the flight data tapes were copied to optical disks (in a 9-file format) for verification and analysis.

#### **1.4 FLIGHT DATA VERIFICATION AND ANALYSIS**

After arrival of the CIRRIS 1A instrument at Kennedy Space Center (KSC), the flight data tapes were removed and transported to Hanscom Air Force Base following the procedure outlined in "CIRRIS-1A Recovery Operations Plan," SDL/91-082. The tapes were duplicated following the procedure outlined in "CIRRIS 1A Flight Tape Duplication Report," SDL/91-093.

In general, the CIRRIS 1A data processing system processed data in the following order: duplicate the data onto analog tapes; separate and digitize the interferometer and radiometer data streams; preprocess the data and store on optical disks; and provide analytical tools for data analysis.

The flight data are currently being verified and analyzed by the computer aided data display and analysis system, OPUS (Optical Physics User System), which was developed jointly by Phillips Laboratory, SDL, and Boston College, and coded by Boston College. OPUS is a timeline based, user friendly software system that can display the flight data using a variety of processing algorithms. The system uses both the preflight and post flight calibration data. OPUS reads the 9-file raw data format and displays the timeline, filter, amplifier, tangent height, and many other parameters that are required to certify the data. The data can be displayed as voltages, calibrated spectra, and radiances, and are stored in an ASCII file format for further analysis.

## 2. CALIBRATION METHODS

### 2.1 CALIBRATION HISTORY

Calibration of electro-optical systems is necessary to verify the instrument design and to create algorithms to assist in pre-mission readiness certification and post flight data reduction. SDL personnel performed the first preflight engineering calibration on CIRRIS 1A during 1984/85. The results of this calibration effort are reported in "An Engineering Calibration of CIRRIS 1A," CSE/86-011. When CIRRIS 1A was returned to SDL/USU in 1986 after the Challenger disaster, additional calibration efforts were performed to further characterize the instrument's performance envelope. Various aspects of the 1986 calibration are presented in "CIRRIS 1A Final Calibration Test Report, Appendices A, B, and C," CSE/87-039.

SDL/USU personnel upgraded the CIRRIS 1A instrument during the time delays after the Challenger disaster. Because of these refurbishments, much of the original calibration was invalidated, and recalibration became necessary.

SDL/USU personnel performed a preflight engineering evaluation on the CIRRIS 1A instrument during October through December 1988. The purpose of the engineering evaluation was to verify that the system was operational and in compliance with the design specifications. Data from this evaluation also provided preliminary calibration coefficients to quantify the flight data. The preflight engineering evaluation is described in "CIRRIS 1A Final Engineering Calibration Report," (SDL/91-056).

After flight, SDL/USU personnel performed a full post flight calibration on the primary infrared sensors and ancillary sensors. The first phase of data collection began on 21 October 1991 and was completed on 8 December 1991. The preliminary results of this effort are found in "CIRRIS 1A Post Flight Calibration Interim Report," SDL/92-004. A second calibration data collection period, Phase 2, was performed from 14 to 29 February 1992 to complete the full calibration. This second test was used to complete partial calibration data sets, and to resolve problems from the Phase 1 data collection period. The post flight calibration concentrated on instrument characterization. The data collected were used to update the calibration coefficients used in the OPUS software and to resolve instrument behavior questions.

### 2.2 PROCEDURES

The CIRRIS 1A post flight calibration followed the procedures outlined in "CIRRIS 1A Post Flight Calibration Test Plan" (SDL/91-011). SDL/USU personnel performed the calibration with a multifunction calibrator, and collected data with the multifunction calibrator control and monitor system (CMS). SDL/USU personnel and subcontractors, Atmospheric Radiation Consultants, Inc. (ARC) and Yap Analytics, Inc. participated in the analysis of the data.

### 2.3 CALIBRATION APPROACH

SDL characterized the overall responsivity of the CIRRIS 1A radiometer and interferometer in terms of separate radiometric parameters. These parameters included: absolute responsivity

over the sensor's dynamic range, spectral responsivity, spatial responsivity (the two-dimensional field of view), and temporal responsivity (frequency response). The goal of the calibration was to characterize each radiometric parameter independently of the others. Together, these individually characterized parameters comprise a complete calibration for the radiometric sensor.

To accomplish this task, a specific calibration equation and radiometric model were generated for each sensor. The calibration equation and radiometric model describe the overall responsivity of the sensor in terms of separate radiometric parameters (Wyatt, 1978). The calibration equation correlates sensor output to measured flux, while the radiometric model relates the measured flux to the true scene flux (Jacobsen and Sargent, 1990). The calibration equations for the radiometer and interferometer are presented in Section 3 and Section 4, respectively.

The CIRRIS 1A post flight calibration included an estimation of measurement uncertainties. This report provides these uncertainties, including descriptions of their applicability to any particular measurement objective. Four general classes of uncertainties are addressed: random uncertainties, calibration residual uncertainties, nonideal sensor performance uncertainties, and standard source uncertainties. Random uncertainties include short term repeatability (noise) and long term repeatability. Calibration residual uncertainties are uncertainties associated with parameters in the calibration equation, such as the uncertainty of a gain or bias-mode normalization parameter. Nonideal sensor performance uncertainties are a result of nonideal sensor characteristics and are addressed in the radiometric model. The fourth category is uncertainty in standard sources used in the calibration, such as uncertainty in the temperature of a blackbody simulator.

## 2.4 CALIBRATION SOURCE

The post flight calibration was performed with a multifunction calibration system that has several types of infrared sources contained within one instrument, including a collimated energy source, diffuse scatter source, extended-area source, and Jones source. The multifunction source has exterior windows allowing use of external blackbody sources. The multifunction calibration source eliminates the time consuming and costly warmup/cool-down cycles associated with single-function calibration sources, such as those used in the CIRRIS 1A engineering evaluation.

SDL/USU personnel performed the CIRRIS 1A post flight calibration with the multifunction calibrator developed under the SPIRIT II program. This calibrator is known as the Multifunction Infrared Calibrator #2, or MIC 2, and is described in "SPIRIT II Infrared Sensor Calibration Test Plan" (SDL/89-026A). Figure 6 shows the four optical configurations of MIC 2. In addition to these four configurations, data were also collected with the sensors' internal sources, without any source (i.e., dark noise state), and with the external Bomem interferometer as a modulated source. It was necessary to rotate the calibrator 90° to fit the CIRRIS 1A entrance aperture to the calibrator exit port so that the calibrator completely filled the CIRRIS 1A entrance aperture. Figure 7 presents this configuration. CIRRIS 1A was moved forward in the shipping container and remounted to allow it to be bolted directly to the calibrator exit aperture.

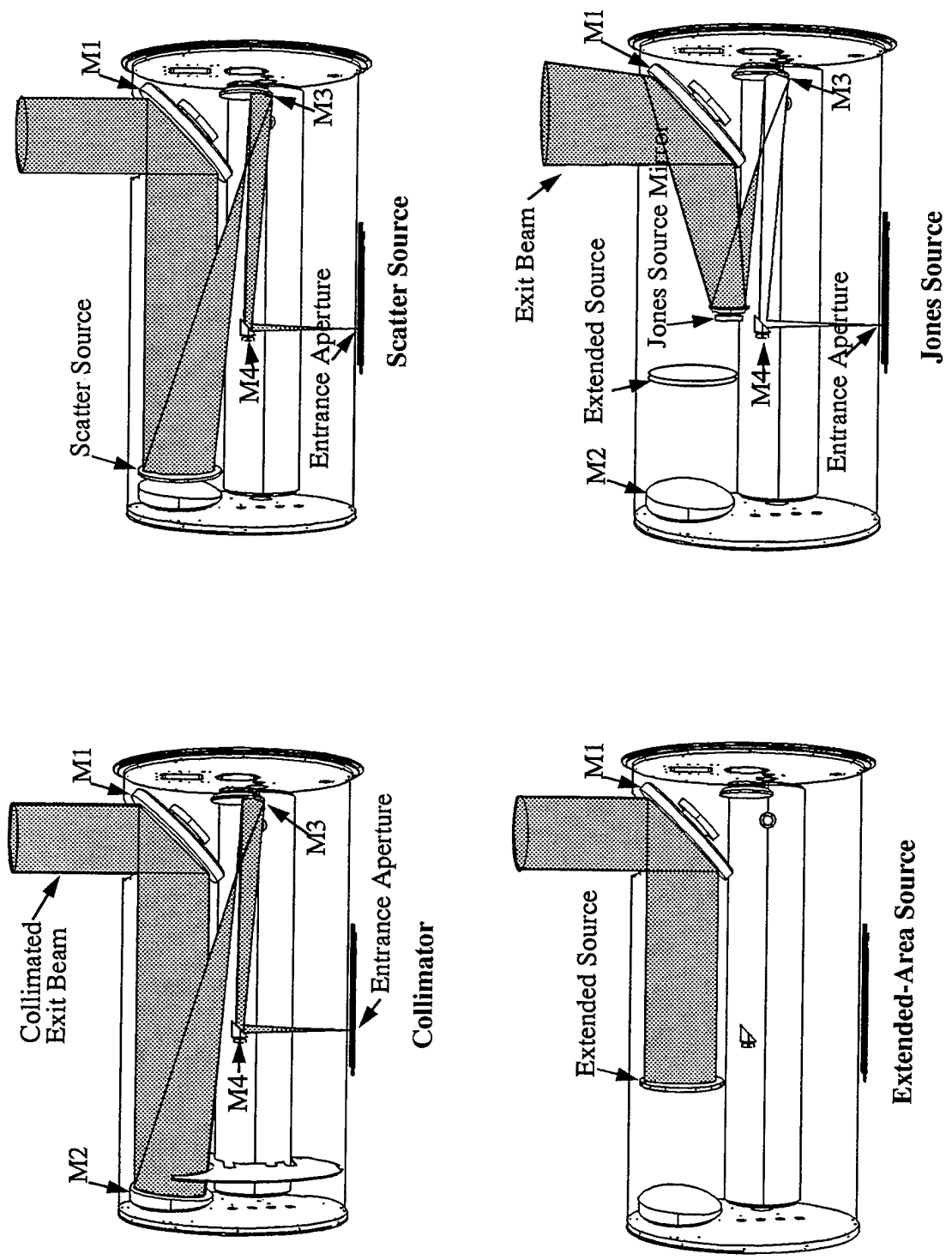
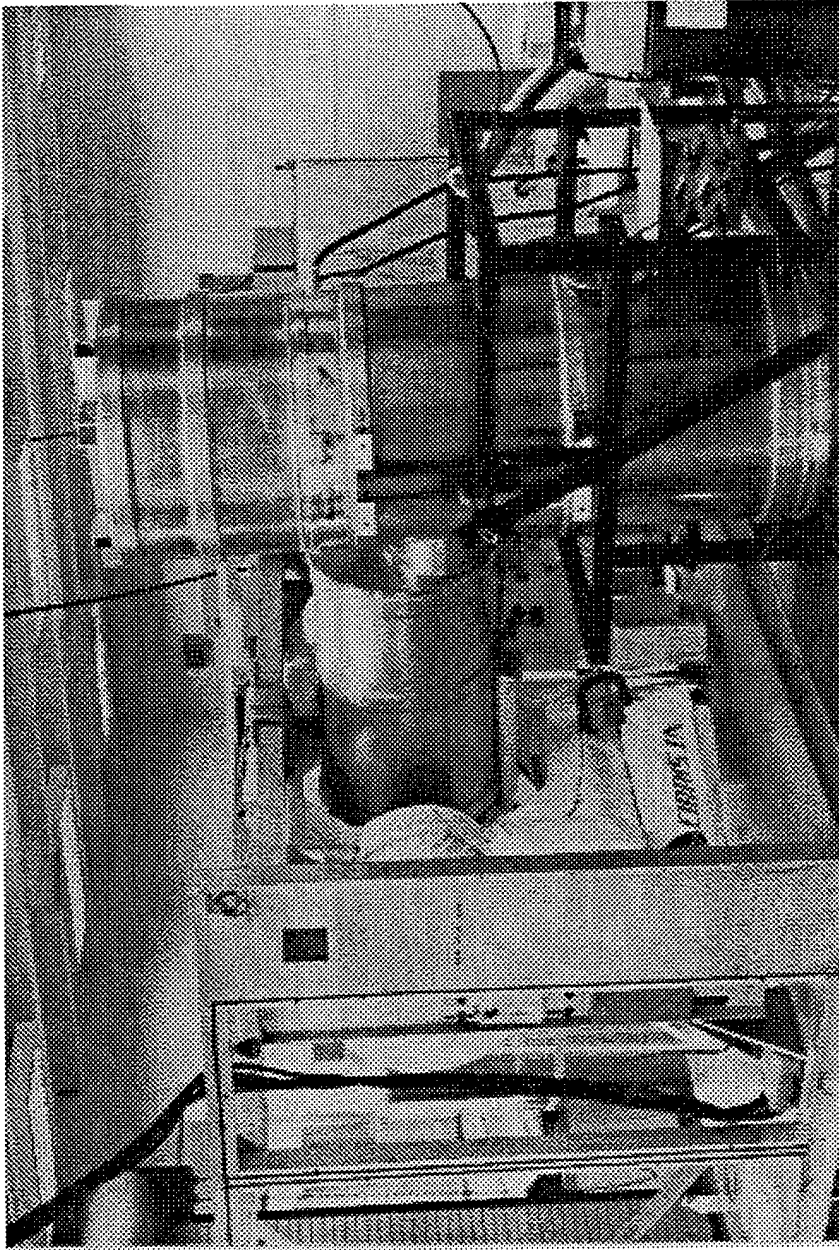


Figure 6. Optical configurations of multifunction infrared calibrator 2 (MIC2).



**Figure 7. CIRRIS 1A mated to the multifunction calibrator.**



## 2.5 CALIBRATION DATA ANALYSIS SYSTEM

SDL/USU personnel developed a computerized data analysis system to control the calibration sources, record data, process recorded data through calibration algorithms, and analyze the resulting calibration data. Data analysis was performed with commercially available software, standard calibration programs developed by SDL/USU, and new software written specifically for this calibration.

Figure 8 shows the data collection setup. The command and monitor system (CMS), a COMPAQ, 20MHz, 386 personal computer, provided commands to the calibrator and collected data from the CIRRIS 1A instrument. This system automatically tagged the calibration data samples with a 512 byte header describing the current configuration of the calibration source. These data were then sent to the host network computer, a DECstation 5000, for archival and distribution. The real-time monitor system collected and displayed data from CIRRIS 1A, and provided a real-time data quality check.

Figure 9 shows the data distribution setup. Five 486-class personal computers were networked to the host computer that obtained the data from the CMS. One computer performed the point source analysis, two computers performed the radiometer analysis, and two performed the interferometer analysis. The network host computer also transferred data to Sony, 640 MB optical disks for storage and archive.

During calibration SDL/USU personnel used the calibration data system to record data. This system automatically tagged these data with a header describing the current configuration of the calibration source and then stored the sample on optical disks. The format of the stored data is described in SDL/90-056A (Elwell and Kemp, 1991).

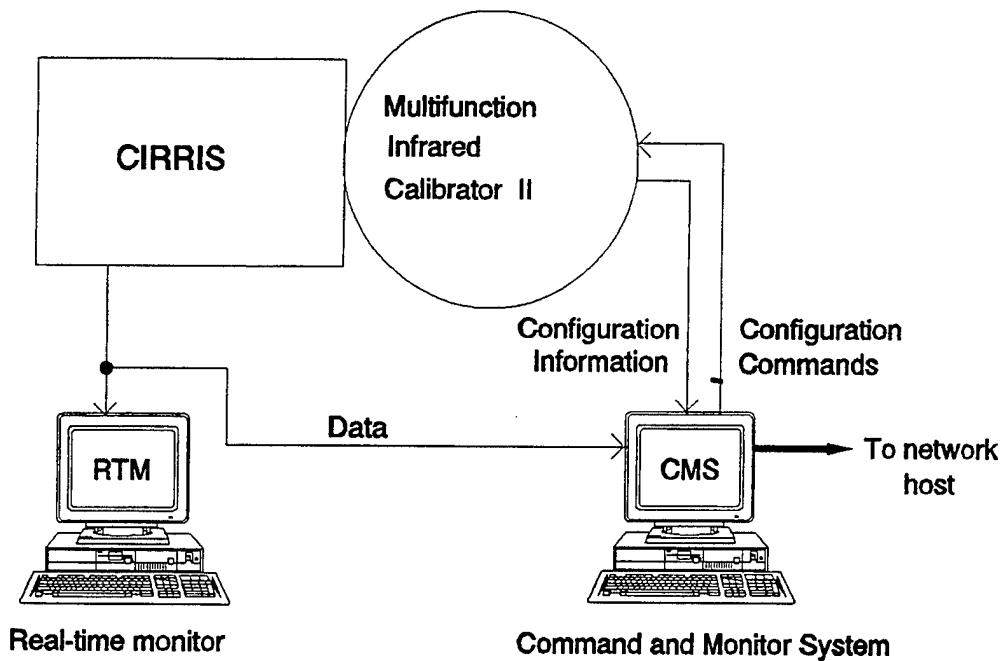


Figure 8. CIRRIS 1A calibration data collection setup.

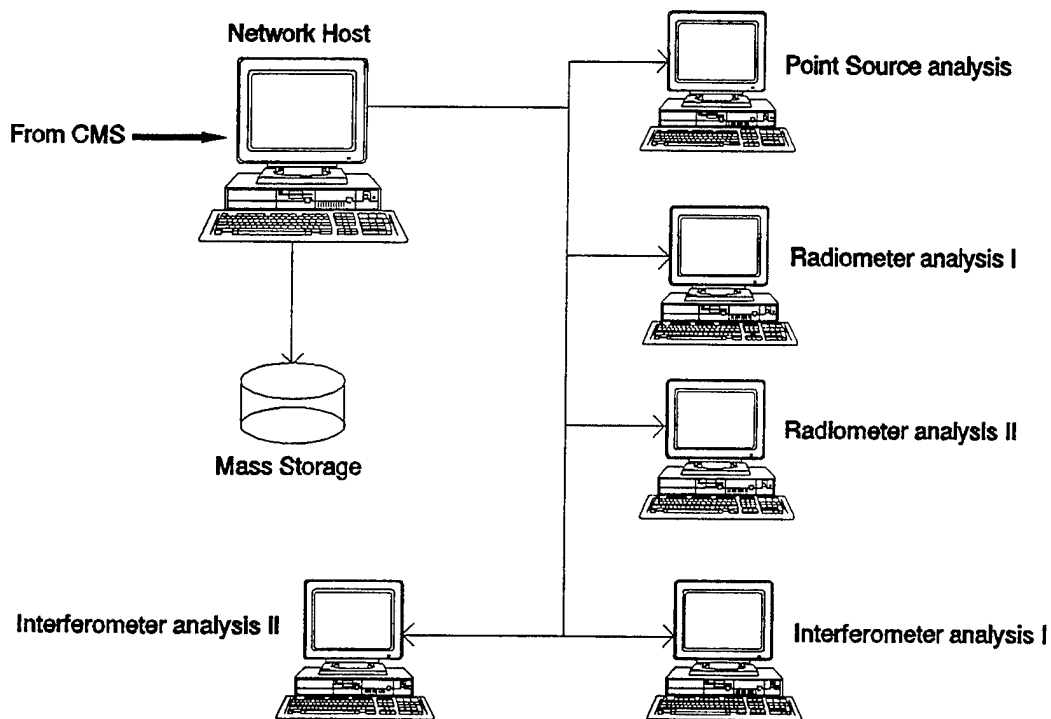


Figure 9. CIRRIS 1A calibration data distribution setup.

### 3. RADIOMETER CALIBRATION RESULTS

#### 3.1 INTRODUCTION

##### 3.1.1 Radiometer Description

The CIRRIS 1A radiometer is a sensitive spatial radiometer that measures the radiation or intensity of infrared radiation in the spectral range between  $2.5\mu\text{m}$  and  $25\mu\text{m}$  over an 8-order dynamic range. It features 14 detectors that are arrayed on two focal planes, providing an overall field of view of  $21\text{ mr} \times 2.0\text{ mr}$ . The radiometer design uses optical filters to reduce photon noise. In addition, it allows for adjusting bias over three functional levels and conditions detector output signals at two electronic gain levels.

Major functional sensor elements include the focal plane assembly, radiometer control electronics (RCE) and radiometer signal conditioning electronics (RSCE). Energy from the telescope is first modulated by the tuning fork chopper and then enters the focal plane optics in a diverging beam; an optical element converts this to a converging beam before it enters the beamsplitter proper. The beamsplitter divides the energy, sending part through the filter wheel to a 9-element focal plane, and part through the fixed  $2.95\mu\text{m}$  filter to a 5-element focal plane. The signals induced in the detectors are dc-coupled in the cold preamplifiers, go through the RSCE process of gain ranging and analog-to-digital conversion, and are formatted and recorded by the data formatting equipment (DFE). The chopper operation, filter wheel position, and focal plane assembly temperatures are all monitored and controlled in the RCE.

The radiometer focal plane arrays (FPA) consist of a 9-element focal plane, referred to as FPA 1, and a 5-element focal plane, referred to as FPA 2. Individual detectors are referred to as detector X-N, where X refers to the FPA and N designates the individual detector on that array. For example, detector 1-4 refers to detector 4 on focal plane array 1. FPA 1 is located behind a filter wheel that contains a precision set of optical filters. FPA 2 has a  $2.95\mu\text{m}$  fixed filter. Table 1 lists the radiometer filter characteristics. Santa Barbara Research Center (SBRC) designed and fabricated the radiometer 9-element FPA, and Aerojet ElectroSystems Company (AESC) designed and fabricated the radiometer 5-element FPA. FPA 1 contains bulk-type detectors fabricated from Si:As material, while the FPA 2 detectors were fabricated from Si:Bi material. Detector 1-9 was delivered to SDL with a failed pre-amplifier circuit, but was accepted for flight due to time constraints.

Figure 10 shows the arrangement of the CIRRIS 1A radiometer focal planes, showing the location and resolution of the individual detectors and individual detector numbers. The focal planes are shown in object space. The figure includes field-of-view (mr) and resolution (km) data for some of the detectors.

Table 1. CIRRIS 1A Radiometer Filter Wheel Characteristics

Position Number	Description	Bandpass $\mu\text{m}$
FPA 2	Fixed narrow bandpass	3.3 short pass
0	Filter wheel wide bandpass	8.0 - 17.5
1	Filter wheel narrow bandpass	4.1 - 4.6
2	Filter wheel narrow bandpass	5.0 - 7.0
3*	Filter wheel narrow bandpass	6.0 - 9.0
4	Filter wheel blank	Closed
5*	Filter wheel narrow bandpass	11.0 - 13.0
6*	Filter wheel high bandpass	> 17.0
7	Filter wheel wide bandpass	8.0 - 12.0

\* These filters are cascaded to improve out-of-band rejection.

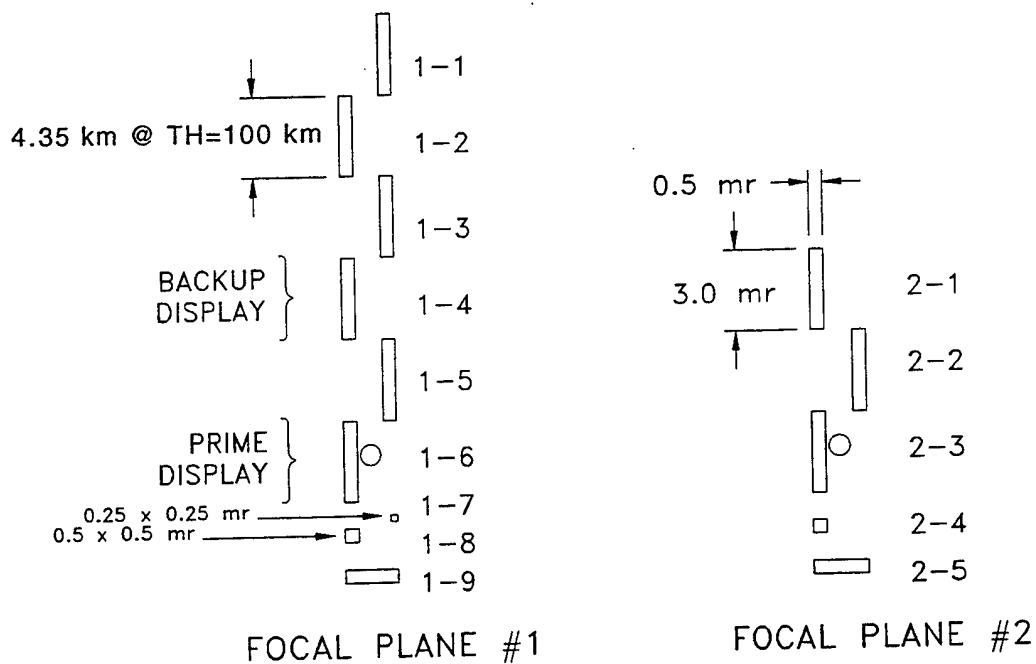


Figure 10. CIRRIS 1A radiometer focal plane array configuration.

### 3.1.2 Radiometer Calibration Equation

The CIRRIS 1A radiometer calibration equation correlates the radiometer's response to measured flux and allows the estimation of the measurement uncertainty. The CIRRIS 1A calibration was designed to provide the coefficients needed to complete the equation. Equation (1) is the radiometer calibration equation for the Chopper On condition. Because only one data set was collected in the Chopper Off mode during flight, only two Chopper Off conditions required calibration. Therefore, the Chopper Off equation is not presented here.

Chopper On

$$\Phi_{m_{d,f,b,g}} = \frac{1}{\mathfrak{R}_{d,f,b,g}} [L_{d,b,g} [DC(Resp_{d,f,b,g})]] \pm \sigma_{d,f,b,g} \quad (1)$$

where

d	=	radiometer detector number
f	=	radiometer filter position (focal plane 1 only)
b	=	bias gain (unitless)
g	=	electronic gain (unitless)
$\Phi_{m_{d,f,b,g}}$	=	measured flux in $W\ cm^{-2}\ sr^{-1}$
$\mathfrak{R}_{d,f,b,g}$	=	absolute responsivity in volts/ $W\ cm^{-2}\ sr^{-1}$
$L_{d,b,g} [ ]$	=	linearity correction function (unitless)
DC ( )	=	DC restoration function (unitless)
$Resp_{d,f,b,g}$	=	radiometer response in volts
$\sigma_{d,f,b,g}$	=	measurement uncertainty

### 3.1.3 Radiometer Radiometric Model

The radiometric model relates the radiometer's measured radiance from Equation (1) to the true scene radiance incident on the CIRRIS 1A telescope entrance aperture. The radiometric model characterizes the CIRRIS 1A radiometer's spatial, spectral, and temporal responsivity domains. The spatial domain is characterized by point source response functions (PSRs), modulation transfer functions (MTFs), detector positions, effective field-of-view solid angles, and detector-to-detector crosstalk. The spectral domain analysis includes the radiometer's in-band relative spectral responsivity, out-of-band spectral blocking, and spectral purity (Wyatt 1978). The radiometer's relative frequency responsivity characterizes the temporal domain.

Each term in the calibration equation and each domain in the radiometric model describe a specific radiometric parameter. The goal of calibration is to characterize each parameter independently of the others. Together, these individually characterized radiometric parameters comprise a complete calibration of the CIRRIS 1A radiometer.

## 3.2 RADIOMETER CALIBRATION TESTS AND RESULTS

The calibration products described in this report were provided to Phillips Laboratory in computer-compatible formats. The products include the data from tables and graphs of this report and raw telemetry data files collected during the ground calibration.

This section contains the reduced calibration data for the primary radiometer detectors, 1-6 and 2-3. Volume 2 of this report contains the reduced data in for all of the radiometer detectors, where applicable.

### 3.2.1 Point Source Spatial Response

The point source calibration determines the shape of several radiometer spatial response functions. These functions include the effective field-of-view solid angles and relative spatial lines of sight for each radiometer detector. The point source calibration also allows calculation of modulation transfer functions (MTFs) and derives the scatter coefficients for each detector.

The radiometer point source (spatial) response (PSR) was mapped seven times during the post flight calibration. Each map was generated by moving a point source across the focal planes in regular steps to provide an array of response measurements. The output of each detector was recorded for each location so that scattering, crosstalk, and point source response could be determined.

In the PSR survey, preliminary detector locations were determined relative to the position of the calibrator's pointing mirror. In addition, peak detector responses were checked for saturation. For the PSR survey, data were collected over a large spatial area to determine the focal plane's approximate position. Data for the PSR maps were collected by positioning the collimator pointing mirror at discrete locations on the focal plane. Incrementing was performed in the X direction for constant values of Y. For each data point, collimator position and 40 minor frames were collected using automated data collection routines. For each constant scan in Y, one data file was created containing each point in X. The radiometer chopper was turned on for each measurement. These maps were processed to give each detector's response as a function of a two-dimensional point source position.

The PSR data were preprocessed according to the following steps:

1. DC restoration
2. Transforming constant Y value files into a file for each detector containing response as a function of X,Y position
3. Exchanging X and Y axes, and mirroring X to obtain object space
4. Peak normalizing each detector's response

After preprocessing, data were processed to obtain individual PSR parameters. For many parameters, this included referencing the previously relative X,Y coordinates to the calculated centroid of detector 3-2.

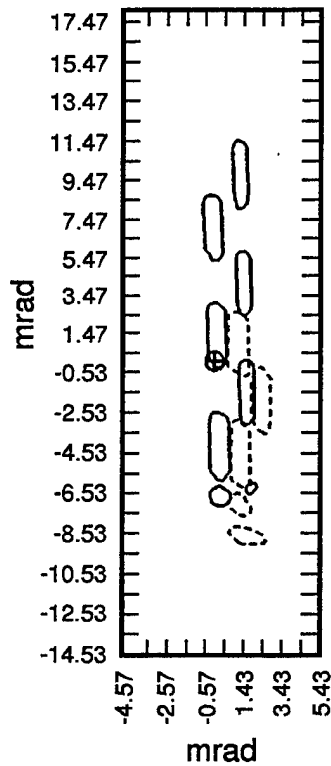
The specific configuration used to generate each of the four PSR maps are given in Table 2.

**Table 2. Point Source Response Map Parameters**

Map	$\Delta X$	$\Delta Y$	Source ( $\mu\text{rad}$ )	Detector	Filter	Filter $\lambda(\mu\text{m})$
A	0.1	0.25	40	All	1	2.5-4.3
B	0.05	0.05	40	1-7, 1-8	1	2.5-4.3
C	0.1	0.25	40	All	6	>17
D	0.05	0.05	40	1-7, 1-8	6	>17
E	0.05	0.05	40	1-7, 1-8	1	2.5-4.3
F	0.05	0.05	40	1-7, 1-8	5	11.0-13.0
G	0.05	0.05	40	1-7, 1-8	6	>17

### 3.2.1.1 Detector Positions

The position viewed in object space, or line-of-sight, of each radiometer detector must be characterized to interpret the sensor's response to spatially modulated scenes. To generate this map, the point-source response tables for each detector were normalized to that detector's peak response. Using this peak-normalized data, a contour was drawn to enclose the area whose response was above 0.1. Using responses greater than 10% avoids including scatter response in the centroid summation. The 10% response contours for the two radiometer focal planes are shown in Figure 11, which qualitatively shows the detector positions. The detectors are mapped in object space, which is the mirror image of the physical focal plane layout. To convert the raw data to object space, the X and Y axes were exchanged and the X axis was mirrored. The axes were also offset-corrected to transfer the reference point of the map, 0,0, to the centroid of interferometer detector 3-2. Coalignment of the ancillary sensors, along with other spatial references, are also referenced to the center of detector 3-2. These contours can be compared with the focal plane designs shown in Figure 10.



Transposed  
 Mirrored in X  
 (object space)  
 Peak Normalized  
 Power Contours (10%)

DESCRIPTION  
 Detector FP2L  
 Starting X 7.50  
 Starting Y -2.00  
 Number of X 101  
 Number of Y 131  
 Delta X 0.10  
 Delta Y 0.25  
 Minimum -0.001493  
 Maximum 0.8616  
 D:\RPSMAP6\M6FP2SUM

Figure 11. Composite detector response contour map of radiometer focal planes 1 and 2.

The contours cannot be used directly in a computer processing data system. To provide machine usable lines of sight, the same data used to develop the 0.1-response contours were also analyzed to determine the response center of each detector, defined as the X- and Y-centroids of response and given by:

$$Centroid_x = \frac{\sum_{Above\ 0.10} X\ Resp}{\sum_{Above\ 1.10} Resp} \quad (2)$$

$$Centroid_y = \frac{\sum_{Above\ 0.10} Y\ Resp}{\sum_{Above\ 0.10} Resp} \quad (3)$$

where

- Centroid = X or Y response centroid in mrad
- Resp = offset-corrected, peak-normalized response amplitudes
- X = X response coordinate in mrad
- Y = Y response coordinate in mrad



Table 3 gives the object-space position coordinates for the radiometer detectors.

**Table 3. Summary of Radiometer Detector Centroids**

Detector	Centered	
	X (mrad)	Y (mrad)
1-1	1.351	9.985
1-2	-0.092	7.194
1-3	1.489	4.179
1-4	0.023	1.495
1-5	1.567	-1.475
1-6	0.163	-4.247
1-7	1.806	-6.279
1-8	0.174	-6.859
2-1	1.175	1.034
2-2	2.389	-1.737
2-3	1.199	-4.622
2-4	1.246	-7.202
2-5	1.496	-8.711

### 3.2.1.2 Scatter

The scatter coefficient is the fraction of a detector's response that is due to scatter, when exposed to a spatially uniform scene, in other words, a detector's response to light that originated outside of the field of view of the detector. Scatter coefficients are used to interpret data from spatially modulated scenes. Scatter is determined from the point source response data using the equation:

$$Scatter = \left[ \frac{\sum_{scat} Resp}{\sum_{det} Resp + \sum_{scat} Resp} \right] 100 \quad (4)$$

where

- Scatter = scatter coefficient
- Resp = offset corrected, peak-normalized point source responses

Equation (4) uses summations of the response to avoid exaggeration of low-signal, noisy responses. If only the amplitude of noisy responses is summed, noise is rectified and is incorrectly interpreted as scatter.

Scatter was calculated by assuming that response below an amplitude threshold level is due to scatter. This assumption falsely includes the portion of the in-field-of-view response below the threshold as scatter. However, its effects are relatively small if scatter is significant. Equation (4) numerically represents the summation of the detector response below the scatter threshold divided by the total detector response. Scatter was calculated for two thresholds, 0.1% and 0.5% levels.

The scatter coefficients for each CIRRIIS 1A radiometer detector are given in Table 4 at both the 0.1% and 0.5% levels. As these coefficients show, the CIRRIIS 1A radiometer detectors had no significant scatter sources.

**Table 4. Summary of Radiometer Detector Scatter**

Detector	Scatter <0.1 of peak (%)	Scatter <0.5 of peak (%)
1-1	8.1	35.1
1-2	3.3	26.5
1-3	7.9	26.6
1-4	7.8	36.1
1-5	7.4	29.6
1-6	1.6	28.1
1-7	32.2	52.8
1-8	12.9	49.0
2-1	7.4	31.0
2-2	42.0	61.6
2-3	7.5	34.0
2-4	9.2	45.2
2-5	14.6	53.9

### 3.2.1.3 Crosstalk

Point source response maps showed no significant crosstalk between the detectors at the 1% level (0.01).

### 3.2.1.4 Point Source Response Maps

The spatial response of a detector can be graphically displayed by a contour map. Such maps are useful to subjectively evaluate the spatial response of a detector. This analysis is especially useful to reveal vignetting problems and locate sources of scatter.

Figure 12 gives the point source response map for the radiometer focal planes 1 and 2. These maps were derived from the offset-corrected and peak-normalized spatial response tables. Each contour represents a response of  $\sqrt{2}$  below the preceding contour. The detector's peak response is a single point and is not shown in the contour maps. The first contour encloses the area whose response is at least  $\sqrt{2}^{-1}$  (0.707) of the peak response, the second contour encloses the area whose response is at least  $\sqrt{2}^{-2}$  of the peak response, and the  $n^{\text{th}}$  contour encloses an area whose response is at least  $\sqrt{2}^{-n}$  of the peak response. The maps show all contours above the noise level for each detector.

Figure 12 shows that the response of CIRRS 1A focal planes was not affected by scatter or glints. The response surface of each of the detectors follows the physical contour of the detector and the response of a point source at any location on the detector surface is not less than a factor of  $\sqrt{2}^{-1}$  than that of any other point on the surface. This invalidates the concern raised by the engineering calibration that the detectors may have a significantly varied response (SDL/91-056). The varied response reported in the engineering report can be attributed to a larger calibrator position uncertainty in the older calibration equipment. The sharpness of the roll off of the signal as it crosses the detector is limited by the resolving power of the telescope. The designed blur circle of the telescope is 0.5 mr, and the detector response is compatible with this specification (discussed further in Section 3.2.1.6, MTF).

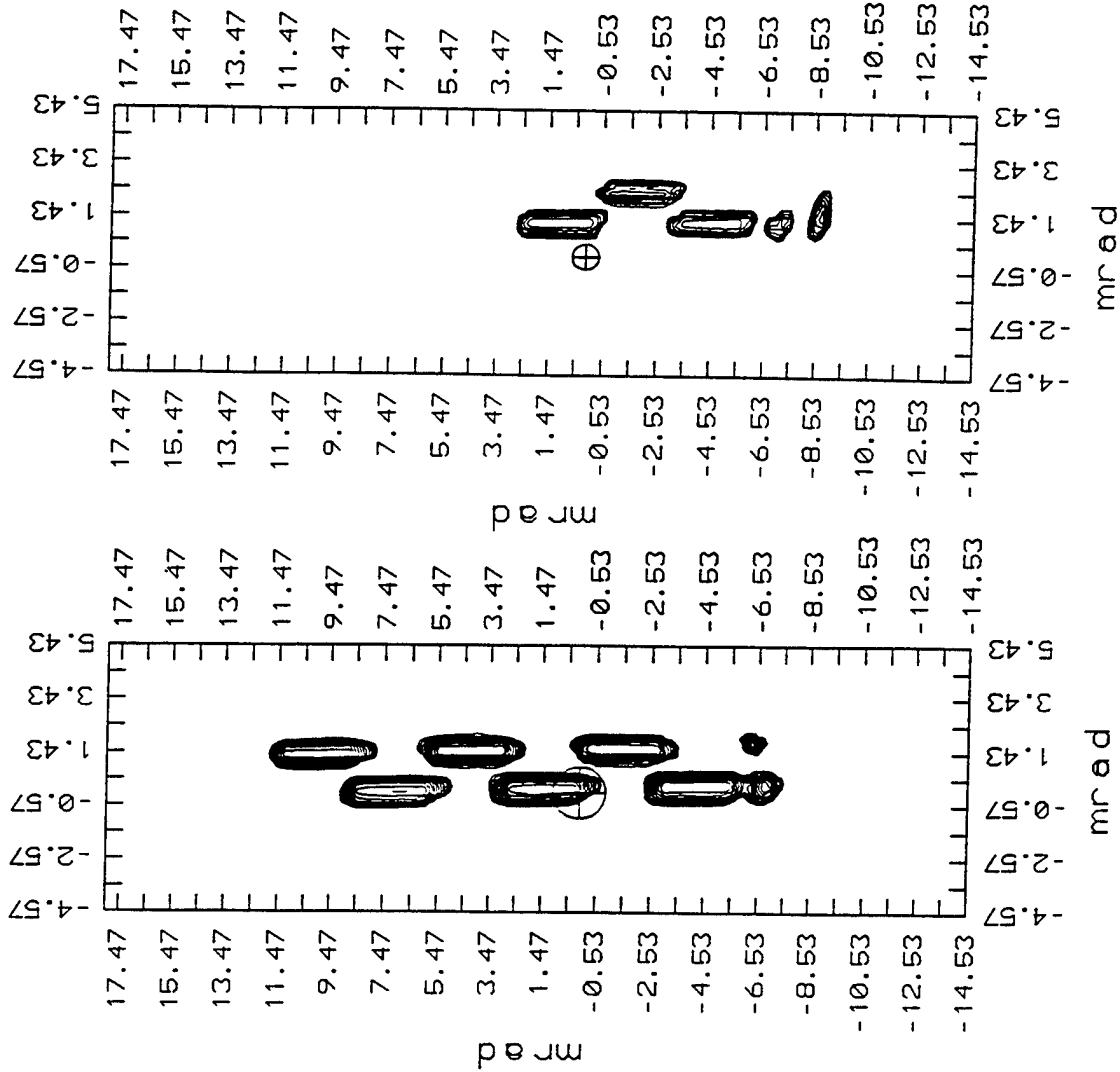
Figures 13 and 14 show the three-dimensional, absolute scale (non-normalized) plots of the point source response maps for radiometer focal planes 1 and 2, respectively. These plots provide detailed visual presentations of the actual variation of the response of each detector surface to point source (0.5 mr) stimulation. The point-to-point variation of each surface is shown to be less than  $0.3\sqrt{2}^{-1}$  of the detector output. These figures also clearly show significant vignetting in the odd detectors of the radiometer focal planes. Detector response of the odd numbered detectors is about 50% of that of the even numbered detectors when exposed to a uniform source of radiance (discussed further in Section 3.2.2).

### 3.2.1.5 Effective Field-of-View Solid Angles

The effective field-of-view solid angle of a physical sensor is defined in terms of the field-of-view solid angle of a hypothetical, spatially ideal sensor. This hypothetical ideal sensor has the following characteristics:

1. The ideal sensor's response is zero at all spatial positions outside its field of view.
2. The ideal sensor's response to a point source at all spatial positions within its field of view is equal to the actual sensor's peak spatial response.
3. The ideal sensor's response to an extended, spatially uniform source is equal to the actual sensor's response to the same spatially uniform source.

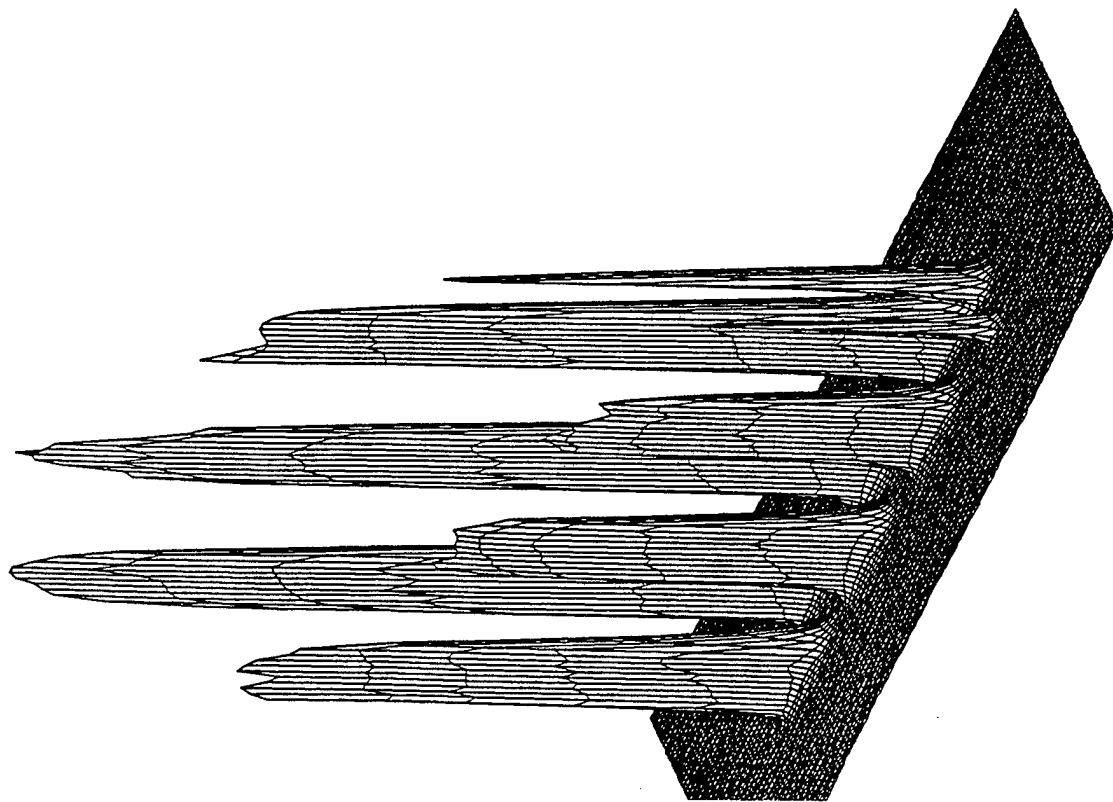
Transposed  
 Mirrored in X  
 (Object space)  
 Peak Normalized  
 Power Contours



DESCRIPTION  
 Detector...: FP1L FP2L  
 Starting X...: 7.50  
 Starting Y...: -2.00  
 Number of X: 101  
 Number of Y: 131  
 Delta X...: 0.10  
 Delta Y...: 0.25  
 Minimum: -0.001492  
 Maximum: 0.8616  
 D:\RPSMAP6\M6FP1SUF

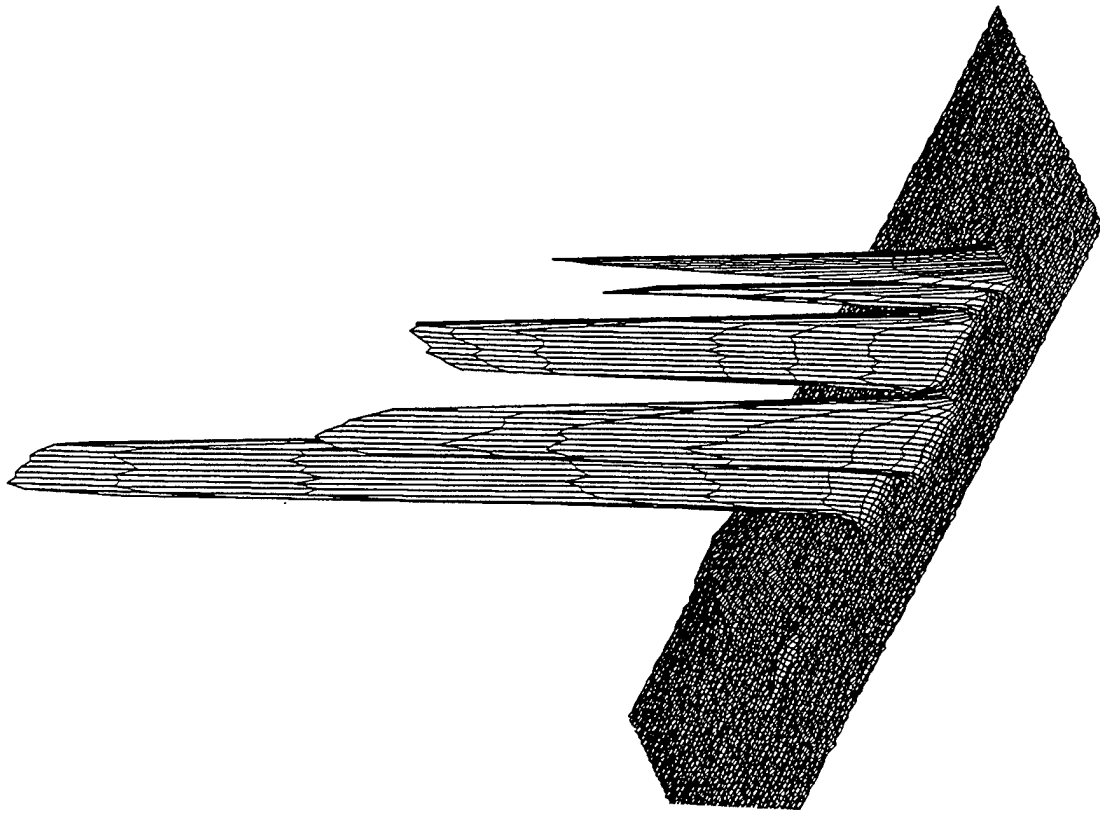
Figure 12. Point source response maps for radiometer focal planes 1 and 2.

Transposed  
Mirrored in X  
(Object space)  
Peak Normalized  
Power Contours



DESCRIPTION  
Detector...: 1-1L  
Starting X...: 7.50  
Starting Y...: -2.00  
Number of X: 101  
Number of Y: 131  
Delta X...: 0.10  
Delta Y...: 0.25  
Minimum -0.00149  
Maximum 0.8616  
D: \RPSMAP6\M6FP1.SUR

Figure 13. Three-dimensional plots of the point source response maps for radiometer focal plane 1.



```

DESCRIPTION
Detector . . . . FP2
Starting X . . . 7.50
Starting Y . . . -2.00
Number of X . . 101
Number of Y . . 131
Delta X . . . . 0.10
Delta Y . . . . 0.25
Minimum      -0.00091
Maximum      0.2652
D:\RPSMAP6\M6FP2SUI

```

Figure 14. Three-dimensional plots of the point source response maps for radiometer focal plane 2.

The effective field-of-view solid angle for the CIRRIS 1A radiometer is the field-of-view solid angle for this hypothetical, spatially ideal sensor and was computed for the radiometer from the point-source data by:

$$\Omega_{eff} = \Delta X \Delta Y \left[ \sum_{TotalFP} Resp \right] \quad (5)$$

where

- $\Omega_{eff}$  = effective field-of-view solid angle in steradians
- $\Delta X \Delta Y$  = incremental solid angle for each spatial response data point
- Resp = offset corrected, peak-normalized point-source responses

To avoid including noise response in the solid angle summation, only the radiometer responses greater than 50 percent of each detector's peak response were included in Equation (5). Table 5 gives the radiometer effective field-of-view solid angles. The solid angles of the larger detectors on both focal planes fall well within the design specifications of the CIRRIS 1A radiometer. However, the smaller detectors show some apparent deviations from the design response. Detector 1-7 is a 0.25 x 0.25 mr detector, and its apparent field of view is broadened significantly by the convolution of its shape with the 0.5 mr resolving power of the telescope. Detectors 1-8 and 2-4 show a similar but smaller broadening of the theoretical detector solid angle. The view of detector 2-5 is significantly smaller than anticipated, about one-half of the detector view being restricted by the previously mentioned odd side vignetting.

**Table 5. CIRRIS 1A Radiometer Effective Fields-of-View Solid Angles**

Detector	Effective FOV (sr) (10 <sup>-6</sup> )	Theoretical FOV (sr) (10 <sup>-6</sup> )	% Error
1-1	1.327	1.500	13.04
1-2	1.655	1.500	-9.36
1-3	1.407	1.500	6.61
1-4	1.575	1.500	-4.76
1-5	1.402	1.500	6.99
1-6	1.705	1.500	-12.02
1-7	0.135	0.063	-53.70
1-8	0.359	0.250	-30.36
2-1	1.850	1.500	-18.92
2-2	2.047	1.500	-26.72
2-3	1.718	1.500	-12.69
2-4	0.462	0.250	-45.89
2-5	0.580	1.500	158.62

### 3.2.1.6 Modulation Transfer Function

The spatial response of a sensor can also be evaluated in terms of its modulation transfer function (MTF). The MTF of a sensor describes its relative response to different spatial frequencies. The MTF of an optical system is the ratio of the modulation of the image scene to that of the object scene. It is measured by scanning the detector with an extremely fine point source. The MTF is limited by the effective aperture and the diffraction limit of the optical system, and is therefore wavelength dependent. The MTF of a system is the product of the optical system and the detector MTF, and is defined as:

$$MTF = \frac{2}{\pi} [\phi - \cos \phi \sin \phi] \quad (6)$$

where

$\phi$	=	$\arccos(\lambda FN)$
$\lambda$	=	wavelength of interest
F	=	relative aperture (f-number)
N	=	spatial frequency

The MTF is zero when  $\phi$  is zero. This defines the limiting spatial frequency of a system. In other words,  $N_L = 0$  defines a spatial structure that is of sufficiently high frequency that sensor response is averaged to a smooth response by the optical system. This limiting frequency  $N_L$  is given in cycles/mm by  $N_L = 1/(\lambda F)$ , or in cycles/radian by multiplying by the effective focal length,  $N_L = D/\lambda$ . The f-number for the CIRRIIS radiometer was 4, with a 6-inch aperture and 24-inch focal plane.

SDL subcontractor, Yap Analytics, performed the MTF analysis. Figures 15 to 21 show examples of this analysis. Figure 15 displays data consistency between preflight, flight, and post flight measurements of the system's MTF for detectors 1-6 and 2-3. The post flight MTF measurement for detectors 1-6 and 2-3 taken with filters 1 and 6 compared favorably with the MTF calculations developed during the flight celestial calibration. Both the ground and celestial MTFs are consistent with the response expected from a sharp-edged detector convolved with a 0.5 mrad telescope blur circle. These MTF measurements are significant improvements over the preflight measurements. The preflight measurements were limited by aliasing and measurement pointing error limitations of the calibration equipment.



## C1A RAD MTFs Y AXIS

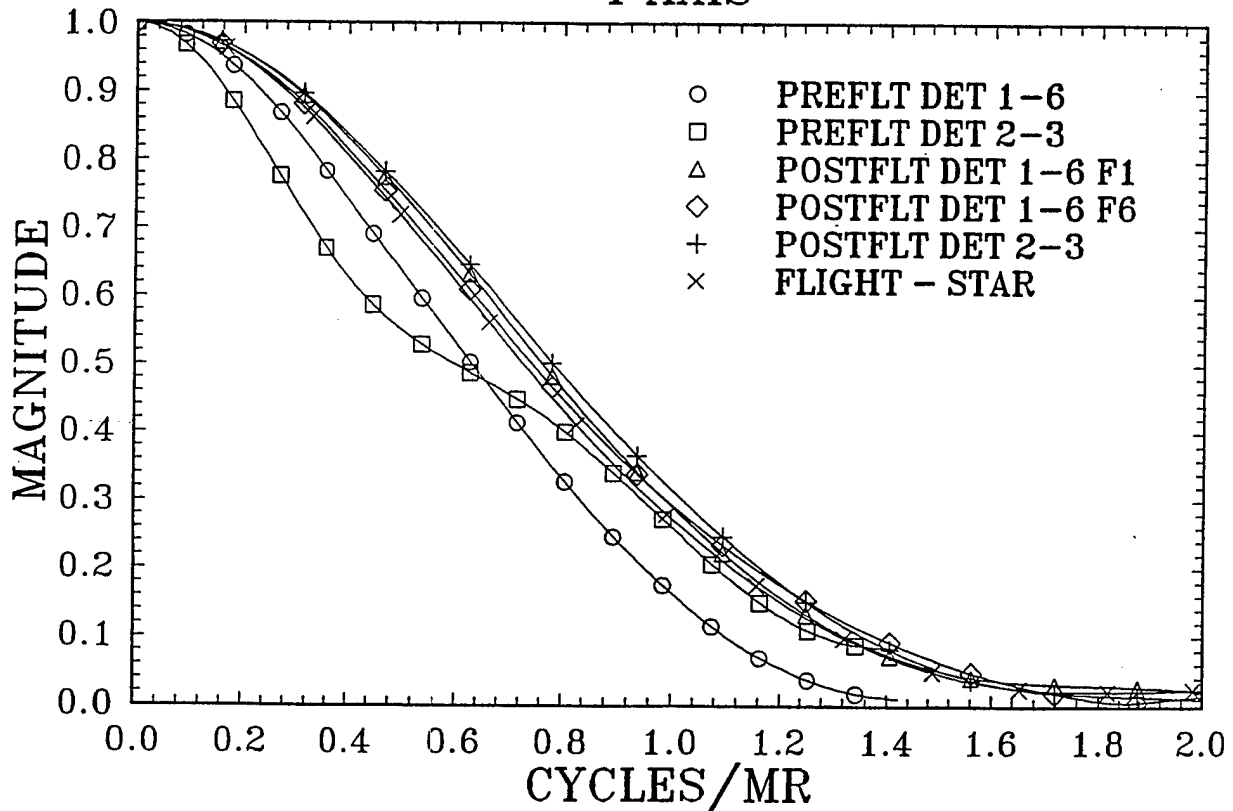


Figure 15. CIRRIIS 1A radiometer Y-axis modulation transfer function (MTF).

The X- and Y-axis MTFs for Map A, detectors 1 through 6, are given in Figure 16. The only discrepancies were the slightly higher MTF responses for detectors 1-1, 1-3, and 1-5 in the narrow dimension (Y axis). This discrepancy was not present in the long dimension (X axis) MTFs. An analysis of the map A data indicated that the higher MTF was due to a slight positioning error in the calibrator scan mirror. The position error was within the specification of the collimator, but occurred on the scan that overlaid the edge of the detectors.

The X- and Y-axis MTFs for detector 1-7, shown in Figure 17, are consistent for Map F, while the X-axis MTFs for detector 1-8, shown in Figure 18, are slightly magnified over the Y-axis values. This higher response is visually evident on the detector contours shown in Figure 12. The larger MTF of these detectors with respect to detector dimensions is consistent with the convolution of the detector size with the telescope blur circle.

Figure 19 gives the Y-axis MTFs for detectors 2-1, 2-2, and 2-3, and Figure 20 provides the X- and Y-axis MTFs for detector 2-4. Detectors 2-1 and 2-3 MTFs are similar, as expected. The vignetting effect of detector 2-2 is evident in the MTF values. The X-axis MTFs of detector 2-4 are slightly higher after the 1.2 cycle/mrad level.

Figure 21 gives the X- and Y-axis MTFs of detector 2-5. The higher magnitude of the X-axis MTFs is consistent with its limited field of view due to telescope vignetting (Section 3.2.1.5).

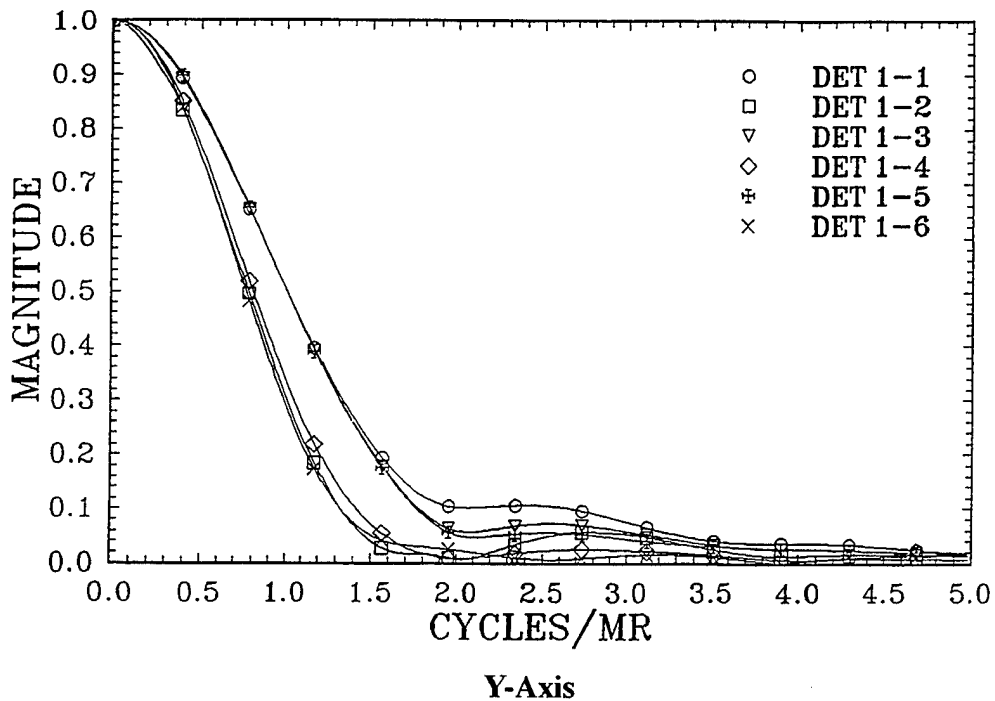
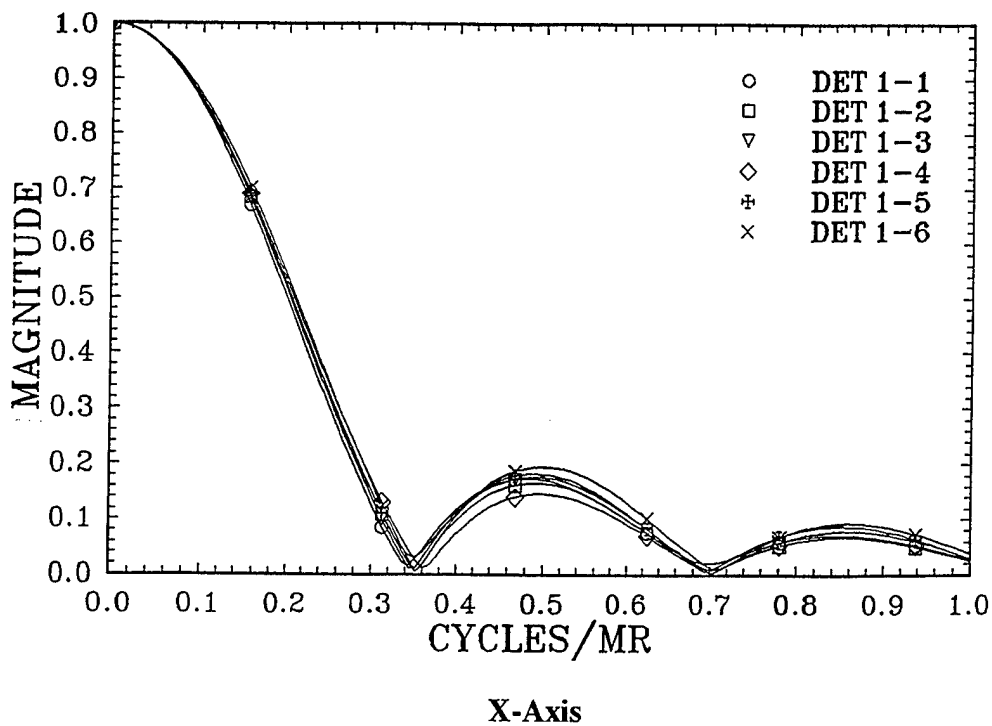


**Figure 16. CIRRIS 1A radiometer X- and Y-axis modulation transfer function (MTF), Map A (D1-1 to D1-6).**

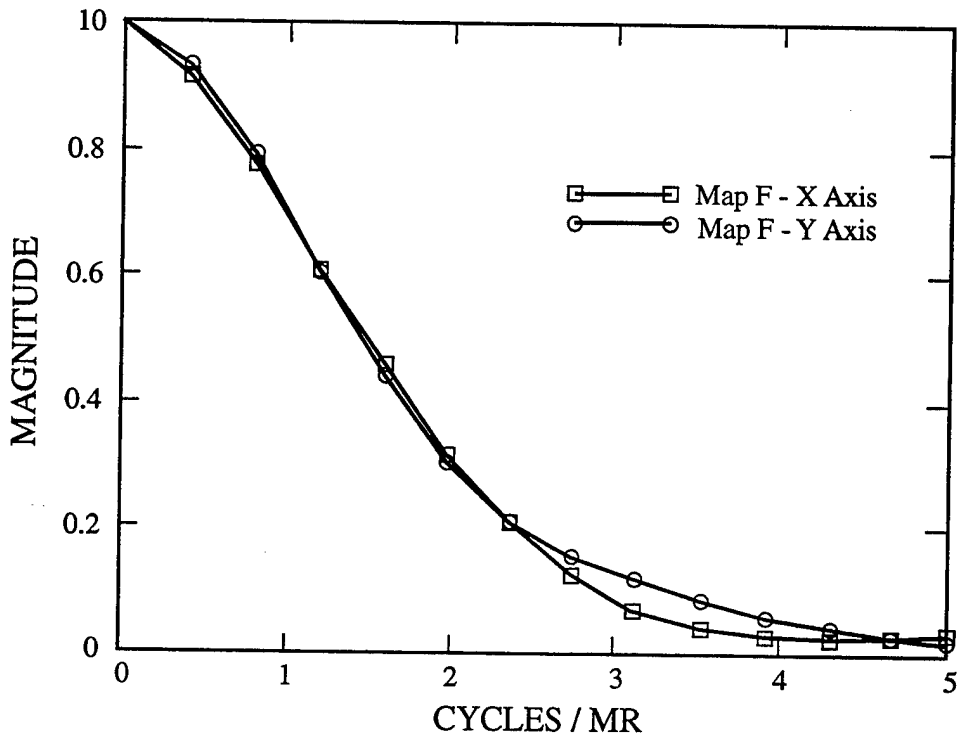


Figure 17. CIRRIIS 1A radiometer detector 1-7 modulation transfer function (MTF) (Map F).

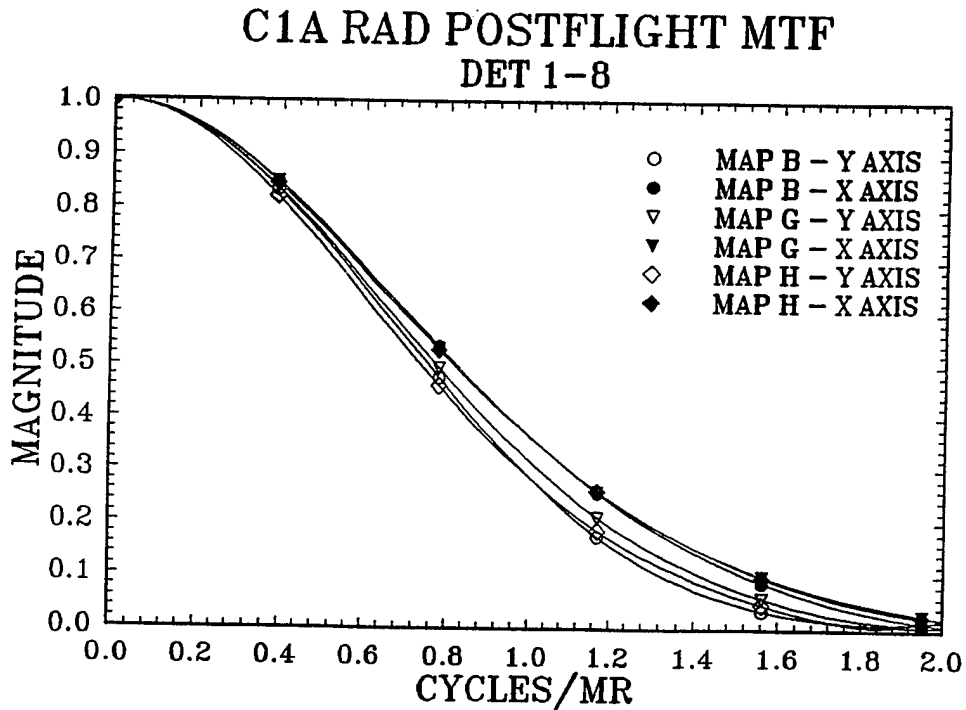


Figure 18. CIRRIIS 1A radiometer detector 1-8 modulation transfer function (MTF) (Maps B, G, H).

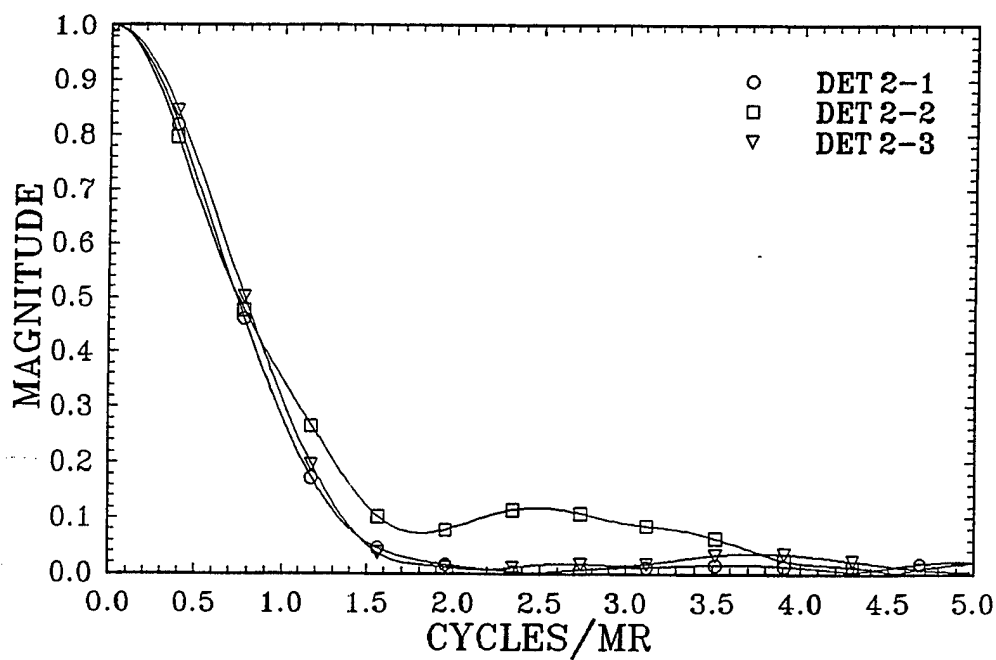


Figure 19. CIRRIS 1A radiometer Y-axis modulation transfer function (MTF), Map A (D2-1 to D2-3).

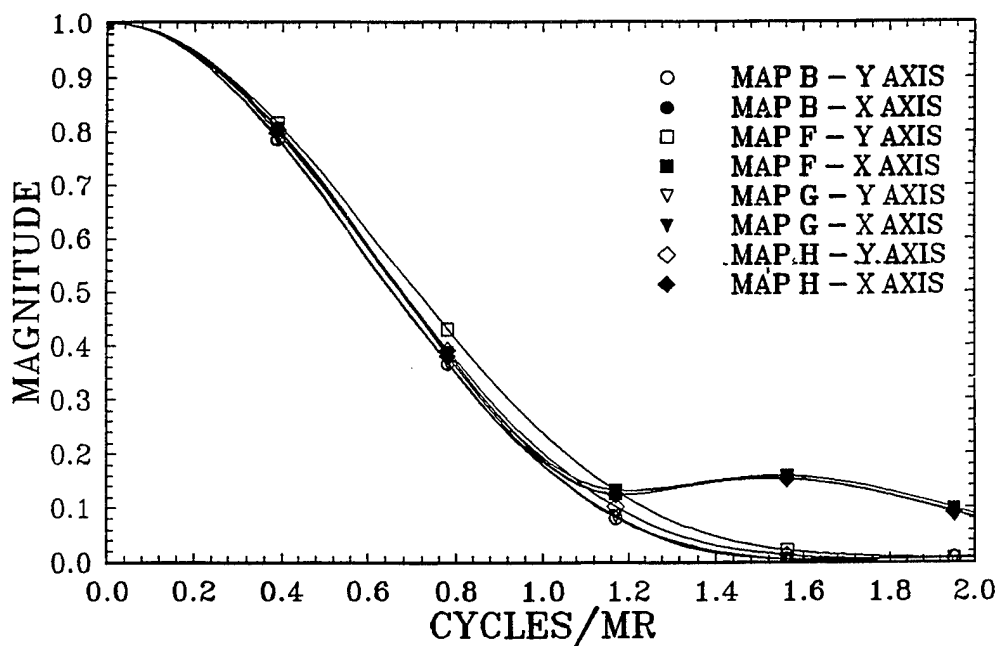


Figure 20. CIRRIS 1A radiometer detector 2-4 modulation transfer function (MTF) (Maps B, F, G, H).

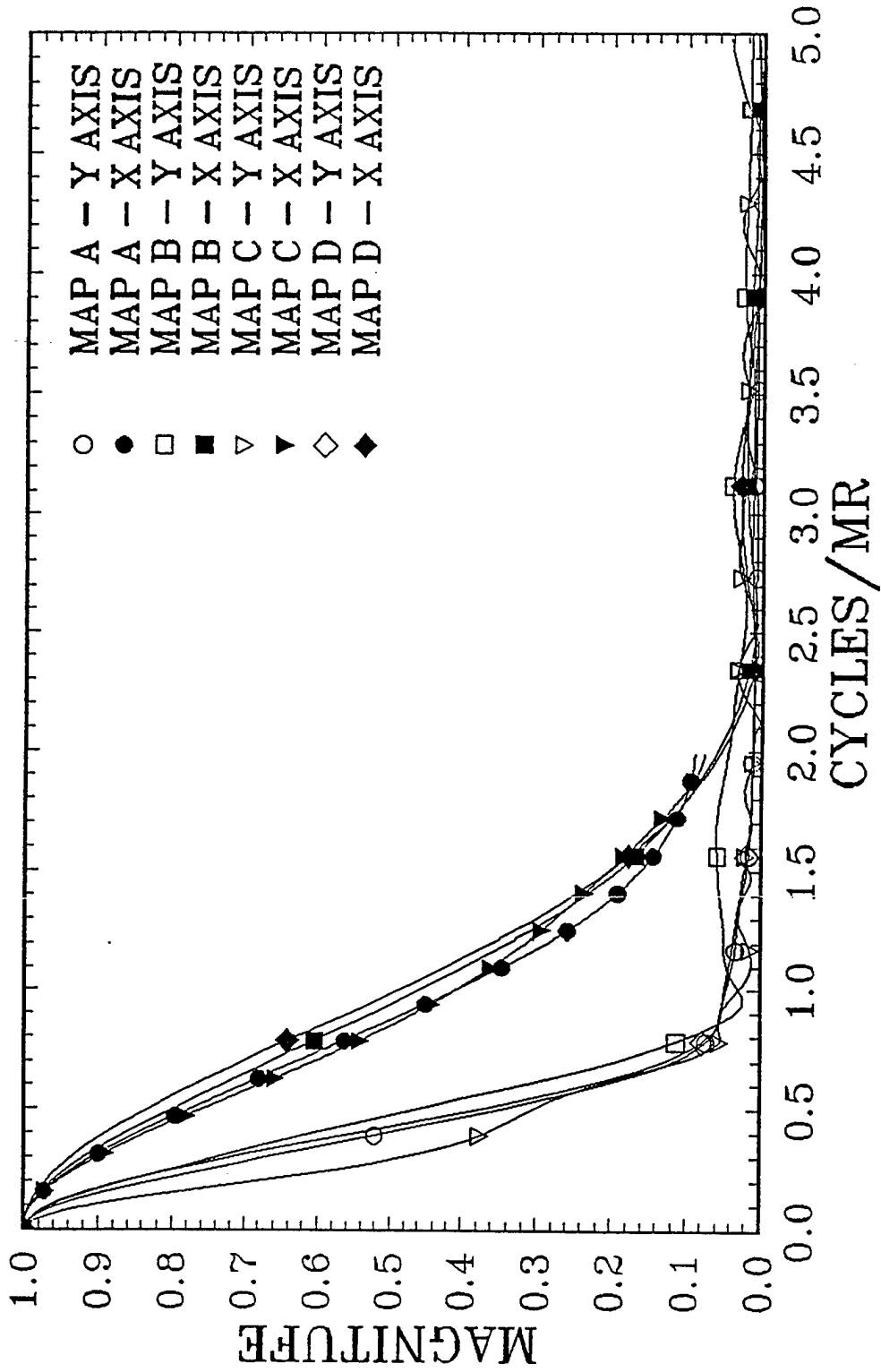


Figure 21. CIRRIS 1A radiometer detector 2-5 modulation transfer function (MTF) (Maps A, B, C, D).

### 3.2.2 Jones Cone Response

SDL personnel performed diagnostic measurements to investigate the vignetting of the CIRRIS 1A radiometer focal planes. Calibration personnel determined the actual entrance aperture area used by each detector by recording the detector response while scanning a small aperture source across the entrance aperture using a Jones source configuration. The Jones source is a near-field, out-of-focus source that is placed in the Jones cone of the sensor. The Jones cone of the sensor is defined by the sensor field of view and the entrance aperture. Figure 22 shows a simplified diagram of a Jones cone. Theoretically, a small area source placed inside the Jones cone will provide spatially uniform illumination to the whole detector focal plane. If irregularities exist in the collection efficiency of locations in the collecting aperture, scanning the source across these areas will result in a reduced response.

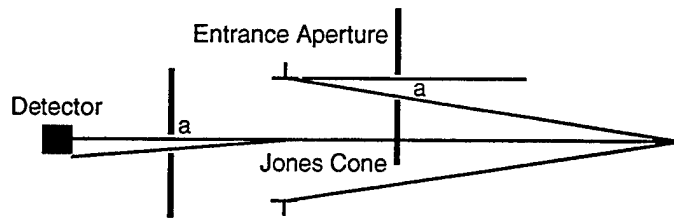


Figure 22. Simplified diagram of a Jones cone.

The CIRRIS 1A entrance aperture was mapped using the Jones source configuration with filter 0 and a 0.158 mrad source. The calibrator pointing mirror was used to spatially position the Jones source over different locations within the CIRRIS Jones cone. Limitations on the calibrator pointing mirror range did not allow parts of the Jones cone to be mapped for some detectors; however, as a minimum, a partial section of each detector was mapped. Figure 23 gives the orientation of the entrance aperture for the Jones cone maps.

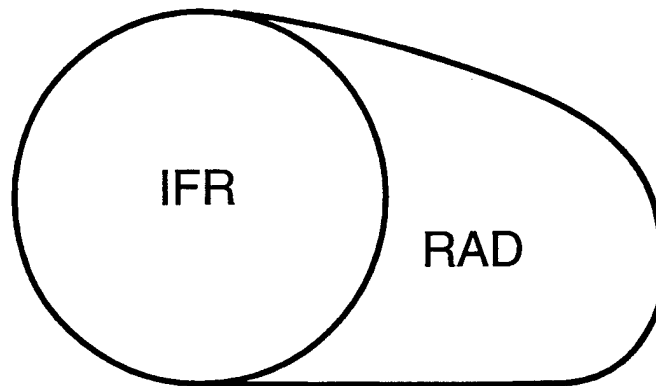


Figure 23. Orientation of the entrance aperture for the Jones cone maps.

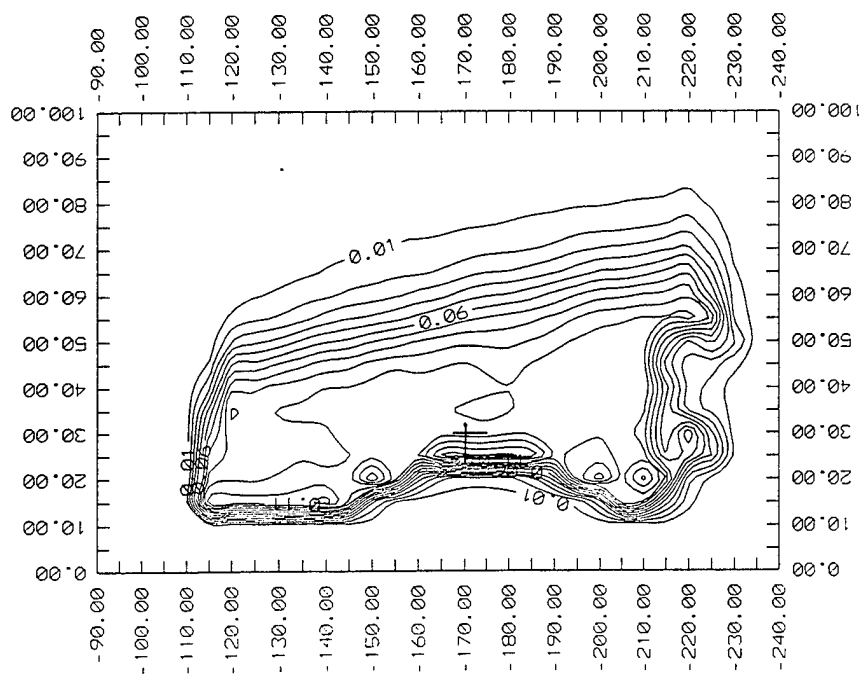
Figure 24 shows the results of the Jones source maps for detectors 1-1 and 1-6, and Figure 25 shows the results for detectors 2-2 and 2-3. Volume 2 contains the partial maps for all detectors. These results show that the odd-numbered detectors (1-1, 1-3, and 1-5) are narrower in the long dimension of the entrance aperture than the even-numbered detectors (1-2, 1-4, 1-6). This is consistent with the vignetting observed in the point source field-of-view maps described in Section 3.2.1.5. The vignetting is especially evident in detector 2-2 where only a small portion of the entrance aperture was used by the detector. Although no quantitative analysis was performed on the Jones cone maps, they did provide significant insight into the spatial uniformity of the collection aperture.

### 3.2.3 Radiometric Response Functions

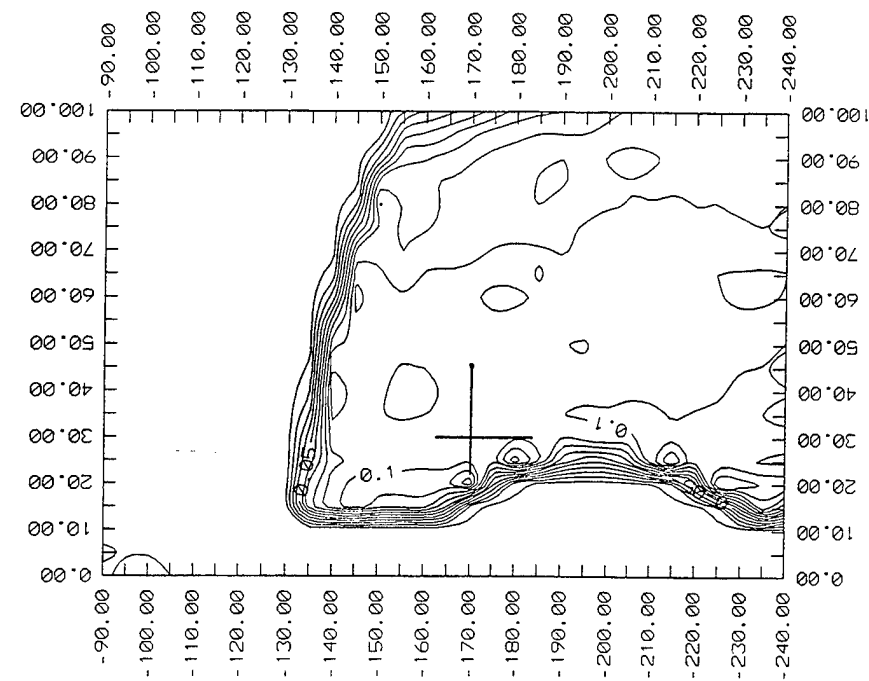
The CIRRIS 1A sensor was designed to provide a wide dynamic range to include many different response ranges. These included three bias gains and two electronic gains. Each of the detectors must be calibrated across all of these ranges. A simple approach to describing the sensor response is to provide a separate response equation for each range. This procedure requires significant care, because the largest errors occur at the ends of these equations. Providing a uniformly accurate equation across each range change is the goal of the uniform calibration equation (Equation (1)). Because of the need to examine the response of CIRRIS 1A across these many conditions, and because non-ideal sensor responses can invalidate various measurement techniques, more than one measurement method was used to determine each of the terms in the radiometric calibration equation. These measurements are described below.

#### 3.2.3.1 Electronic Gain Response

The absolute electronic gain response for each radiometer detector was determined with the chopper on and off using the Jones, point, and extended sources. During this calibration, high electronic gain data were only processed with the high bias range because this was the only combination used in flight. The output of each detector was routed to X1 and X100 amplifiers and both channels were digitized. Bias gain ranging circuits switched the bias level of the whole group to a lower bias range when the low gain output of the group detector lowest in the atmosphere reached an ac peak of 7.2 volts. The bias gain range was switched up when the low gain channel of the lowest detector in the bias group reached 1.2 volts. The detector bias groups are shown in Table 6. At the low end of the dynamic range (high gain, bias high), the high gain channel should saturate before bias gain control circuitry reduced the bias. In flight, where a steep atmospheric radiance gradient exists, some high gain data are valid on the upper detectors of a bias group when the group was in low or medium bias. While calibration equations were not developed for these areas, they can be processed by dividing the voltage by the high gain coefficient and using the low gain equation. Table 7 presents radiometer electronic gains observed using the Jones source with calibrator apertures 1 through 11. The gains were calculated by taking the ratio of high gain to low gain at each data point and averaging the data points. The table shows that the electronic gains are within 0.5% of the theoretical value of 100.



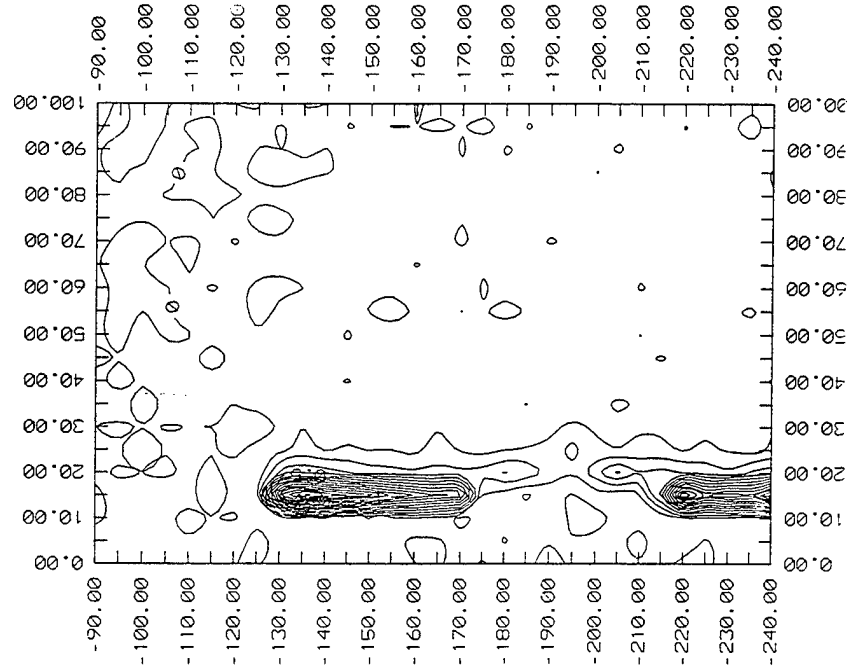
DESCRIPTION  
 Detector...: 1-1L  
 Starting X.: 0.00  
 Starting Y.: -240.00  
 Number of X.: 21  
 Number of Y.: 31  
 Delta X.....: 5.00  
 Delta Y.....: 5.00  
 Minimum 0.00000  
 Maximum 0.14199  
 D:\RPSMAP10\M10D11L



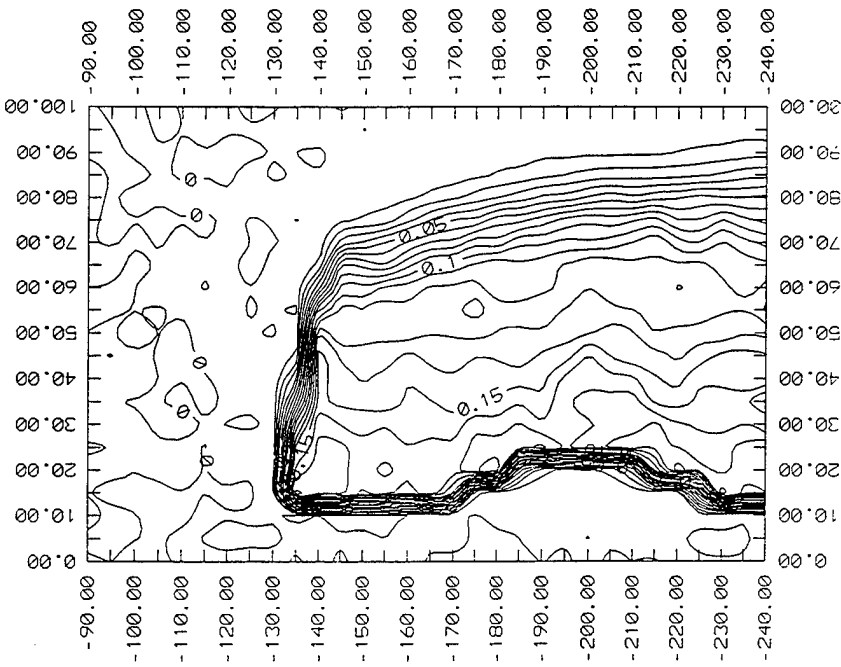
DESCRIPTION  
 Detector...: 1-6L  
 Starting X.: 0.00  
 Starting Y.: -240.00  
 Number of X.: 21  
 Number of Y.: 31  
 Delta X.....: 5.00  
 Delta Y.....: 5.00  
 Minimum -0.00013  
 Maximum 0.12991  
 D:\RPSMAP10\M10D16L

Figure 24. Jones source maps for radiometer detectors 1-1 and 1-6.





DESCRIPTION  
 Detector...: 2-2H  
 Starting X.: 0.00  
 Starting Y.: -240.00  
 Number of X: 21  
 Number of Y: 31  
 Delta X.....: 5.00  
 Delta Y.....: 5.00  
 Minimum -0.05535  
 Maximum 1.56265  
 D:\RPSMAP10\M10D22f



DESCRIPTION  
 Detector...: 2-3H  
 Starting X.: 0.00  
 Starting Y.: -240.00  
 Number of X: 21  
 Number of Y: 31  
 Delta X.....: 5.00  
 Delta Y.....: 5.00  
 Minimum -0.00277  
 Maximum 0.19387  
 D:\RPSMAP10\M10D23f

Figure 25. Jones source maps for radiometer detectors 2-2 and 2-3.

**Table 6. CIRRIS 1A Radiometer Bias Groups**

Bias Group	Detector
1 - 1	2-1, 2-4, 2-5
1 - 2	1-4, 1-7, 1-8, 1-9
2 - 1	2-2, 2-3
2 - 2	1-1, 1-3, 1-5, 1-6, 1-2

**Table 7. CIRRIS 1A Radiometer Electronic Gains**

Detector	Gain	Mean
1-1	x100/x1	99.48
1-2	x100/x1	99.48
1-3	x100/x1	99.67
1-4	x100/x1	99.84
1-5	x100/x1	99.74
1-6	x100/x1	100.32
1-7	x100/x1	99.66
1-8	x100/x1	100.05
2-1	x100/x1	100.08
2-2	x100/x1	100.55
2-3	x100/x1	100.21
2-4	x100/x1	99.74

### 3.2.4 Absolute Responsivity

The absolute responsivity calibration determines the absolute radiance responsivity for each radiometer array and the relative detector-to-detector responsivity (flat field matrix) for each detector within each array. It provides the transfer function of linearized sensor response to absolute flux. In addition, this calibration verifies the linearity correction function and the relative spectral responsivity calibrations.

CIRRIS 1A used bulk silicon detectors, which are subject to dielectric relaxation effect (DRE). Results from the engineering calibration (SDL/91-056) showed evidence of DRE in the radiometer detectors. To adequately describe the DRE on the CIRRIS 1A response, an absolute response calibration equation was developed for each gain, filter, and bias range. This equation was then used in the OPUS software. The coefficients for these equations were developed from the extended source data set with temperatures ranging from 20 K to 300 K. Responses outside of the extended source range were developed by merging the linearity data for the range and filter combination under study with the absolute response data. Only the Chopper On condition was evaluated, as only a few minutes of Chopper Off data were collected during flight. Collecting this data set was the most time consuming effort of the post flight calibration. The CIRRIS 1A radiometer has 13 active detectors, eight which have eight filter options, and each detector has three bias levels, with one bias level having two gains; therefore, the absolute response calibration required 414 equations.

To build each response equation, the extended source was stabilized at the desired temperature and a file was collected for each filter, gain, and bias combination. Each file was dc restored and dark noise offset corrected. The extended area source absolute flux was calculated by multiplying the peak-normalized Bomem-measured relative spectral response curves for the filter by the Planck function at the given temperature and then integrating (see Section 3.2.6). A second degree equation with no constant term was then fit. Standard regression techniques were implemented using a fit weighted with  $1/Y^2$ . Because the extended source illuminates all of the detectors, data at that temperature for each detector showing a valid response could be fit by the equation for that detector. Estimates for the extended source temperature set points were calculated using a response model developed with CIRRIS 1A engineering evaluation data (SDL/91-056). To calculate the absolute response equations, effective flux,  $\Phi_{eff}$ , was calculated for each extended source temperature using the equation:

$$\Phi_{eff} = \int_{rf} L_{bb}(V) \times (RSR_f(v) dv) \quad (7)$$

where

- f = filter
- rf = range of the filter
- $L_{bb}$  = blackbody flux calculated from the Planck equation
- $RSR_f$  = peak normalized measured radiometer system relative spectral response

Figure 26 graphically explains the need to calculate the effective flux in the filter bandpass region. As the extended source increases in temperature from  $T_1$  to  $T_4$ , the spectrum of flux

changes significantly. At each temperature, the  $\Phi_{eff}$  is plotted against the radiometer restored dc value (Figure 26(b)). The line fit provides the equation:

$$V_F = R_F \times \Phi_{eff} \quad (8)$$

which is rearranged for measurements collected with filter F:

$$\Phi_m = \frac{V_F}{R_F} \quad (9)$$

Because of the convolution of  $L_{bb}$  with a peak normalized  $RSR_f$ , and because the spectrum of  $\Phi_m$  is probably not the same as  $\Phi_{eff(bb)}$ ,  $\Phi_m < \Phi_{source}$ .

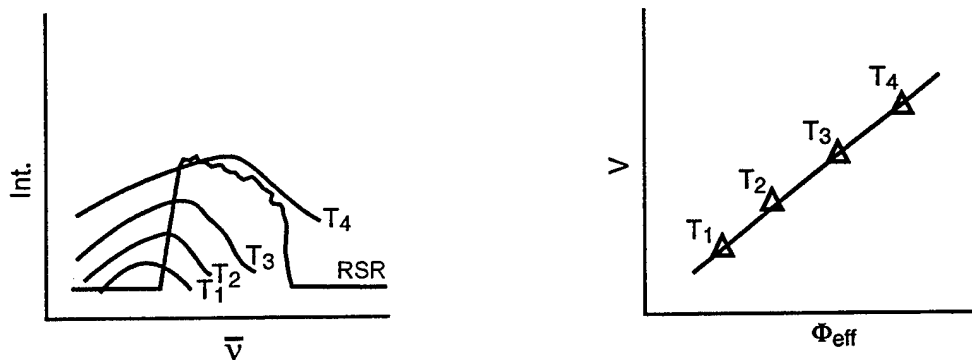


**Figure 26.** A schematic of the calculation of the effective flux ( $\Phi_{eff}$ ) and the use of  $\Phi_{eff}$  to develop the radiometer response equations.

An example of this effect can be seen in Figure 27, which shows typical, normalized flight data spectra plotted over the normalized  $RSR$  for each filter associated with focal plane 1. For example, in filter 2, energy entering the radiometer focal plane from the  $NO$  emission at  $1900\text{ cm}^{-1}$  has been attenuated about 50% by the filter. Only when the emitted energy occurs at the peak of  $RSR_f(\nu)$  is  $\Phi_m = \Phi_{source}$ .

# FILTER RSR and OPUS SPECTRA

(dash: filter rsr; solid: opus spectrum)

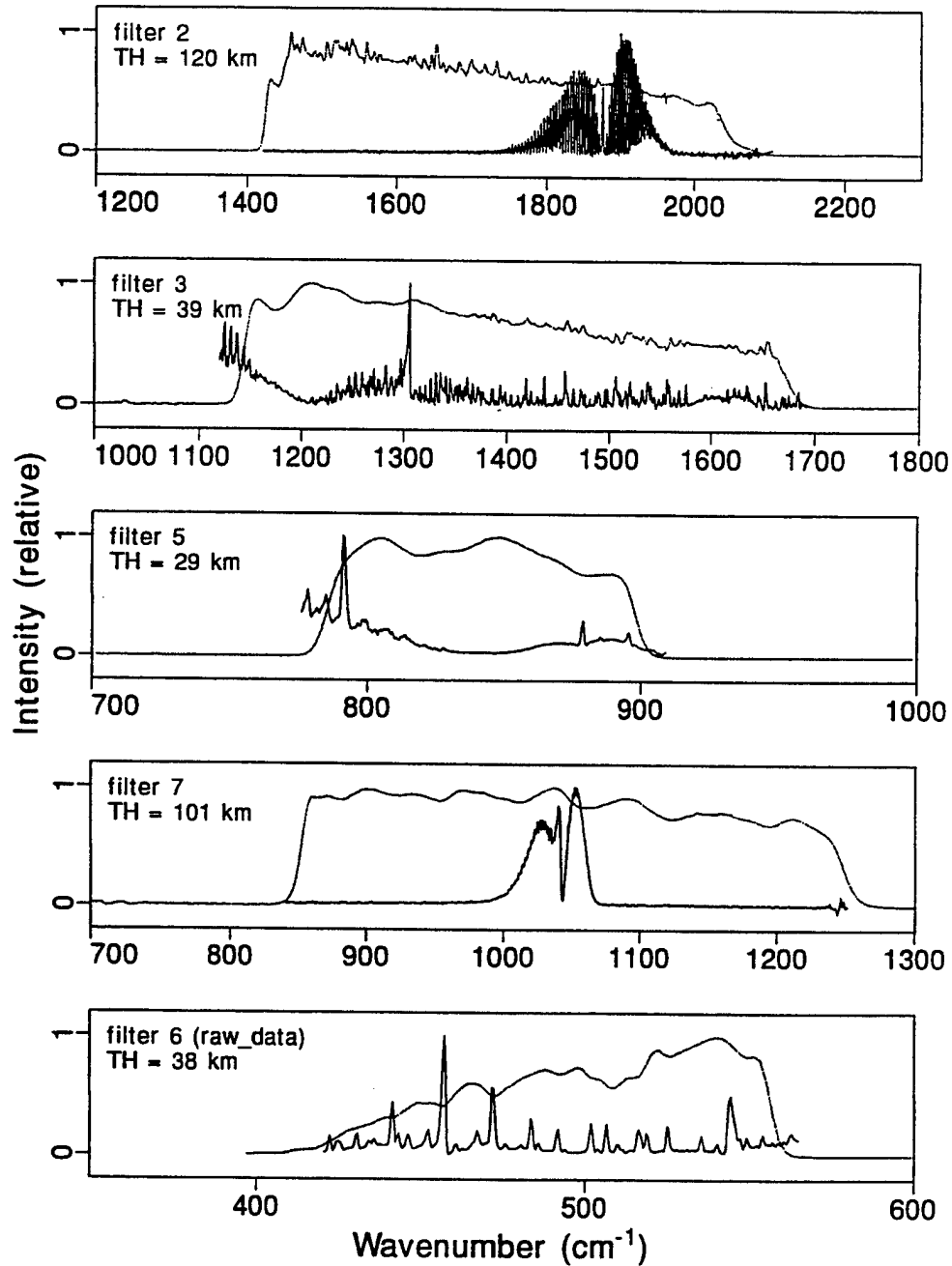
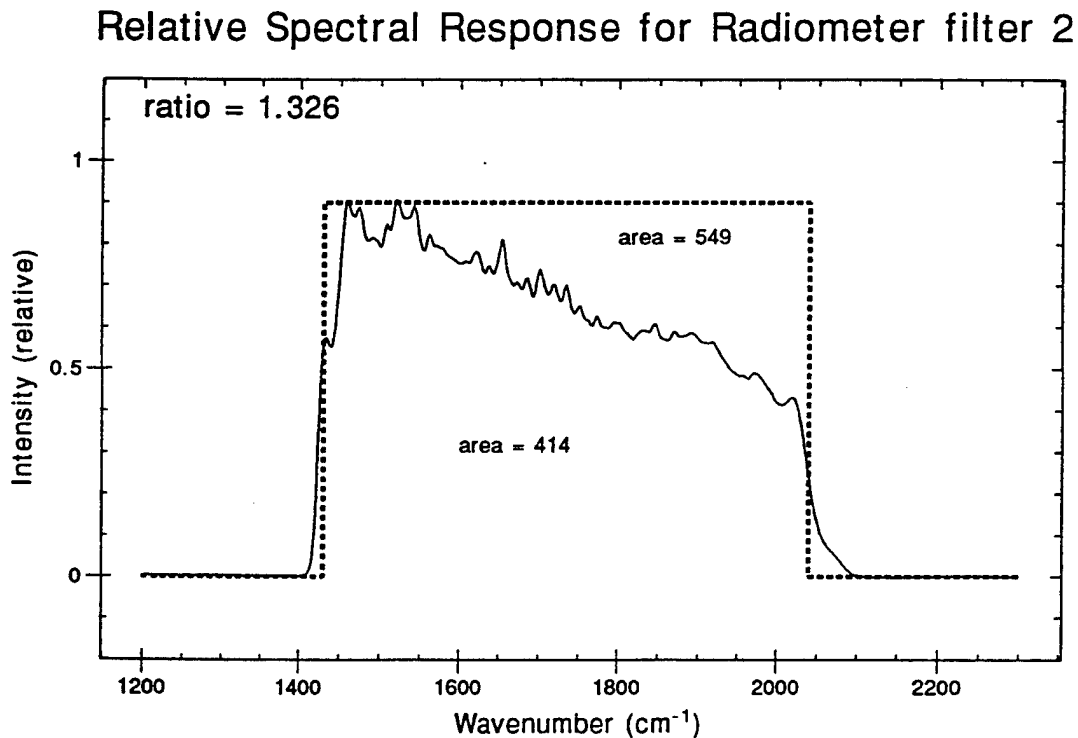


Figure 27. A comparison of the CIRRS 1A filter RSR and typical atmospheric spectra in each band.

This effect can be partially compensated by assuming the source is white (constant (1)) and ratioing out the attenuation of the filter. An example is shown in Figure 28, where the area integral ratio,  $549/414 = 1.326$ , is used to develop a measured flux multiplier, (K). Using this approach to the radiometer calibration equation, Equation (9) becomes

$$\Phi_m = \frac{KV_F}{R} \quad (10)$$

In our filter 2 example, using Equation (9)  $\Phi_m = \sim 0.5 \Phi_{\text{source}}$  while using Equation (10),  $\Phi_m = 1.326 \times 0.5 = 0.663 \Phi_{\text{source}}$ , a small improvement in this case, but a major improvement where the spectral shape is more uniform. The equations used in OPUS (see Table 9) have been multiplied by this whitening ratio and do not provide a direct fit to the actual data.



**Figure 28. Development of the band flux ratio used to partially correct the CIRRI 1A data for the non-ideal RSR.**

The only method available to make  $\Phi_m = \Phi_{\text{source}}$  where spectrally structured radiation is being measured involves the use of the interferometric spectra collected at the same time. If these

spectra are available, which they are with the CIRRIS data sets, then one can correct for spectral dispersion exactly. Using the interferometer:

$$\Phi_s \approx \int_{if} \Phi_c(\nu) d\nu \quad (11)$$

where

$$\Phi_c(\nu) = \int_{if} \frac{\Phi(\nu)}{R \times RSR_{if}(\nu)} d\nu$$

$\Phi(\nu)$  = uncalibrated transform  
 $R$  = interferometer absolute responsivity  
 $RSR_{if}$  = interferometer filter RSR

The result is  $\Phi_s$ , the calibrated interferometer spectra, which is assumed to have a consistent relative spectral calibration, but may have a larger absolute error. A new radiometer sealing factor can be calculated using:

$$K_I = \frac{\int_{if} \Phi_c(\nu) d\nu}{\int_{if} \Phi_c(\nu) \times RSR_{if}(\nu) d\nu} \quad (12)$$

which should provide the exact K value necessary to set  $\Phi_m = \Phi_{source}$ .

In summary, because the spectral distribution of the radiation measured by CIRRIS is not readily available to the radiometer user, the coefficients used in OPUS to calibrate each radiometer range have been multiplied by a constant. This constant allows the radiometer to report proper flux values when the distribution of energy in the measurement bond is constant (white) across the whole spectrum. The values of the constants used in OPUS are shown in Table 8. These coefficients were developed by integrating the radiometer filter RSRs between their 10% transmission points. The effect of this constant on the fit of the coefficients and equations of Table 9 are shown in Figure 29. These fits and multipliers were developed by Yap Analytics, Inc. under contract to SDL/USU. Details are reported in Yap Analytics Final Report, June 1992.

Table 9 lists an example of the responsivity equation coefficients for data taken with filter 0 at different blackbody temperature settings with bias hi, gain hi, and bias lo, gain lo. Response for all detector filters and bias ranges are given in Volume 2 of this document. Individual detector voltage responses were used in each of the four bias-gain configurations found during flight: bias high, gain high; bias high, gain low; bias medium, gain low; and bias low, gain low. For the high flux regions of the short wavelength filters (1, 2, focal plane 2) which exceeded the capability of the extended source, some point source files were included to extend the range of the calibration equation. Point source files make up about 20% of the total number of points in those three filter data sets. Where the point source was used, data were collected in an overlap region to scale the point source to the extended source radiance level.

DET 1-6 Filter-0

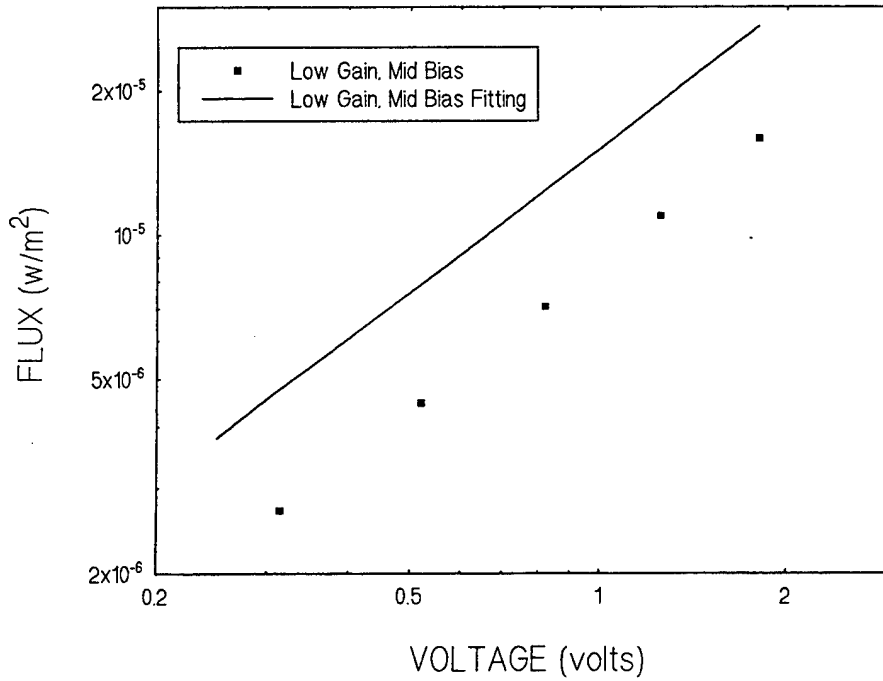


Figure 29. The effect of constants on fit of coefficients for filter 0, detector 6, response function.

Table 8. Constants Used in OPUS

Filter	Filter Efficiency	Multiplier
0	0.588	1.70068
1	0.828	1.20773
2	0.638	1.5674
3	0.675	1.48148
5	0.799	1.25156
6	0.599	1.66945
7	0.822	1.216545
FP2	NA	NA



**Table 9. CIRRI 1A Radiometer Linearity Coefficients  
(filter 0, bandpass, linear fit)**

Det	Bias	Gain	A1	A2	S.D.	Min. Volt.	Max. Volt.
1-1	HI	LO	4.04044E+00	-4.06883E-01	1.97368E-04	5.90900E-04	1.59300E+00
1-2			2.15022E+00	-2.16524E-01	1.97925E-04	5.90900E-04	1.59300E+00
1-3			4.86650E+00	-4.90052E-01	1.97816E-04	5.90900E-04	1.59300E+00
1-4			2.07024E+00	-2.08483E-01	1.97037E-04	5.90900E-04	1.59300E+00
1-5			5.00050E+00	-5.03538E-01	1.98077E-04	5.90900E-04	1.59300E+00
1-6			2.03032E+00	-2.04303E-01	1.60217E-02	5.90900E-04	1.59300E+00
1-7			7.39075E+01	-7.44237E+00	1.97930E-04	5.90900E-04	1.59300E+00
1-8			1.75018E+01	-1.76244E+00	1.97691E-04	5.90900E-04	1.59300E+00
1-1	HI	HI	4.07042E-02	-4.09890E-03	1.97782E-04	5.90900E-04	1.59300E+00
1-2			2.50027E-02	-2.51783E-03	1.97397E-04	5.90900E-04	1.59300E+00
1-3			5.00054E-02	-5.03565E-03	1.97397E-04	5.90900E-04	1.59300E+00
1-4			2.14022E-02	-2.15520E-03	1.97737E-04	5.90900E-04	1.59300E+00
1-5			5.30055E-02	-5.33764E-03	1.97733E-04	5.90900E-04	1.59300E+00
1-6			2.13023E-02	-2.14517E-03	1.97491E-04	5.90900E-04	1.59300E+00
1-7			7.60085E-01	-7.65435E-02	1.97162E-04	5.90900E-04	1.59300E+00
1-8			1.95020E-01	-1.96384E-02	1.97798E-04	5.90900E-04	1.59300E+00
1-1	MED	LO	3.03414E+01	0.00000E+00	3.13351E-03	1.49600E-01	6.12700E-01
1-2			1.71432E+01	0.00000E+00	3.10408E-03	2.72600E-01	1.09300E+00
1-3			3.16675E+01	0.00000E+00	1.10090E-02	1.43500E-01	5.86800E-01
1-4			1.57333E+01	0.00000E+00	4.32499E-03	2.98000E-01	1.19200E+00
1-5			3.60025E+01	0.00000E+00	2.35026E-03	1.26700E-01	5.17200E-01
1-6			1.51775E+01	0.00000E+00	1.06077E-02	3.14700E-01	1.80100E+00
1-7			5.84064E+02	0.00000E+00	6.15571E-03	8.06100E-03	4.67200E-02
1-8			1.16936E+02	0.00000E+00	2.67001E-03	3.83000E-02	2.31100E-01
1-1	MED	HI	0.00000E+00	0.00000E+00	0.00000E+00	0.00000E+00	0.00000E+00
1-2			0.00000E+00	0.00000E+00	0.00000E+00	0.00000E+00	0.00000E+00
1-3			0.00000E+00	0.00000E+00	0.00000E+00	0.00000E+00	0.00000E+00
1-4			0.00000E+00	0.00000E+00	0.00000E+00	0.00000E+00	0.00000E+00
1-5			0.00000E+00	0.00000E+00	0.00000E+00	0.00000E+00	0.00000E+00
1-6			0.00000E+00	0.00000E+00	0.00000E+00	0.00000E+00	0.00000E+00
1-7			0.00000E+00	0.00000E+00	0.00000E+00	0.00000E+00	0.00000E+00
1-8			0.00000E+00	0.00000E+00	0.00000E+00	0.00000E+00	0.00000E+00
1-1	LO	LO	2.89243E+02	0.00000E+00	1.91450E-02	9.81800E-02	2.27600E+00
1-2			1.60492E+02	0.00000E+00	1.54137E-02	1.74400E-01	1.97400E+00
1-3			3.13617E+02	0.00000E+00	3.04576E-02	9.05800E-02	2.09500E+00
1-4			1.46450E+02	0.00000E+00	1.95774E-02	1.87300E-01	2.16500E+00
1-5			3.46726E+02	0.00000E+00	3.67822E-02	8.16700E-02	1.89400E+00
1-6			1.41526E+02	0.00000E+00	7.86006E-03	2.92700E-01	2.25100E+00
1-7			5.89601E+03	0.00000E+00	5.77316E-02	1.81800E-02	1.32600E+00
1-8			1.11848E+03	0.00000E+00	3.80401E-02	3.75300E-02	2.17600E+00
1-1	LO	HI	0.00000E+00	0.00000E+00	0.00000E+00	0.00000E+00	0.00000E+00
1-2			0.00000E+00	0.00000E+00	0.00000E+00	0.00000E+00	0.00000E+00
1-3			0.00000E+00	0.00000E+00	0.00000E+00	0.00000E+00	0.00000E+00
1-4			0.00000E+00	0.00000E+00	0.00000E+00	0.00000E+00	0.00000E+00
1-5			0.00000E+00	0.00000E+00	0.00000E+00	0.00000E+00	0.00000E+00
1-6			0.00000E+00	0.00000E+00	0.00000E+00	0.00000E+00	0.00000E+00
1-7			0.00000E+00	0.00000E+00	0.00000E+00	0.00000E+00	0.00000E+00
1-8			0.00000E+00	0.00000E+00	0.00000E+00	0.00000E+00	0.00000E+00

### 3.2.5 Linearity

A linearity equation was not developed for the CIRRIIS 1A radiometer. Because the radiometer used bulk silicon detectors, the high bias response region exhibits DRE (Wyatt, 1987) and cannot be linearized. Therefore, each bias range was fit with a separate equation. The ends of the response equations for each range were compared to verify a smooth response across the range change region. Response equation fitting was performed by Yap, Inc., under the direction of PL. DRE effects were observed as a very linear response in focal plane 1 at high voltages (above about 0.7 volts (dc restored)) in the high bias modes. DRE was not observed in the medium or low bias modes of focal plane 1 or in any of the bias settings of focal plane 2. An example of the observed DRE effect is shown in Figure 30.

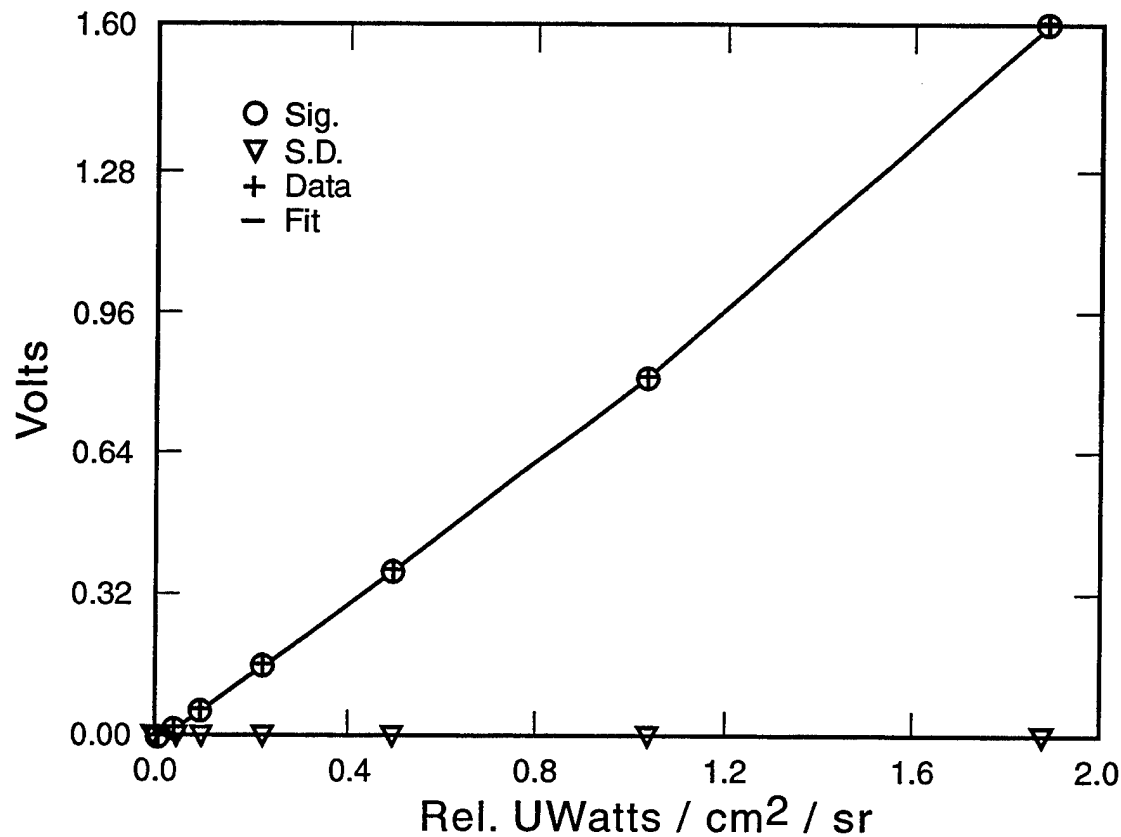


Figure 30. An example of the DRE effect observed in focal plane 1 in high bias above a voltage of about 0.75 V (dc restored).

### 3.2.5.1 Jones Source - Aperture Linearity Measurements

Calibration personnel used the Jones source and aperture method to develop a data set that covered the radiometer dynamic range at all bias and electronic gains. This is the most common method of determining a sensor's linearity. The data set was developed by varying the input flux in known ratios with the set of calibrator precision apertures, while using multiple source temperatures to increase fluxes by 50% of the aperture set flux variance range. Because most of the data collected by CIRRIS 1A was in the Chopper On mode, the data were collected in the Chopper On mode.

The radiometer responses to each input were offset corrected with dark noise responses and fit to the relative flux transfer function. The individual range and temperature curves show significantly more nonlinearity and variation than is known to exist in the CIRRIS 1A sensor. The aperture adjusted Jones source was not linear due to vignetting, which caused variations in the collecting aperture for each detector. Therefore, calibration personnel concluded that the linearity calibration based on the Jones cone aperture area was unreliable, and it was not used in the linearity analysis.

### 3.2.5.2 Extended Source Linearity Measurements

Data collected for absolute response measurements can also be used to determine the sensor linearity for some regions of response. Extended source data were used as the primary range calibration data. Extended source data cover most of the operational range of the CIRRIS sensor, except at the higher voltage ranges of the shorter wavelength filters. An example of the data coverage available for linearity analysis is shown in Figures 31 and 32, which show the extended source data set available for detector 1-6 for all filters, and detector 2-3 for focal plane 2, respectively. To be specifically useful, the data must be collected on either side of the automatic gain change region. Therefore, additional data were collected using manual bias control. The linearity data set was developed using filter 2, a short wavelength narrow band filter. This filter was used because: 1) the extended area source temperatures are hotter for measurements in the sensor dynamic range at short wavelengths, minimizing small inaccuracies in temperature to the black-body curve; and 2) inaccuracies in the measurement of the in-band filter function is not as critical for narrow band as wide bands. These data confirm the DRE effect observed in high bias in both high and low gain (Figure 30). Because of these data, the decision was made not to try to combine the CIRRIS calibration data into a single linearized response equation.

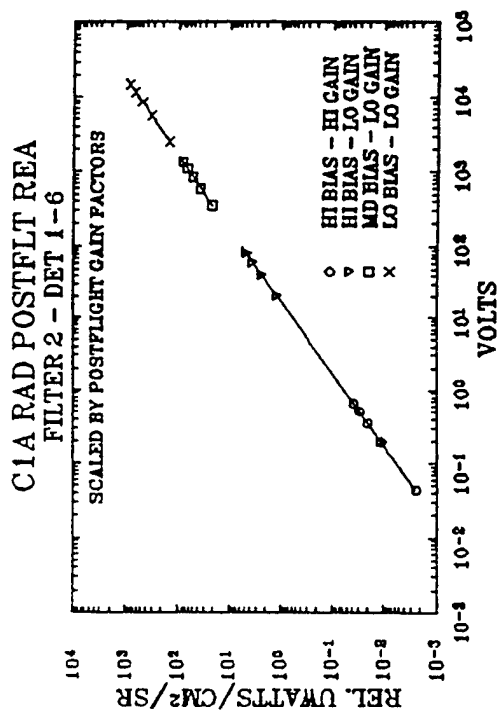
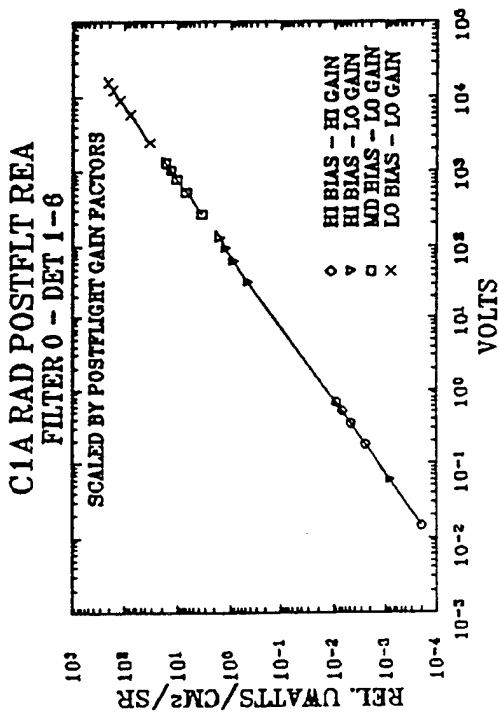
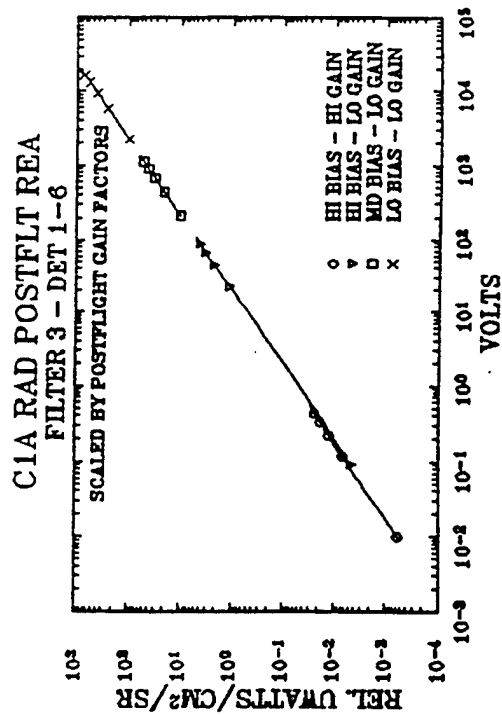
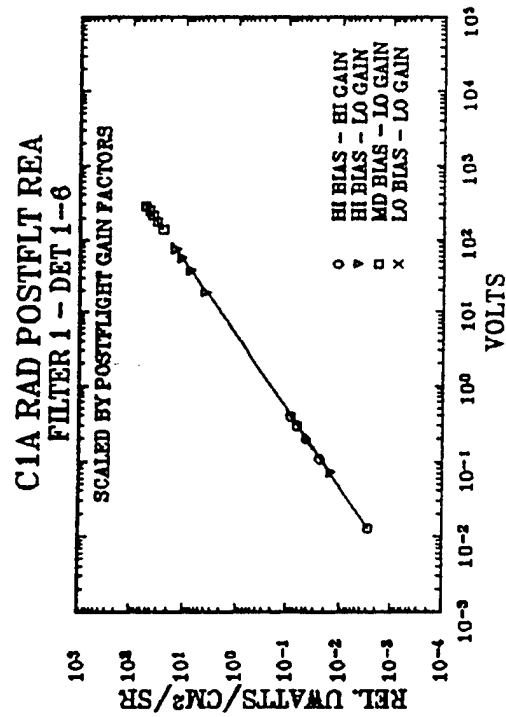


Figure 31. Extended source linearity calibration for radiometer detector 1-6.

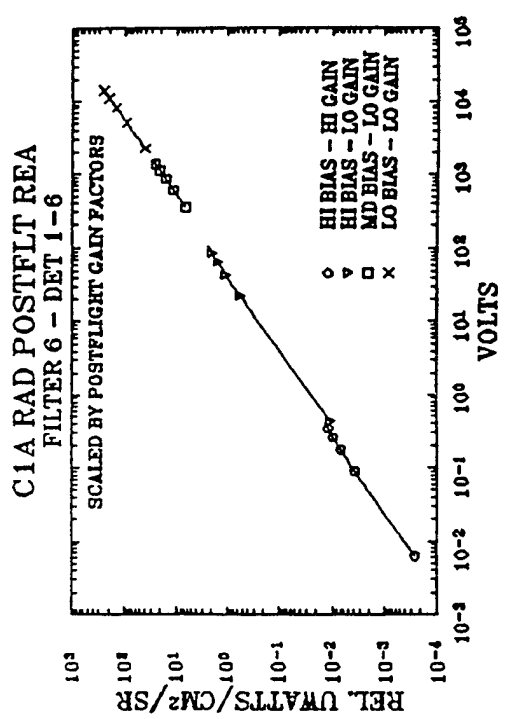
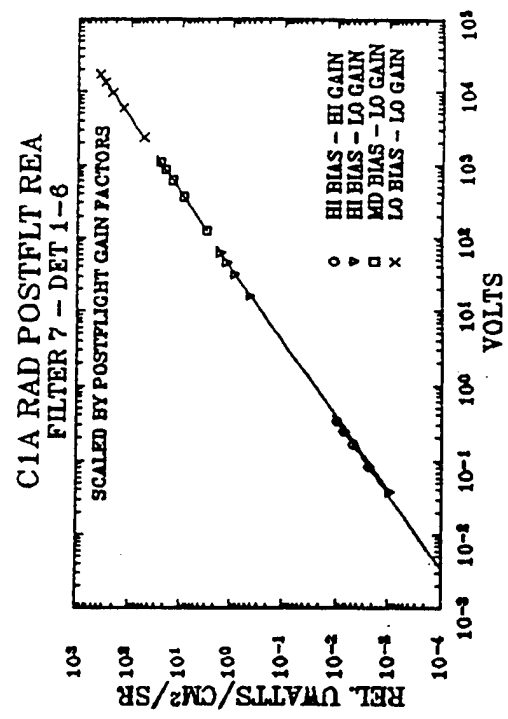
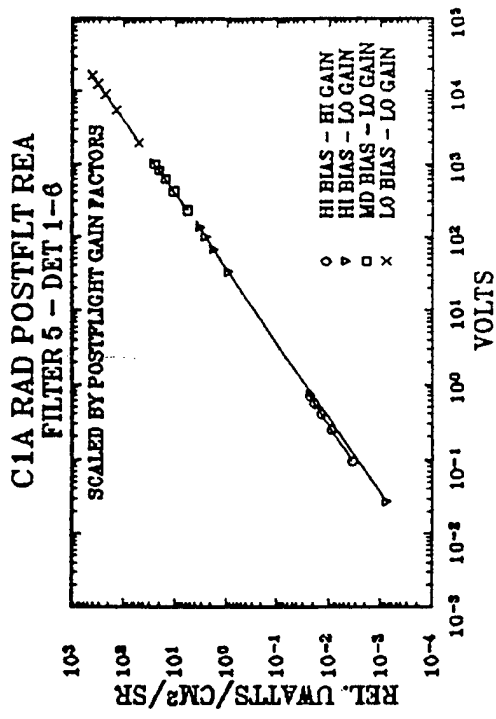


Figure 31 (cont). Extended source linearity calibration for radiometer detector 1-6.

CIRRIIS 1A Radiometer  
 Det. 2-3, Gain LO, Bias LO, Jones & Point Source Data

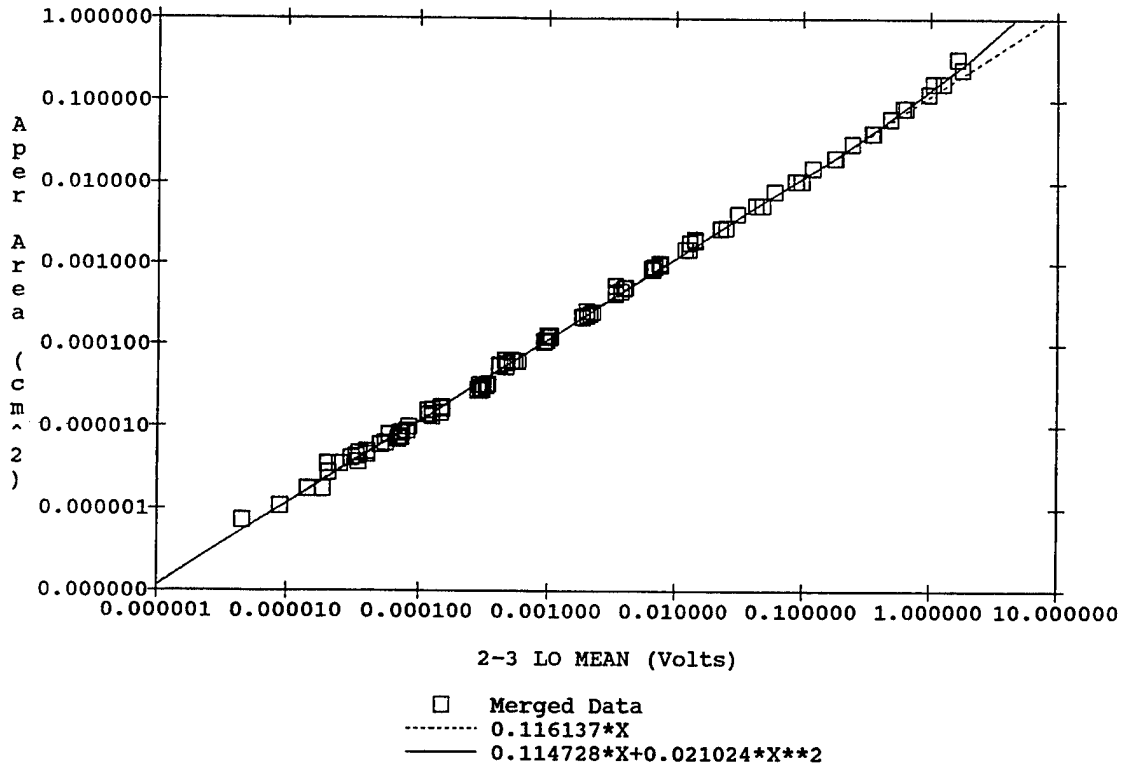


Figure 32. Extended source linearity calibration for radiometer detector 2-3.

### 3.2.5.3 Point Source - Aperture Linearity Measurements

The point source - aperture variation method was used to extend the extended source linearity analysis for the high voltage regions of the short wavelength detectors. The analysis was performed by exposing the detector to increasingly large areas of illumination. The method assumes uniform detector spatial response. Although Section 3.2.1.4 shows that the point source response of the detectors are not exactly spatially uniform, the central 0.5 x 0.5 mr region of each detector is uniform to within a few percent. Although this method is accurate only until the illuminated area expands beyond the edge of the detector, it is effective for extending the extended source linearity measurement to the high end of the dynamic range (bias = lo, gain = lo). This method enabled calibration personnel to apply a small area of intense (high temperature) broad band energy to the detector, allowing for calibration in the regions of intense narrow band, short wave emissions such as those viewed by focal plane 2.

### 3.2.5.4 Small Signal Response Linearity Measurements (ac/dc)

The scatter in the data collected in the Jones source, point source, and extended source methods makes it difficult to separate small nonlinearities from noise. SDL calibration personnel developed the small signal (ac/dc) linearity analysis technique under the SPIRIT II program in an effort to obtain a more definitive measurement. The small signal, or ac/dc, linearity data is pro-

cessed to provide the first derivative of the dc or absolute linearity function. This method was also investigated using CIRRIS 1A.

SDL personnel first performed the ac/dc linearity test with the CIRRIS 1A chopper off and an external chopper modulating an external blackbody source at 90 Hz to provide a constant ac signal. A chopper frequency of 90 Hz was chosen to duplicate the CIRRIS 1A internal chopper. The ac signal was input into the calibrator in the Jones source configuration. The extended-area source of the calibrator was also in position and provided a dc background flux. This configuration allowed the dc flux to be increased while holding the ac flux constant. Figure 33 is a typical amplitude plot of this configuration.

Data were collected and averaged at each extended-area source temperature to find the dc voltage. The ac voltage was calculated by Fourier transforming the data into a power spectrum distribution (PSD), integrating over a small band about the chopping frequency, and taking the square root. Figure 34 shows a typical integrated power spectrum.

Sample results of the ac-dc linearity test are shown in Figures 35 and 36 for detectors 1-1 and 1-3, respectively. The figures show an increased response in the high bias configuration that is not as evident in the medium and low biases. This change in response is consistent with that caused by the dielectric relaxation effect (DRE).

SDL/USU performed a second ac-dc linearity calibration during Phase 2 of the calibration data collection to further study this technique. During this test, the CIRRIS chopper was on, and an external chopper modulating an external source at 15 Hz was used. The externally modulated source was input into the calibrator in the Jones source configuration. The externally modulated signal was held constant and the extended area source temperature was increased in temperature in the background to provide an unmodulated background. The change in detector response to the modulated source was then measured against the changing background.

The results of the linearity analysis confirm the presence of DRE in the high bias response. Because of the DRE effect, the radiometer dynamic range cannot be characterized in a single equation using simple bias and gain multipliers. Therefore, it is necessary to treat each detector bias combination as separate calibrations. The data validate the preflight decision to use individual range response curves in OPUS. The range response curves describe the absolute response of the sensor over that range, eliminating the need for a linearity correction. Therefore, although the linearity data were not used in the CIRRIS 1A calibration, the significant technique development that occurred will be useful for calibrating sensors that do not exhibit DRE.

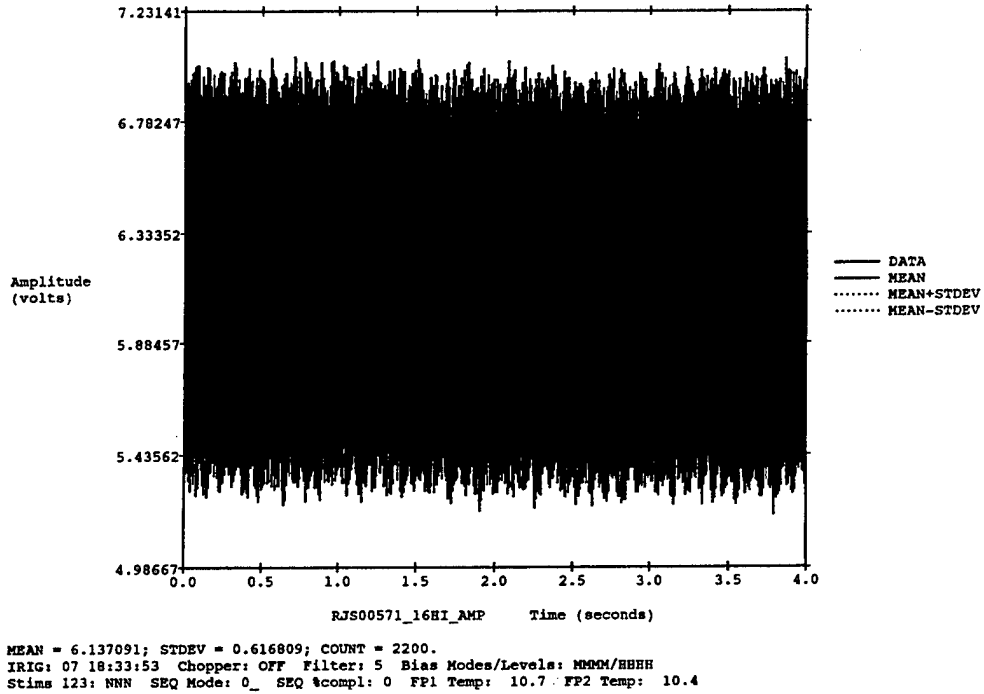


Figure 33. Typical amplitude plot for linearity coefficient, detector 1-6.

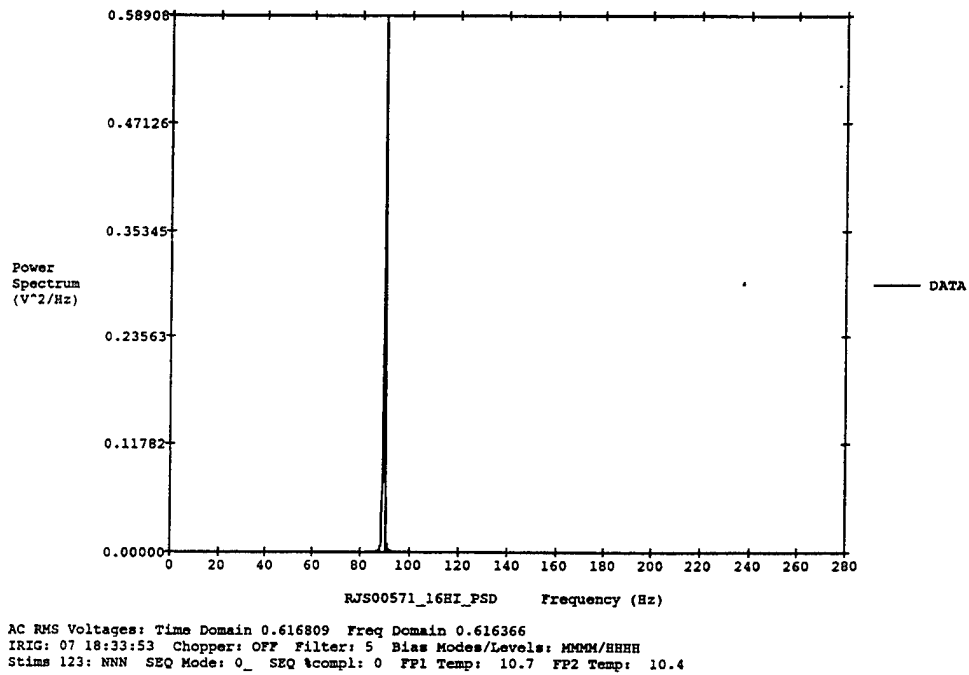


Figure 34. Typical integrated power spectrum for linearity coefficient, detector 1-6.



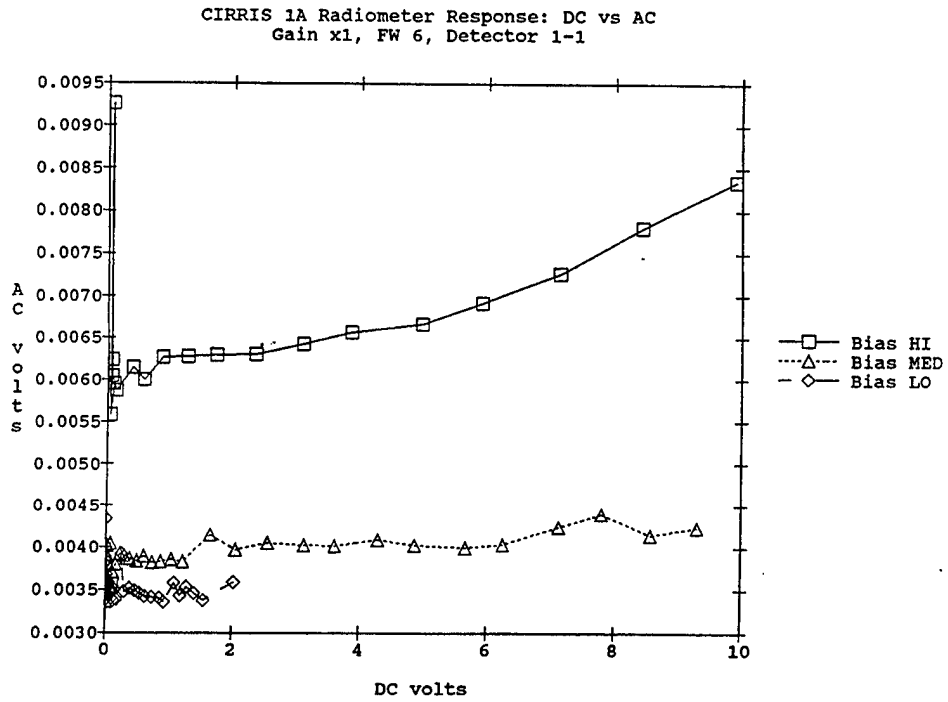


Figure 35. AC-DC linearity for radiometer detector 1-1.

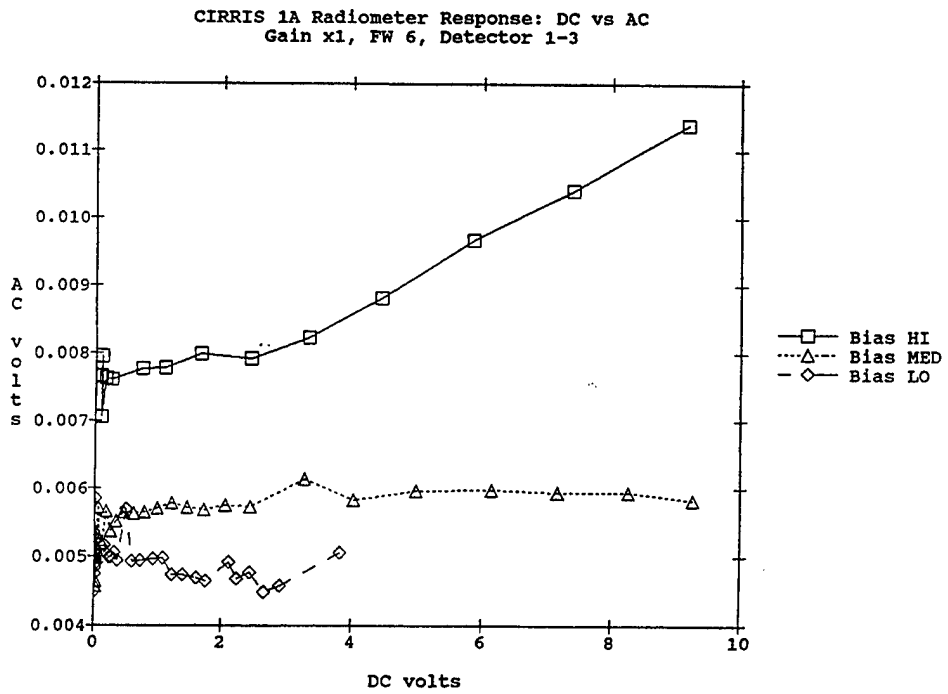


Figure 36. AC-DC linearity for radiometer detector 1-3.

### 3.2.6 Relative Spectral Responsivity

A radiometer's relative spectral response is its peak-normalized response to radiation at different wavelengths both within and outside its spectral passband. Calibration personnel measured the spectral passband and the out-of-band rejection for each radiometer filter. The relative spectral response data are required to calculate the effective flux for the absolute calibration.

Calibration personnel determined the relative spectral response of each of the CIRRIS 1A radiometer filters in situ using the Bomem interferometer through the collimator to provide known relative spectral flux. In this configuration, the interferometer is used with the CIRRIS 1A detector to provide an extremely sensitive Fourier transform spectrometer or interferometer. The interferometer is used as a spectrally coded source and the analog output of detector 1-4 is fed back into the interferometer data system to complete the interferometer. The radiometer chopper was turned off for these measurements. If the interferometer source has been spectrally calibrated, the spectral response of the system being tested (i.e., CIRRIS 1A) can be measured directly. The spectral response of each radiometer filter was then normalized to its own peak to provide the relative spectral response (RSR) function.

The out-of-band rejection measurements were also made with the Bomem interferometer and collimator source. In this measurement, the passband region of the CIRRIS 1A filter is blocked by a filter in the collimator. This allows the CIRRIS 1A detector to be used in its most sensitive mode to look for leaks in the blocker regions of the filter. Since the source radiation is spectrally coded by the interferometer, the spectral location of the transmitting regions is determined by the transform process.

Accurate assessment of the RSR of a sensor requires the relative spectral emission of the interferometer source to be well known. The relative spectral strength of the Bomem source was measured using the CIRRIS 1A interferometer. To eliminate double wavelength coding, this required the CIRRIS interferometer moving mirror to be stopped while the Bomem source was being injected into the CIRRIS interferometer. The Bomem source was then measured using the CIRRIS interferometer within a clocked sampling scheme. To complete the measurement, the CIRRIS relative spectral response was divided out of the measured response.

The out-of-band rejection measurements can be summarized mathematically by the following equation:

$$B(\nu) = \left[ \frac{M(\nu)}{IFR(\nu)} \right] \quad (13)$$

where

- B( $\nu$ ) = Bomem relative spectral source emission as a function of wavenumber
- M( $\nu$ ) = Bomem source measured with the CIRRIS interferometer
- IFR( $\nu$ ) = CIRRIS relative spectral response measured from an independent black-body calibration

Once the Bomem source relative spectral emission is known, the radiometer in-band (out-of-band requires more steps) relative spectral response is calculated by the following equation:

$$RSR(\nu) = \left[ \frac{R(\nu)}{B(\nu)} \right] \quad (14)$$

where

- RSR( $\nu$ ) = radiometer relative spectral response as a function of wavenumber
- R( $\nu$ ) = raw response of the radiometer to the Bomem source
- B( $\nu$ ) = Bomem source relative spectral response emission from Equation (13)

Use of the Bomem interferometer as a source for radiometer relative spectral response measurements provides high spectral resolution. The accuracy of the RSR measurement is limited by the ability to calibrate the Bomem source. Two problems were discovered with using the CIRRIIS interferometer to calibrate the relative spectral source strength of the Bomem interferometer. The Bomem relative spectral response was calibrated using the C-1A interferometer. At wavelengths beyond (21  $\mu\text{m}$ ), the throughput of the Bomem source into the interferometer was not great enough to allow division by the C-1A interferometer signal without adding significant noise to the radiometer RSR. As a result, the Bomem RSR was assumed to be flat at wavelengths greater than 500  $\text{cm}^{-1}$ . The second problem is that the CIRRIIS interferometer relative spectral response used in Equation (14) may not be completely valid when the moving mirror is held steady. Small changes in alignment, which occur as the interferometer mirror scans, tend to attenuate large wavenumber energy more relative to that at the smaller wavenumbers. This causes the Bomem source in Equation (13) to give the appearance of more relative energy at large wavenumbers. When the Bomem source is divided through in Equation (14), it causes the radiometer RSR to show less energy at larger wavenumbers. An attempt to quantify the effective amount of large wavenumber attenuation was not performed, but the error is thought to be less than 5%.

### 3.2.6.1 In-Band Response

Figures 37 and 38 show the linear plots of the radiometer relative spectral responses for detectors 1-4, all filters, and 2-3, respectively. The RSR of focal plane 2 was determined using detector 2-3. The solid line in these figures is the corrected relative response data and the dashed line represents the vendor-supplied filter transmission curve for the filter. The RSR is primarily a convolution of the filter transmission curve and the detector response. A small factor is added by the beam splitter. Figures 39 and 40 show the vendor-supplied detector responsivities for focal plane 1 and focal plane 2 respectively. Figure 41 is the beamsplitter transmission for the radiometer.

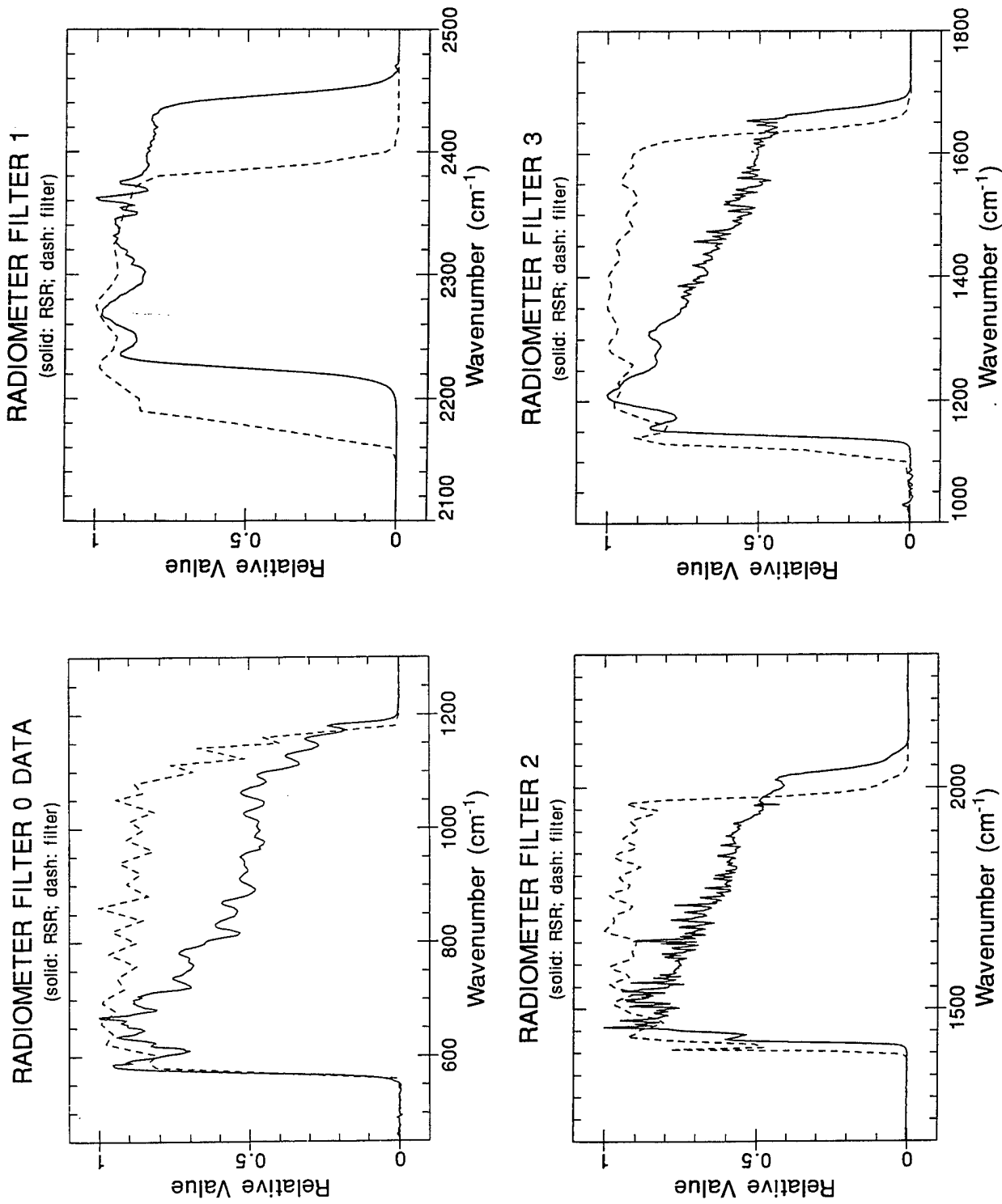


Figure 37. Relative spectral response for radiometer detector 1-4.

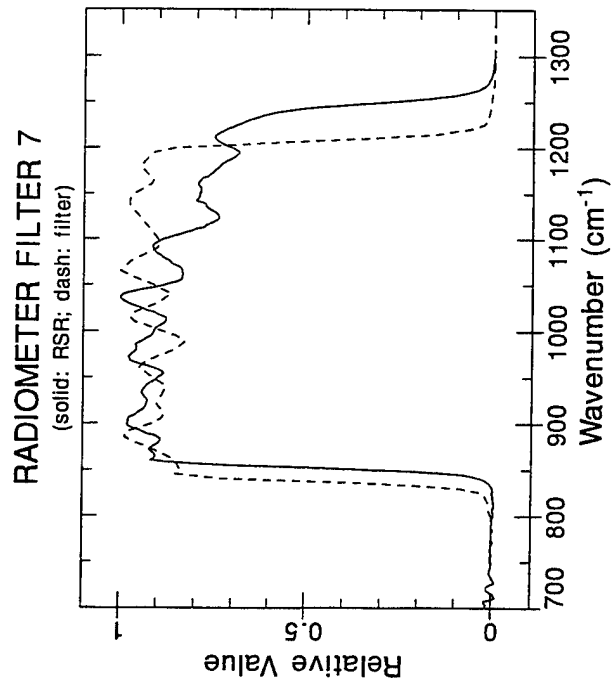
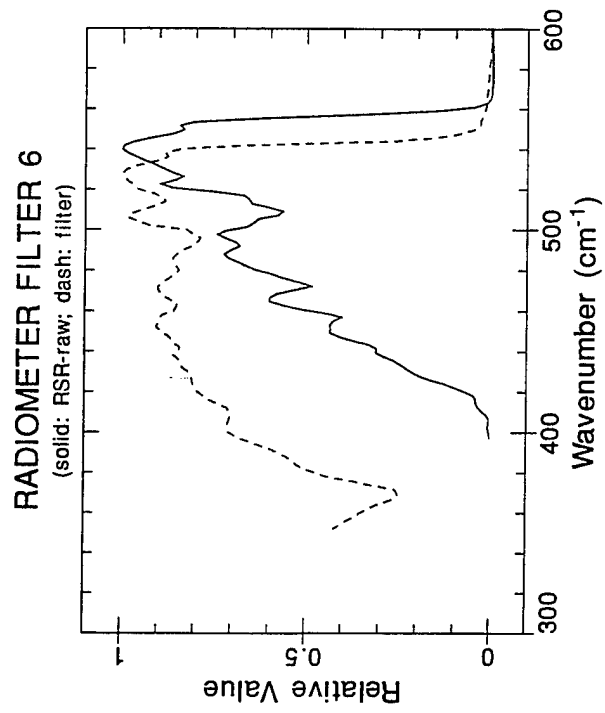
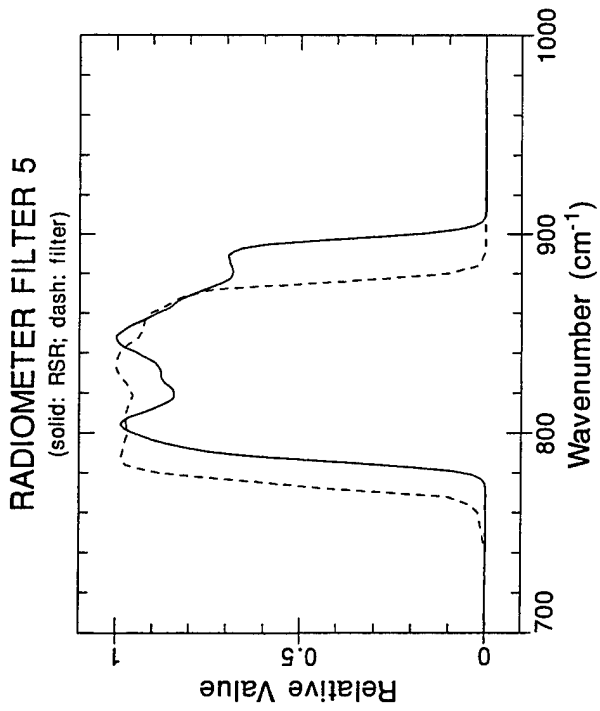


Figure 37 (cont). Relative spectral response for radiometer detector 1-4.

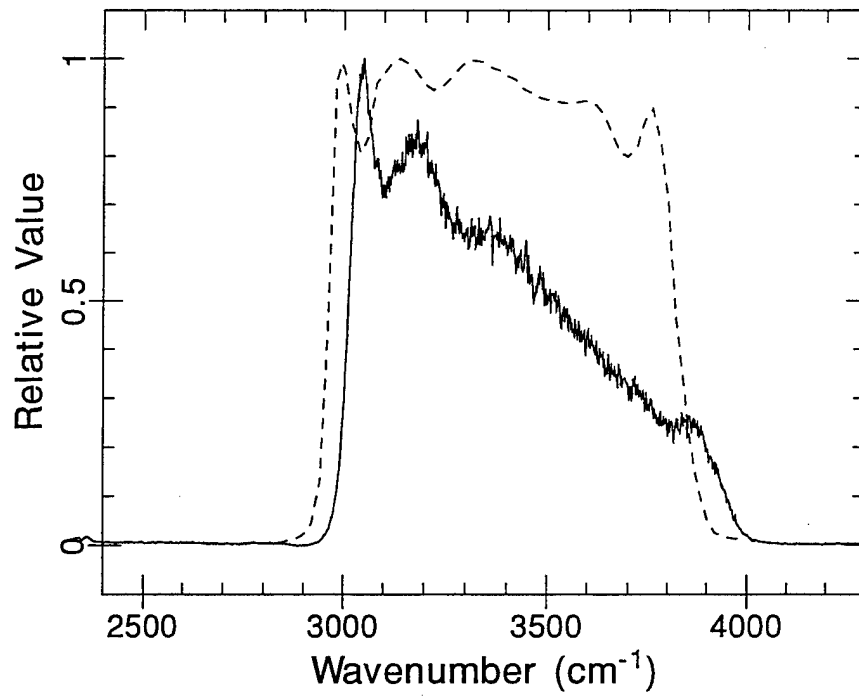


Figure 38. Relative spectral response for radiometer detector 2-3.

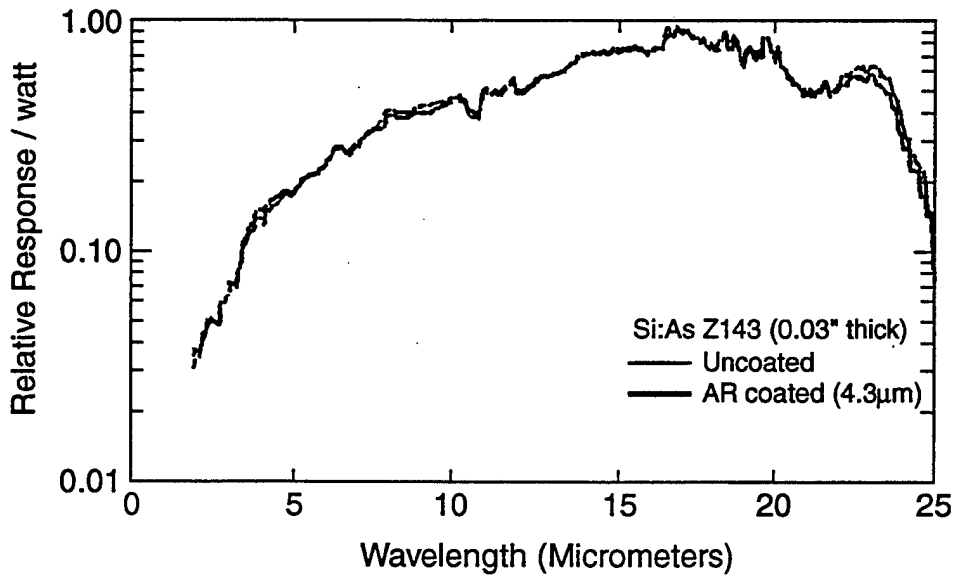


Figure 39. Vender-supplied detector responsivities for radiometer focal plane 1.

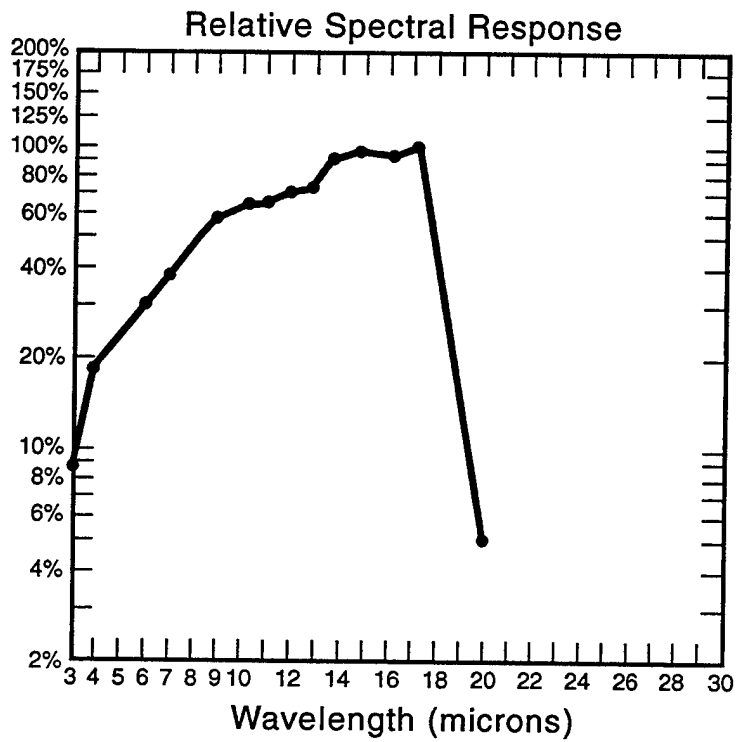


Figure 40. Vender-supplied detector responsivities for radiometer focal plane 2.

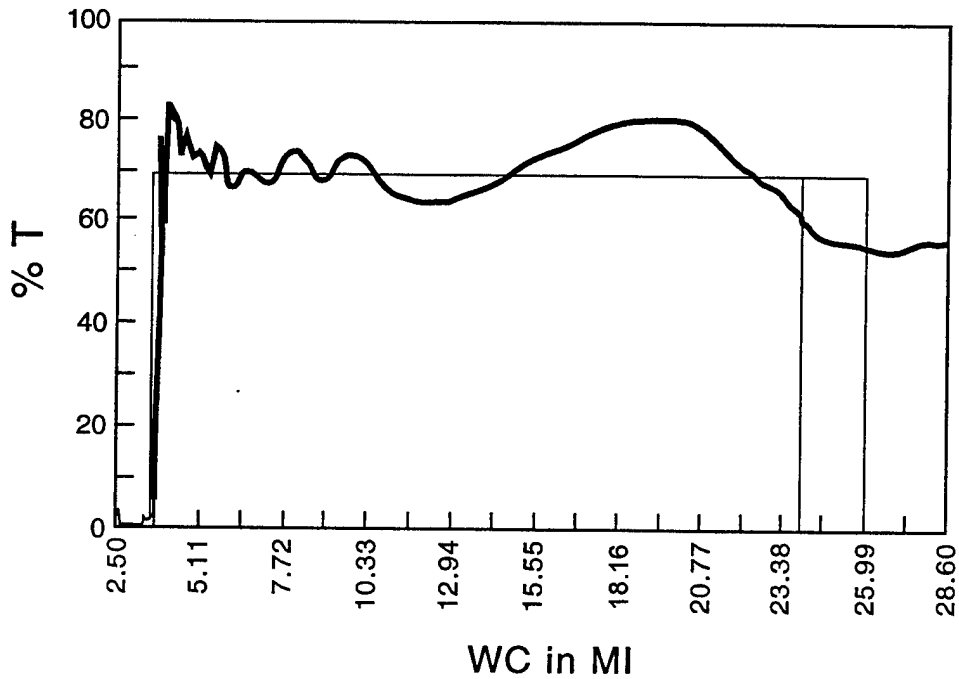


Figure 41. Radiometer beamsplitter transmission.

### 3.2.6.2 Out-of-Band Rejection

The radiometer out-of-band (OOB) rejection was measured using the cascaded filter Fourier transform spectrometer (CFFTS) method (Kemp et al., 1989). This method allowed out-of-band rejection of the filters to be measured to approximately  $10^{-6}$ .

The rejection of OOB radiation can be quantified as a relative spectral transmission (RST( $\nu$ )) function of the filter. RST( $\nu$ ) is defined as:

$$RST(\nu) = \frac{\tau(\nu)}{\tau(\nu_p)} \quad (15)$$

where

- $\tau(\nu_p)$  = peak transmission of the filter at the spectral resolution of the system
- $\tau(\nu)$  = filter transmission function over the wavenumber ( $\nu$ ) sensitivity bandwidth of the detector

Both transmission values included in Equation (15) should be measured at the same spectral resolution. The measurement of RST( $\nu$ ) of optical filters over wide bandwidth regions and/or to less than  $10^{-6}$  is extremely difficult. The CFFTS technique makes this measurement possible by combining a Michelson interferometer and a blackbody emitter to provide a source of frequency encoded radiation. This frequency encoded radiation is passed into the CIRRS 1A entrance aperture through the filter under test using the calibrator's collimator. This system is more efficient than a monochromator because the interferometer transmits information from the entire range of the passband spectrum during each time element of the measurement, whereas the monochromator transmits only in a very narrow band. In addition, the interferometer can utilize a large aperture of the instrument under test without limiting the spectral resolution of the system. In a CFFTS measurement, interferometrically encoded radiation is fed through a blocker filter and into the entrance aperture of the system under test.

Under the CFFTS strategy, radiation in the passband of the filter under test is blocked from reaching the detector, while a region of the filter's OOB blocker is exposed to the full intensity of the frequency encoded blackbody radiation from the interferometer. The filter arrangements needed to make the CFFTS strategy work are shown in Figure 42. The test filter passband is blocked using the passband filters in the calibrator. The passband of the filter under test should be sufficiently blocked that a large majority of the photons reaching the detector have passed through the blocker region of the test filter. As all of the modulated photons reaching the detector are frequency resolved, small leaks in the test filter pass band regions are not critical to the calculation of RST. When the passbands of both the blocking and test filters do not overlap, the absolute radiance level at the detector is very low and the detector can be operated at near maximum sensitivity.



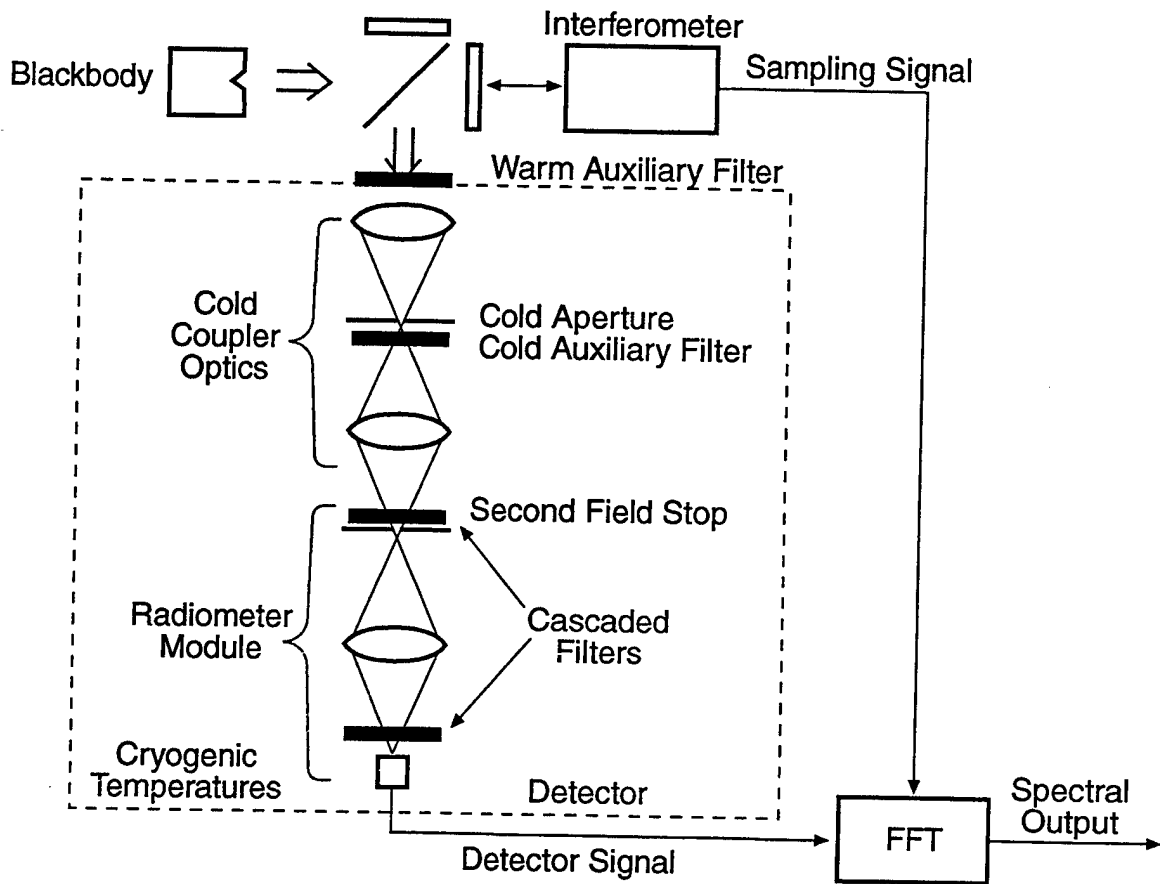


**Figure 42. Basic measurement setup using external interferometer and auxiliary filter to test filter out-of-band rejection.**

The RST( $\nu$ ) measurement requires the determination of four separate  $\tau(\nu)$  functions to remove the characteristics of the IR source, optics, detector, and sampling and transforming techniques. When properly combined, these spectra provide an RST( $\nu$ ) that represents only the filter trans-

mission ratio. We define  $RST(\nu)$  functionally by the following equation:

$$RST(\nu) = \left[ \frac{\tau_c(\nu)}{\tau_R(\nu)} \right] X \left[ \frac{1}{\tau_B(\nu)} \right] * \left[ \frac{1}{(\tau_{Tp}/\tau_{Rp})(\nu)} \right] \quad (16)$$

where

- $\tau_R(\nu)$  = interferometer system reference transmission function (i.e., the transmission of the interferometer source through the system with no filters in optical path)
- $\tau_T(\nu)$  = test filter transmission function (no blocking filter)
- $\tau_B(\nu)$  = blocking filter transmission function (no test filter)
- $\tau_c(\nu)$  = cascaded filter transmission (a composite made from the passband regions of the blocking filters with both blocking and test filters in the optical path)
- $p$  = spectral peak value
- $X$  = multiplication of each point in the respective functions (i.e., the dot product)
- $*$  = multiplication of each point in the transmission function by a constant (scaler product)

Because of the large differences in absolute spectral transmission that are involved in the calculation of Equation (16), the system gains must be accurately characterized. Because the CIRRIS 1A system has been well quantified, this did not require additional measurements.  $\tau_R(\nu)$  provides the characterization of the system source and transmission, allowing the other transforms to be correctly normalized. The transform of each of the other interferograms is divided point by point by the transform of the reference scan to develop the normalized transmission of each filter. For maximum accuracy, a reference scan should be taken through the CIRRIS 1A system using filter 0 and the same bias and electronic gain as the measurement scan. The transform of the test filter interferogram provides the peak transmission and wavenumber  $[\tau(\nu_p), \nu_p]$ . To calculate  $RST(\nu)$  in the passband region of the test filter,  $\tau_T(\nu)$  is substituted for  $\tau_c(\nu)$ , with  $\tau_B(\nu)$  set to unity. Functionally dividing by  $\tau_B(\nu)$  in the passband region of each blocking filter normalizes the function for the non-ideal transmission of each filter. Developing a composite function which only includes the high transmission portions of each blocking curve eliminates the noise that would be added by including the blocking regions.

CFFTS measurements were made on all of the regions of the CIRRIS 1A filters for which blocker filters were available. Because of the wide range of filters necessary to overlap the complete out-of-band range of all the C-1A filters, not all regions of the filters could be measured using the MIC2 filter set. These figures are a combination of all available bandpass coverage that did not overlap the main filter passband. The legends on the side of the figures indicate the various MIC2 filters used. Special filters were not ordered for this test, and some areas of the CIRRIS 1A filter blocker regions were not tested. However, all of the regions that were exposed to high intensity bands in flight were tested. Only two areas of slight OOB leakage were discovered, and these had been predicted by modeling (Kemp et al., 1989). Examples of the CIRRIS

1A measurements are shown in Figures 43 through 49. The upper curve is the C-1A measured RSR of the filter. The lower curve is the out-of-band rejection ratio.

Figure 46 shows the OOB and relative spectral response of CIRRIS radiometer filter 3, which has a good cascade filter match. The blocking of the  $15 \mu\text{m CO}_2$  to better than  $10^{-5}$  is demonstrated. Measurements of all the filters show the  $10^{-6}$  capability of the technique. The regions of slight leakage that are shown in these figures occur in filter 1, filter 2, filter 5, and the filter over focal plane 2. The spike at  $440 \text{ cm}^{-1}$  is believed to be a noise spike caused by dividing through the transform by the C-1A interferometer RSR which is very steep and quite noisy below  $550 \text{ cm}^{-1}$  and above  $3300 \text{ cm}^{-1}$  (Figure 71). These regions do not overlap earthlimb emitters, and did not reduce CIRRIS 1A measurement performance.

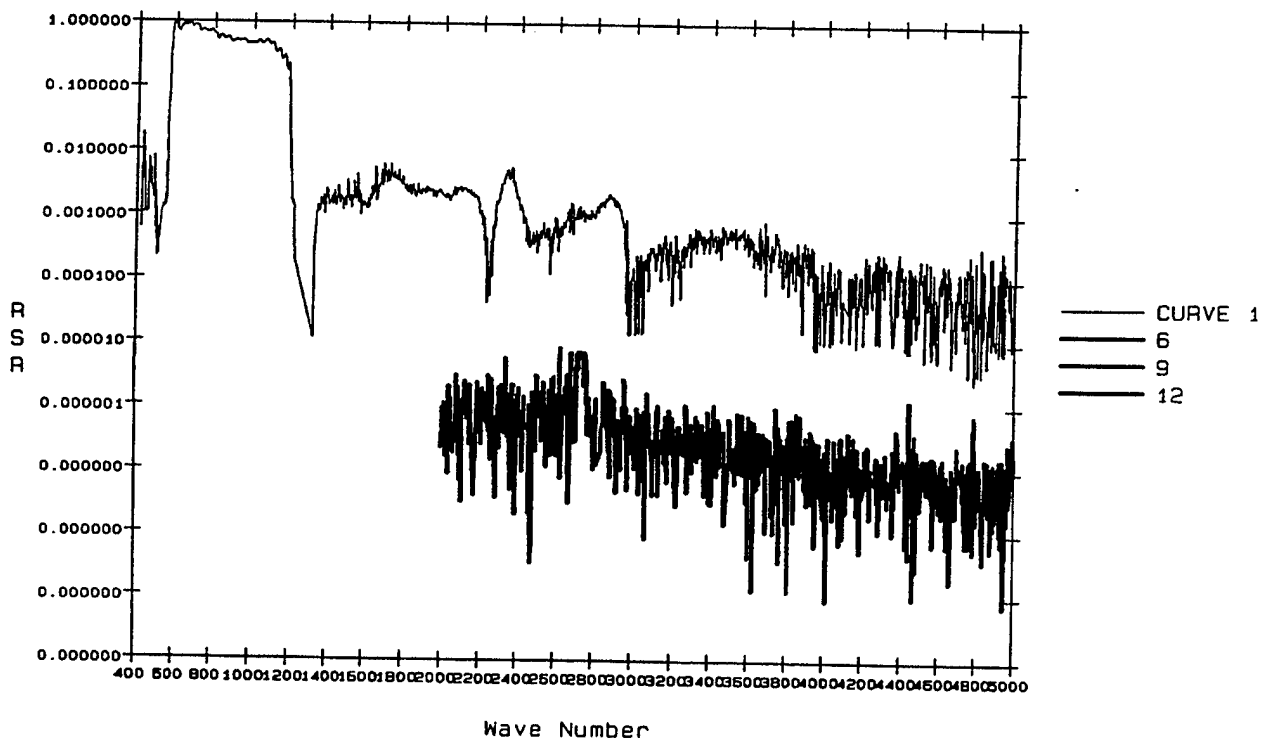
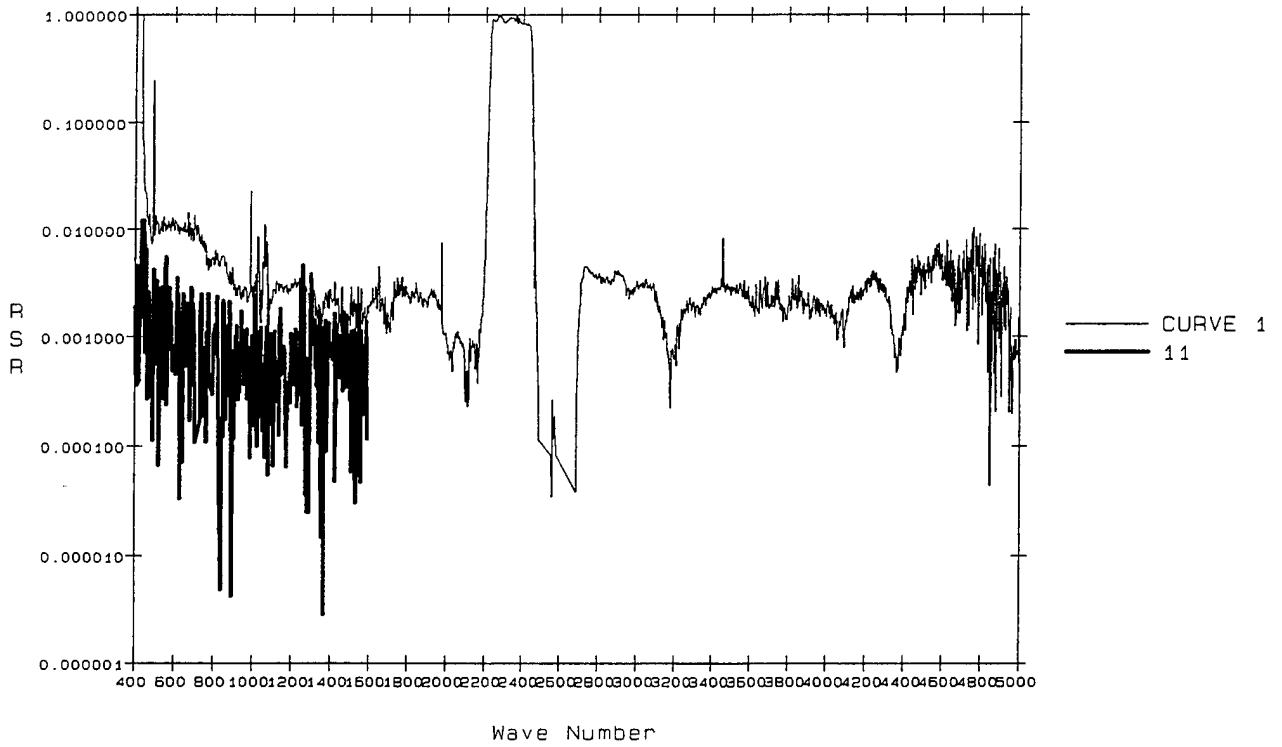
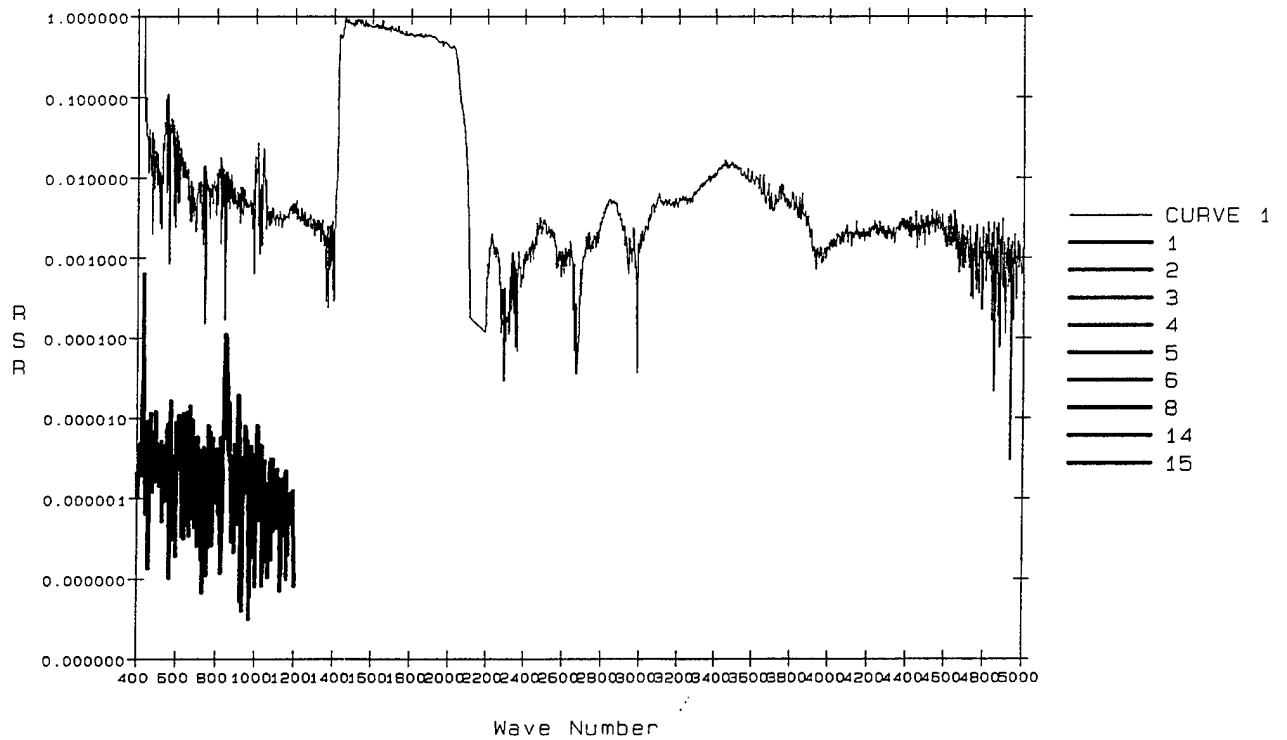


Figure 43. Radiometer out-of-band rejection, filter 0.



**Figure 44. Radiometer out-of-band rejection, filter 1.**



**Figure 45. Radiometer out-of-band rejection, filter 2.**

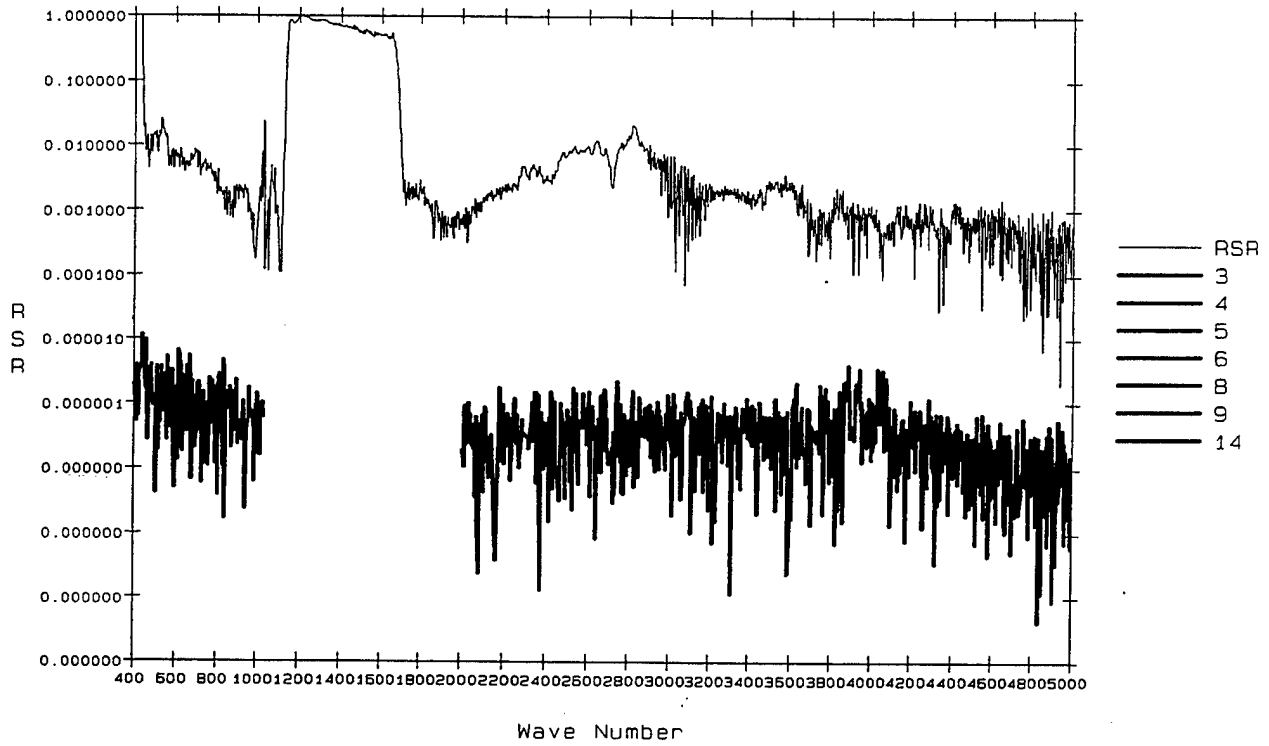


Figure 46. Radiometer out-of-band rejection, filter 3.

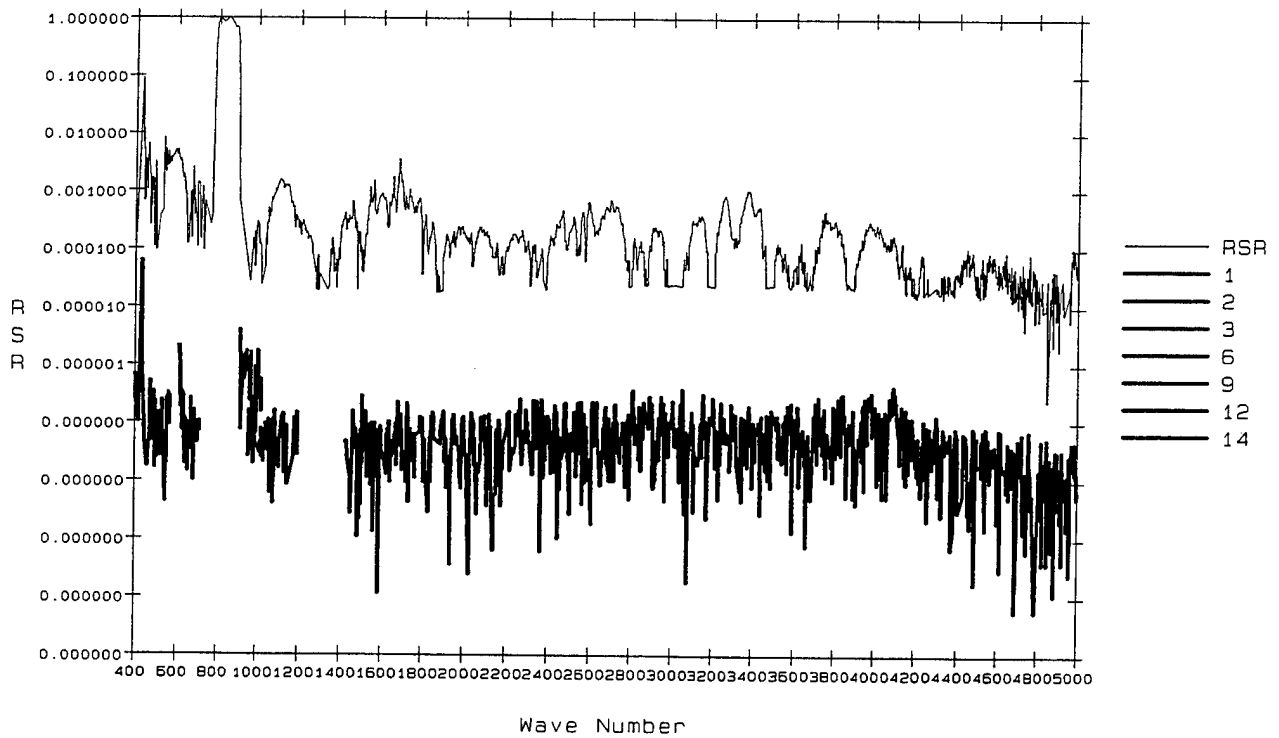


Figure 47. Radiometer out-of-band rejection, filter 5.

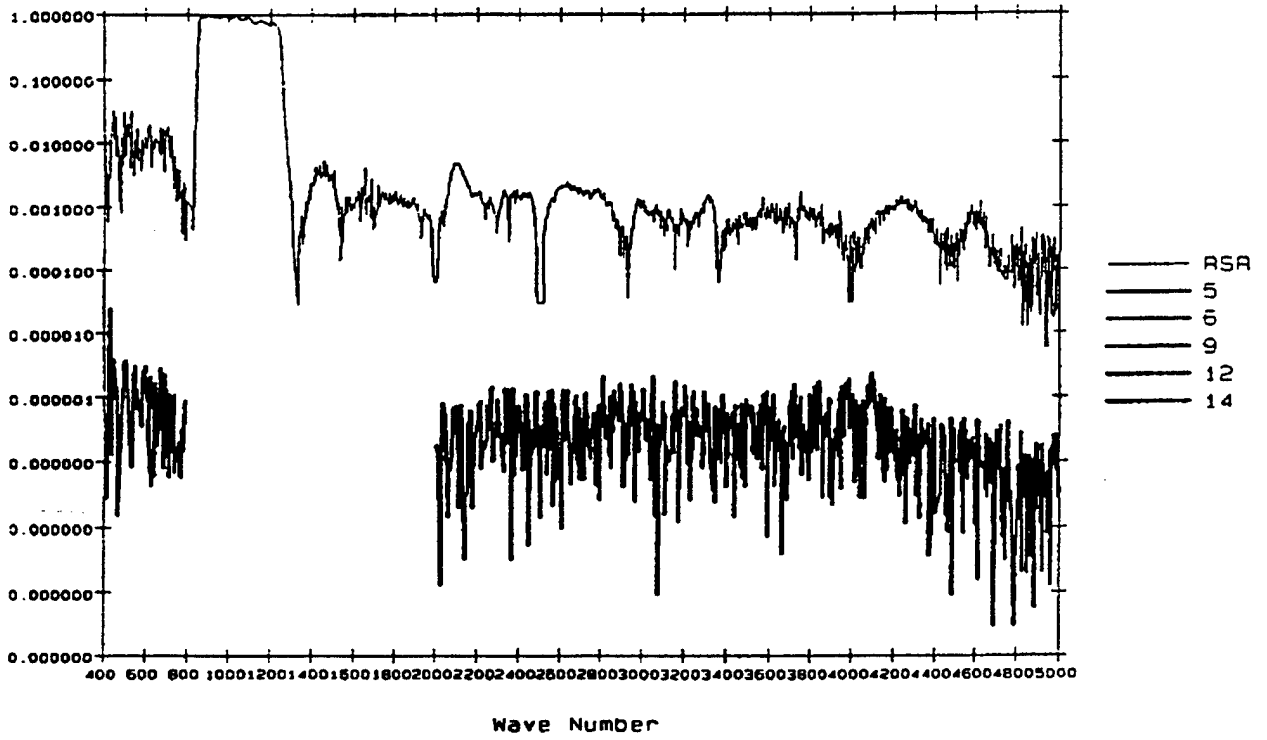


Figure 48. Radiometer out-of-band rejection, filter 7.

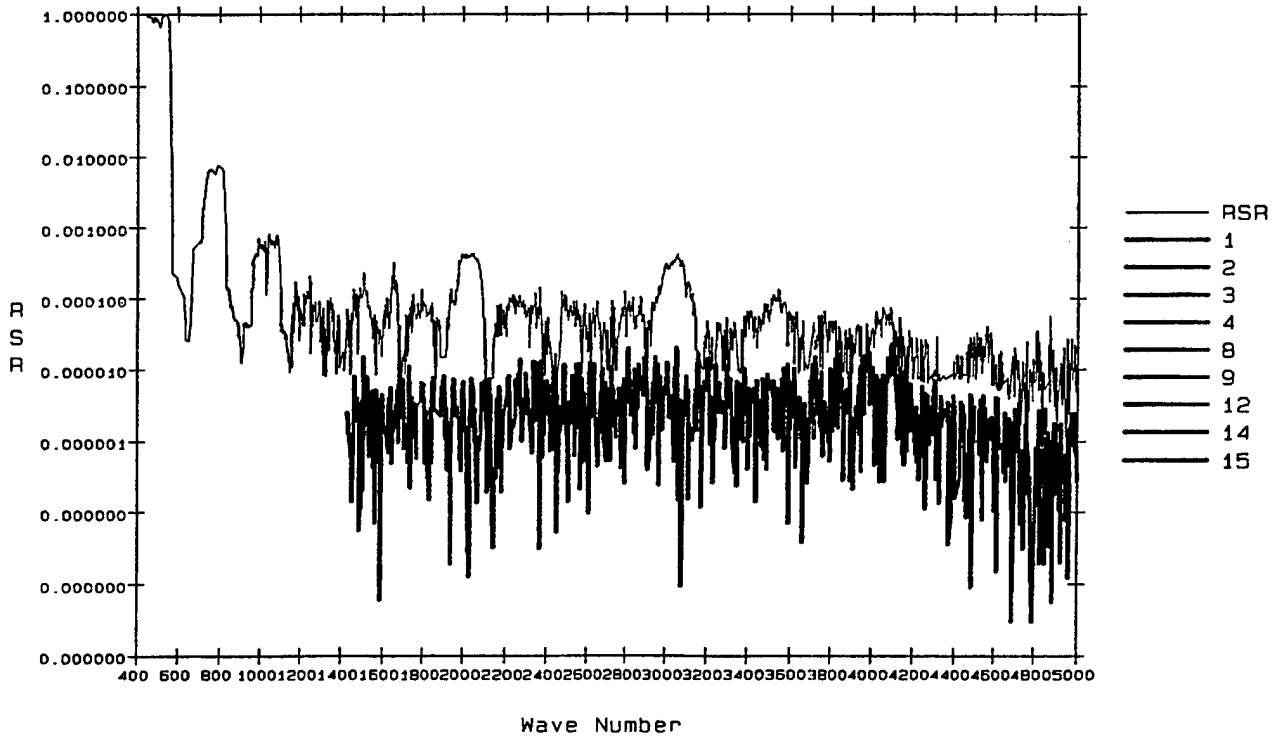


Figure 49. Radiometer out-of-band rejection, focal plane 2.

### 3.2.7 Measurement Uncertainties

SDL/USU calibration personnel performed various analyses to quantify the uncertainty of the CIRRIS 1A calibration and to provide guidance to the flight data users as to the confidence that can be placed in any particular measurement. The classes of uncertainties considered are: random (noise) uncertainties, calibration residual uncertainties, nonideal sensor performance uncertainties, and standard calibration source uncertainties (Wyatt 1991). Random uncertainties and nonideal sensor performance uncertainties are derived from the radiometric model discussed in paragraph 3.1.3. Random uncertainties include short term repeatability (noise) and long term repeatability. Calibration residual uncertainties are uncertainties of parameters in the calibration equation. These uncertainties include the effects of dark offset drift and nonuniformity correction repeatability. Standard source uncertainties, contribute to the uncertainty of the absolute radiance responsivity.

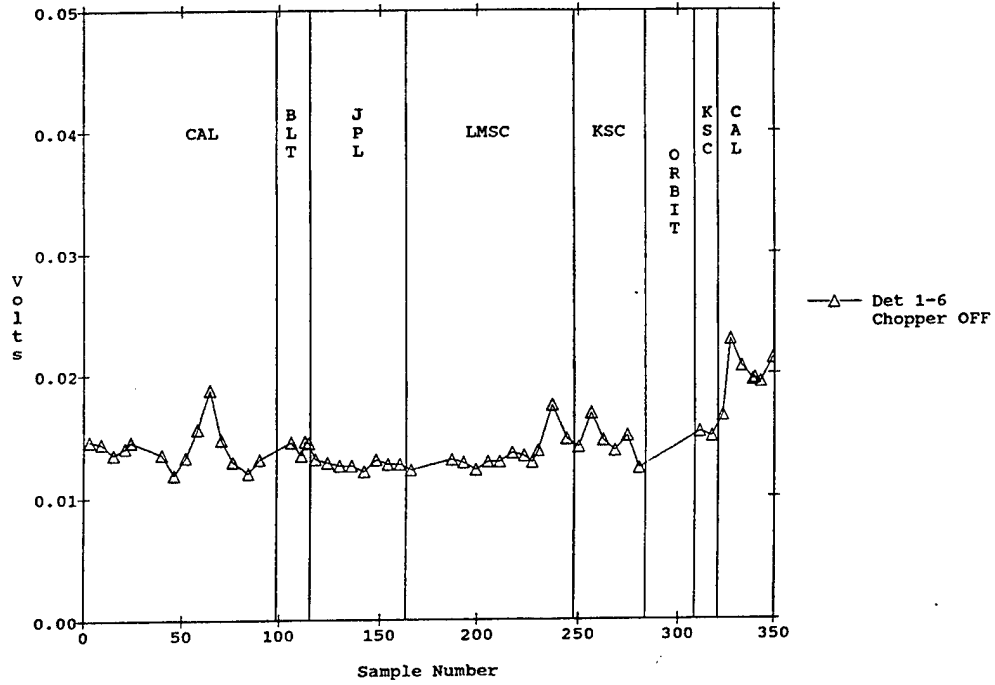
The radiometer noise response was determined by measuring the dark noise and the signal-to-noise ratio over the dynamic range of the instrument for all bias/gain combinations. Dark noise is the uncertainty of individual measurements at the minimum detectable signal level. It provides a useful diagnostic parameter to monitor system degradation. The objective of the dark noise measurement is to check for leaks in the calibrator, evaluate electrical crosstalk, and to determine dark offset.

The noise over dynamic range calibration characterizes short-term temporal measurement uncertainties for different levels of illumination throughout the dynamic range of the radiometer. The objective of this calibration is to determine the smallest detectable modulation in a given background to quantify noise as a function of the flux.

#### 3.2.7.1 Dark Noise

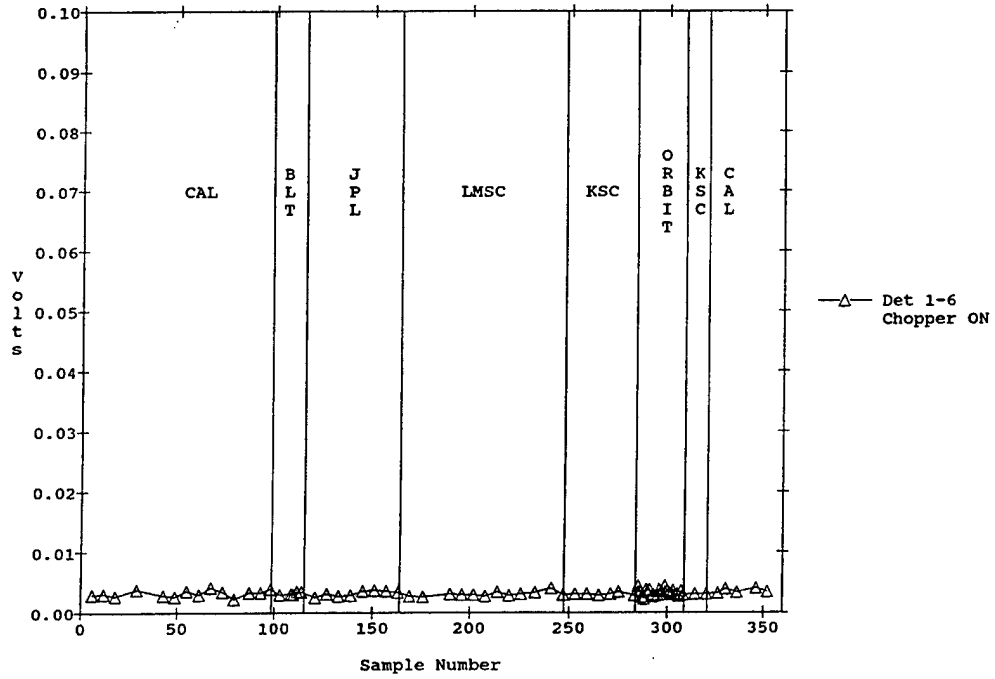
SDL personnel measured the dark noise of the CIRRIS 1A radiometer throughout the history of its testing, integration, flight and calibration. Figures 50 and 51 show the rms noise histories for the radiometer prime detectors, 1-6 and 2-3, respectively. Volume 2 contains the noise histories for all of the radiometer detectors. These figures show that the dark noise has been relatively stable for all detectors. They also show that the dark noise data are consistent with the fact that the dark noise of a DC-coupled system is usually larger than the noise of a chopped and DC-restored system. Because of these measurements, most of the CIRRIS 1A flight data were collected in the Chopper On mode.

Figures 52 and 53 are graphs showing the mean amplitude and standard deviation, respectively, for the relative dark voltages for all detectors. Figure 54 shows the mean amplitude under dark conditions for detector 1-6, and Figure 55 is its associated power spectrum. Noise levels remained consistent through the flight, except for the presence of gamma ray induced spikes in the detector output. These spikes exist in both the data and dark noise. As a result, despiking routines were developed which removed most of the spikes. Once these routines had been applied to the dark noise measurements, the flight deck noise levels were almost identical to those observed pre and post launch.



Gain = HI (x100), Bias = HHHH, FW 4, Sept 1988 - Feb 1992.

### Chopper Off

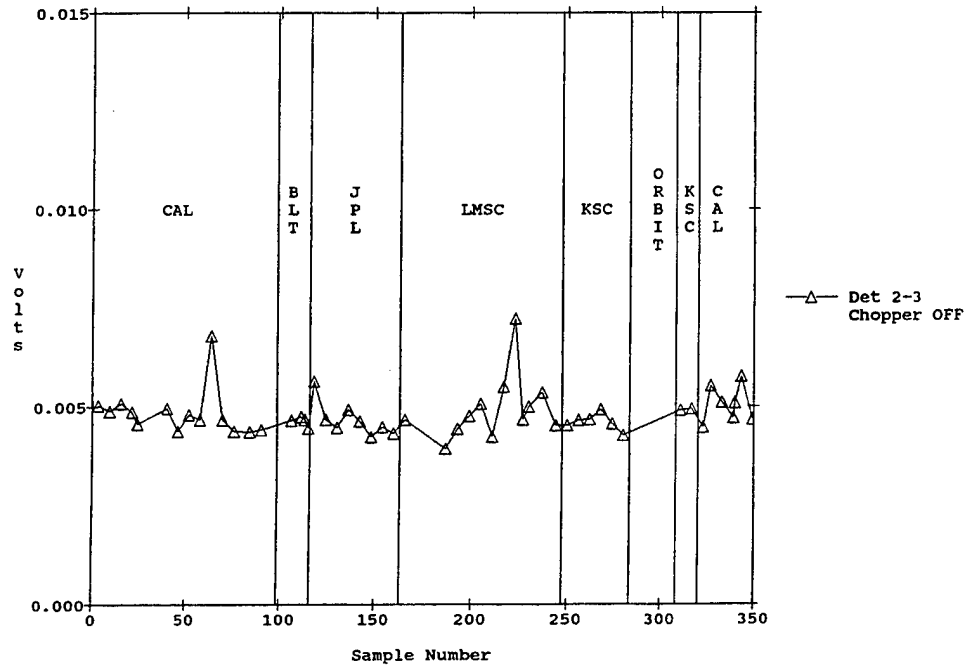


Gain = HI (x100), Bias = HHHH, FW 4, Sept 1988 - Feb 1992.

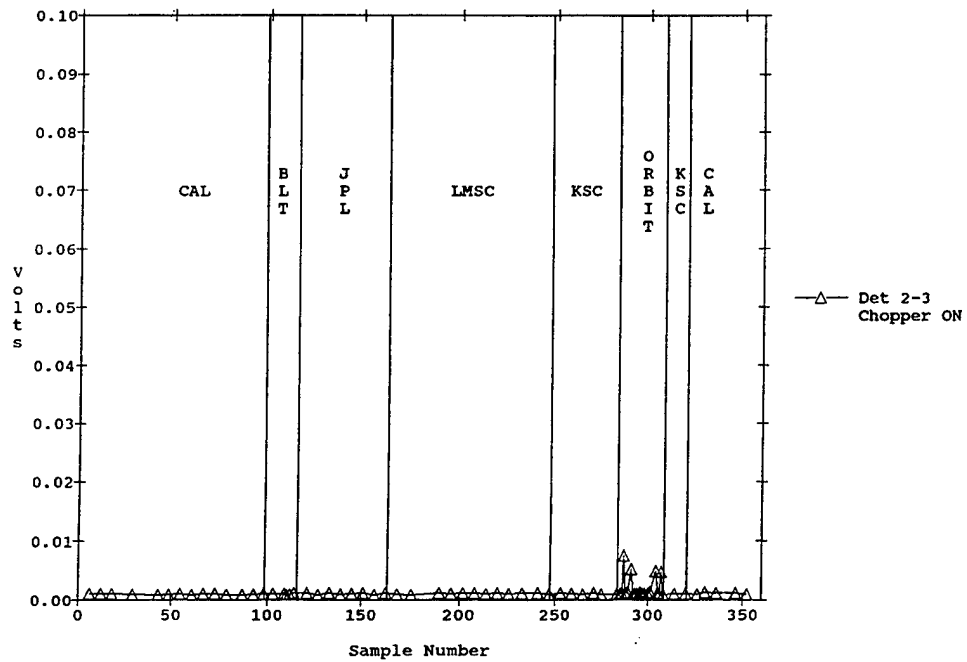
### Chopper On

Figure 50. RMS noise history for radiometer detector 1-6.



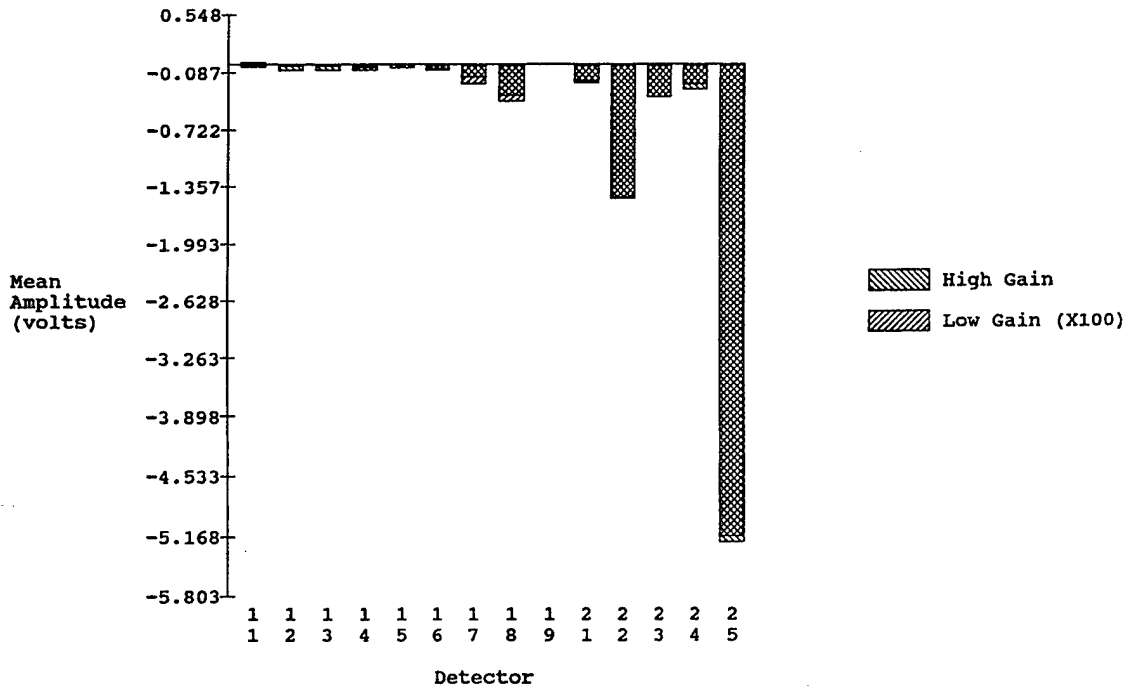


### Chopper Off



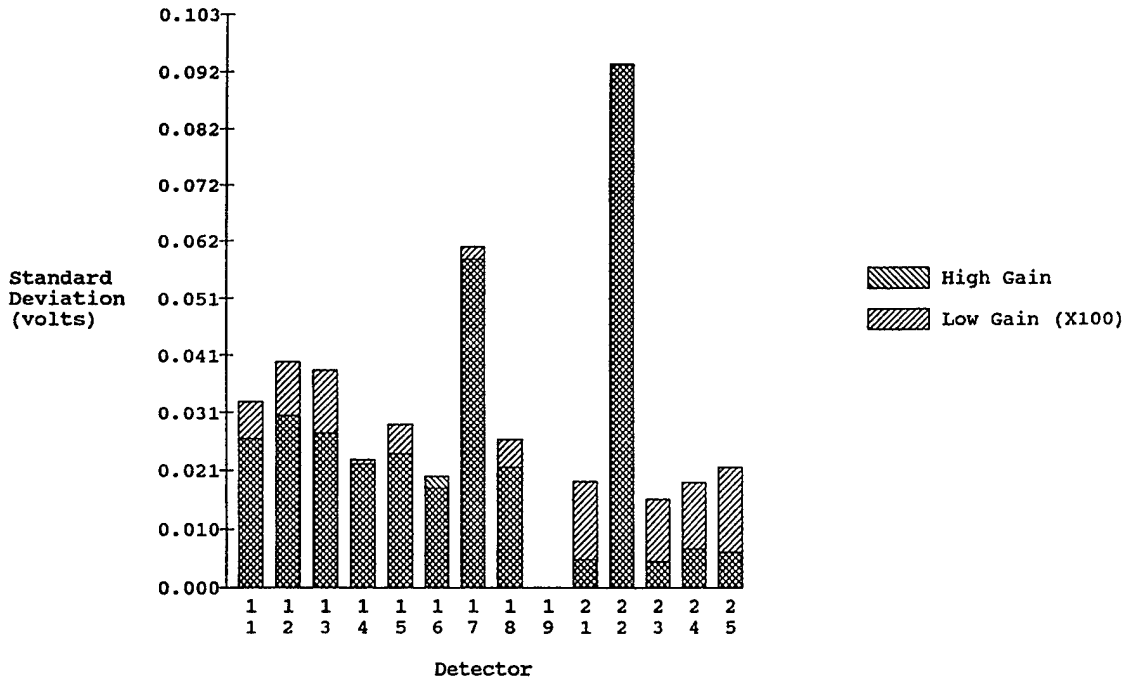
### Chopper On

Figure 51. RMS noise history for radiometer detector 2-3.



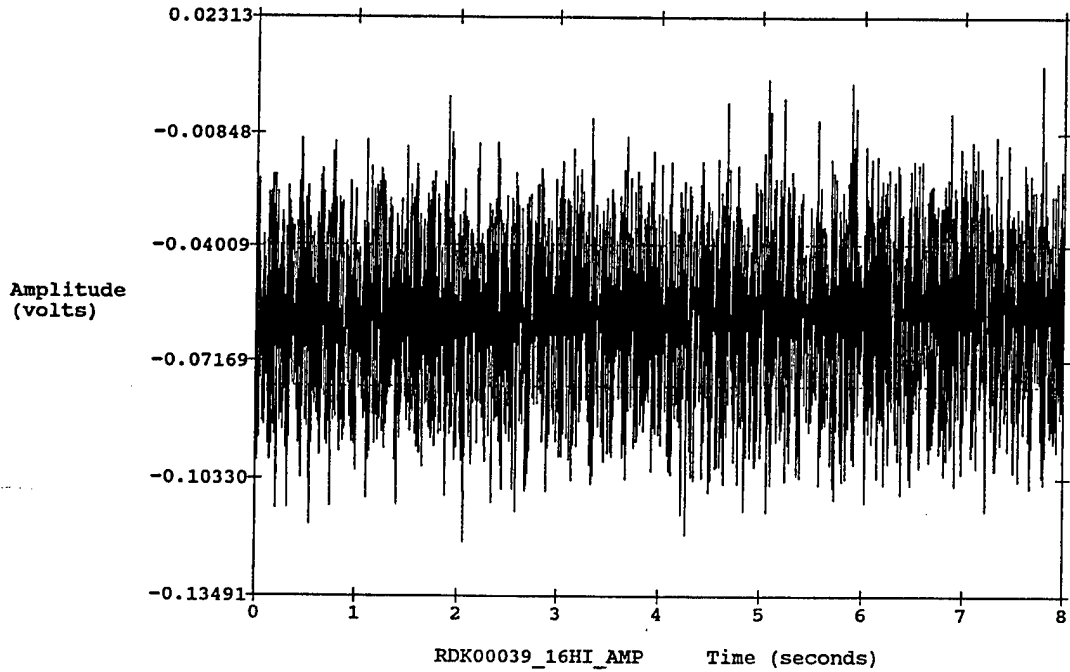
IRIG: 04 10:39:34 Chopper: OFF Filter: 4 Bias Modes/Levels: MMM/HHH  
 Stims 123: NNN SEQ Mode: 0\_ SEQ %compl: 0 FP1 Temp: 10.9 FP2 Temp: 10.5

Figure 52. Mean amplitude for the relative dark voltages for all radiometer detectors.



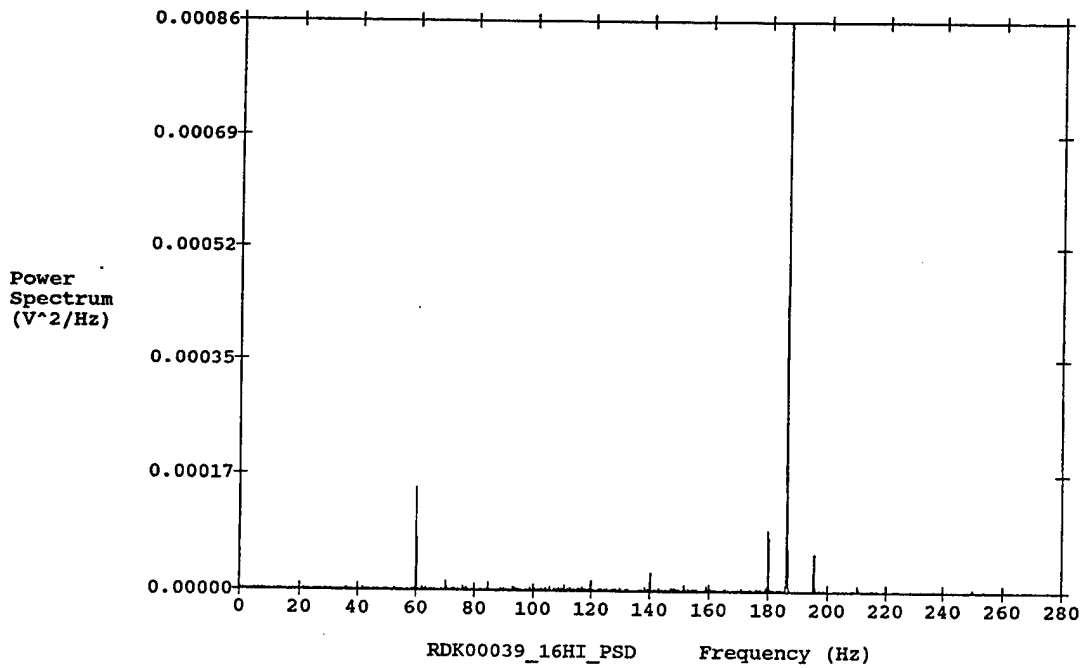
IRIG: 04 10:39:34 Chopper: OFF Filter: 4 Bias Modes/Levels: MMM/HHH  
 Stims 123: NNN SEQ Mode: 0\_ SEQ %compl: 0 FP1 Temp: 10.9 FP2 Temp: 10.5

Figure 53. Standard deviation for the relative dark voltages for all radiometer detectors.



MEAN = -0.058988; STDEV = 0.019501; COUNT = 4400.  
 IRIG: 04 10:39:34 Chopper: OFF Filter: 4 Bias Modes/Levels: MMM/HHH  
 Stims 123: NNN SEQ Mode: 0\_ SEQ %compl: 0 FP1 Temp: 10.9 FP2 Temp: 10.5

Figure 54. Mean amplitude under dark conditions for detector 1-6.



AC RMS Voltages: Time Domain 0.019501 Freq Domain 0.019517  
 IRIG: 04 10:39:34 Chopper: OFF Filter: 4 Bias Modes/Levels: MMM/HHH  
 Stims 123: NNN SEQ Mode: 0\_ SEQ %compl: 0 FP1 Temp: 10.9 FP2 Temp: 10.5

Figure 55. Power spectrum under dark conditions for detector 1-6.

### 3.2.7.2 Dark Offset

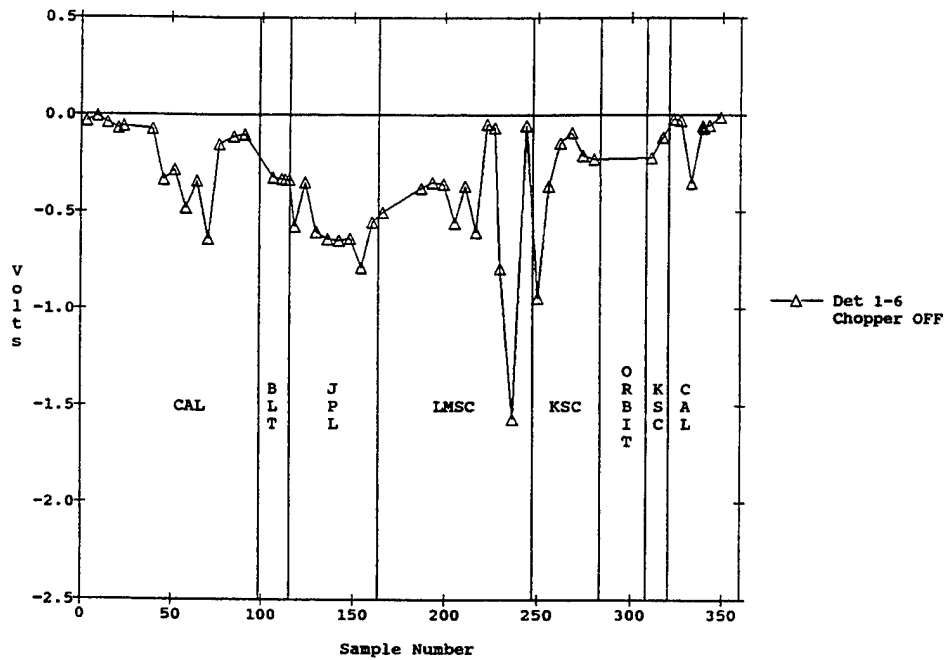
The dark offset of each detector in the CIRRIS 1A radiometer was measured by tracking the dc offset during each dark noise data collection. The data have been logged in a dc offset history which has been kept throughout testing, integration, flight, and calibration of the CIRRIS 1A instrument. Figures 56 and 57 show the offset histories for radiometer detectors 1-6 and 2-3, respectively. Offset histories for all radiometer detectors are in Volume 2. Throughout its operation, the dc drift of the radiometer has remained small enough to not affect the dynamic range of the sensor. These figures shows that the dc offset of the system has remained fairly constant throughout the testing, flight, and calibration.

### 3.2.7.3 Noise versus Flux

The dark noise uncertainty only determines the measurement uncertainty at the bottom of a sensor's dynamic range. At higher flux levels, another noise source, photon noise, must also be considered. The noise versus flux measurement is an indication of the effect of increased radiance on the noise.

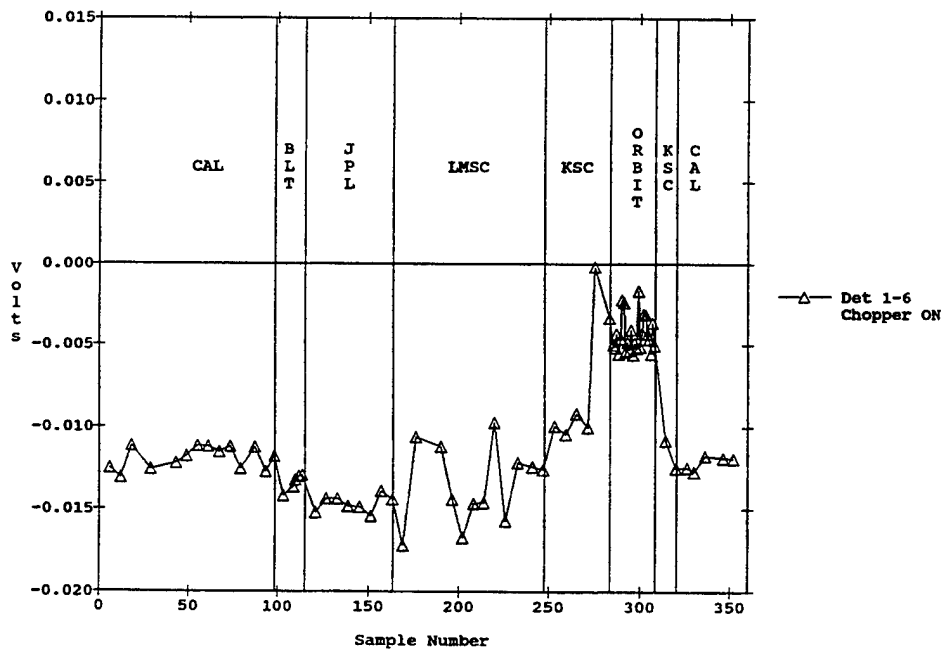
The noise of a measurement is defined as the one sigma standard deviation of the measured detector output voltage of several samples over the full dynamic range of the detector. The noise measurement of the CIRRIS 1A radiometer detectors was obtained using an extended area black-body source. The extended area source was chosen because it is a full field and full aperture illuminating source. The incident radiance is varied by varying the temperature of the source. Because the noise measurement is a photon-noise-limited curve, these data are provided in terms of absolute flux on the detector, and can be adapted to each filter using the spectral response functions developed in Section 3.2.6.

Noise versus flux for the radiometer was calculated using extended area source data taken during Phase 1 of the postflight calibration. To ensure proper characterization of noise versus flux over the instrument's dynamic range, the instrument was exposed to a wide range of radiance values that covered the dynamic range of the instrument. Data were taken over a black-body temperature range of 25 to 300 K. Dark offset measurements were collected at each gain and bias setting observed on flight.



Gain = HI (x100), Bias = HHHH, FW 4, Sept 1988 - Feb 1992.

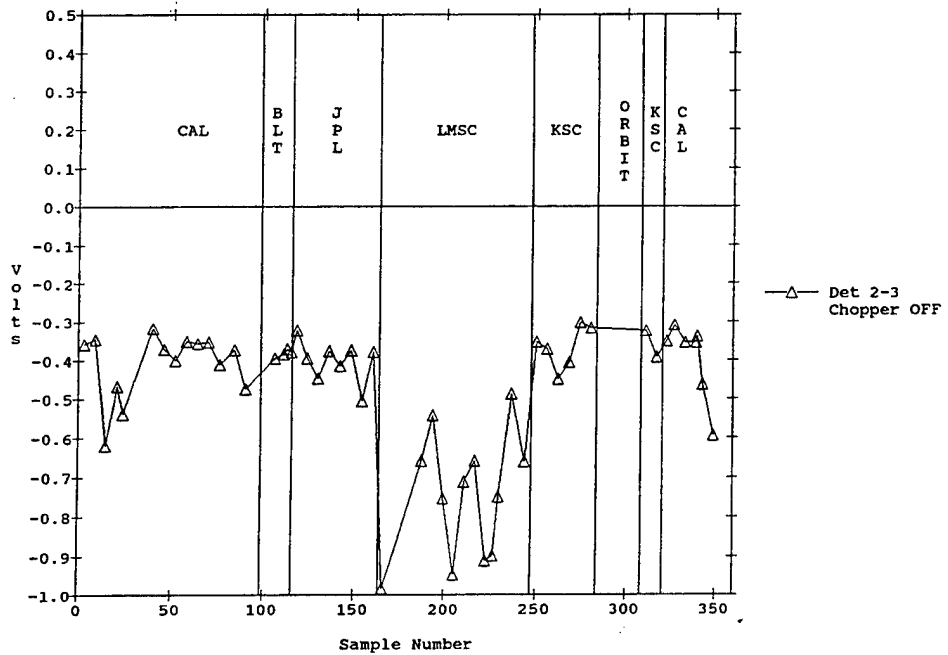
### Chopper Off



Gain = HI (x100), Bias = HHHH, FW 4, Sept 1988 - Feb 1992.

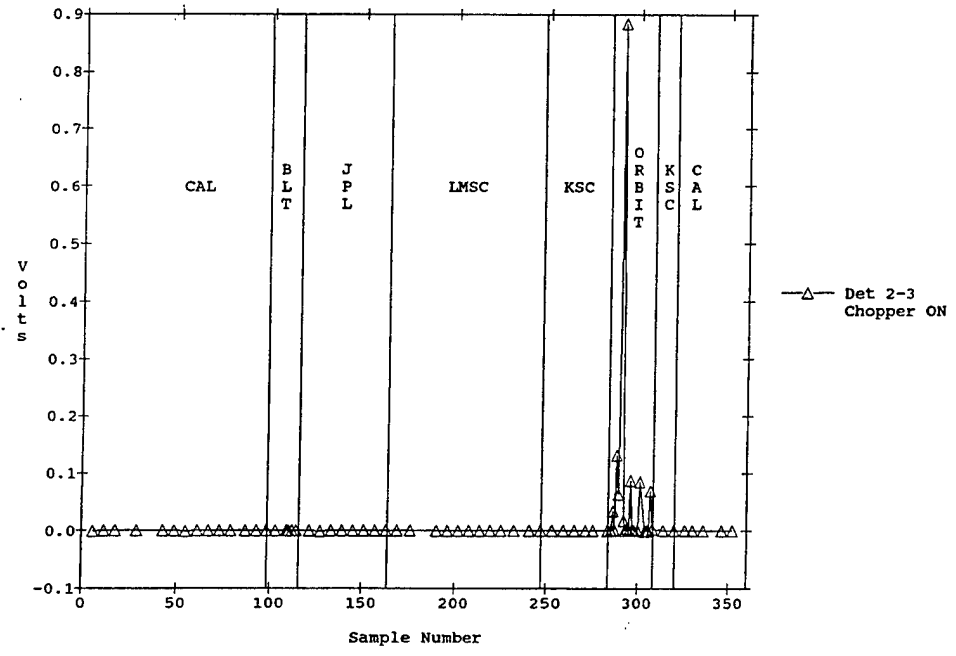
### Chopper On

Figure 56. Offset history for radiometer detector 1-6.



Gain = HI (x100), Bias = HHHH, FW 4, Sept 1988 - Feb 1992.

### Chopper Off



Gain = HI (x100), Bias = HHHH, FW 4, Sept 1988 - Feb 1992.

### Chopper On

Figure 57. Offset history for radiometer detector 2-3.

All of the collected extended area source data were dark offset corrected using the corresponding dark offset measurement. The ac individual range response equations and coefficients were used to linearize the offset corrected detector noise voltages to obtain linearized noise voltages, as shown in the following equation:

$$V_{LIN} = A_0 \times V_M + A_1 \times V_M^2 \quad (17)$$

where

$V_{LIN}$	=	linearized voltage
$A_0, A_1$	=	linearity coefficient
$V_M$	=	measured voltage

The following steps were followed to accomplish the noise voltage linearization:

1. linearize the mean detector voltage
2. linearize the mean voltage plus the standard deviation of that detector voltage
3. subtract the linearized mean voltage from the linearized mean plus standard deviation voltage

This method resulted in a linearized standard deviation voltage or linearized noise voltage. The absolute responsivity coefficients that were derived from this analysis were then multiplied by the detector noise voltages to convert these voltages to flux in units of watts/(cm<sup>2</sup> sr).

The incident in-band flux was calculated by integrating the relative spectral response and Planck's equation over the known bandpass of the filter at the known temperature of the black-body source. The in-band flux is also in units of watts/(cm<sup>2</sup> sr).

Figures 58 and 59 show noise versus flux graphs with filter 0 and all bias and gain combinations for detectors 1-6 and 2-3, respectively. Volume 2 contains the noise versus flux graphs for all filters and all bias and gain combinations for all radiometer detectors.

#### 3.2.7.4 Noise Equivalent Radiance (NER)

Calibration personnel used the noise versus flux graphs to compute the noise equivalent radiance (NER), which is the dark noise divided by the radiance responsivity, for each detector. The NER provides an estimate of the bottom of a detector's dynamic range in absolute terms. Table 10 lists the NERs for all radiometer detectors and all filters. The first number for each filter/detector combination is the average of dark noise measurements made during the calibration period. The second number represents the average of dark noise measurements during flight, and the lowest number is from the noise versus flux data taken with the extended source using eight points on the noise versus flux curves.

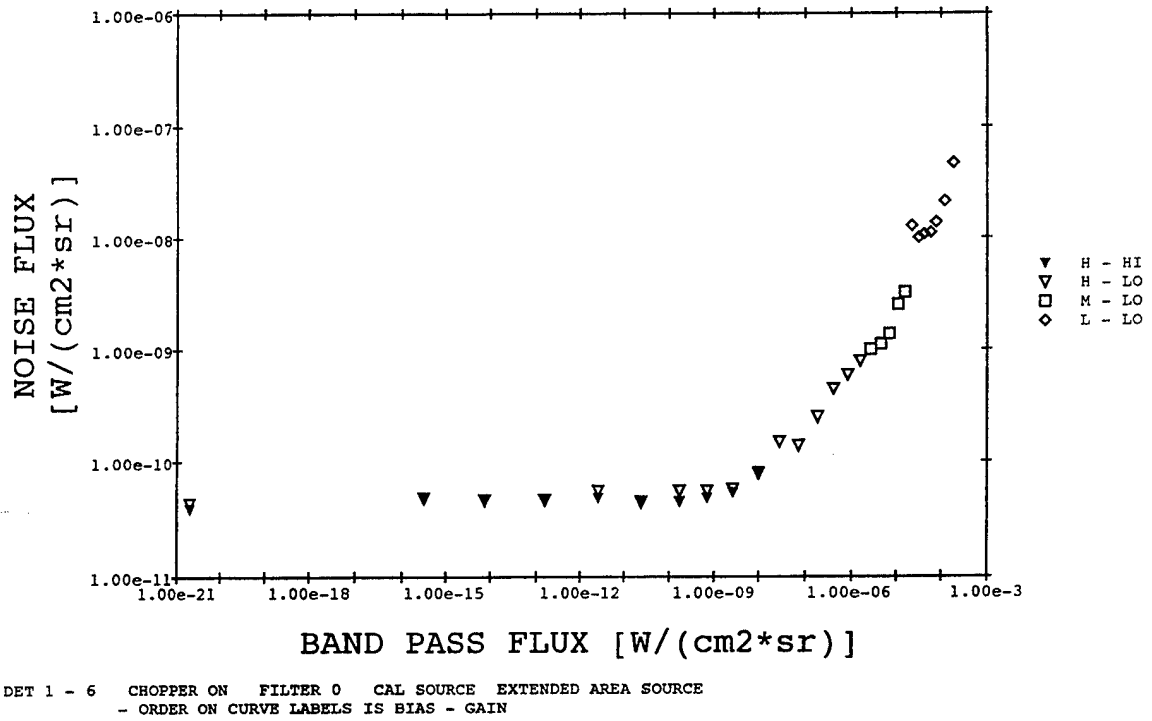


Figure 58. Noise flux versus band pass flux for radiometer detector 1-6, filter 0.

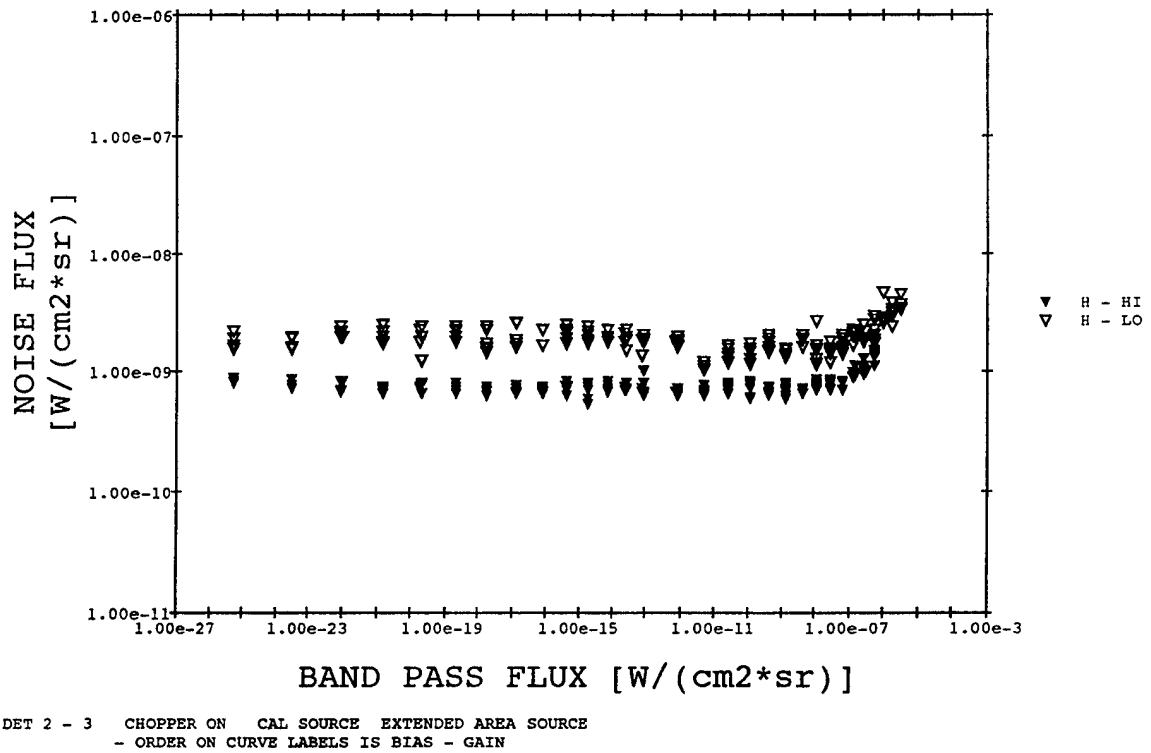


Figure 59. Noise flux versus band pass flux for radiometer detector 2-3.



**Table 10. Radiometer Noise Equivalent Radiances\***

Detector		Filter 0	Filter 1	Filter 2	Filter 3	Filter 5	Filter 6	Filter 7
1-1	Calib	2.1E-10	1.5E-09	7.3E-10	5.3E-10	2.7E-10	1.5E-10	2.7E-10
	Flight	2.0E-10	1.4E-09	6.7E-10	4.9E-10	2.5E-10	1.4E-10	2.5E-10
	Orig	1.3E-10	1.0E-09	3.8E-10	3.4E-10	2.2E-10	1.0E-10	2.0E-10
1-2	Calib	1.7E-10	1.1E-09	4.9E-10	3.7E-10	2.0E-10	1.2E-10	1.9E-10
	Flight	2.0E-10	1.3E-09	5.7E-10	4.3E-10	2.3E-10	1.3E-10	2.3E-10
	Orig	1.1E-10	7.6E-10	2.9E-10	2.2E-10	1.5E-10	7.4E-11	1.7E-10
1-3	Calib	2.7E-10	2.1E-09	9.7E-10	6.9E-10	3.4E-10	1.7E-10	3.4E-10
	Flight	2.8E-10	2.2E-09	1.0E-09	7.2E-10	3.6E-10	1.8E-10	3.6E-10
	Orig	1.5E-10	1.5E-09	5.1E-10	4.7E-10	2.5E-10	1.0E-10	2.8E-10
1-4	Calib	1.0E-10	7.1E-10	3.4E-10	2.4E-10	1.3E-10	8.4E-11	1.2E-10
	Flight	8.0E-11	5.5E-10	2.6E-10	1.9E-10	1.0E-10	6.5E-11	9.4E-11
	Orig	5.5E-11	4.9E-10	1.8E-10	1.6E-10	9.0E-11	5.1E-11	8.0E-11
1-5	Calib	2.6E-10	2.1E-09	9.2E-10	6.2E-10	3.2E-10	1.8E-10	3.2E-10
	Flight	2.3E-10	1.8E-09	7.9E-10	5.4E-10	2.8E-10	1.6E-10	2.8E-10
	Orig	1.5E-10	1.4E-09	5.1E-10	3.9E-10	2.2E-10	1.1E-10	2.2E-10
1-6	Calib	7.8E-11	6.0E-10	2.7E-10	1.9E-10	9.9E-11	5.1E-11	9.7E-11
	Flight	7.2E-11	5.5E-10	2.5E-10	1.7E-10	9.1E-11	4.7E-11	8.9E-11
	Orig	4.4E-11	4.6E-10	1.8E-10	1.3E-10	7.9E-11	3.1E-11	9.2E-11
1-7	Calib	9.4E-09	7.9E-08	3.7E-08	2.5E-08	1.2E-08	6.5E-09	1.3E-08
	Flight	8.7E-09	7.3E-08	3.4E-08	2.3E-08	1.1E-08	6.0E-09	1.2E-08
	Orig	5.5E-09	5.5E-08	2.1E-08	1.9E-08	8.4E-09	4.3E-09	1.0E-08
1-8	Calib	9.3E-10	6.4E-09	3.1E-09	2.2E-09	1.2E-09	5.6E-10	1.1E-09
	Flight	8.7E-10	6.0E-09	2.9E-09	2.0E-09	1.1E-09	5.6E-10	1.1E-09
	Orig	5.1E-10	4.5E-09	1.8E-09	1.4E-09	8.8E-10	4.4E-10	8.6E-10
		Fixed Filter						
2-1	Calib	9.8E-10						
	Flight	1.5E-09						
	Orig	5.1E-10						
2-2	Calib	1.9E-08						
	Flight	1.5E-08						
	Orig	1.1E-08						
2-3	Calib	1.1E-09						
	Flight	2.0E-09						
	Orig	7.2E-10						
2-4	Calib	1.2E-08						
	Flight	1.3E-08						
	Orig	6.1E-09						
2-5	Calib	7.4E-09						
	Flight	9.3E-09						
	Orig	3.3E-09						

\* NER values in units  $W\ cm^{-2}\ sr^{-1}$

### 3.2.7.5 Radiometer Precision

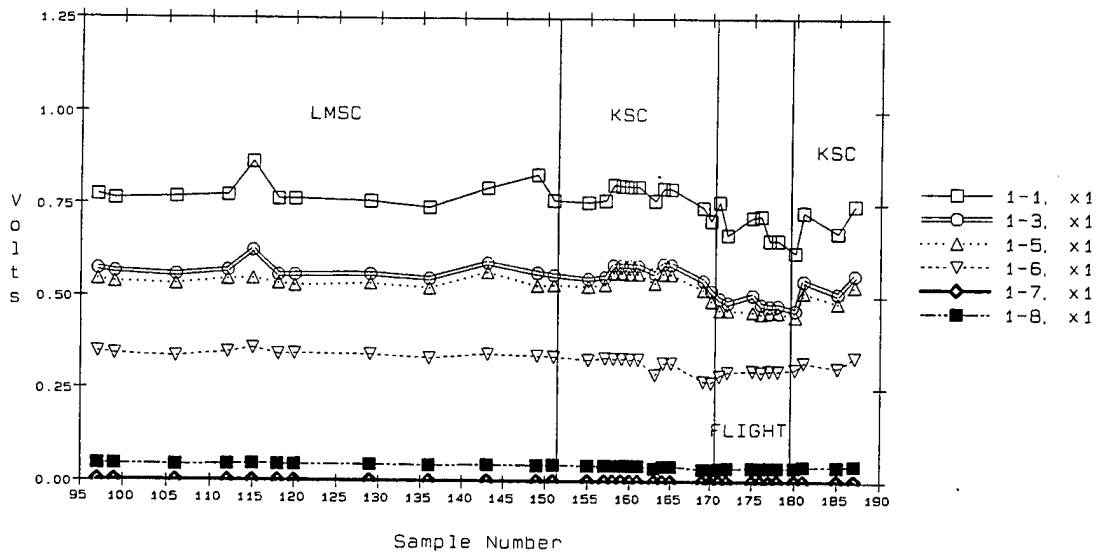
The radiometer long-term repeatability or precision was calculated from the internal stimulator tracking history. Figures 60 and 61 show the stim tracking histories of focal planes 1 and 2, respectively. The stims include both wideband 1 (WB1) and radiometer stim 3 (stim3). The precision of each detector is calculated as the standard deviation percentage of the mean. The results of this calculation are given in Table 11 for the two focal planes.

Detectors 1-2 and 1-4 were saturated for the stim tracking history. Because they are similar in size to detectors 1-1, 1-3, 1-5, and 1-6, their response could be considered to be the average of the other detectors. The low response of 1-7 and 1-8 may make the precision calculation somewhat larger.

The precision of detector 2-2 low is shown in Figure 61 and Table 11. Its precision is affected by the higher electronic gain.

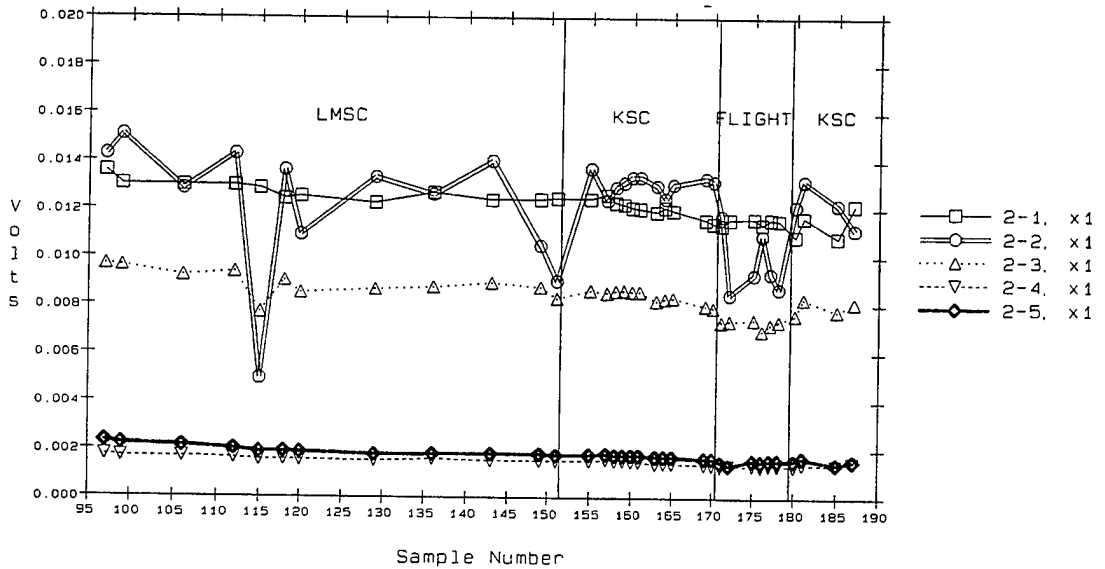
**Table 11. CIRRI 1A Radiometer Precision**

Detector	Mean	Standard Deviation	Standard Deviation % of Mean
1-1	0.751885	0.052962	7.043946
1-2	Saturated	Saturated	Saturated
1-3	0.547107	0.040595	7.420010
1-4	Saturated	Saturated	Saturated
1-5	0.520154	0.038166	7.337453
1-6	0.320909	0.023152	7.214525
1-7	0.003103	0.000403	12.974083
1-8	0.043334	0.003504	8.086497
2-1	0.012104	0.000612	5.057708
2-2	0.012001	0.002083	17.357366
2-3	0.008278	0.000675	8.159182
2-4	0.001487	0.000117	7.873210
2-5	0.001740	0.000219	12.612926



Ground & despiked flight data. Chopper ON. FW 0. RAD Stim 3 & IFR WB 1 ON. Bias = HMHH. 1-2 & 1-4 SATURATED at x1 & x100. Data for Sample Numbers 173, 174 & 179 w/ warm/hot cover.

**Figure 60. CIRRIS 1A radiometer focal plane 1 internal source tracking.**



Ground & despiked flight data. Chopper ON. 2.9 um fixed filter. RAD Stim 3 & IFR WB 1 ON. Bias = HMHH.

**Figure 61. CIRRIS 1A radiometer focal plane 2 internal source tracking.**

## 4. INTERFEROMETER CALIBRATION RESULTS

### 4.1 INTRODUCTION

#### 4.1.1 Interferometer Description

The CIRRIS 1A interferometer is a high resolution Michelson design that provides infrared spectra of auroral, airglow, and other targets. It features a flex-pivot mirror translation system and a 5-element focal plane which is located behind an 8-position filter wheel. The design of the SPIRIT II and SPIRIT III interferometers is similar to the CIRRIS interferometer except that the SPIRIT II and SPIRIT III filters are attached to the detectors and therefore do not have filter wheels. This design provides simultaneous data for all wavelength bands at the expense of dynamic range.

The CIRRIS interferometer focal plane detectors respond to infrared energy in the spectral range of 2.5  $\mu\text{m}$  to 25  $\mu\text{m}$ . The spectral range is achieved using a potassium bromide beamsplitter. Three moving mirror scan modes provide unapodized spectral resolution ranging between 1 and 8  $\text{cm}^{-1}$  (full width first zero) over an 8-order dynamic range. When launched in 1991, the CIRRIS interferometer was the most sensitive, highest resolution interferometer ever flown to collect atmospheric emission data.

Major interferometer elements include the optical filter wheel, the optical modulator or interferometer proper, the interferometer control electronics (ICE), and the interferometer signal conditioning electronics (ISCE). Collimated energy enters from the telescope, passes through the 8-position filter wheel and impinges on the beamsplitter. The beamsplitter divides the energy, sending part to a stationary mirror and part to a translating (moving) mirror. The energy returning from these mirrors recombines on the beamsplitter and passes through the aspheric Ritchey-Chretien focal plane optics to the detectors. The resultant electrical signal passes through the (ISCE) signal conditioning process of gain ranging and analog-to-digital conversion and is formatted and recorded by the data formatting and recording (DFR) system. The average dc level of the signal measured during the retrace is subtracted off and reported separately. The remaining signal is ac coupled. A redundant position reference laser system spatially controls the rate of sampling. An auto-alignment system using geared stepper motors provides the capability of realignment in space, and internal sources are available for alignment and calibration verification during flight.

The output of a Michelson interferometer, a spatially sampled interferogram, must be Fourier transformed to provide a spectral domain output. A Fourier transform requires data that are sampled at evenly spaced intervals. The CIRRIS interferogram's reference laser, a 632.99 nm helium-neon (HeNe) laser, commands the analog-to-digital converters to sample data from the main channels. Each interferometer detector is sampled twice during every laser wavelength. The CIRRIS interferometer has two identical HeNe lasers for redundancy. During most of the ground calibration, laser 1 was selected.

The interferometer focal plane array (FPA), designed and fabricated by Santa Barbara Research Center (SBRC), has five impurity band conduction (IBC) detectors. CIRRIS provided the first

actual satellite sensor application of the IBC technology. Prototype focal planes manufactured from the IBC material were flown on the Kuiper Airborne Observatory in 1985 to test their ability to withstand operational environments (Russell et. al., 1987).

The interferometer FPA is referred to as FPA 3. Individual detectors are referred to as Detector X-N, where X refers to the FPA and N designates the individual detector on that array. For example, detector 3-2 refers to detector 2 on FPA 3. Figure 62 shows the configuration of the CIRRIS interferometer focal plane, identifying detector number, footprint (km), and field-of-view (mr) data for the individual detectors. The focal planes are shown in object space (as if looking out of the aperture).

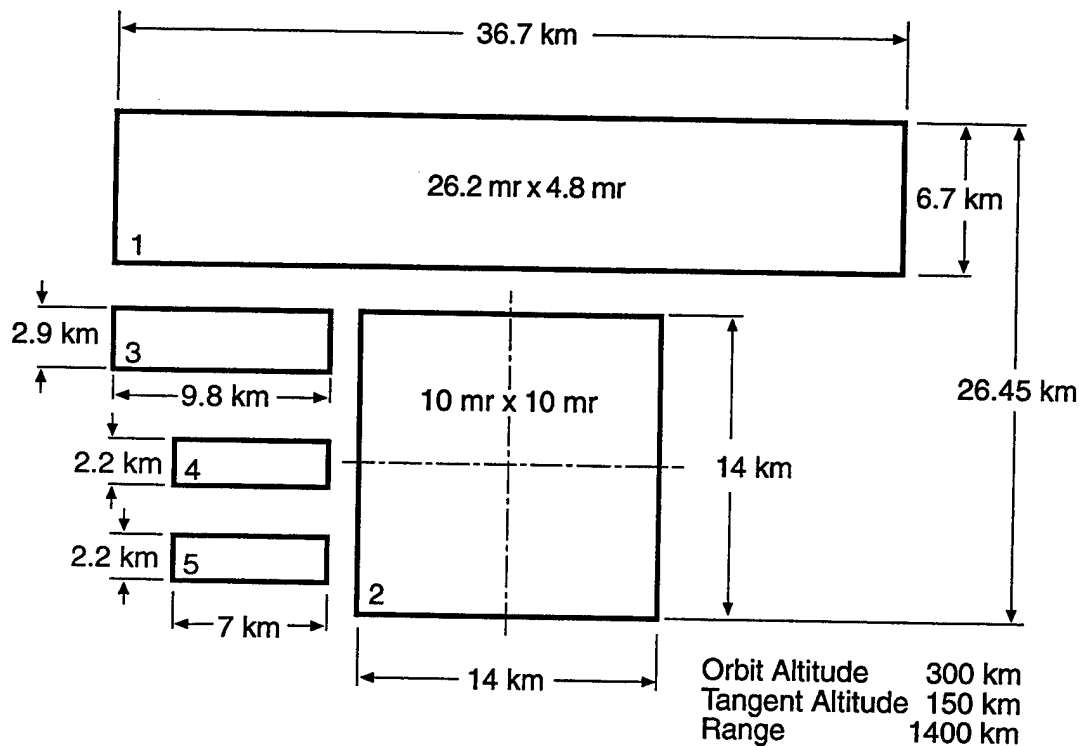


**Figure 62. CIRRIS 1A interferometer focal plane array configuration.**

The interferometer focal plane functions behind a filter wheel that contains a precision set of optical filters. Table 12 lists the characteristics of the CIRRIS interferometer filter.

**Table 12. CIRRIS 1A Interferometer Filter Wheel Characteristics**

Position Number	Description	Bandpass <sup>a</sup> μm
0	Open	
1	Low pass	< 4.9
2	Low pass	< 3.7
3	Wide bandpass	4.7 - 13.0
4	Narrow bandpass - spatial pinholes	2.6 - 4.05
5	Narrow bandpass	11.0 - 13.0
6	High pass	> 17.0
7	Wide bandpass	8.0 - 13.0

a. The actual relative spectral response for each filter is given in Section 4.2.2.1.

#### 4.1.2 Interferometer Calibration Equation

To determine atmospheric gas concentrations and molecular emission mechanics from the flight spectral measurements, the interferometer calibration includes both spectral and radiometric parameters. The CIRRIS interferometer calibration equation, Equation (18), correlates the interferometer's response with incident spectral radiance.

$$\Phi_{m_{d,f,b}}(n) = \frac{1}{\mathcal{R}a_{d,f,b}} \left[ \frac{1}{\mathcal{R}r_{d,f,b}(n)} \mathfrak{F} [L_{d,b}(\text{Resp}_{d,f,b}(p))] \right] \pm \sigma_{d,f,b}(n) \quad (18)$$

where

- b = detector bias voltage
- d = interferometer detector number
- f = interferometer filter position
- $\Phi_{m_{d,f,b}}(n)$  = measure flux in  $W \text{ cm}^{-2} \text{ sr}^{-1} \text{ cm}$  as a function of wavenumber
- $\mathcal{R}a_{d,f,b}$  = absolute responsivity in volts  $\text{cm}/W \text{ cm}^{-2} \text{ sr}^{-1} \text{ cm}$
- $\mathcal{R}r_{d,f,b}(n)$  = relative responsivity (unitless) as a function of wavenumber (relative spectral response, RSR)
- $\mathfrak{F} [ ]$  = Fourier transform operation results in volts  $\text{cm}$  as a function of wavenumber
- $L_{d,b} [ ]$  = linearity correction function (unitless)
- $\text{Resp}_{d,f,b}(p)$  = interferometer response in volts as a function of interferometer slide position
- $\sigma_{d,f,b}(n)$  = measurement uncertainty

Unlike the bulk silicon detectors used in the radiometer, the CIRRIS interferometer used state-of-the-art impurity band conductor (IBC) detectors. The primary reason for developing these detectors was to eliminate dielectric relaxation effects (DRE). Eliminating DRE should allow the radiometric response of the CIRRIS interferometer detector to be fit with a single equation. The CIRRIS calibration was designed to provide the coefficients needed for the calibration equation.

#### **4.1.3 Calibration Requirements**

The radiometric model given in Equation (18) relates the interferometer's electrical signal to the true scene spectral radiance presented to the sensor. The radiometric model characterizes the CIRRIS interferometer's spatial and spectral responsivity domains and random uncertainties. This characterization of the nonideal performance of the sensor is necessary to perform measurement uncertainty analysis. The Optical Physics User System (OPUS) software, developed by PL/OP, SDL, and Boston College, and coded by Boston College, presently uses individual range response equations to characterize the interferometer's radiometric performance. Using individual equations allowed data analysis and quality control to proceed while the final calibration information was being developed.

Calibration of the spectral domain includes an analysis of the interferometer's spectral resolution, spectral position, and ghost spectra (harmonics) due to nonlinearity, crosstalk, and out-of-band spectral leakage. The spatial domain calibration characterizes the spatial response of the sensor, including the point source response functions (PRFs), detector positions, scatter, and effective field-of-view solid angles. Repeatability analysis includes short term repeatability, long term repeatability, dark noise, and dark offset.

Each term in the calibration equation and each domain in the radiometric model describe a specific radiometric parameter. The goal of calibration is to characterize each parameter independently of the others. Together, these individually characterized radiometric parameters comprise a complete calibration of the CIRRIS interferometer (Wyatt, 1978).

## **4.2 INTERFEROMETER CALIBRATION TESTS AND RESULTS**

Many of the calibration products described in this report were provided to Phillips Laboratory in computer-compatible formats. These products include the data from tables and graphs in this report, and processed, OPUS format data files collected during the ground calibration. These products were included in the OPUS data verification and analysis software package, and were used in the verification of the flight data base.

This section contains the reduced calibration data for the primary interferometer detector, 3-2. Volume 2 of this report contains the reduced data for the remaining interferometer detectors, where applicable.

### **4.2.1 Spatial Response Functions**

The point source response calibration determines the shape of the interferometer spatial response function. This calibration includes the point source response map, effective field-of-

view solid angles, and relative spatial lines of sight for each interferometer detector. It also identifies and measures scatter sources and locates the interferometer field stop.

The interferometer point source response function (PRF) was mapped twice during the post flight calibration. Each map was generated by moving a point source across the focal planes in regular steps to provide an array of response measurements. The output of each detector was recorded for each location determine scattering, crosstalk, and point source response. The specific configuration used to generate each of the four PRF maps is given in Table 13.

**Table 13. Point Source Response Map Configuration**

Map	$\Delta X$ Step Size (mrad)	$\Delta Y$ Step Size (mrad)	Source Diameter ( $\mu$ rad)	Detector	Filter	Filter Passband $\lambda(\mu\text{m})$
E	0.7	0.3	158	All	2	<3.7
F	0.7	0.3	448	3-5	6	>17

The initial point source measurements provided a PRF survey from which preliminary detector locations were determined relative to the calibrator's pointing mirror. In addition, peak detector responses were checked for interferogram saturation. For the PRF survey, data were collected over a large spatial area to determine the focal plane's approximate position. Detailed PRF maps were then collected by manually positioning the collimator pointing mirror at the desired initial locations and then using automated data collection routines to collect 40 minor frames of data at each point over the entire field of view. The scan mirror was stopped and a 5-Hz clock was used to update dc values of the interferometer PRF measurements. Data were processed extracting the dc values as a function of the X,Y position of the collimator.

#### 4.2.1.1 Point Source Response Maps

The spatial response of a detector can be graphically displayed by a contour map. Such maps are useful to subjectively evaluate the spatial response, to reveal vignetting problems, and to locate sources of scatter.

Figure 63 provides a contour point source response map for the interferometer detectors. This map was derived from the offset-corrected and peak-normalized spatial response tables. Each contour represents a response of  $\sqrt{2}$  below the preceding contour. The detector's peak response is a single point and is not shown in the contour maps. The first contour encloses the area whose response is at least  $\sqrt{2}^{-1}$  of the peak response, the second contour encloses the area whose response is at least  $\sqrt{2}^{-2}$  of the peak response, and the  $n^{\text{th}}$  contour encloses an area whose response is at least  $\sqrt{2}^{-n}$  of the peak response. Figure 63 shows the contours of the data for each point minus an offset equal to  $2\sigma$  of the nonresponsive region. The remaining points in the region outside of the active detector area are single points. They are believed to be noise because they did not repeat in the second map, and glint regions should include several points. The map shows all contours above the noise level for each detector.



The contour point source response map shows some vignetting on the side of the focal plane housing detectors 3, 4, and 5. The vignettted performance of the telescope was first identified during the initial engineering evaluation. Because the interferometer is not sensitive enough to measure astronomical point sources, factors correcting for vignetting are not included in OPUS.

Figure 64 shows the three-dimensional plot of the point source response map for the interferometer detectors. This plot provides a detailed visual presentation of the actual variation of the response of each detector's surface to point source stimulation (the CIRRIS blur circle is 0.5 mrad). The smooth response of each detector to the point-to-point variation of each surface shows detector spatial variability to be less than  $0.5\sqrt{2}$  of the detector output, when vignetting is not considered. The significant right side vignetting is evident in the contours of the long interferometer detectors. Due to vignetting, the response of the left side of detector 3-1 is about one-third less than that of the right side.

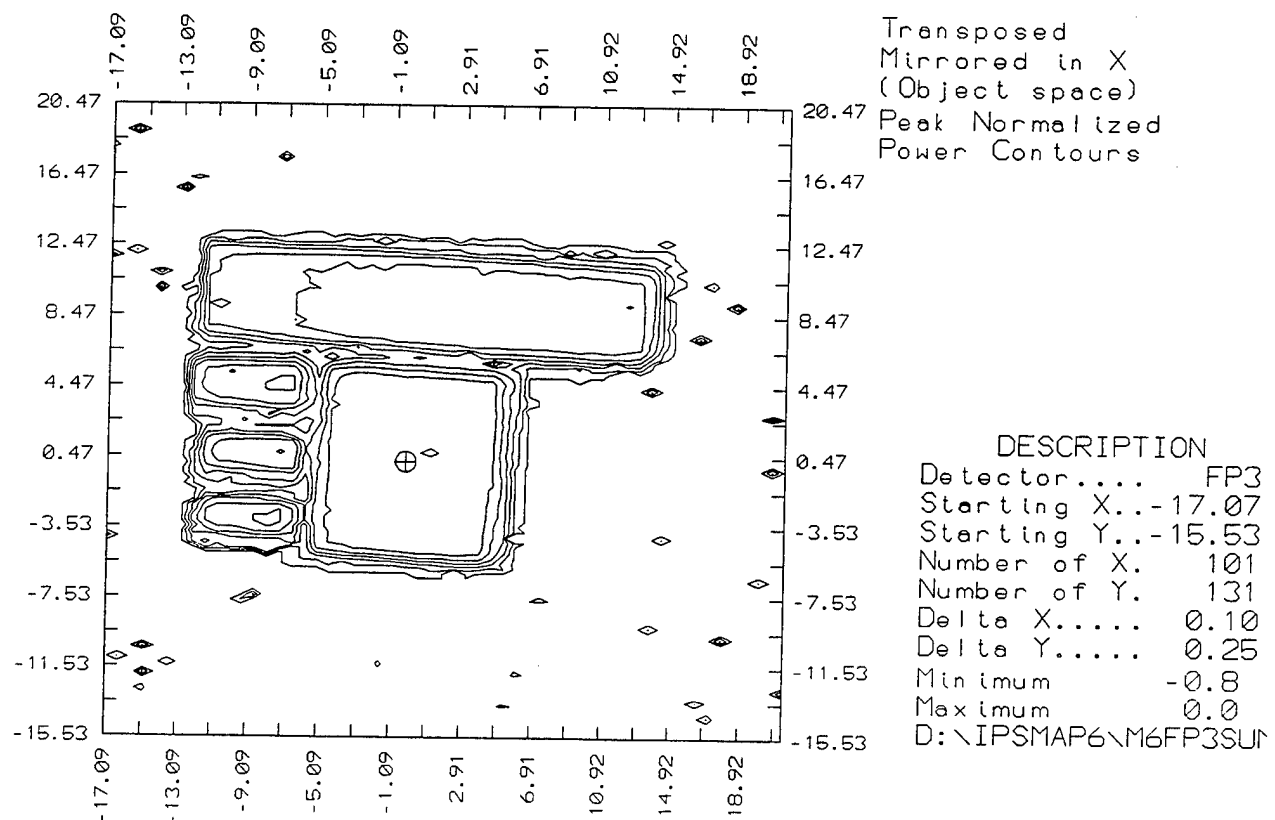
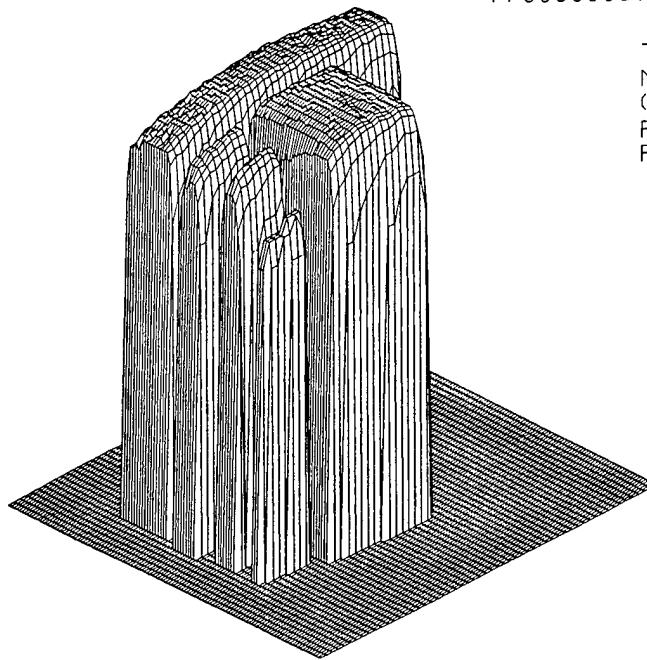


Figure 63. Point source response map for the interferometer detectors.

Recorded : 30-OCT-91 09:40:12  
Processed: 30-OCT-91 15:11:45



Transposed  
Mirrored in X  
(Object space)  
Peak Normalized  
Power Contours

DESCRIPTION  
Detector.... FP3  
Starting X...-17.07  
Starting Y...-15.53  
Number of X. 101  
Number of Y. 131  
Delta X..... 0.10  
Delta Y..... 0.25  
Minimum -0.8  
Maximum 0.0  
D:\IPSMAP6\M6FP3SUR

**Figure 64. Three-dimensional plot of the point source response map for the interferometer detectors.**

#### 4.2.1.2 Effective Field-of-View Solid Angles

The effective field-of-view solid angle of a physical sensor is defined in terms of the field-of-view solid angle of a hypothetical, spatially ideal sensor having the following characteristics:

1. The ideal sensor's response is zero at all spatial positions outside its field of view.
2. The ideal sensor's response to a point source at all spatial positions within its field of view is equal to the actual sensor's peak spatial response.
3. The ideal sensor's response to an extended, spatially uniform source is equal to the actual sensor's response to the same spatially uniform source.

The effective field-of-view solid angle for the actual sensor is the field-of-view solid angle for this hypothetical, spatially ideal sensor and was computed for the interferometer from the point-source data using Equation (19).

$$\Omega_{eff} = \Delta X \Delta Y \left[ \sum_{TotalFP} Resp \right] \quad (19)$$

where

- $\Omega_{eff}$  = effective field-of-view solid angle in steradians
- $\Delta X \Delta Y$  = incremental solid angle for each spatial response data point
- Resp = offset corrected, peak-normalized point source responses

Equation (19) uses summations of the response to avoid exaggeration of low-signal, noisy responses. If only the amplitude of noisy responses is summed, noise is rectified and is incorrectly interpreted as true response. Table 14 lists the interferometer effective field-of-view solid angles. The field of view measured by the PRF is within 15% of the theoretical value of the horizontal.

**Table 14. CIRRIIS 1A Interferometer Field-of-View Solid Angles**

Detector	Effective FOV (sr × 10 <sup>-6</sup> )	Theoretical FOV (sr × 10 <sup>-6</sup> )	% Error
3-1	109.310	125.8	15.09
3-2	85.356	100.0	17.16
3-3	14.565	14.5	-0.45
3-4	10.065	7.9	-21.51
3-5	6.930	7.9	14.00

#### 4.2.1.3 Detector Positions

The center of the position in object space of each detector must be characterized to interpret the interferometer's response to spatially modulated scenes. To generate this map, the point source response tables for each detector were normalized to the detector's peak response. Using this peak-normalized data, a contour was drawn to enclose the area whose response was above 10% of the peak response (0.1). Using responses greater than 10% avoids including scatter response in the centroid summation. Figure 65 shows the contour composite detector response map of the CIRRIIS interferometer and radiometer focal planes. The detectors are mapped in object space, which is the mirror image of the physical focal plane layout. To convert the raw data to object space, the X and Y axes were exchanged and the X axis was mirrored. Because detector 3-2 is the theoretical center of alignment, all field-of-view data have been normalized to its centroid in object space.

The pointing resolution of the MIC2 collimator is specified at 40 μrad. The source of the 10 - 15% error in the field-of-view measurements can be shown to be a result of the 0.3 and 0.7 mrad step sizes chosen for the point source maps. Because the measured angles fall within the map error, the actual field of view is assumed to be the theoretical value.

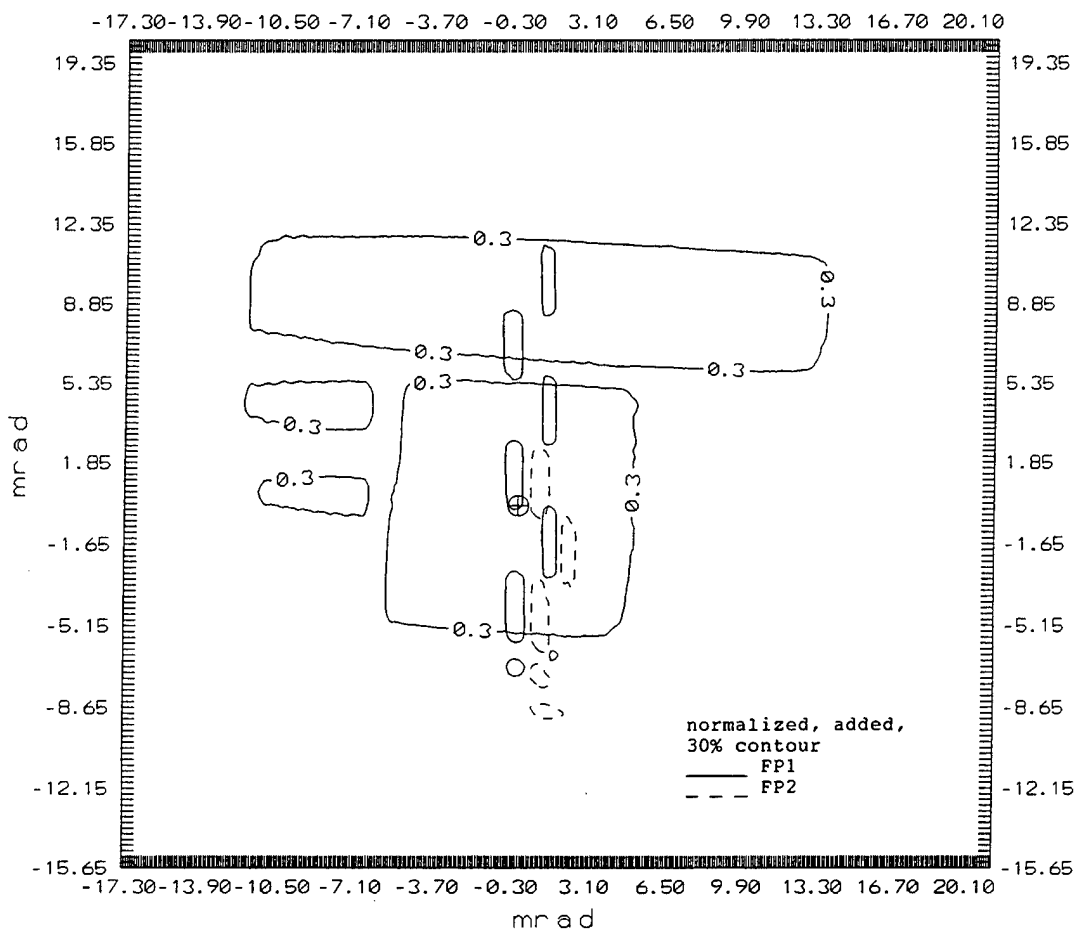


**Figure 65. Composite detector response contour map of the CIRRIS 1A interferometer and radiometer focal planes.**

The contour line-of-sight data cannot be directly used in a computer processing data system. To provide machine usable lines of sight, the same data used to develop the 0.1-response contours were also analyzed to determine the response center of each detector, defined as the X- and Y-centroids of response and given by:

$$Centroid_x = \frac{\sum_{Above\ 0.10} X\ Resp}{\sum_{Above\ 0.10} Resp} \tag{20}$$

$$Centroid_y = \frac{\sum_{Above\ 0.10} Y\ Resp}{\sum_{Above\ 0.10} Resp}$$

where

- Centroid = X or Y response centroid in mrad
- Resp = offset-corrected, peak-normalized response amplitudes
- X = X response coordinate in mrad
- Y = Y response coordinate in mrad

Table 15 lists the object-space position coordinates for the interferometer detectors.

**Table 15. Interferometer Detectors' Object-Space Position Coordinates**

Detector	Centroid	
	X (mrad)	Y (mrad)
3-1	2.198	9.057
3-2	0.000	0.000
3-3	-9.032	4.541
3-4	-8.811	0.643
3-5	-8.964	-2.996

#### 4.2.1.4 Interferometer and Radiometer Detector Coalignment

Two design goals of CIRRS were to locate detector 3-2 on the optical axis of the telescope, and to overlay radiometer detectors 1-6 and 2-3 with the centroid of interferometer detector 3-2. The point source response data presented in Figure 63 show that the response of detector 3-2 is flat and uniform, indicating that the design goal of locating that detector on the telescope field-of-view centerline was met. The goal of coaligning the other focal planes was not met, however. Figure 65 shows that the centerline of the telescope is at the base of detector 1-4, and at the base and to the right of detector 2-1. The vertical axis centerpoint between the two focal planes is separated by 2.3 mrad. The radiometer focal planes are slightly angled with respect to the vertical axis of the interferometer focal plane. The measured angle between the two focal planes is 1.9 degrees. However, because the focal planes were pinned and could not be adjusted without warming and completely disassembling the instrument, the measured level of coalignment was determined to be acceptable.

#### 4.2.1.5 Scatter

The scatter coefficient describes a detector's response to light that originated outside of the field of view of the detector. The coefficient is the fraction of a detector's response that is due to scatter when exposed to a spatially uniform scene. Scatter coefficients are used to interpret data from spatially modulated scenes, and is determined from the point source response data using Equation (21):

$$Scatter = \left[ \frac{\sum_{scat} Resp}{\sum_{det} Resp + \sum_{scat} Resp} \right] 100 \quad (21)$$

where

- Scatter = scatter coefficient
- Resp = offset corrected, peak-normalized point source responses

The scatter calibration attempted to locate scatter sources around and between the detectors. Calibration personnel recorded the interferometer response to a 1.3 by 1.3 mrad collimated source positioned in a raster scan over the entire interferometer focal plane. The map extent was approximately 25 mrad in both the X (cross-scan) and Y (with-scan) dimensions and was centered over the interferometer field stop. Apparent scatter source locations measured over this map are shown in Figure 63. Each of the scatter responses occur at a single measurement point in the grid. The response did not repeat at any of the six surrounding points. Because scatter sources usually occur over larger areas, it is assumed these responses are noise in the map and that no significant scatter sources exist in the interferometer.

Scatter was calculated by assuming that response below an amplitude threshold level is due to scatter. This assumption falsely includes the portion of the in-field-of-view response below the threshold as scatter. However, its affects are relatively small if scatter is significant. Equation (21) numerically represents the signed summation of the detector response below the scatter threshold divided by the total detector response. If only the amplitude of noisy responses is summed, noise is rectified and is incorrectly interpreted as scatter. Scatter was calculated for two thresholds, 0.1% and 0.5%, of the peak response.

The scatter coefficients for each CIRRIIS interferometer detector are given in Table 16 at both the 0.1% and 0.5% levels. As these coefficients show, the CIRRIIS interferometer detectors had no significant scatter sources.

**Table 16. Summary of Interferometer Scatter Data**

Detector	Scatter <0.1 of peak (%)	Scatter <0.5 of peak (%)
3-1	1.5	13.3
3-2	3.7	12.9
3-3	0.5	21.1
3-4	3.4	21.9
3-5		

#### 4.2.1.6 Crosstalk

Point source response maps (Figure 63) showed no significant crosstalk between the detectors at the 0.01% level.

#### 4.2.1.7 Field Stop Location

Ancillary sensor alignment was referenced to a small boresight mirror located behind a window near the CIRRIIS front aperture. The position and angle of the boresight mirror was referenced to the interferometer field stop by theodolite measurements made at SSG before the telescope was delivered to SDL.

To determine the field of view of the primary sensors with respect to the ancillary sensors, it was necessary to determine the location of the interferometer field stop with respect to the line of sight of detector 3-2. Calibration personnel measured the field stop location during the Phase 1 data collection period by scanning a point source perpendicular to each edge of the field stop at three positions. The edge of the stop was determined by the increased response of detector 3-2 as the beam reflected from the edge of the stop. Figure 66 shows the results of this analysis. This figure shows that the edge of detector 3-1 is slanted slightly with respect to the adjacent stop. During the Phase 2 post flight measurement period, this procedure was repeated several times along the edge of the stop adjacent to detector 3-1 to determine the degree of rotation of the interferometer focal plane. It was concluded that the interferometer focal plane is rotated 27.5 mrad clockwise, and is offset 0.965 below and 1.871 mrad to the left of the center of the field stop. Figure 66 also shows the resultant field stop coordinates along with the geometric center of the field stop. The center of the field stop is shown on the figure by the cross in the middle of detector 3-2. The centroid of the detector is shown on the figure by  $\oplus$ .

Table 17 lists the field stop locations obtained from the data. The values in Table 17 have been offset corrected using the calibrator scale to reference them to the centroid of detector 3-2. The field stop width and height are shown with the corresponding preflight measurements reported by System Sensor Group (SSG) without the focal planes installed.

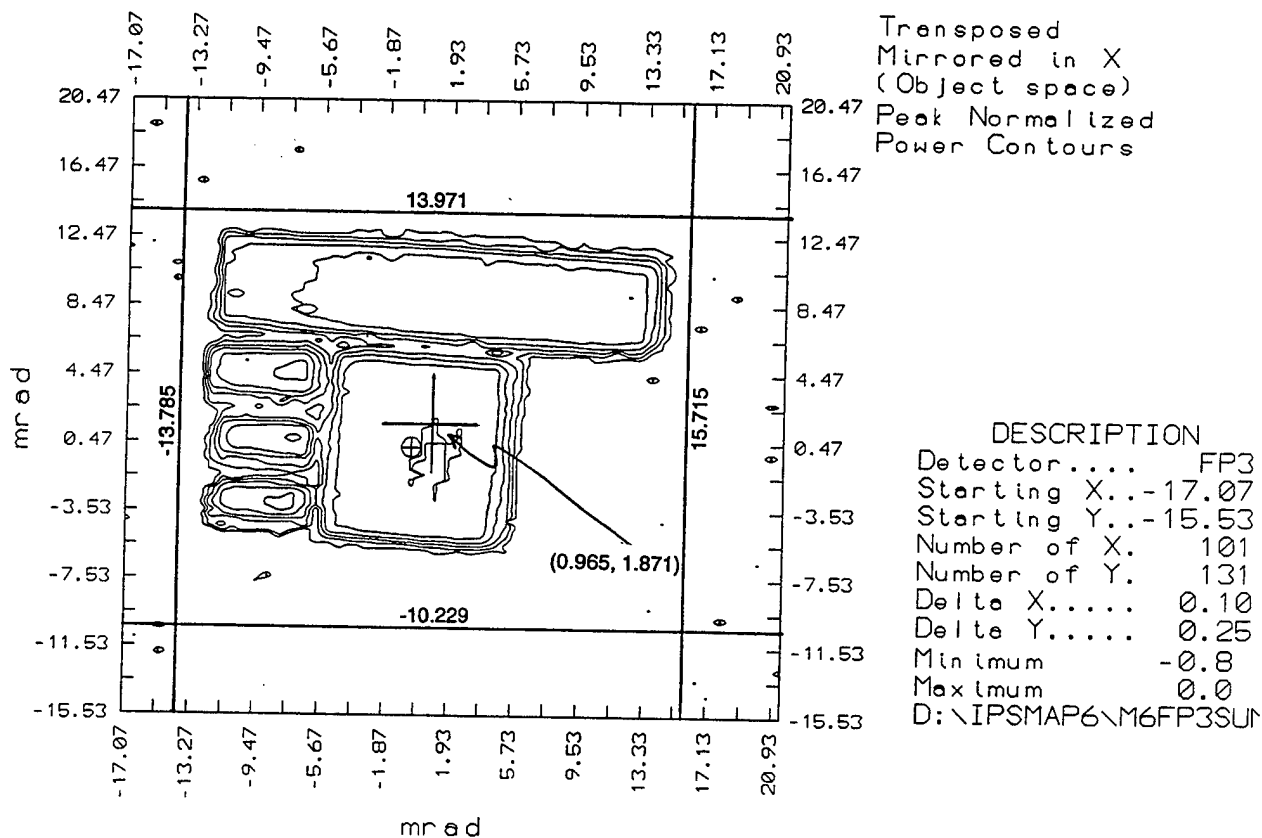


Figure 66. Interferometer field stop coordinates (indicating geometric center of the field stop and centroid of the detector).

**Table 17. CIRRIS 1A Field Stop Location**

Location	Post Flight Calibration Field Stop Locations (mrad)	SSG-Predicted Locations (mrad)
-X	-13.785	
+X	15.715	
-Y	-10.229	
+Y	13.971	
X Center	0.965	
Y Center	1.871	
X Width	29.5	29.55
Y Height	24.2	24.35

#### **4.2.2 Interferometer Radiometric Response**

The radiometric calibration of the interferometer evaluates the absolute emission level of a given measurement. The calibration consists of two measurements, relative spectral response and absolute response, which are used together to establish the absolute calibration of the flight data instrument response shape. The relative spectral response measurement quantifies the spectral response across the full spectral range of the system with respect to that of a known source. The absolute response measurement allows a small section of raw volt  $\text{cm}^{-2}$  transform to be correlated to the emission of a known source. A nonlinearity correction is then developed to remove harmonic distortion from the spectral output. This section provides details of each measurement.

##### **4.2.2.1 Relative Spectral Responsivity**

An interferometer's relative spectral response (RSR) function quantifies its output to radiation at different wavelengths both within and outside its spectral passband. It is determined using a high temperature source that provides spectrally uniform radiation across the entire range. The RSR provides an indication of the interferometer's relative sensitivity to different wavelengths within each filter's passband. It also provides an indication of the out-of-band blocking of the filters.

For the CIRRIS interferometer, 600 K and 1200 K sources were used to provide radiation at a high signal-to-noise ratio at the short wavelengths of the filter bandpass region. Because the total emission from even a small source at these temperatures saturated the CIRRIS detectors, the source emissions were strongly attenuated in a spectrally uniform manner to eliminate saturation. However, this attenuation destroys the absolute traceability of the source, and the absolute responsivity measurement is then used to determine the absolute response of the sensor.



The RSR of the interferometer in any given wavelength region is dominated by the convolution of the detector and filter spectral response curves. Small effects are added by the telescope and beamsplitter. The detector response function, provided by SBRC, is shown in Figure 67.

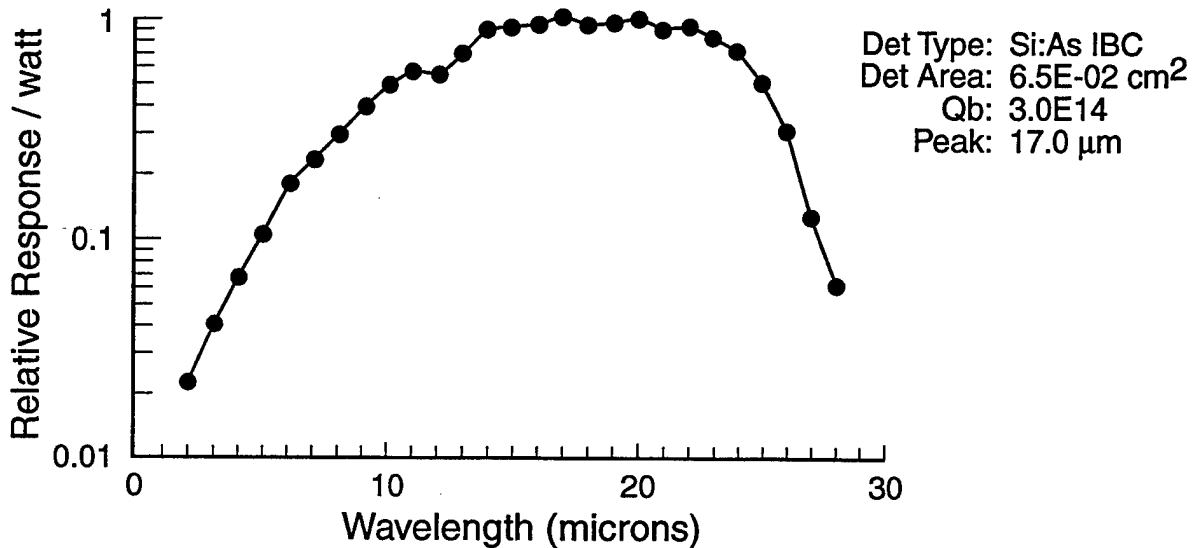


Figure 67. Interferometer focal plane 3 manufacturer's (SBRC) response curve.

The calibration RSR data are used in the OPUS software to normalize the spectral response of the flight data. The signal-to-noise ratio of the RSR interferograms must be as large as possible to minimize the noise added to the flight data when multiplied by the calibration RSR. To obtain RSR data with the correct detector response and the desired signal-to-noise ratio, several combinations of blackbody temperatures, calibration sources, and data collection techniques were used for the CIRRIS interferometer calibration. The actual RSR function required varies with apodization and the number of points in a flight interferogram. In OPUS, the RSR is stored as a reference interferogram and the flight RSR is calculated for the specific conditions desired. Before processing a flight interferogram, the corresponding reference interferogram is selected based on detector, bias, and gain. The reference interferogram is then truncated to the same length as the flight interferogram and processed with the selected correction options to develop a proper RSR for the flight interferogram. This allows the correct relative spectral responsivity to be calculated for any interferogram length and choice of apodization function (Zachor, 1992).

SDL initially planned to collect RSR data using the calibrator scatter source, coadding 25 long scans of data for each detector, filter, and bias combination at 600 K and 1300 K blackbody source temperatures. Two temperatures were specified to allow an analysis of system response at mid-range and near saturation. The Jones source was to be used at flux values higher than those possible with the scatter plate. However, preliminary tests showed that the scatter source did not scatter enough energy onto the detectors to obtain a good signal-to-noise ratio for most of the de-

tectors and bias-gain ranges. In addition, data obtained with the Jones source indicated that extra channel spectra were being introduced into some of the data. Therefore, a test was performed with each calibrator source to determine the optimum source with which to collect RSR calibration data.

Figure 68 shows the relative spectral response curves obtained with each of the four sources for detector 3-3, filter 6. This figure shows that each type of source resulted in a slightly different spectral response. These data were compared with the RSR observed during flight, and it was concluded on the basis of theory and observation that over a small passband, the extended source RSR most closely represented that observed during flight. Therefore, each of the calibrator sources were compared to the extended source RSR, and a close correlation was found between the spectral response of the extended area source and the collimator, or point source.

As a result of this study, SDL and PL personnel agreed to use the point source response to calculate the RSR for most detector/filter combinations. However, the scatter source was used for detectors 3-1 and 3-2 with filters 0 and 3 because the point source saturated these detectors at the required blackbody temperatures.

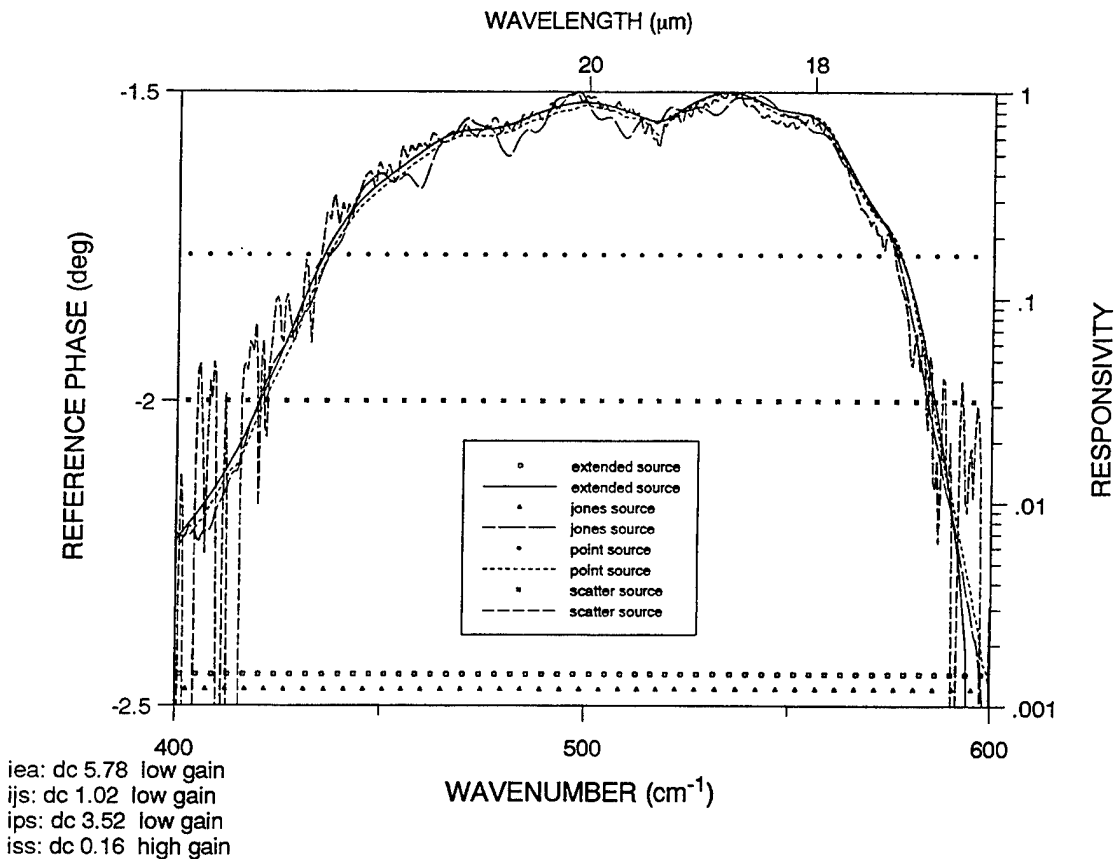


**Figure 68. Relative spectral response curves obtained with each of the four sources for detector 3-3, filter 6.**

In an effort to increase the signal-to-noise ratio of the reference interferograms, it was determined that coadding sequential scans greatly increased the ratio. Figures 69 and 70 show an example of this method. Figure 69 compares a spectrum based on one scan (a), and the spectrum for the same conditions based on 61 coadded scans (b). The noise level in the coadded spectrum is reduced by an order of magnitude, clearly allowing the second harmonic to be resolved. The standard deviation of the region between the dotted lines was used along with the peak signal value to develop the SNR data shown in Figure 70.

This procedure was then applied to the calibration data to develop data sets for the reference interferograms. To develop data sets for the reference interferograms, two files, each containing an interferogram developed from coadding 25 to 30 scans, were developed at each setting. The coadded interferograms from both files were again coadded to provide a reference interferogram developed from a total of between 50 to 60 scans for each condition. Each interferometer scan was inspected for spikes or other abnormalities before it was coadded with the rest of the scans. This method increased the signal-to-noise ratio of the reference interferogram by about an order of magnitude, as shown in Figure 70. The benefit of coadding to increase the signal-to-noise ratio is demonstrated in Figure 69.

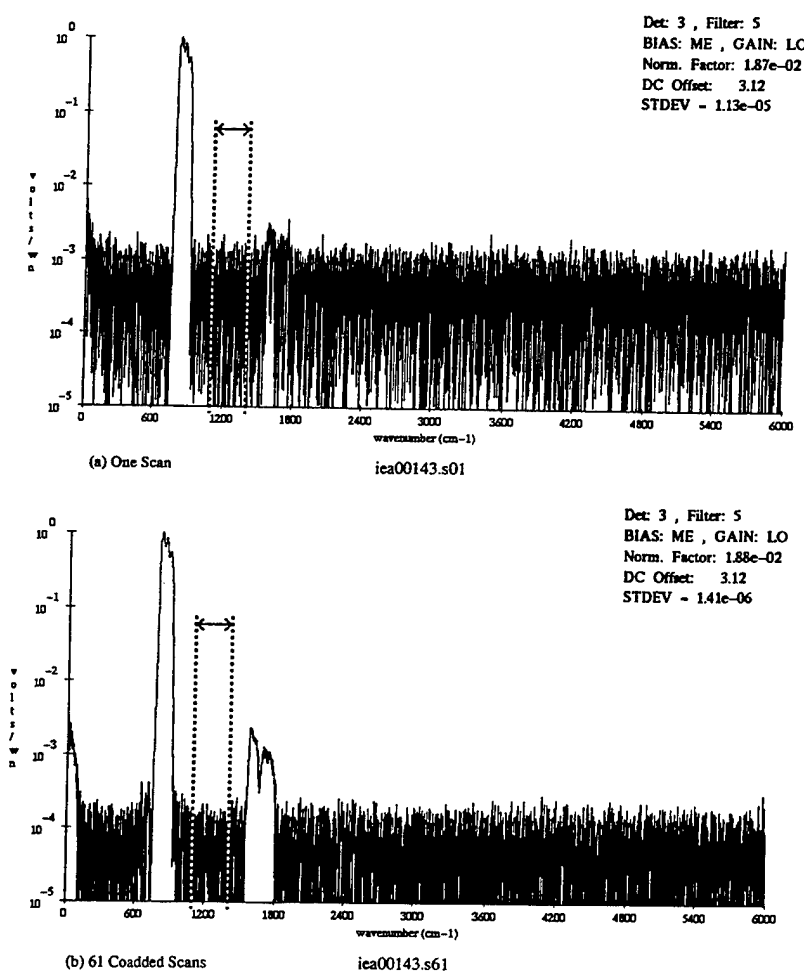
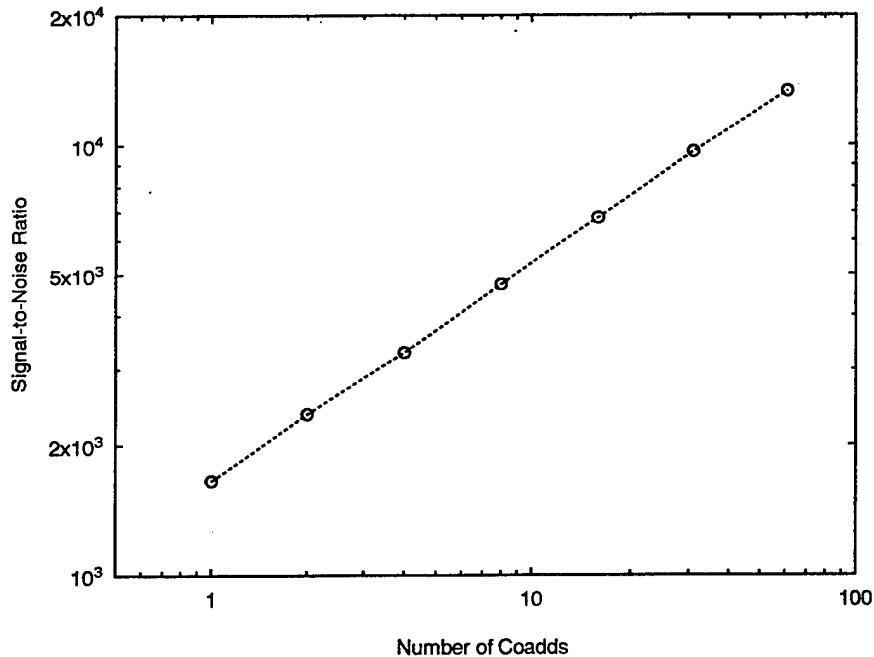


Figure 69. Example of coadding to increase signal-to-noise ratio.



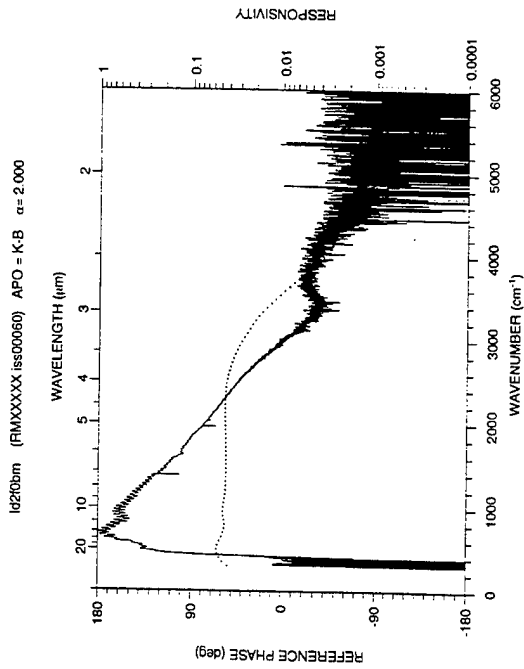
**Figure 70. Coadded scans to increase signal-to-noise ratio.**

After a reference interferogram was developed for each detector, filter, and bias condition, a sample RSR was calculated using software provided by Atmospheric Radiation Consultants (ARC) (file name: relre2.exe). The RSR software normalized the response by dividing out the temperature-dependent Planck function of the interferogram. The ARC software provided the sample RSR using the same routines coded into OPUS. The ARC software provided both a file and hard copy output of the relative spectral response for each detector, filter, and bias. The printed output was inspected to confirm the adequacy of the signal-to-noise ratio, the nonlinearity effects on the output, and other data analysis considerations.

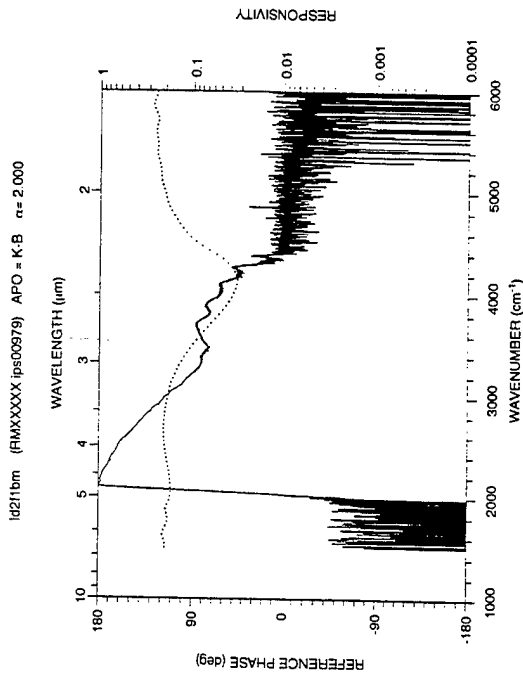
Figure 71 shows the relative spectral response data for interferometer detector 3-2 (all filters) under long scan and medium bias conditions. The RSR data for the other detectors are similar and can be ordered in digital form from PL for further comparison. The dotted line in each figure represents the reference phase, which is indicated on the left Y-axis, and the solid line represents the relative spectral response, which is indicated on the right Y-axis.

The relative spectral responsivity was calculated for both medium and low bias for each detector and filter combination. SDL and Phillips Laboratory personnel agreed to use medium bias interferograms as the reference interferograms in OPUS for both medium and low bias because of the significantly reduced nonlinearity of medium bias. Low bias nonlinearities pose a particular problem in the wide band and open filters, where the bandwidth of the filter is large enough to contain harmonics of some of its lower frequencies. Using the medium bias data for the relative spectral responsivity reference data reduces the uncertainty introduced into the relative spectral response from nonlinearities present in the sensor while operated in low bias. The nonlinearity correction routines developed (see Section 4.2.3) correct most of this error, and are now being implemented in OPUS.

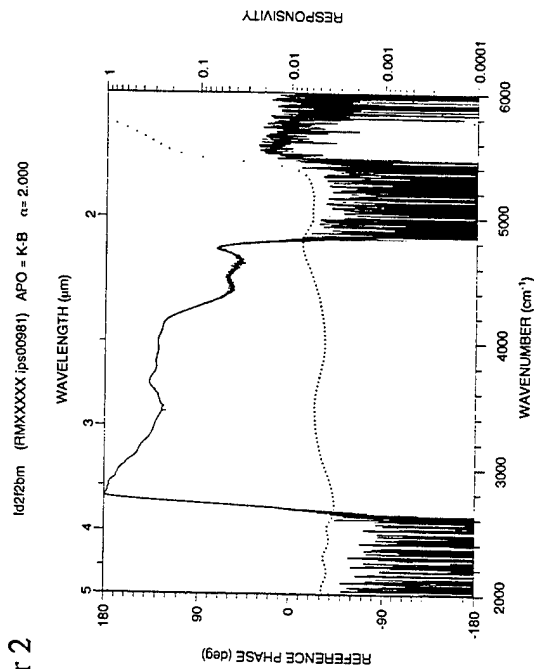
Filter 0



Filter 1



Filter 2



Filter 3

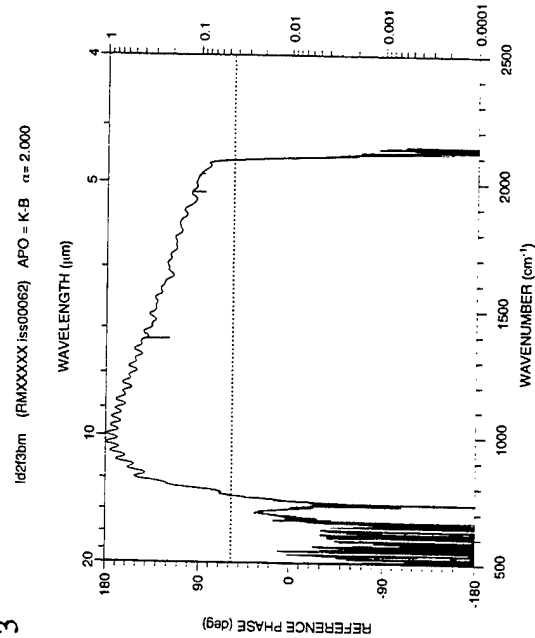
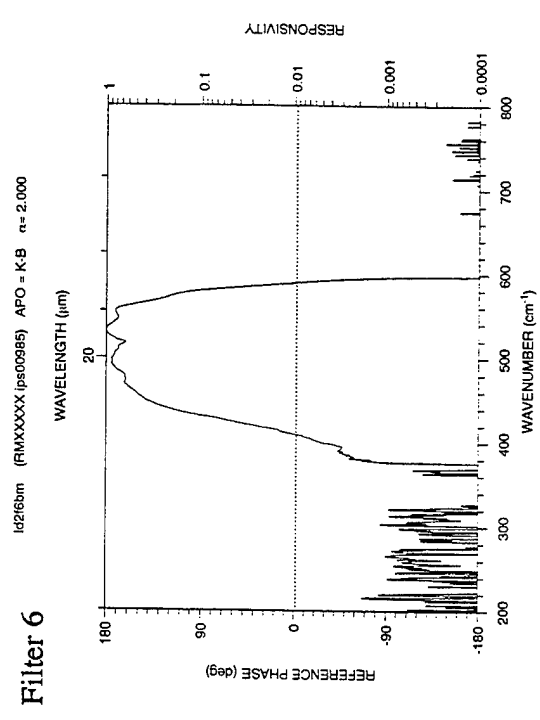
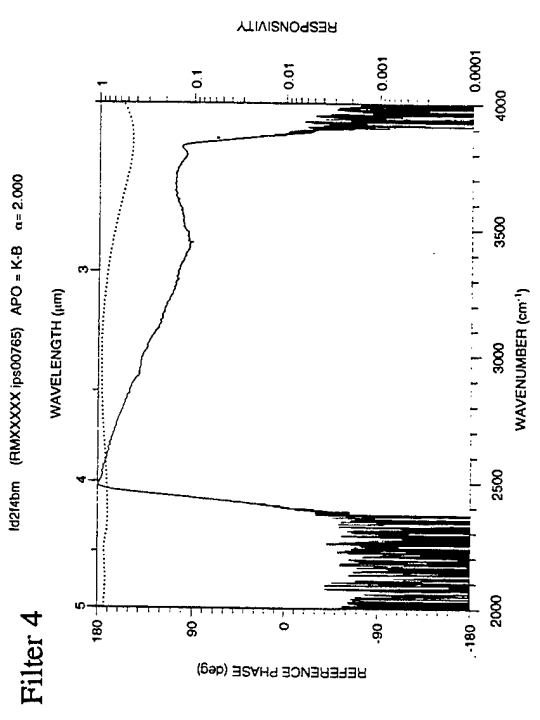
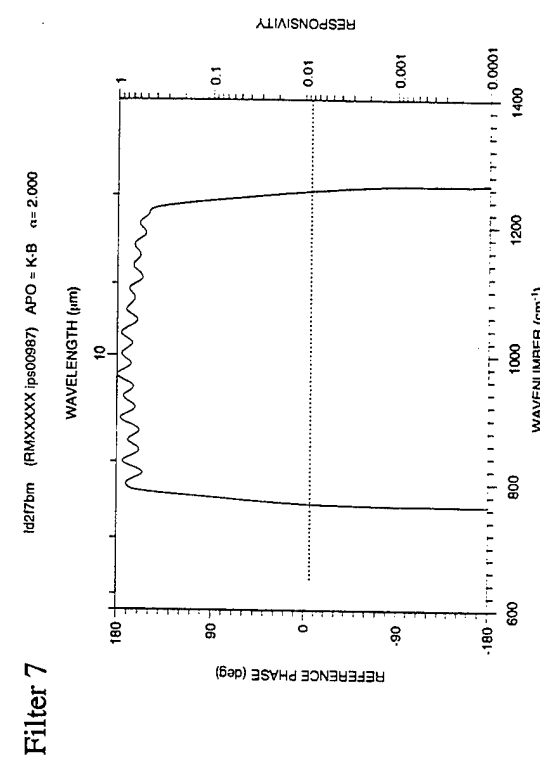
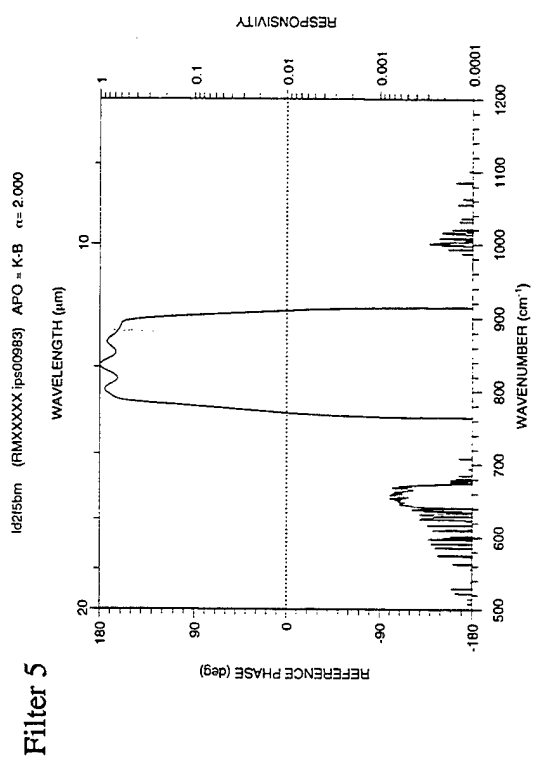


Figure 71. Relative spectral response data for interferometer detector 3-2, filters 0-7, under long scan and medium bias conditions.



**Figure 71 (cont). Relative spectral response data for interferometer detector 3-2, filters 0-7, under long scan and medium bias conditions.**

### 4.2.2.2 Absolute Responsivity

The absolute responsivity calibration determines the absolute radiance for the interferometer and the relative detector-to-detector responsivity (flat field matrix). It provides the transfer function of linearized sensor response to absolute flux. The absolute response data are collected using a full aperture, unattenuated source for traceability. With a sensitive instrument like CIRRIS, this source must be at a low temperature to prevent saturation. The RSR developed from a low temperature source will overplot only a short segment of the high temperature RSR. The absolute flux for this region of spectral overlap can be calculated by integrating the spectral output of the blackbody (Planck) curve for this region to develop the absolute scaling factor for that dc signal level, range, bias, and filter. An example of this procedure is shown in Figure 72. This figure shows the range of integration region used for all flux values collected for this filter. By using the integrated flux in the overlap region, the absolute calibration coefficient can be calculated for all spectral resolution and apodization conditions.

Absolute responsivity calibration coefficients were calculated using software provided by Atmospheric Radiation Consultants (ARC), which uses the following equations:

$$\frac{Ref (V cm)}{BB_{ref} (W cm^{-2} sr^{-1} cm)} \times \frac{1 (W cm^{-2} sr cm)}{Max (V cm)} = \mathfrak{R} (\lambda) \quad (22)$$

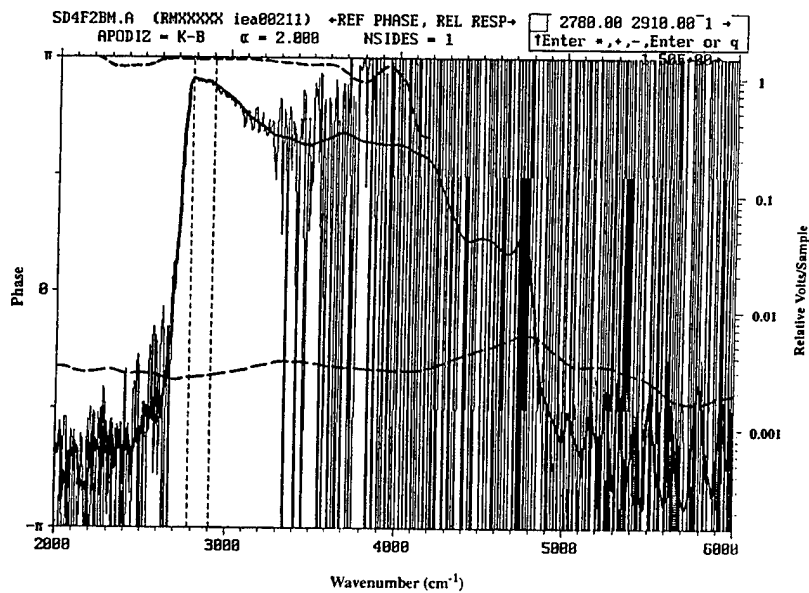
$$\frac{A_{ref} (V cm)}{BB_{ref} (W cm^{-2} sr^{-1} cm)} = K \left( \frac{V cm}{W cm^{-2} sr^{-1} cm} \right) \quad (23)$$

$$\mathfrak{R} (\lambda)_{cal} = K \times \mathfrak{R} (\lambda) \left( \frac{V cm}{W cm^{-2} sr^{-1} cm} \right) = \quad (24)$$

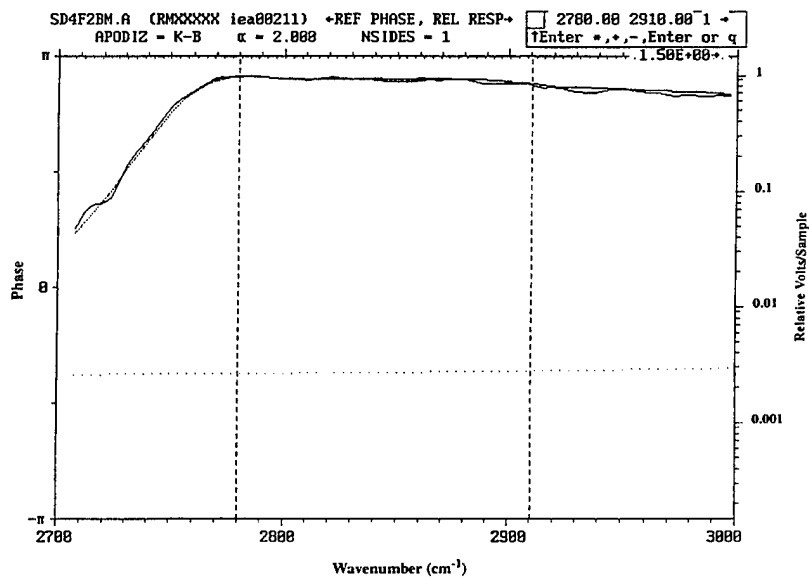
$$FR (V cm) \times \frac{1 (W cm^{-2} sr cm)}{\mathfrak{R} (\lambda)_{cal} (V cm)} = \phi FC (\lambda) (W cm^{-2} sr cm) \quad (25)$$

where

Ref (V cm)	=	spectral Response of reference interferogram
BB <sub>ref</sub> (W cm <sup>-2</sup> sr cm)	=	blackbody curve for temperature used to collect Ref
A <sub>ref</sub> (V cm)	=	spectral Response to extended Area Source
BB <sub>Aref</sub> (W cm <sup>-2</sup> sr cm)	=	blackbody curve for temperature used to collect A <sub>ref</sub>
$\mathfrak{R} (\lambda)$ (unitless)	=	relative Spectral Response
K (V cm/W cm <sup>-2</sup> sr cm)	=	absolute Response Coefficient
$\mathfrak{R} (\lambda)_{cal}$ (V cm/W cm <sup>-2</sup> sr cm)	=	calibrated RSR (absolute response spectrum)
FR (V cm)	=	flight response spectrum (uncalibrated)
FC (W cm <sup>-2</sup> sr cm)	=	calibrated Flight response spectrum



(a)



(b) Blowup of the integration region

**Figure 72.** The overlay of the measured extended source file at 242 K on the RSR of filter 2 to develop the absolute coefficient. All files for filter 2 were integrated in this same region.



The output of the software is a file that contains an absolute responsivity coefficient for each temperature within the flux range of each detector/bias combination.

The absolute responsivity calibration data were collected with the extended-area source, at temperatures from 44 K to 300 K. Data were taken at 5 K to 10 K steps with the interferometer in auto range, auto bias mode. This temperature step allowed several points to be collected in each filter, detector, bias, and gain combination over the dynamic range of the detectors. The data were taken in two different sets at different times during the calibration data collection effort. The first set was taken from 44 K to 150 K in short scans for filters 0, 3, 5, 6, and 7. The second set was taken from 90 K to 300 K in long scans for filters 1, 2, and 4. The second collection set also included two points on filter 5 and two points on filter 7.

After the calibration data was collected, absolute coefficients were calculated for every extended source data point by matching the best possible region between the filter-detector RSR and the blackbody corrected extended source transform. At the lowest temperature, this match occurred on the side of the RSR cuton, which added some noise to the process. Theoretically, the absolute calibration coefficient should be constant with flux. Absolute coefficients based on the mean values for each condition in both high and low bias are shown in Table 18, along with a bias gain calculation. Open places in Table 18 are filter-detector combinations which could not be collected because the in-band flux from the 300 K extended source fell below the NESR of the detector. This is not a serious limitation since no flight data were collected with these combinations.

**Table 18. Mean Absolute Long Scan Coefficients and a Mean Based Bias Gain for the CIRRIS 1A Interferometer**

		0	1	2	3	4	5	6	7
D1	M	2.24E10	1.48E9	4.56E8	1.32E10	8.67E7	1.21E10	4.63E9	1.39E10
	L	1.01E10	5.09E8	1.56E8	5.05E9	2.87E7	4.61E9	2.5E9	5.39E9
	Bias gain	2.22	2.91	2.92	2.61	3.02	2.62	1.85	2.58
D2	M	2.75E10	1.62E9	5.08E8	1.54E10	9.44E7	1.41E10	5.62E9	1.59E10
	L	1.45E10	6.59E8	1.82E8	6.88E9	3.52E7	6.90E9	3.32E9	7.71E9
	Bias gain	1.90	2.46	2.79	2.24	2.68	2.04	1.69	2.06
D3	M	3.08E9	1.52E8	4.07E7	1.62E9	8.28E6	1.32E9	6.30E8	1.64E9
	L	1.35E9	6.68E7		7.78E8		5.90E8	2.21E8	7.83E8
	Bias gain	2.28	2.28		2.08		2.24	2.85	2.09
D4	M	1.99E9	1.08E8	2.86E7	1.09E9	6.12E6	1.04E9	3.75E8	1.14E9
	L	9.01E8	5.35E7		5.22E8		4.62E8	1.36E8	5.64E8
	Bias gain	2.21	2.02		2.09		2.25	2.76	2.02
D5	M	1.05E6	6.79E5		5.89E6		5.23E6	1.88E6	6.28E6

Figure 73 presents normalized absolute response data collected for detector 3-3. Data for the other detectors can be extracted from OPUS. This figure shows the relationship of detector 3 long scan absolute coefficients for medium bias versus detector adjusted dc values for each filter. The vertical lines separate the data collected with each of the electronic gains (x100, x10, x1). The normalized coefficients show a range in variation of about 15%. In addition to the expected point-to-point noise, the variation across the flux (dc) range shows a definite slope.

The absolute coefficients and other data for detector 3 filter 3 based on this data are shown in Table 19. The table includes the absolute coefficients for short, medium, and long scans; the coefficient to be used for calculating short, medium, and long scans using the integral method; and the region of integration used to determine the coefficients. OPUS initially used linear extrapolations between each data point to calculate a coefficient for each flight dc value. The data for all of the detectors and filters are available in computer readable form. Low bias data discussed in this report has been non-linearity corrected using the nonlinearity correction described in Section 4.2.3. This correction is now being implemented and should be available in OPUS v.4 and subsequent versions. The nonlinearity correction is greatest for dc values above 0.5 volts in low bias. Only a slight nonlinearity was observed in medium bias data, to which no correction was applied.

To improve the accuracy of the data-retrieval routines, significant effort has been invested to separate instrument function from calibration noise.

Two conditions are obvious in the gain adjusted dc vs. absolute coefficient data. The data include a significant amount of point-to-point noise, and there is a low dc to high dc log relationship evident in most of the medium bias data. The combined variation (noise and trend) is about 15%. Three processes have been applied to improve the application of the absolute calibration data. These include an improved coefficient development method, grouping the data for each detector, and applying a curve fit to the data. Details of each process follow.

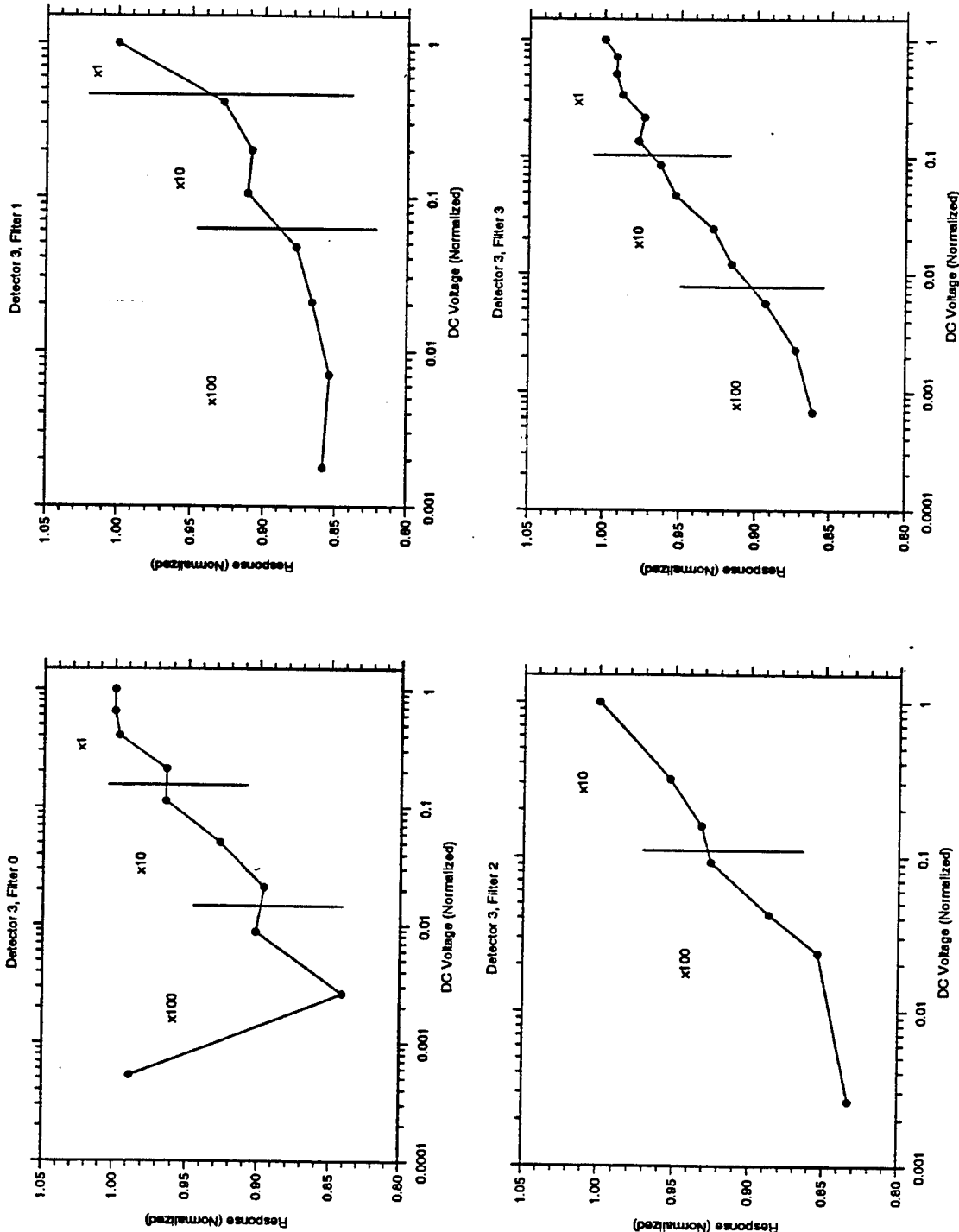


Figure 73. Normalized absolute response data for interferometer detector 3 medium bias  
 -- raw data (filters 0,1,2,3).

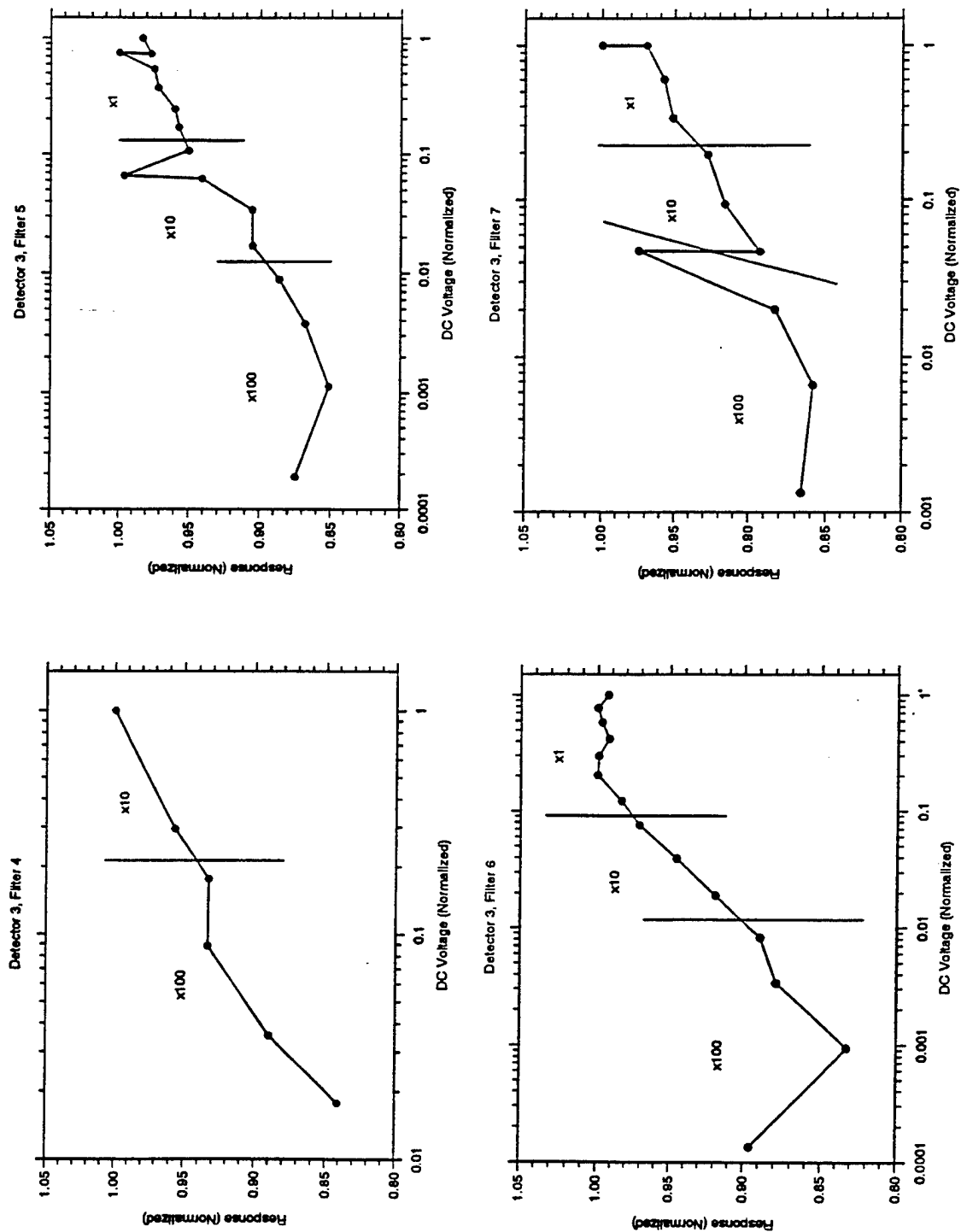


Figure 73 (cont). Normalized absolute response data for interferometer detector 3 medium bias -- raw data (filters 4,5,6,7).

**Table 19. A Sample of the Absolute Coefficient Tables Generated for Each Interferometer Detector, Filter, and Bias**

File type	Extended source file	Gain	Extended source temp. (K)	RSR file	No. points/IFG			Scan coefficient			DC volts (pre-gain)	Integral coefficient	Integration band	
					S	M	L	Short	Med	Long				
SD3F3BM	iea00067	100	79.02	ips00993	1792	3840	14664	1.410E+09	1.457E+09	1.471E+09	3.906E-03	9.057E+10	948.85	1032.28
SD3F3BM	iea00072	100	84.27	ips00993	1792	3840	14664	1.429E+09	1.477E+09	1.491E+09	1.328E-02	1.192E+11	925.71	1032.28
SD3F3BM	iea00077	100	89.06	ips00993	1792	3840	14664	1.463E+09	1.512E+09	1.526E+09	3.281E-02	1.225E+11	929.57	1036.14
SD3F3BM	iea00082	10	93.81	ips00993	1792	3840	14664	1.499E+09	1.549E+09	1.564E+09	7.031E-02	1.256E+11	929.57	1036.14
SD3F3BM	iea00087	10	98.76	ips00993	1792	3840	14664	1.519E+09	1.570E+09	1.585E+09	1.406E-01	1.366E+11	929.57	1043.85
SD3F3BM	iea00092	10	103.71	ips00993	1792	3840	14664	1.560E+09	1.613E+09	1.628E+09	2.734E-01	1.354E+11	929.57	1040.00
SD3F3BM	iea00097	10	108.91	ips00993	1792	3840	14664	1.577E+09	1.630E+09	1.645E+09	4.921E-01	1.322E+11	933.42	1040.00
SD3F3BM	iea00102	1	113.72	ips00993	1792	3840	14664	1.600E+09	1.654E+09	1.670E+09	7.812E-01	1.342E+11	933.42	1040.00
SD3F3BM	iea00107	1	118.75	ips00993	1792	3840	14664	1.594E+09	1.648E+09	1.664E+09	1.250E+00	1.337E+11	933.42	1040.00
SD3F3BM	iea00112	1	123.86	ips00993	1792	3840	14664	1.618E+09	1.672E+09	1.688E+09	1.953E+00	1.404E+11	929.57	1040.00
SD3F3BM	iea00117	1	128.90	ips00993	1792	3840	14664	1.624E+09	1.679E+09	1.695E+09	2.968E+00	1.362E+11	933.42	1040.00
SD3F3BM	iea00122	1	133.77	ips00993	1792	3840	14664	1.623E+09	1.678E+09	1.694E+09	4.140E+00	1.361E+11	933.42	1040.00
SD3F3BM	iea00127	1	138.74	ips00993	1792	3840	14664	1.637E+09	1.692E+09	1.708E+09	5.781E+00	1.322E+11	933.42	1036.14
SD3F3BL	iea00133	1	149.08	ips00993	1792	3840	14664	2.416E+08	2.497E+08	2.520E+08	2.812E+00	2.173E+10	929.57	1043.85
SD3F3BL	iea00147	1	158.49	ips00993	1792	3840	14664	2.027E+08	2.096E+08	2.115E+08	3.906E+00	2.611E+10	867.86	1043.85
SD3F3BL	iea00153	1	168.35	ips00993	1792	3840	14664	1.759E+08	1.818E+08	1.835E+08	5.156E+00	2.299E+10	864.00	1043.85
SD3F3BL	iea00160	1	178.80	ips00993	1792	3840	14664	1.533E+08	1.584E+08	1.599E+08	6.796E+00	2.055E+10	864.00	1047.71
SD3F3BL	iea00167	1	188.12	ips00993	1792	3840	14664	1.355E+08	1.400E+08	1.413E+08	8.593E+00	1.817E+10	864.00	1047.71
SD3F3BL	iea00174	1	198.31	ips00993	1792	3840	14664	9.524E+07	9.845E+07	9.937E+07	9.921E+00	3.869E+09	937.28	993.71

#### 4.2.2.2.1 Point-to-Point Noise Reduction

To minimize point-to-point noise, the original data were reanalyzed using the method shown in Figure 72. Each transform-RSR fit was carefully analyzed for unusual noise and sufficient signal in the fit region. Data with noise or insufficient signal were rejected from the analysis. Rather than match a single point on the two curves, the areas under both curves in the integration region were set equal using the absolute coefficient (K) (see Equation (24)). An example of the reanalyzed (integral method) coefficient data is shown in Table 20. These are the same points as those presented in Table 19 for comparison.

**Table 20. The Absolute Coefficients Developed for Detector 3, Filter 3, Medium Bias Using the Integral Method**

File type	Extended source file	Gain	Extended source temp. (K)	RSR file	No. points/IFG			Scan coefficient			DC volts (pre-gain)	Integral coefficient	Integration band	
					S	M	L	Short	Med	Long				
SD3F3BM	iea00067	100	79.02	ips00993.c	1792	3840	14664	1.408E+09	1.456E+09	1.470E+09	3.906E-03	1.134E+11	940.0	1040.0
SD3F3BM	iea00072	100	84.27	ips00993.c	1792	3840	14664	1.420E+09	1.468E+09	1.482E+09	1.328E-02	1.144E+11	940.0	1040.0
SD3F3BM	iea00077	100	89.06	ips00993.c	1792	3840	14664	1.459E+09	1.508E+09	1.522E+09	3.281E-02	1.175E+11	940.0	1040.0
SD3F3BM	iea00082	10	93.81	ips00993.c	1792	3840	14664	1.496E+09	1.546E+09	1.560E+09	7.031E-02	1.204E+11	940.0	1040.0
SD3F3BM	iea00087	10	98.76	ips00993.c	1792	3840	14664	1.521E+09	1.572E+09	1.587E+09	1.406E-01	1.224E+11	940.0	1040.0
SD3F3BM	iea00092	10	103.71	ips00993.c	1792	3840	14664	1.559E+09	1.612E+09	1.627E+09	2.734E-01	1.255E+11	940.0	1040.0
SD3F3BM	iea00097	10	108.91	ips00993.c	1792	3840	14664	1.577E+09	1.630E+09	1.645E+09	4.921E-01	1.269E+11	940.0	1040.0
SD3F3BM	iea00102	1	113.72	ips00993.c	1792	3840	14664	1.600E+09	1.654E+09	1.669E+09	7.812E-01	1.288E+11	940.0	1040.0
SD3F3BM	iea00107	1	118.75	ips00993.c	1792	3840	14664	1.594E+09	1.648E+09	1.663E+09	1.250E+00	1.283E+11	940.0	1040.0
SD3F3BM	iea00112	1	123.86	ips00993.c	1792	3840	14664	1.616E+09	1.671E+09	1.686E+09	1.953E+00	1.301E+11	940.0	1040.0
SD3F3BM	iea00117	1	128.90	ips00993.c	1792	3840	14664	1.624E+09	1.679E+09	1.694E+09	2.968E+00	1.308E+11	940.0	1040.0
SD3F3BM	iea00122	1	133.77	ips00993.c	1792	3840	14664	1.623E+09	1.678E+09	1.693E+09	4.140E+00	1.307E+11	940.0	1040.0
SD3F3BM	iea00127	1	138.74	ips00993.c	1792	3840	14664	1.633E+09	1.688E+09	1.704E+09	5.781E+00	1.315E+11	940.0	1040.0
SD3F3BL	iea00133	1	149.08	ipsl0993.3	1792	3840	14664	7.334E+08	7.581E+08	7.652E+08	2.812E+00	5.906E+10	940.0	1040.0
SD3F3BL	iea00147	1	158.49	ipsl0993.3	1792	3840	14664	7.535E+08	7.789E+08	7.862E+08	3.906E+00	6.068E+10	940.0	1040.0
SD3F3BL	iea00153	1	168.35	ipsl0993.3	1792	3840	14664	7.589E+08	7.845E+08	7.919E+08	5.156E+00	6.112E+10	940.0	1040.0
SD3F3BL	iea00160	1	178.80	ipsl0993.3	1792	3840	14664	7.500E+08	7.753E+08	7.826E+08	6.796E+00	6.040E+10	940.0	1040.0
SD3F3BL	iea00167	1	188.12	ipsl0993.3	1792	3840	14664	7.336E+08	7.583E+08	7.655E+08	8.593E+00	5.908E+10	940.0	1040.0

The integral method absolute coefficient data were then normalized for each filter, and a least squares fit was calculated for each filter and detector. Data and the fit equation for medium bias, and linearized low bias data for detector 3 are shown in Figure 74. The fit equations and their degree of fit for all detectors and filters are shown in Table 21. Table 21 has been arranged to allow similar filters to be compared. The long wavelength cutoff is the most critical item, since it controls the minimum source temperature at which noise-free data could be obtained. Since the slope of the data appears to be strongly dependent on source temperature, this grouping allows an easier comparison. Calculating the absolute coefficients for an arbitrary dc value using the integral method data curve fit equations reduces the point-to-point noise evident in Figure 73

by about  $\pm 5\%$  over data analyzed using the original OPUS scheme. The trend still exists, and it is steepest at the smallest dc (lowest temperature) values. However, significant variation in the filter-to-filter slope for a single detector still exists when the filters are fit separately (see Table 21).

Figure 74 also shows the linearized low bias absolute coefficient data set. These data were dc corrected and multiplied by a constant (bias gain) to match the absolute coefficient of the highest dc value of the medium bias data set. The variation in the required multipliers and deviation of the data from a uniform trend is evident in the data. On the short wavelength filters, sufficient in-band energy is not available from the extended source (limit 300 K) to develop low bias coefficients. In some cases the low bias data fits the medium bias temperature trend, but the shorter wavelength data collected at the highest extended source temperatures show greater variation and trends that are not consistent with those collected at lower temperatures. In all cases, the bias gain values in Figure 74 are greater than the values derived from the mean values (see Table 18). This is partially due to the slope present in the medium bias data and the lack of slope in most of the low bias data set. The variation in the bias gain shown thus far is at least partially due to wide variation in the filter slope equations, which may be a result of too few points in each curve.

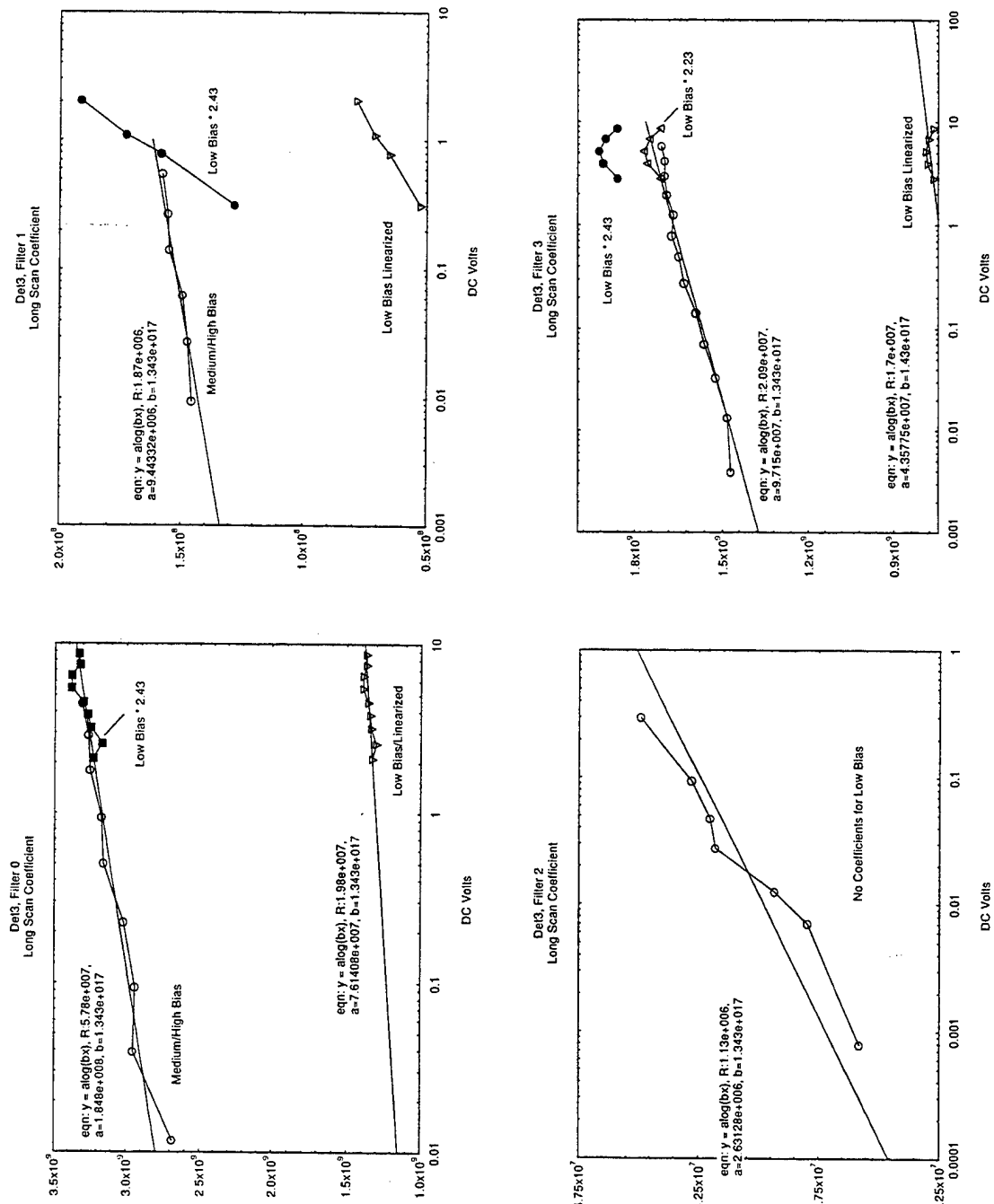


Figure 74. Medium and low bias data for detector 3 and the least squares fit coefficients for the equation  $y = a \log(bx)$ . The bias gain needed to bring the low bias data on to the same line is also shown.



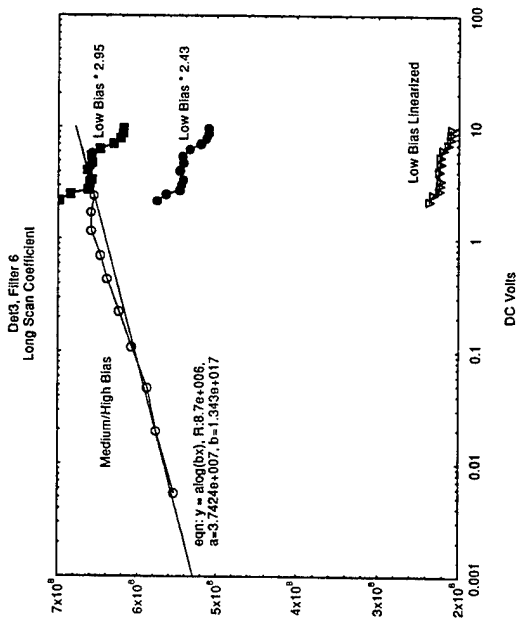
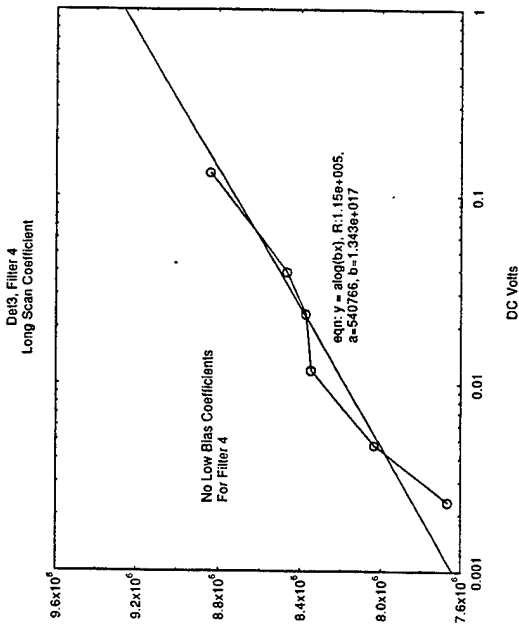
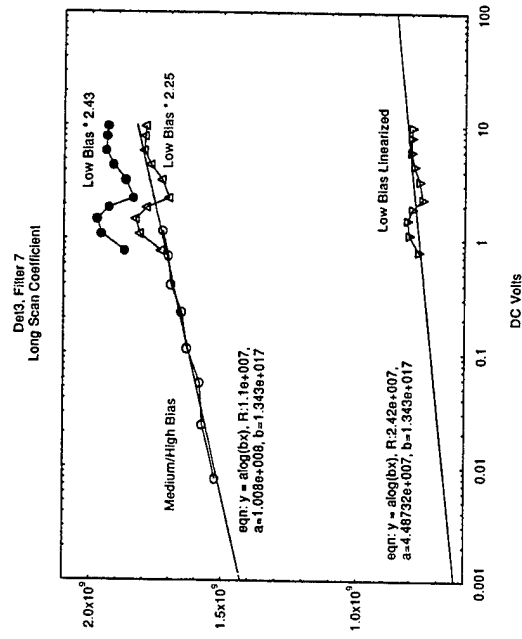
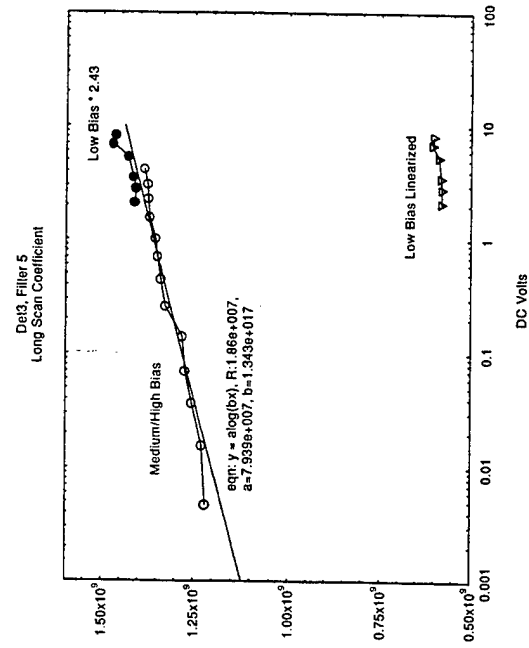


Figure 74 (cont). Medium and low bias data for detector 3 and the least squares fit coefficients for the equation  $y = a \log(bx)$ . The bias gain needed to bring the low bias data on to the same line is also shown.

**Table 21. Fit Coefficient Data**

Filter	0	6	1	2	4	3	5	7
Bandpass (μm)	2.5 - 25	17 - 25	2.5 - 4.9	2.5 - 3.7	1/10 hole plate 2.5 - 4.05	4.17 - 13	11 - 13	8 - 13
Extended source temperature range for medium bias								
D3-1	57 - 70	50 - 85	160 - 210	220 - 280	225 - 280	82 - 110	77 - 110	70 - 95
D3-2	57 - 70	50 - 85	160 - 120	210 - 280	215 - 280	75 - 110	65 - 110	68 - 90
D3-3	57 - 95	60 - 120	180 - 240	225 - 305	240 - 305	75 - 140	77 - 140	75 - 110
D3-4	57 - 100	60 - 110	165 - 265	225 - 305	240 - 305	75 - 140	77 - 150	75 - 120
D3-5	90 - 280	120 - 305	260 - 305	120 - 305	90 - 305	120 - 305	120 - 305	90 - 305
Curve fit offset: a of $Y = a \log (bx)$								
D3-1	2.14E9	6.11E8	1.03E8	7.87E7	1.78E7	1.58E9	1.13E9	1.34E9
D3-2	2.33E9	6.75E8	9.35E7	5.77E7	1.35E7	1.34E9	1.18E9	1.37E9
D3-3	2.21E8	6.62E7	8.45E6	3.68E6	4.84E5	8.48E7	6.74E7	9.67E7
D3-4	1.69E8	2.84E7	9.30E6	4.16E6	9.00E5	6.89E7	6.27E7	8.23E7
Curve fit slope: b of $Y = a \log (bx)$								
D3-1	2.13E10	3.97E7	6.61E14	1.91E6	2.79E5	2.86E8	1.82E10	4.24E10
D3-2	6.98E11	4.91E8	8.86E17	3.33E9	5.24E7	5.16E11	1.79E12	2.42E12
D3-3	2.24E14	5.79E17	1.05E19	5.27E12	8.75E18	3.57E19	1.17E20	6.14E17
D3-4	1.93E12	4.27E13	3.15E12	1.85E8	1.96E8	1.67E16	1.33E16	3.43E14
Degree of fit (R)								
D3-1	3.54E8	6.84E7	6.72E6	6.26E6	1.33E6	6.19E7	8.32E7	9.48E7
D3-2	3.44E8	6.50E7	1.82E7	7.97E6	1.12E6	1.29E8	1.57E8	2.92E8
D3-3	4.63E7	8.41E6	1.38E6	6.12E5	1.38E5	1.40E7	1.10E7	1.04E7
D3-4	4.49E7	1.00E7	1.77E6	9.45E5	1.39E5	1.51E7	1.64E7	6.64E6

**4.2.2.2 Unified Filter Slope Equation**

Several factors could cause the observed deviation from the 0 slope of an ideal sensor. These include problems with the filter RSR curves, extended source temperature errors, or a gain dependence in the sensor. The effect of the light leak observed in the RSR data for filter 0 and 6 will contribute some error to the points collected below 100K. In addition, during the SPIRIT III calibration, temperature gradients were discovered in the surface temperature of the extended source at temperatures above 150 K. The temperature pattern is an annulus around the oval shaped source, with the temperature near the middle of the source being up to 0.5 K lower than

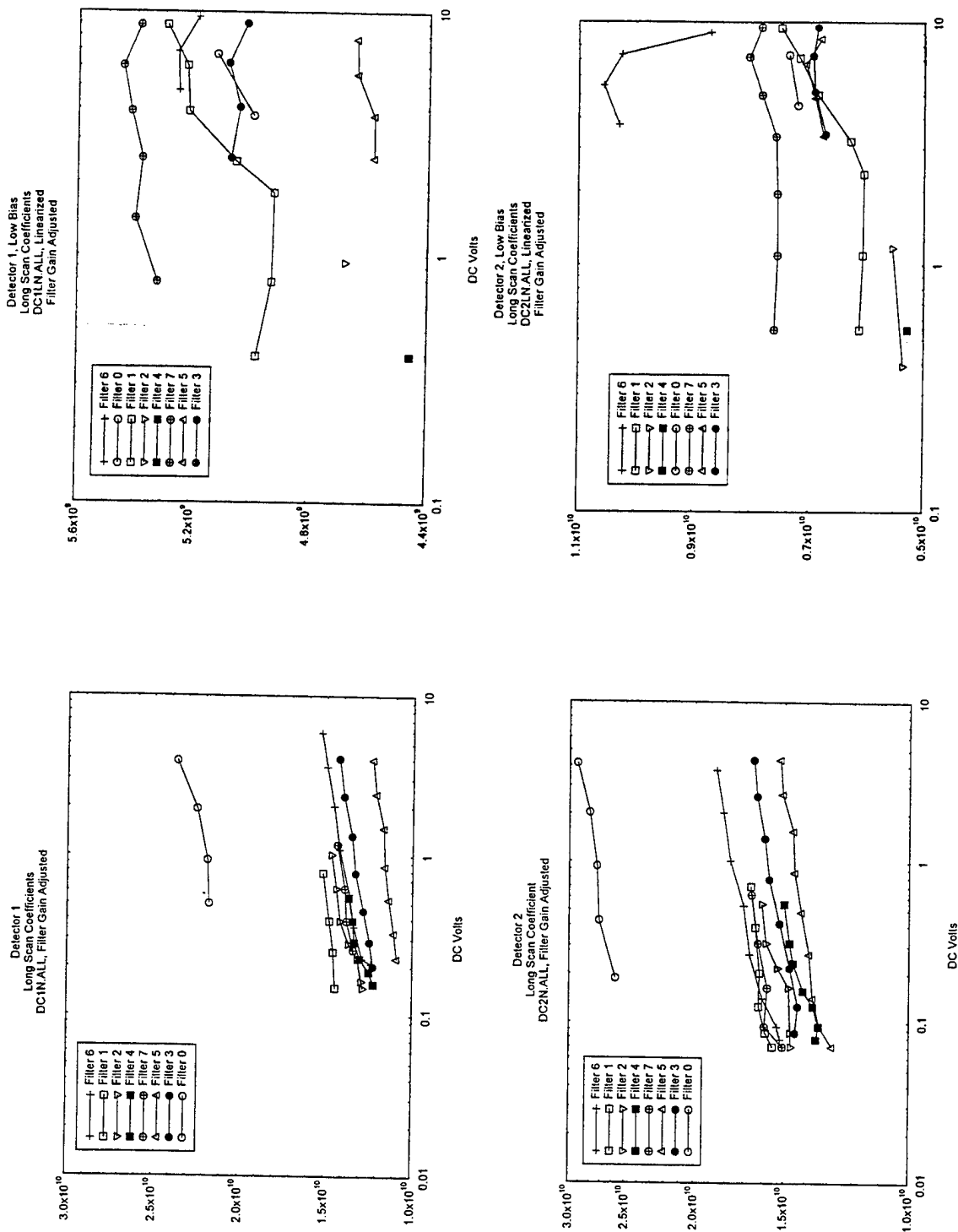
that over the heater. This difference becomes larger as the source temperature increases, and data at the higher temperature for all the filters include this error.

Table 21 shows that significant variation exists in the slopes of the individual fit equations for each of the filters in a given detector (see  $b$  of  $Y = a \log (bx)$ ). If one assumes that the dc reading of the interferometer is proportional to the photon flux received by the detector, the RSR corrected response of a detector should be the same for each filter. Based on this assumption, we could conclude that the variation in the slopes of the fits to the individual curves is due to insufficient data to resolve the true function from the noise. To test this hypothesis, the data for each filter of each detector was adjusted to lie within a few percent of the data for filter 3 and examined visually. These plots are shown in Figures 75 and 76. In these plots, filters 4, 2, 1, 6, and 0 were multiplied by 150, 30, 10, 3, and 0.5 respectively. The curves were purposely not directly overlaid to allow better visualization of each curve.

Figure 75 shows the medium and low bias coefficients for all the filters of each detector as a function of log dc volts or photon flux. The medium bias plots for detectors 1, 2, 3, and 4 show consistent slopes when plotted in this fashion. Figure 76 shows the scaled absolute coefficients as a function of temperature. Figure 77 shows the filter gain adjusted absolute coefficient data for detector 5, medium and low bias against dc and temperature. Detector 5 response as a function of dc value is almost flat, with a dip in response of about 0.5 volts. This dip is most pronounced in filters 0 and 6.

The patterns presented in Figure 77 are most instructive. Because of detector size and filter bandwidth differences, these curves were collected over a wide range of temperatures. A slightly steeper slope is observed for curves taken below 100 K than those that were collected above 150 K at the same dc value. The increased slope of the coefficients with temperature between 50 K and 120 K might suggest a question about the PRT calibration in this range. To determine if a calibration error could cause this type of response, a sensitivity calculation was made (using detector 3, filter 3) to determine the size of a PRT calibration error required to remove the slopes observed in these curves. The sensitivity analysis indicated that at 79.9 K, decreasing the reported extended source temperature by 0.3 K (to 79.6 K) increased the absolute coefficient value sufficient to eliminate the total slope of the line. If one attempts to reduce the higher temperature data to the level of the low temperature data, a larger error is required. At 139 K, the reported temperature had to be increased by 1.3 K (to 140.3 K) to reduce the coefficient to the level of those taken at 80 K. An error of less than 0.1 K in the lower temperature portion (50 K - 70 K) of the PRT calibration curve would be sufficient to provide a consistent slope as a function of temperature to all of the medium bias data.

Despite the relatively small temperature errors required to unify or even remove the slopes of the charts in Figure 76, we do not believe such an error exists. The medium bias data for detectors 1 to 4 all have a similar slope when plotted as a function of log (dc). The RSR corrected spectral intensity for each filter should indicate the same flux on the detector. When the data are plotted against dc, the slopes are parallel. If we adjusted the temperature to change the slope with temperature to be equal for all filters, it would cause the slopes as a function of flux to diverge. Hence, we conclude that no error exists in the low temperature portion of the extended source calibration curve.



**Figure 75. Filter adjusted long scan curves showing the similar slopes to all the medium bias data for each detector. The low bias data shows no consistent pattern. Coefficients for filters 4, 2, 1, 6, and 0 were multiplied by 150, 30, 10, 3, and 0.5 to bring the values into a similar range for comparison.**

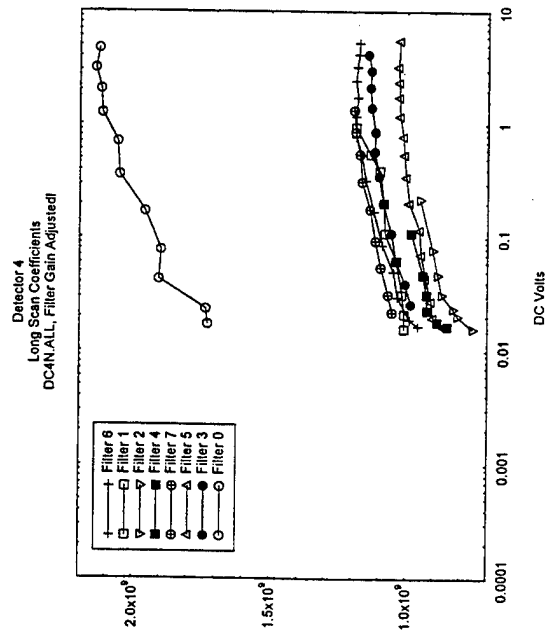
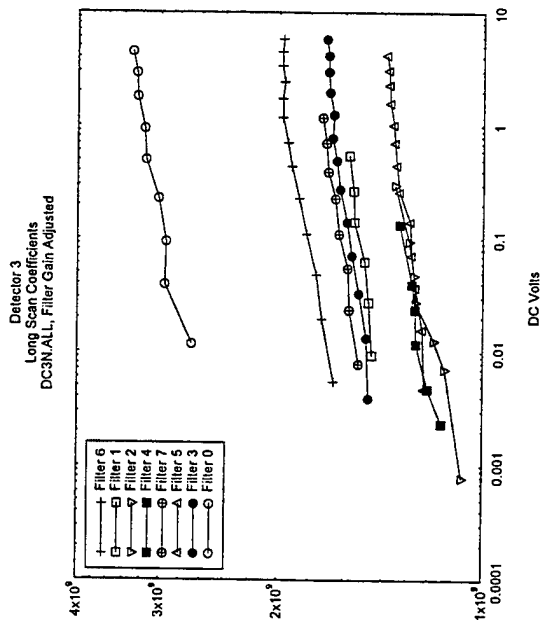
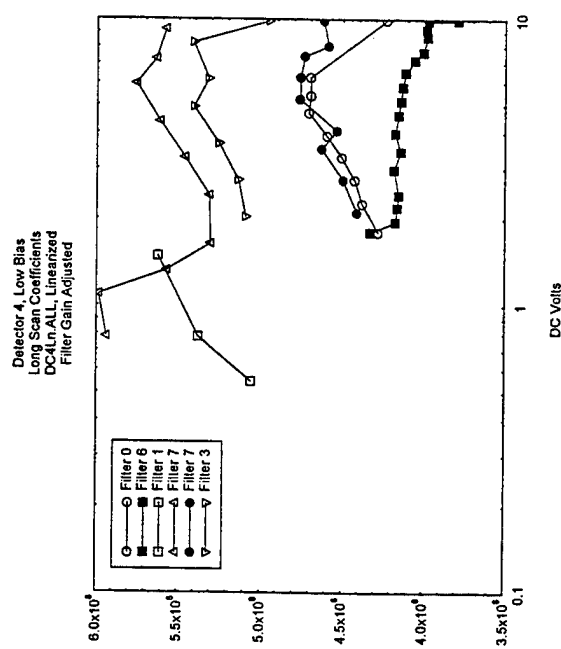
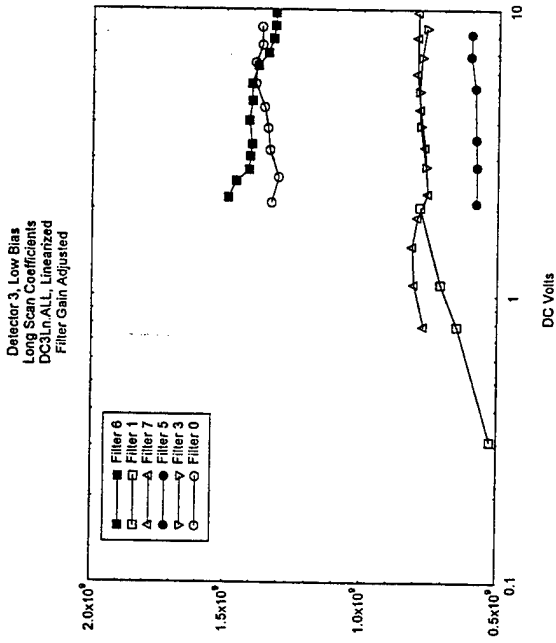


Figure 75 (cont). Filter adjusted long scan curves showing the similar slopes to all the medium bias data for each detector. The low bias data shows no consistent pattern. Coefficients for filters 4, 2, 1, 6, and 0 were multiplied by 150, 30, 10, 3, and 0.5 to bring the values into a similar range for comparison.

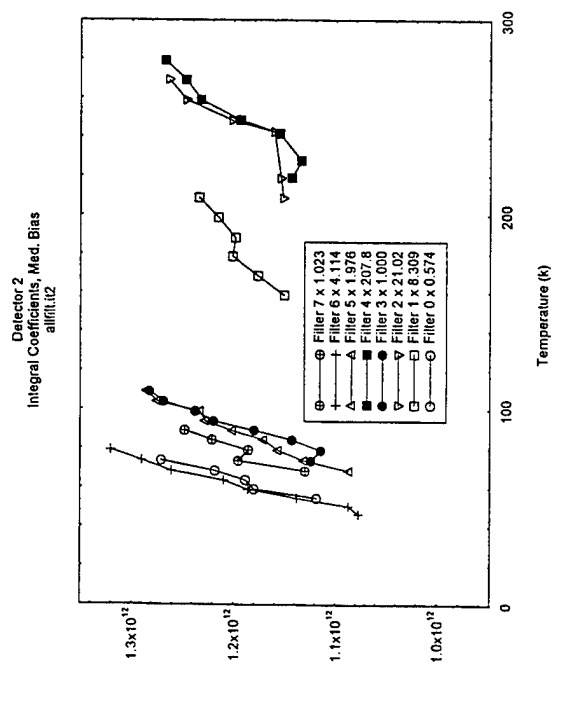
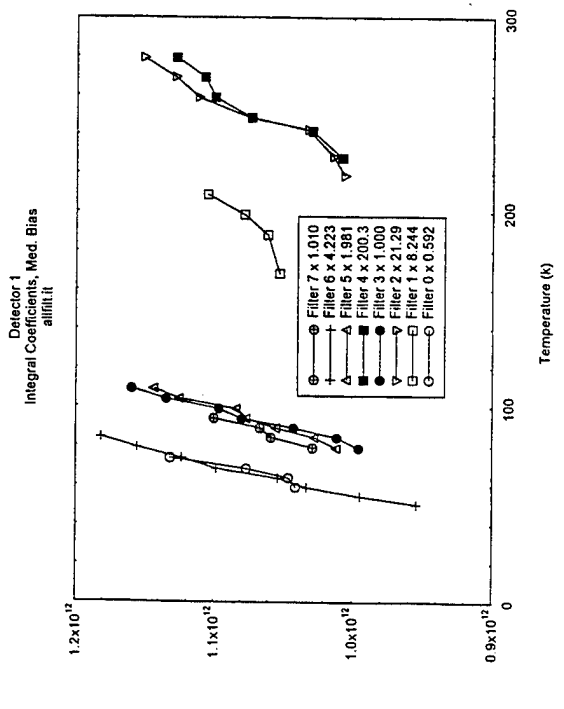
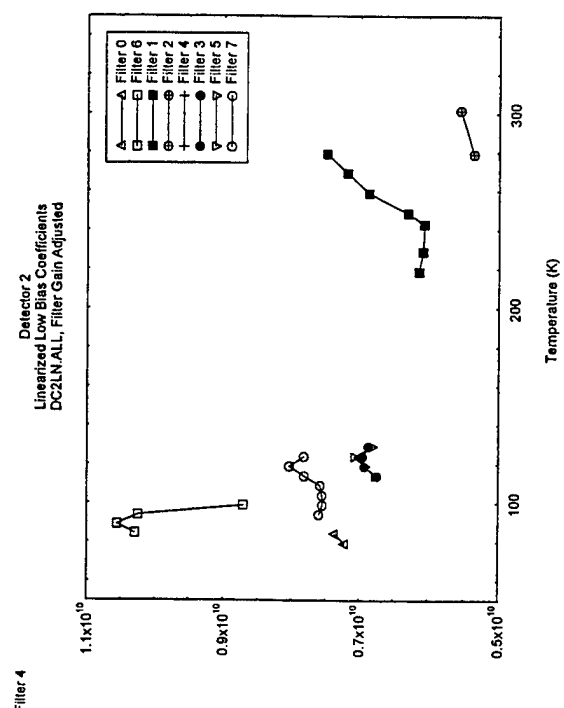
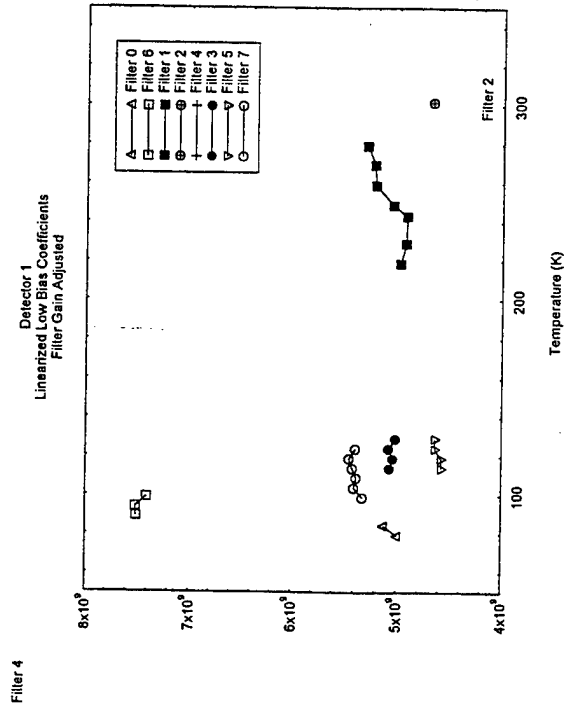


Figure 76. Filter adjusted long scan curves as a function of temperature. Coefficients for filters 4, 2, 1, 6, and 0 were multiplied by 150, 30, 10, 3, and 0.5 to bring the values into a similar range for comparison.

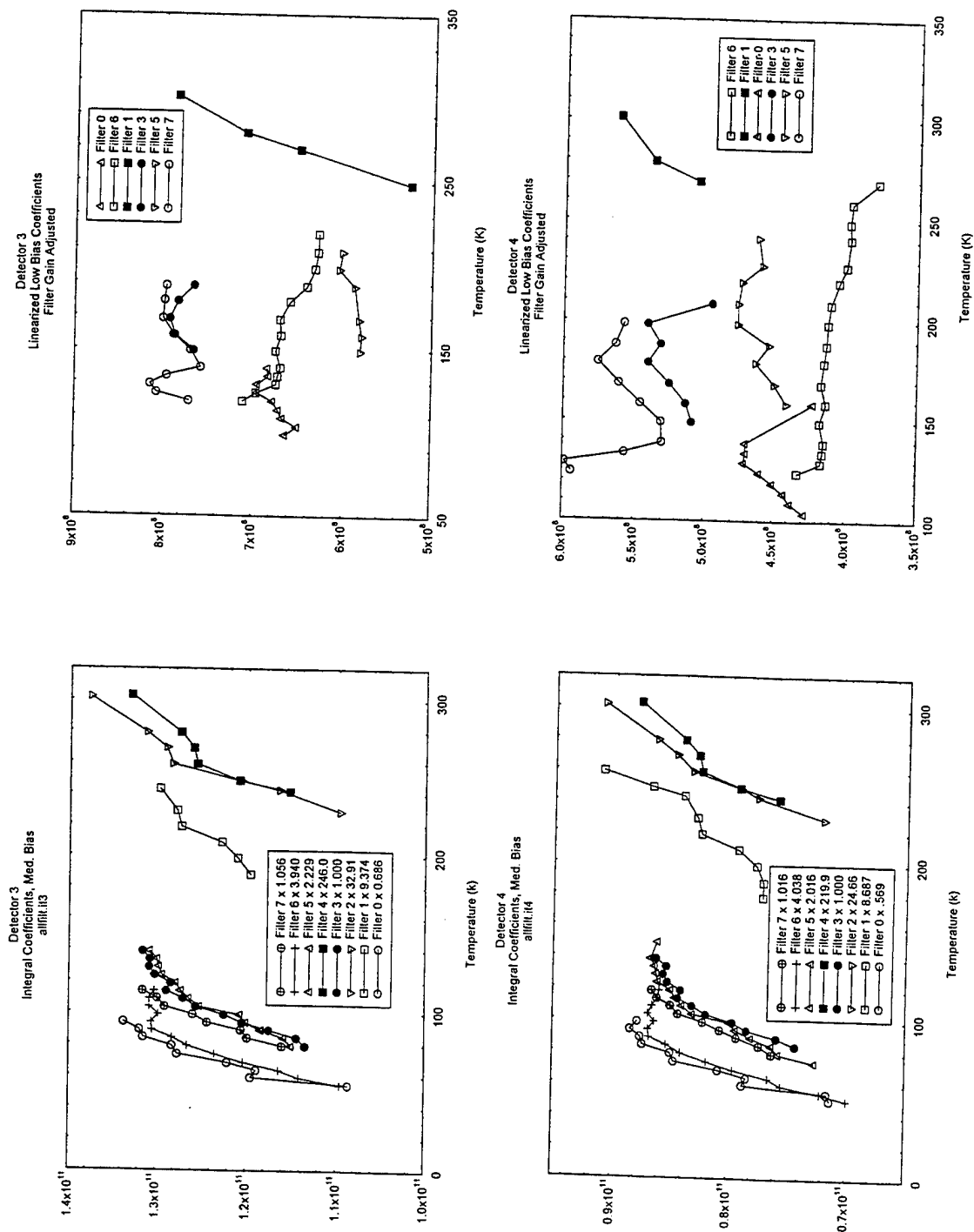


Figure 76 (cont). Filter adjusted long scan curves as a function of temperature. Coefficients for filters 4, 2, 1, 6, and 0 were multiplied by 150, 30, 10, 3, and 0.5 to bring the values into a similar range for comparison.

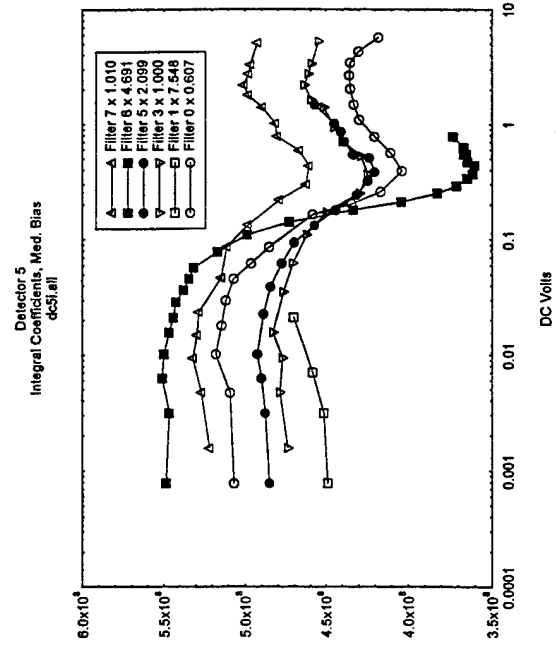
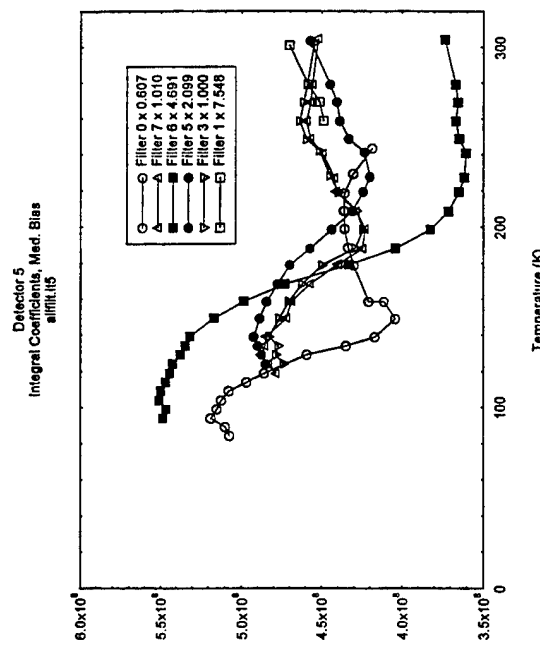
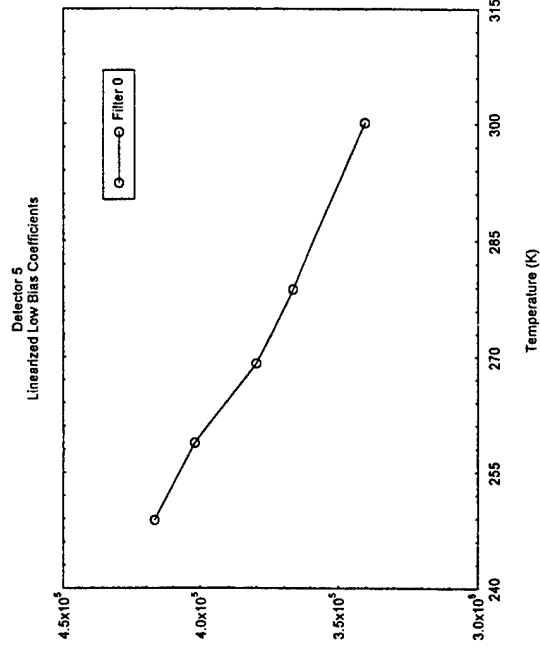
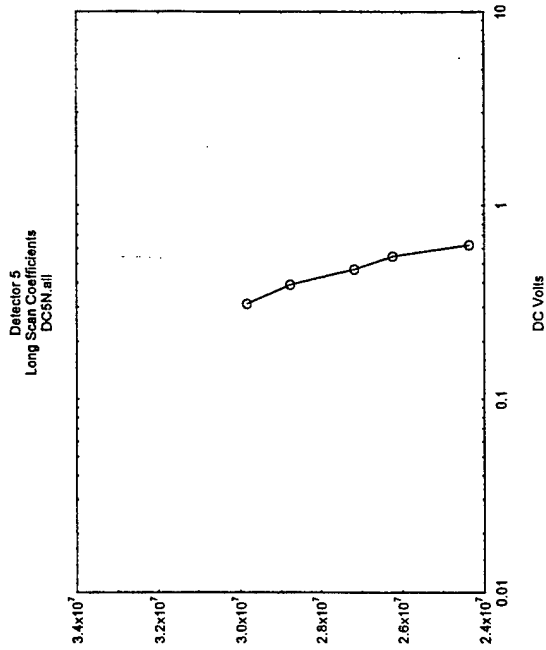


Figure 77. Filter gain adjusted curves for detector 5, medium and low bias against dc and temperature.



At higher extended source temperatures, another error source does appear to become operational. Data collected at temperatures above 200 K show some similar filter-to-filter trends, but much larger variations are present from filter-to-filter at the same temperature. In this region, the data suggest that the temperature of the source was not as accurate or as stable as desired during the period of data collection. Data were collected by bringing the source to the desired temperature, and when the PRT output was stable, collecting data for each filter, sequentially. This required that the source remained at a constant temperature for periods up to one hour. If the source temperature remained constant, but at some error, all of the filter data collected at that temperature should show a similar error. Figures 75 and 76 show that some individual filter deviations from the slope vary at higher temperatures. The figures also show regions where two or three filter coefficients deviate from a consistent function over a few data points. This would indicate that some variations in source surface temperature occurred during data collection. Small temperature fluctuations of this nature in the surface of the source while the data was collected would have gone unnoticed. Our current conclusion is that much of the variation between filters at the higher temperatures results from a problem of consistent source temperature control. The problem with the high temperature data is particularly evident in the low bias data. The shape of these curves with temperature is shown in Figure 76. Here, unlike the low temperature data, there is no consistent pattern to the data, and many of the variations are not random. This leads us to conclude that source stability is a contributing mechanism to this variation.

#### 4.2.2.2.3 Summary

Because of the uniform slope to the data of detector 1, 2, 3, and 4 at medium bias as a function of flux--despite the data being collected at a range of temperatures--we conclude that fitting a single slope for all filters to each of these detectors provides the best interpretation of the calibration data. We believe that this slope is the true instrument response function for medium bias. The filter groups and the response equation from the fits are shown in Figure 78. The offset between the curves after adjusting to the mean of the absolute coefficient for each curve results from the fact that the mean absolute coefficient of each curve occurs at a different dc value. The slope and the base offset for filter 3 is shown in Table 22 for each detector. An offset multiplier is provided to derive the offset for each of the other filters. Detector 5 requires its own solution (see Figure 77). In this case, a linear fit between the data, as was done initially, appears to provide the best interpretation possible for the medium bias data. We do not understand the dc dependent dip at 0.5 Vdc, but conclude that it is an instrument response.

The low bias data does not appear to contain any believable trend. Here, the variations appear to be noise related, either due to source error or interferogram variability. We conclude that a single constant, based on the mean of the integral scan data provides the most believable response for detector 5 low bias. These mean coefficients are provided in Table 22.

**Table 22. Unified Slope Coefficients for Medium Bias Detectors 1, 2, 3, and 4, and Mean Coefficients for Low Bias. A Base Coefficient is Provided for Filter 3 and an Offset Coefficient for the other Filters. No Fit Equation is Provided for Detector 5, Medium Bias**

Y = a log (bx)			Filter							
Det			3	5	7	1	2	4	0	6
	Item	b	a = offset terms for each filter							
D1	Coef	1E10	1.0E11	5.463E10	1.0925E11	1.369E10	5.311E9	5.685E8	1.7912E11	2.562E10
D1	Error		1.17E10	4.22E9	7.9E9	1.82E9	1.34E9	1.46E8	2.9E10	6.08E9
D2	Coef	1E10	1.254E11	6.261E10	1.2551E11	1.551E10	6.143E9	6.225E8	2.091E11	3.0321E10
D2	Error		3.67E10	1.08E10	2.54E10	3.44E9	8.87E8	958E7	3.28E10	4.82E9
D3	Coef	1.91E19	6.651E9	2.9836E9	6.421E9	7.30E8	2.151E8	2.912E7	9.697E9	1.675E9
D3	Error		1.13E9	5.19E8	8.01E8	1.2E8	1.3E8	9E6	4.32E9	4.7E8
D4	Coef	2.201E14	5.98E9	2.9851E9	5.971E9	7.015E8	2.631E8	2.9302E7	1.0507E10	1.41812E9
D4	Error		1.85E9	9.3E8	6.15E8	1.83E8	1.99E8	1.3E7	3.85E9	6.25E8
	Slope (b)	Base offset (a)	Medium bias offset-multipliers							
D1	1.0E10	1.09E11	0.5049	0.9901	0.1213	4.697E-2	4.99E-3	1.689	0.2368	
D2	1.0E10	1.254E11	0.5061	0.9775	0.1204	4.757E-2	4.81E-3	1.742	0.2431	
D3	1.91E19	6.748E9	0.4486	0.9470	0.1067	3.107E-2	4.26E-3	1.458	0.2538	
D4	2.201E14	6.028E9	0.4854	0.9833	0.1151	4.297E-2	4.90E-3	1.757	0.2477	
Relative mean filter gain										
			2.06	1.03	8.63	23.72	210.97	0.60	4.08	
Low bias means										
D1		4.109E11	2.166E11	4.145E11	4.447E10	1.725E10	1.837E9	8.185E11	1.368E11	
D2		5.625E11	2.950E11	5.662E11	5.867E10	2.038E10	2.149E9	1.103E12	1.716E11	
D3		6.007E10	2.505E10	5.696E10	5.862E9			9.823E10	1.112E10	
D4		3.939E10	1.922E10	3.400E10	4.706E9			6.559E10	7.408E9	
D5								2.728E7		
Relative mean filter gain										
		1	2.06	1.01	9.36	25.71	242.8	0.56	4.25	
Integration band										
		940.0 - 1040.0	810.0 - 875.0	900.0 - 1000.0	2100.0 - 2200.0	2780.0 - 2910.0	2480.0 - 2550	630.0 - 730.0	480.0 - 550.0	

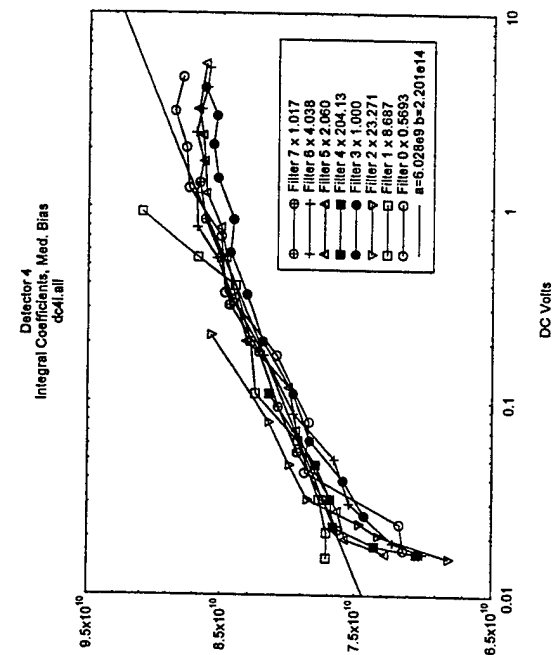
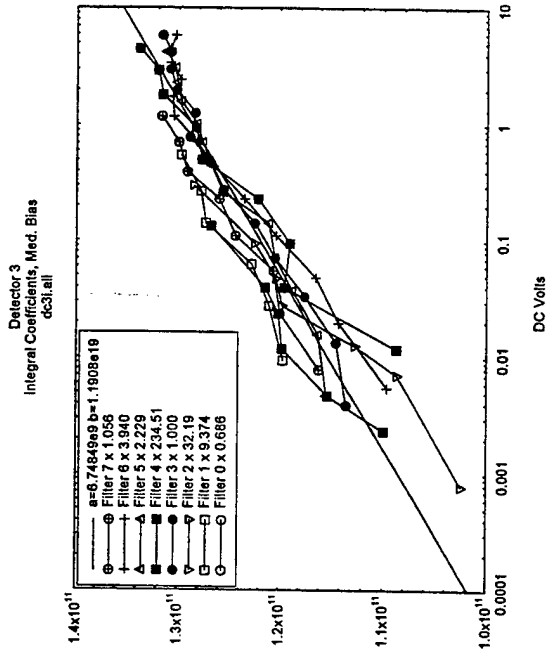
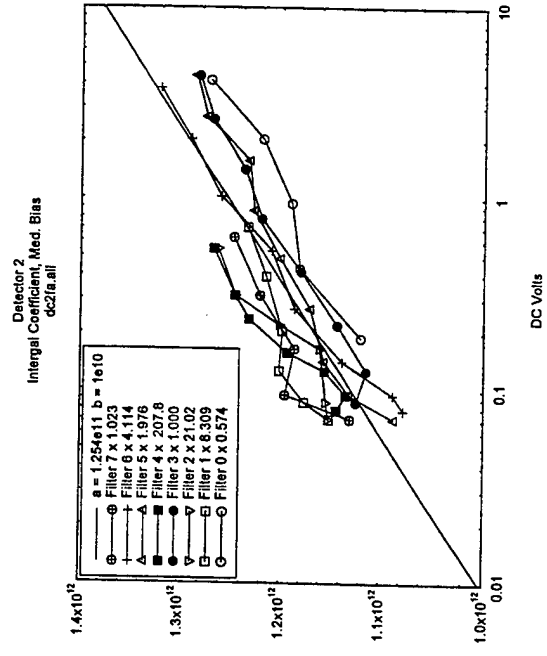
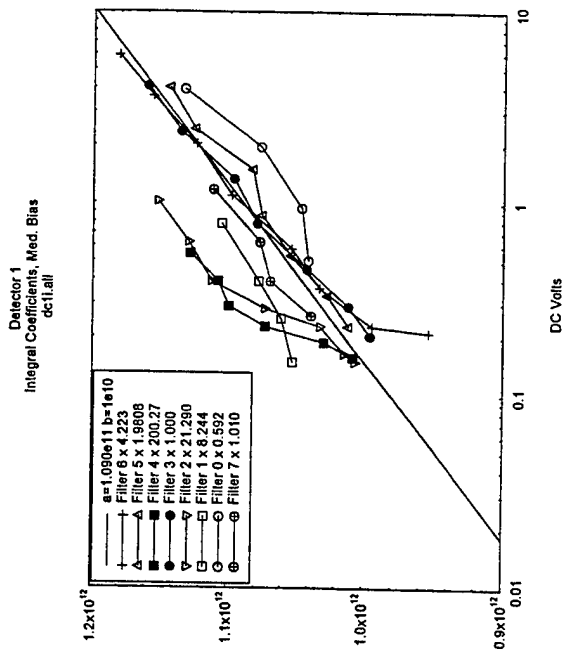


Figure 78. Absolute response coefficients with the single slope equation and offset developed for each detector.

### 4.2.3 Linearity

The interferometer must be calibrated over the entire dynamic range for which data are to be taken with each filter and detector. Some of the dynamic range-extending hardware induce nonlinearities in the output signal. These nonlinearities show up as harmonics (ghost spectra) in the transformed output. A linearity calibration was performed to determine if a transfer function can be developed for converting the actual response to an ideal linearized response throughout the interferometer dynamic range.

In the CIRRIS interferometer, nonlinearities arise from two sources. The first is the pre-amplifier. To correct the detector-preamp nonlinearities, the voltage at the preamp output must be recreated. Recreation of the preamp output requires the ac gain to be divided out and added back to the dc. After the dc has been subtracted, the ac gain is -1.75. Figure 79 is a block diagram of one of the CIRRIS interferometer signal conditioning electronics channels. The second, and most significant, source of nonlinear results from operating the detectors at a reduced bias voltage. CIRRIS used two bias voltages, 0.1 and 1 Vdc. This extends the dynamic range of the interferometer by a factor of three, but introduces noticeable non-linearity. The nonlinearity associated with the low (0.1 Vdc) bias is flux dependent, but unlike DRE, is a repeatable function of the ac voltage developed by the detector.

The total nonlinearity of the CIRRIS interferometer was measured using small signal, or ac/dc, linearity data, which are processed to provide the first derivative of the dc or absolute linearity function. The ac-dc linearity measurement technique is described in detail under radiometer Section 3.2.5.4. The measured ac-dc linearity is the first derivative of the dc linearity function. The physical measurement is made by providing a constant ac signal to the interferometer input while increasing the dc flux level in a step-wise fashion.

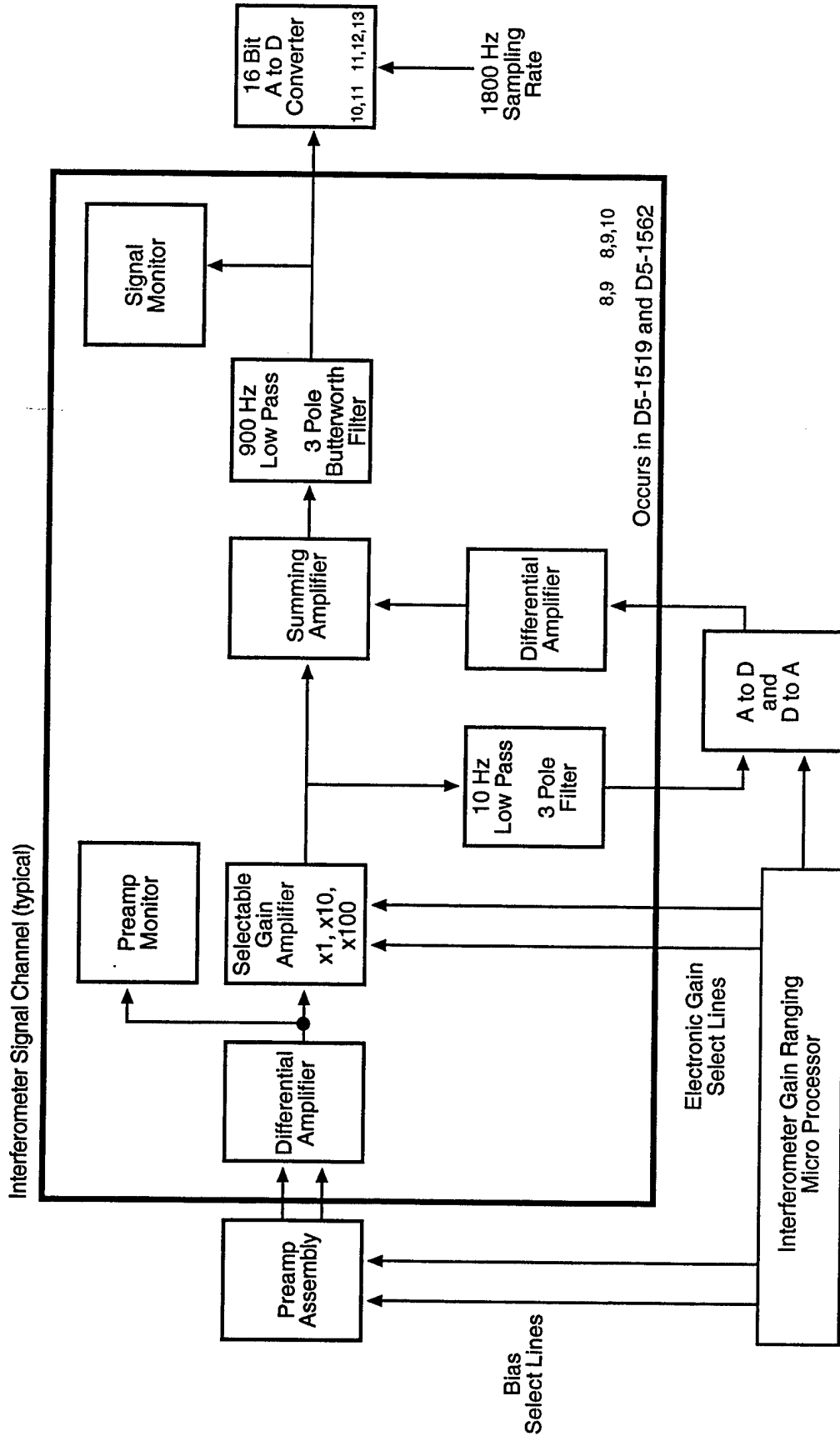


Figure 79. Block diagram of a typical CIRRS 1A interferometer signal conditioning electronics channel.

The ac-dc linearity was performed with the interferometer scan mirror stopped and an external sampling clock being input at 1500 Hz. A clock signal was also input for the retrace signal at 1/5 Hz. An external blackbody source set at 750 K modulated by an external chopper set at 90 Hz modulating provided the constant ac signal. The ac signal was input into the calibrator in the Jones source configuration. The extended-area source of the calibrator was also in position and provided the variable dc background flux. This configuration allowed the dc flux to be increased while holding the modulated flux constant. Figure 80 shows a typical modulated output response with the 25 mv p-p ac offset at the dc (-1.25 V) level.

Extended area source temperatures were chosen to provide approximately 3 data points per decade of response for each detector. The dc value used in the calculation was the dc reported by the CIRRIIS electronics for each channel. The ac values were calculated by Fourier transforming the data and integrating from 50 to 130 Hz. Figure 81 shows the integration band for a typical transformed response.

During the first phase of the post flight calibration, data sufficient to characterize detectors 3-3 and 3-4 low bias were collected. The data set was completed during the second phase. Figures 82 and 83 show the linearity results for detector 3-3, low bias. Figure 82 is the curve fit to the processed ac-dc linearity data and Figure 83 is the linearity correction function that results from the integration of Figure 82. The corrected response in Figure 83 is a piece-wise correction that assumes the sensor output is linear below the point indicated by a circle on the graph. This switch point was selected from correction function minimum of Figure 82.

Figure 84 shows a typical nonlinear interferogram for detector 3-3, filter 5, low bias, before linearization, and Figure 85 shows the interferogram after linearization. The circle is drawn around the center of the interferogram. The companding of the original interferogram is clearly evident. Figure 85 shows the significant improvement that results from the linearity correction. Figure 86 and Figure 87 are the transforms of Figure 84 and Figure 85, respectively. These figures show the harmonic distortion before and after correction. At medium bias, the noise included in the nonlinearity correction process appears to be about the same range as the nonlinearity. For this reason we have not recommended that the medium bias data be linearized.

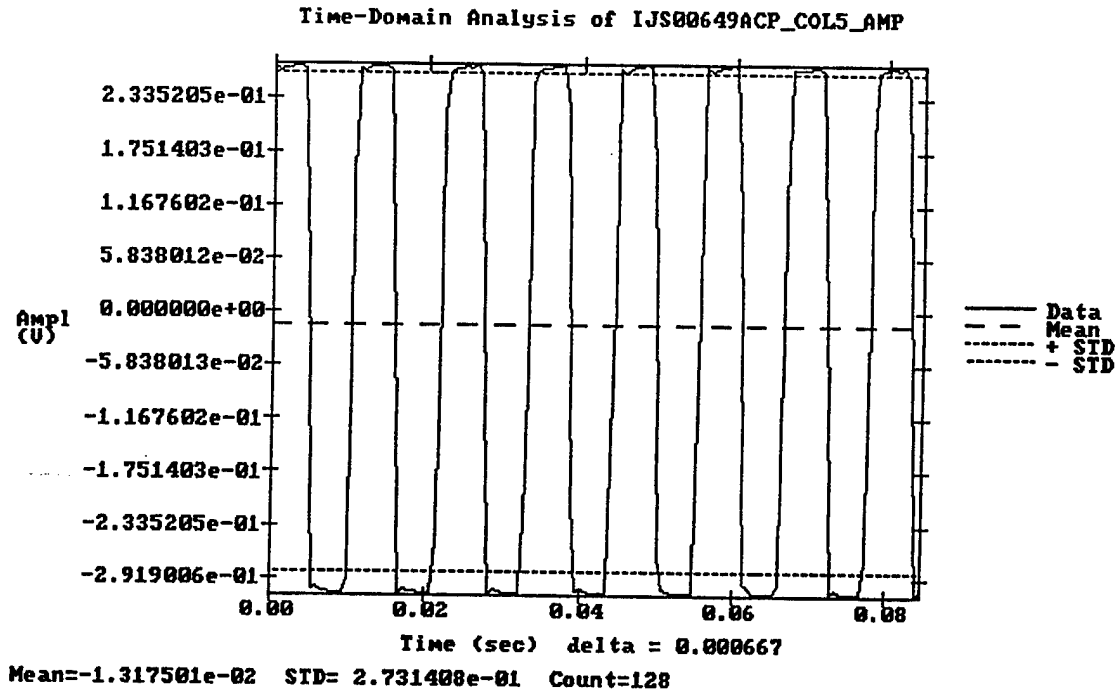


Figure 80. Typical modulated output response for a given dc offset.

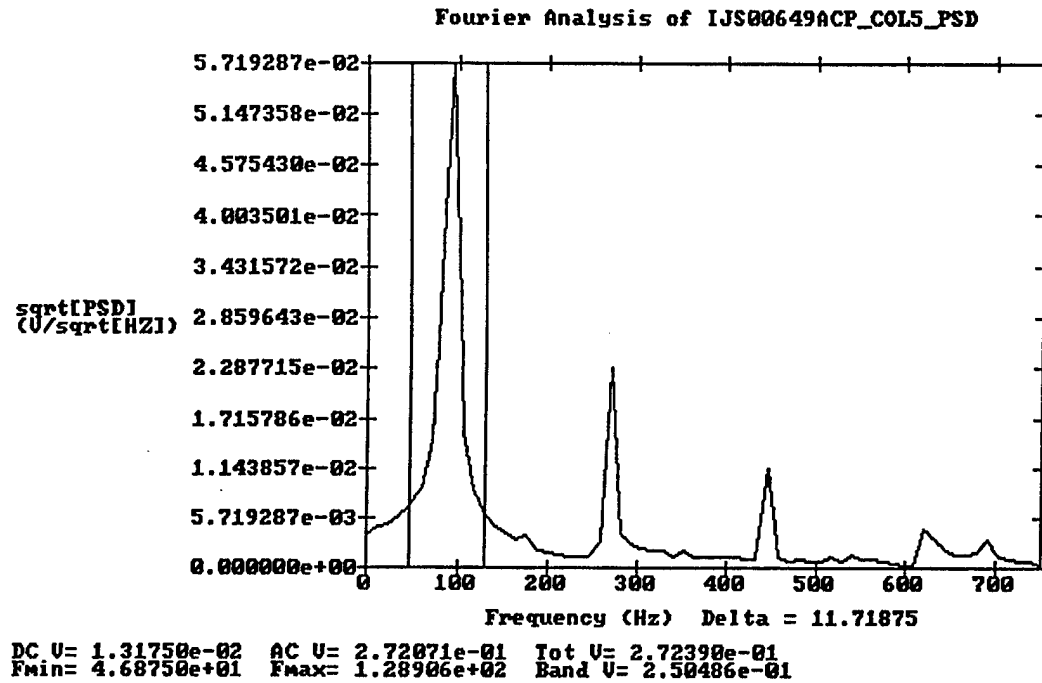


Figure 81. Integration band for a typical transformed response.

CIRRIS 1A IFR AC/DC Response  
 Detector 3, Gain L, Bias L

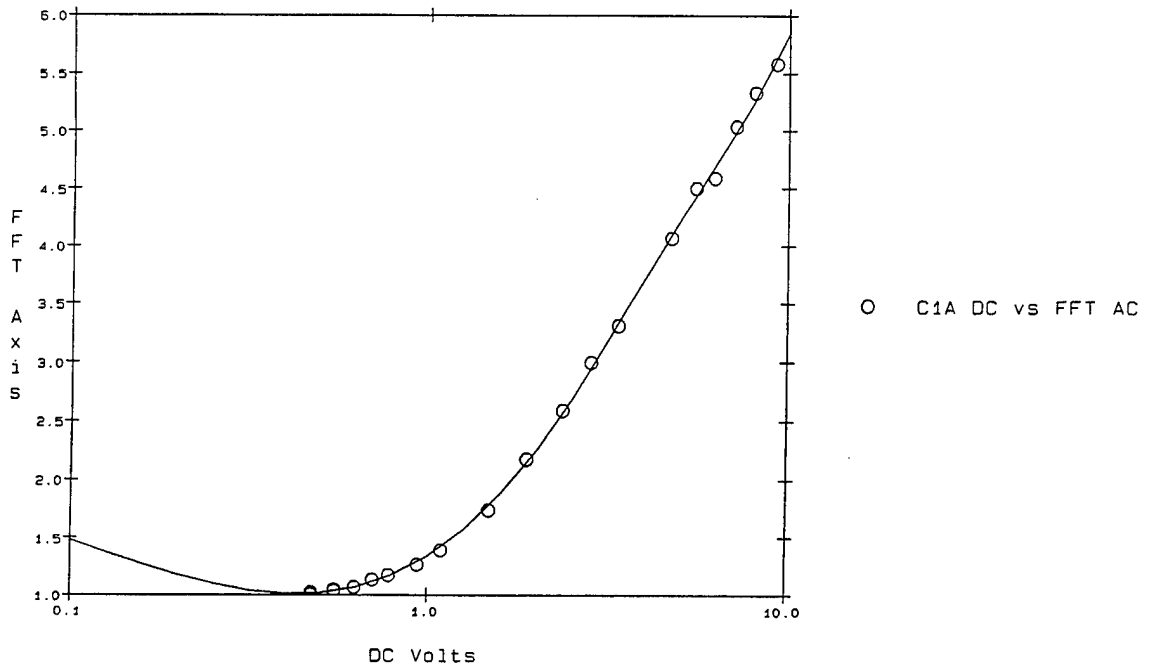


Figure 82. Linearity results for detector 3-3, low bias (raw data with line fit).

CIRRIS 1A IFR Linearization Correction  
 Detector 3, Gain L, Bias L

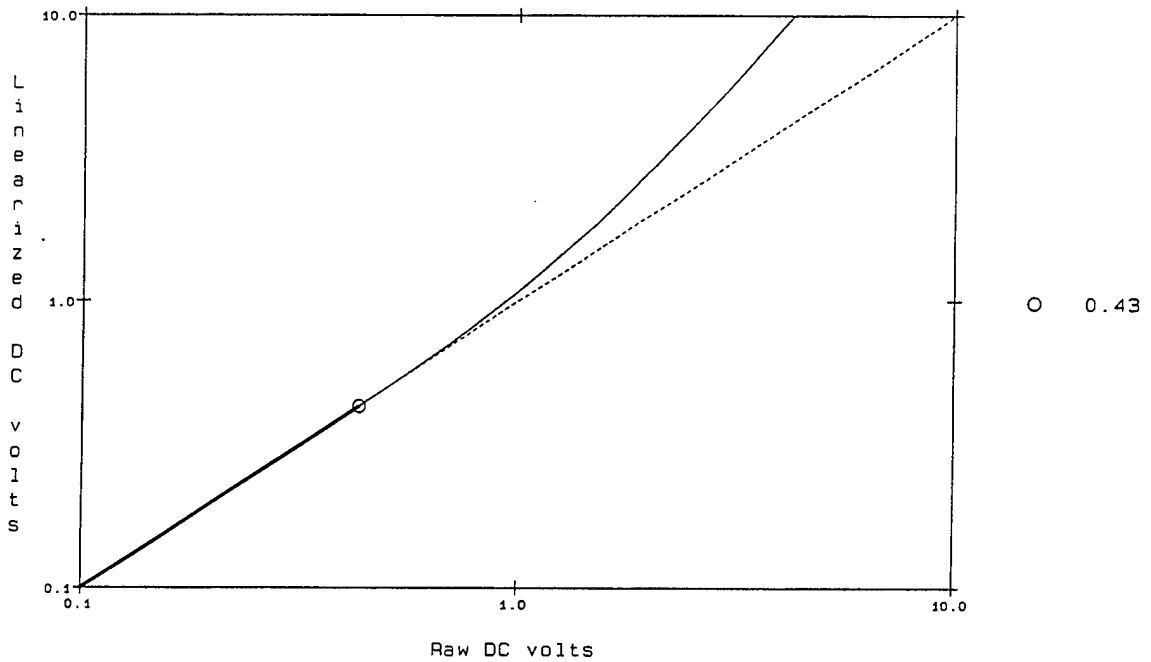
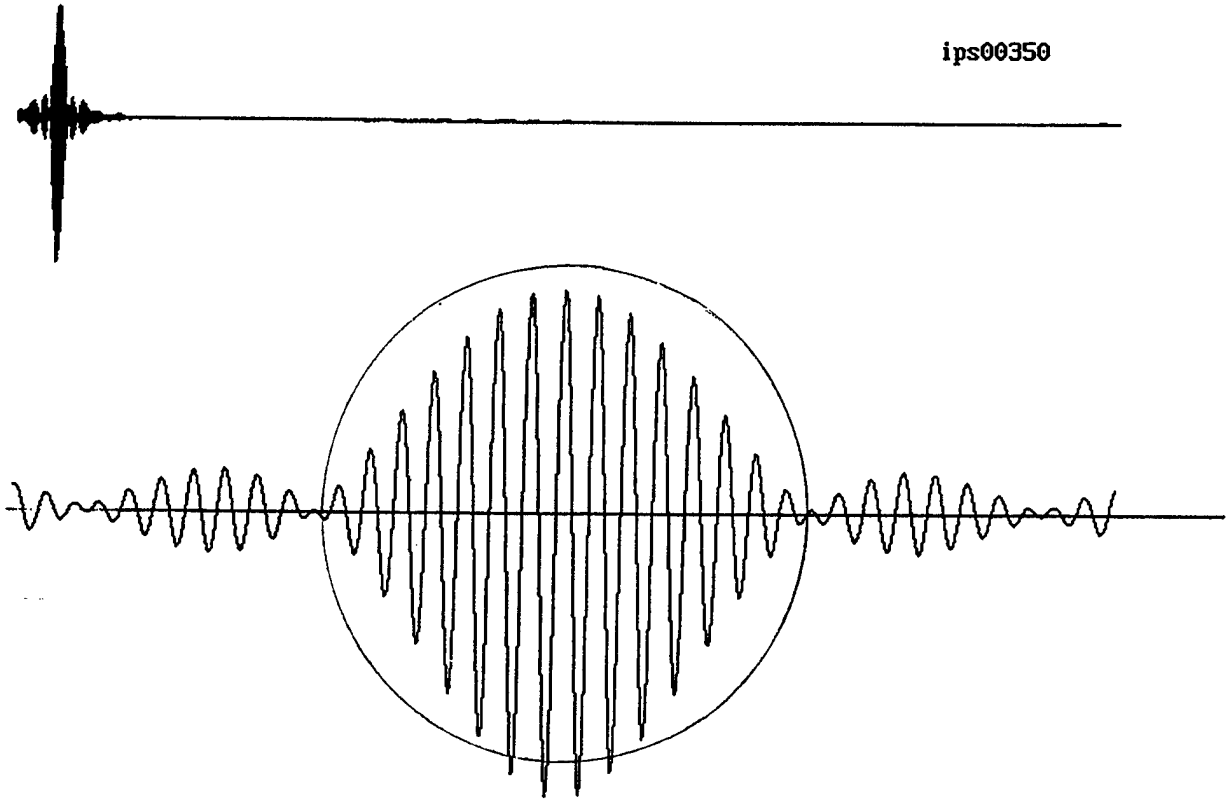


Figure 83. Linearity results for detector 3-3, low bias (linearity correction function).



ips00350



**Figure 84. Relative spectral response interferogram for detector 3-3, filter 5, low bias, before linearization.**

ips00350

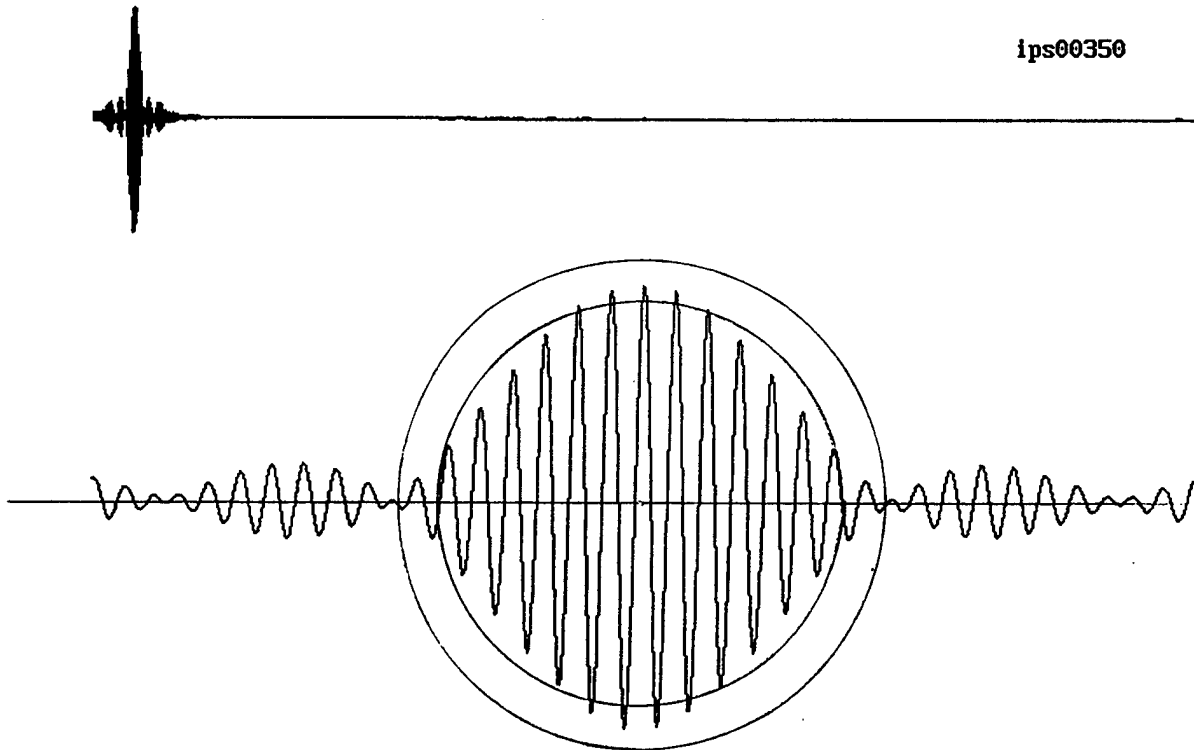


**Figure 85. Relative spectral response interferogram for detector 3-3, filter 5, low bias, after linearization.**

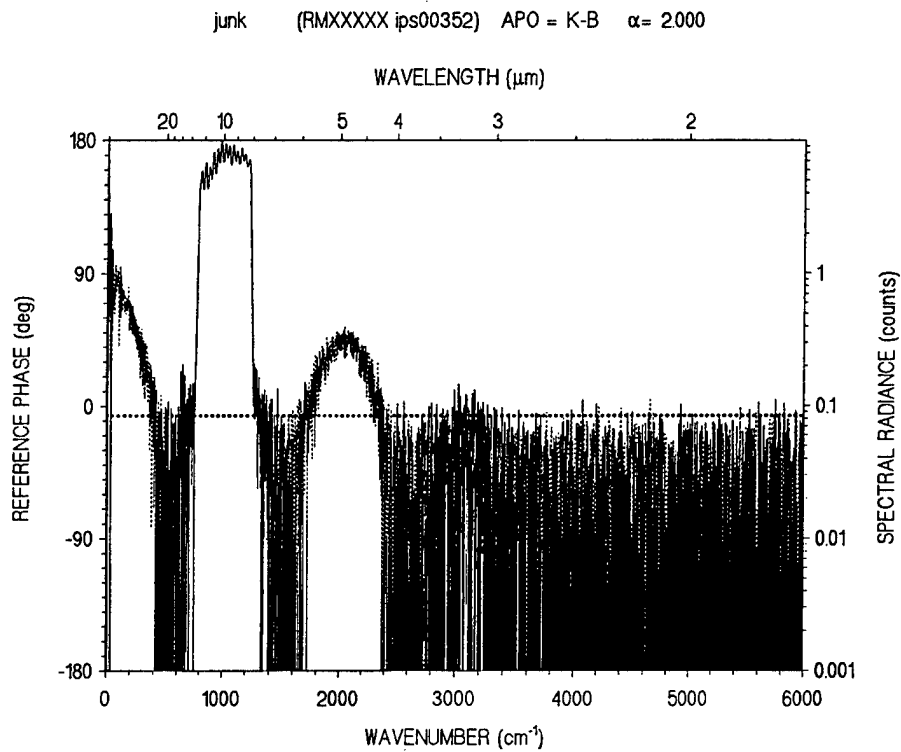


Figure 86. Transform of relative spectral response interferogram for detector 3-3, filter 7, low bias, before linearization.

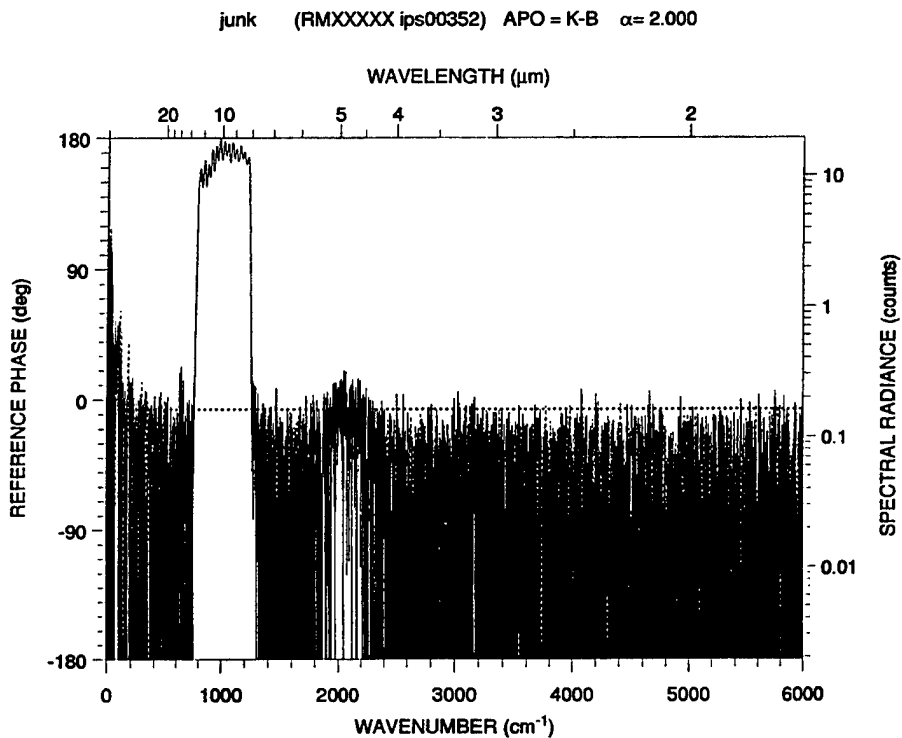


Figure 87. Transform of relative spectral response interferogram for detector 3-3, filter 7, low bias, after linearization. Note increase in signal in main peak, reduction in side lobes.

To linearize a low bias interferogram, the dc level must be added back to each point and the ac gain corrected. After the original preamp output signal has been linearized it must be restored to the interferogram format (an ac interferogram and a dc offset) to allow it to be transformed. This requires a new dc to be calculated and subtracted off, and the resultant (mean removed) interferogram to be multiplied by the ac gain. This process is given in Equation (26).

$$I_L(p) = -1.75 \left[ \left[ \text{Lin} \left( I(p) \left( \frac{1}{-1.75} \right) + DC \right) \right] - DC_L \right] \quad (26)$$

where

$$DC_L = \text{Mean} \left[ \text{Lin} \left( I(p) \left( \frac{1}{-1.75} \right) + DC \right) \right] \quad (27)$$

$I_L(p)$	=	linear interferogram as a function of position
$DC_L$	=	dc value of the linearized interferogram
$DC$	=	dc value of the original interferogram
$I(p)$	=	original interferogram as a function of position
$\text{Lin}$	=	linearity correction function

The original interferogram ( $I(p)$ ) is divided by -1.75 to correct for the ac amplifier gain. The dc value is added and the linearity function applied. The new dc value ( $DC_L$ ) is now calculated and subtracted from each point. Each point is then multiplied by -1.75 to return it to its original form.

The linearity correction function ( $\text{Lin}$ ) was developed by normalizing and fitting the ac/dc linearity data (Table 23) to an equation of the following form:

$$X' = A_1 + A_2 X^{0.5} + A_3 X + A_4 X^{1.5} + A_5 X^2 \quad (28)$$

This equation was integrated to obtain the linearity correction function in the form:

$$X' = A_0 + A_1 X + A_2 X^{1.5} + A_3 X^2 + A_4 X^{2.5} + A_5 X^3 \quad (29)$$

where

$X'$	=	linearized detector response (volts)
$X$	=	raw detector response (volts)

Near the noise floor of the system, it is assumed that the system is linear. A cross over point for the linearity correction function was obtained empirically for each equation.

The results of the AC/DC linearity calibration is given in Table 23 for each detector/bias/gain combination.

**Table 23. Linearity Coefficients for CIRRIIS 1A Low Bias Correction**  
 (Note: no flight data were collected with detectors 1 and 2, high gain; detector 5, low bias)

Detector, Gain, Bias	A <sub>0</sub>	A <sub>1</sub>	A <sub>2</sub>	A <sub>3</sub>	A <sub>4</sub>	A <sub>5</sub>	Switch Point
D1HM	No Data						
D1MM	0.000003	1.000000	0.000000	0.000000	0.000000	0.000000	10.0
D1LM	-0.000919	1.024941	-0.057591	0.029908	-0.017780	0.003229	0.1
D1LL	-0.005248	1.064699	-0.117469	0.068647	-0.022719	0.003040	0.3
D2HM	No Data						
D2MM	0.000001	1.000000	0.000000	0.000000	0.000000	0.000000	10.0
D2LM	-0.000720	1.030569	-0.091501	0.063081	-0.024517	0.003579	0.1
D2LL	0.000307	0.976955	0.104584	-0.147214	0.052371	-0.002898	0.1
D3HM	0.000000	1.000000	0.000000	0.000000	0.000000	0.000000	10.0
D3MM	-0.000278	1.007347	-0.009391	-0.018678	0.008842	-0.001181	0.1
D3LM	0.000253	1.010538	-0.044698	0.010728	0.000000	-0.000136	0.1
D3LL	-0.000528	1.742593	-2.558140	2.565346	-0.702372	0.068067	0.3
D4HM	0.000000	1.000000	0.000000	0.000000	0.000000	0.000000	10.0
D4MM	-0.001830	1.047785	-0.107450	0.054271	-0.017074	0.002212	0.2
D4LM	-0.000132	1.017148	-0.053830	0.011976	0.000000	0.000000	0.1
D4LL	0.013541	1.093760	-1.039931	1.716539	-0.462993	0.042742	0.2
D5HM	0.000000	1.000000	0.000000	0.000000	0.000000	0.000000	10.0
D5MM	-0.000779	1.020192	-0.100247	0.221484	-0.093775	0.011885	0.1
D5LM	0.000428	0.924746	0.326735	-0.366427	-0.141473	-0.017534	0.1
D5LL	No Data						

#### 4.2.4 Measurement Uncertainty

One of the goals of the CIRRIIS interferometer calibration is to estimate the sensor's measurement uncertainty. This section is provided to allow the analyst to estimate the uncertainty of any given in-flight measurement. This calibration report includes a list of possible uncertainty terms and an estimate of these uncertainties within the applicable calibration test discussions.

##### 4.2.4.1 Noise Response

The interferometer noise response was determined by measuring the dark noise and the signal-to-noise ratio over the dynamic range of the instrument for all bias/gain combinations. Dark noise

is the uncertainty of individual measurements at the minimum detectable signal level. It provides a useful diagnostic parameter to monitor system degradation. The dark noise measurement also provides a diagnostic check for light leaks in the calibration setup.

The noise level increases over the dynamic range of the sensor, because increasing flux also increases the photo noise in a measurement. The noise versus flux calibration characterizes short-term temporal measurement uncertainties for different levels of illumination. The objective of this calibration is to determine the smallest detectable modulation in a given spectrum.

#### 4.2.4.1.1 Dark Noise

To characterize the dark noise of the CIRRIS interferometer, the instrument was configured with CIRRIS filter 4 in place, and all sources off. Interferograms were collected and the standard deviation was calculated for each detector. The dark noise reported in this report is the standard deviation in volts divided by the electronic gains and the square root of the bandwidth. The resulting value is in units of volts per root hertz. Because of the difficulty in establishing the zero path difference (ZPD) with no signal present, electronic signal noise provides a more convenient way to track interferometer noise levels. These dark noise measurements are related to NESR in Section 4.2.4.1.3.

The dark noise of the CIRRIS interferometer was measured throughout the history of its testing, integration, flight, and calibration. Figure 88 shows the dark noise history for interferometer detector 3-3. Dark noise histories for all of the interferometer detectors are in Volume 2. These figures show that the dark noise was relatively stable for all detectors throughout the testing period, on orbit, and during the final calibration.

The dark noise interferogram of the CIRRIS interferometer was influenced by a non-modulated light leak occurring inside the interferometer itself. The light leak is attributed to thermal energy from a resistor on the cold preamplifier. The amount of energy scattered into the detectors is dependent on scan mirror position causing a drift in the dc level of two of the detectors. The dc drift is attributed to this light leak results in a larger standard deviation in dark scans for detectors 3-1 and 3-2. This drift has very low ( $>0.5$  Hz) frequency components and therefore transforms outside of the spectral response of the instrument.

The dark noise (short term uncertainty) of an interferometer channel can also be determined by measuring the standard deviation of the signal outside of the passband region and between any regions of harmonic distortion. Since the noise is assumed to be white (contains all spectral frequencies), the same noise level is assumed to exist in the passband region of the sensor. Transform-to-transform variations of the noise equivalent radiance of the sensor were determined for 10 consecutive interferograms collected during the postflight calibration while the interferometer was looking at a 30 K extended source. The 30 K source is below the resolution capability of the CIRRIS interferometer and is equivalent to a dark noise measurement. The average of these standard deviations, and the minimum and maximum standard deviation of the measurements are shown in Table 24. These values represent the smallest signal that can be detected by each channel in the CIRRIS interferometer.

**Table 24. Transform to Transform Variability of 10 Consecutive Interferograms Collected with a 30 K Extended Source**

Detector No	Average $\sigma$ volt $\times$ sample	Minimum $\sigma$ volt $\times$ sample	Maximum $\sigma$ volt $\times$ sample
3-1	0.0221	0.0216	0.0232
3-2	0.0125	0.0122	0.0128
3-3	0.00831	0.00755	0.00842
3-4	0.00614	0.00600	0.00636
3-5	0.00135	0.00123	0.00150

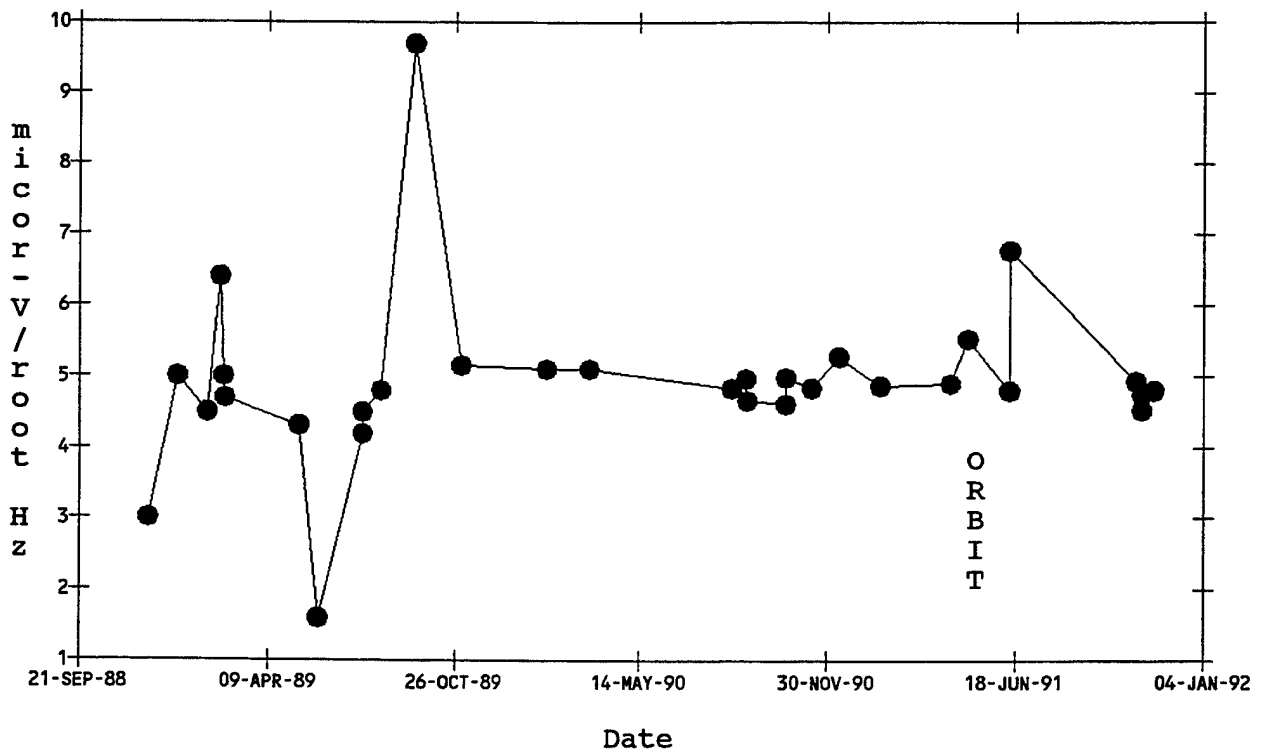


**Figure 88. Dark noise history for interferometer detector 3.**

#### 4.2.4.1.2 Dark Offset

The dark offset of each detector in the CIRRIS interferometer was measured by tracking the dc offset during each dark noise data collection. The data were logged in a dc offset history which was kept throughout testing, integration, flight and calibration of the CIRRIS instrument. Figure 89 shows the offset history for interferometer detector 3-3. Offset histories for all of the interferometer detectors are in Volume 2. Discrete jumps due to bit noise is evident in these figures. The offsets on the detectors, with the exception of detector 3-3, were fairly stable throughout the testing period. Detector 3-3 showed some instability. The dark offset is influenced by the same internal light leak that influences the dark noise. Because the absolute coefficients are tied to the dc level of the interferogram, variations in this light leak add slightly to the uncertainty of the radiometric value of measurements near the noise floor of the interferometer, especially for detectors 3-1 and 3-2, where the light leak has the largest influence. The instability evident in detector 3-3 may also add to the uncertainty of faint measurements on that detector.

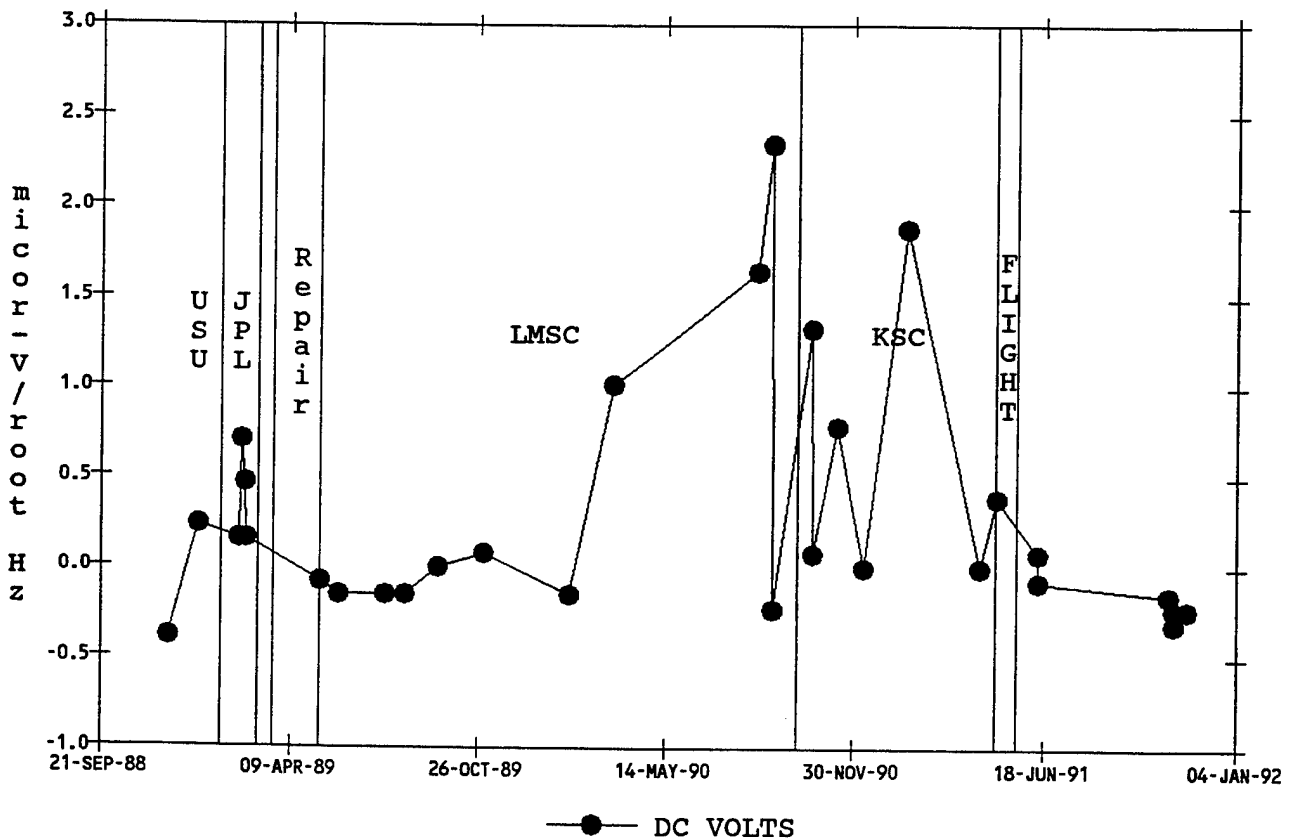


Figure 89. Offset history for interferometer detector 3.

#### 4.2.4.1.3 NESR over Dynamic Range

The minimum detectable signal from the CIRRIS interferometer, the NESR, was calculated by transforming a representative long scan of a 30 K extended source file collected with filter 0, the open filter. The 30 K source is below the interferometer sensitivity and showed no observable energy in the transform. The noise transform was divided by the appropriate RSR and absolute coefficient to convert the file to equivalent absolute radiance. The absolute value of the phase-corrected real transform was then plotted and a 200 point running median calculated to develop a smoothed NESR curve for each detector. An example of the calibrated noise transform and the median curve is shown in Figure 90, with units of  $\text{cm}^{-1}$ . Plots of the NESR for each detector are shown in Figure 91, with units of  $\mu\text{m}$ . The NESR for the interferometer is a function of wavelength, dominated by the detector response curve. In the open filter position, the curve assumes the shape of the inverse of the detector response curve. This shape is evident in Figure 90. The detector size, vignetting, and channel noise level all contribute to the NESR of the system calculated in this fashion. Where a narrow bandpass filter is included in the optical path, the NESR assumes the shape of the inverse of the RSR, touching the filter 0 NESR curve when at the RSR peak.

The dark noise and dark offset uncertainty only determine the spectral uncertainty at the bottom of a sensor's dynamic range. At higher flux levels, other noise sources, such as photon noise and analog-to-digital (A/D) converter noise, must also be considered. The noise versus flux measurement is an indication of the effect of increased flux on the noise.

Noise versus flux for the CIRRIS interferometer was calculated from Jones source data. A complete aperture set of Jones source data was collected at several temperatures. These data along with some extended-area source data were transformed; the standard deviations were then calculated for an area of the transform outside of the filter bandpass and between any areas that contain harmonics of the fundamental. Figure 92 is the transform of detector 3-2 filter 5 data, and indicates the area of the spectrum that was used to calculate the standard deviation of the out-of-band noise.

Figures 93 and 94 show the standard deviations versus flux for the regions indicated in Figure 92. Each curve in Figure 93 indicates a different bias gain combination. Figure 94 presents the data adjusted for electronic and bias gain. Figure 94 clearly indicates a consistently increasing noise level with increased flux and has the  $\sqrt{X}$  shape which is characteristic of photon noise.



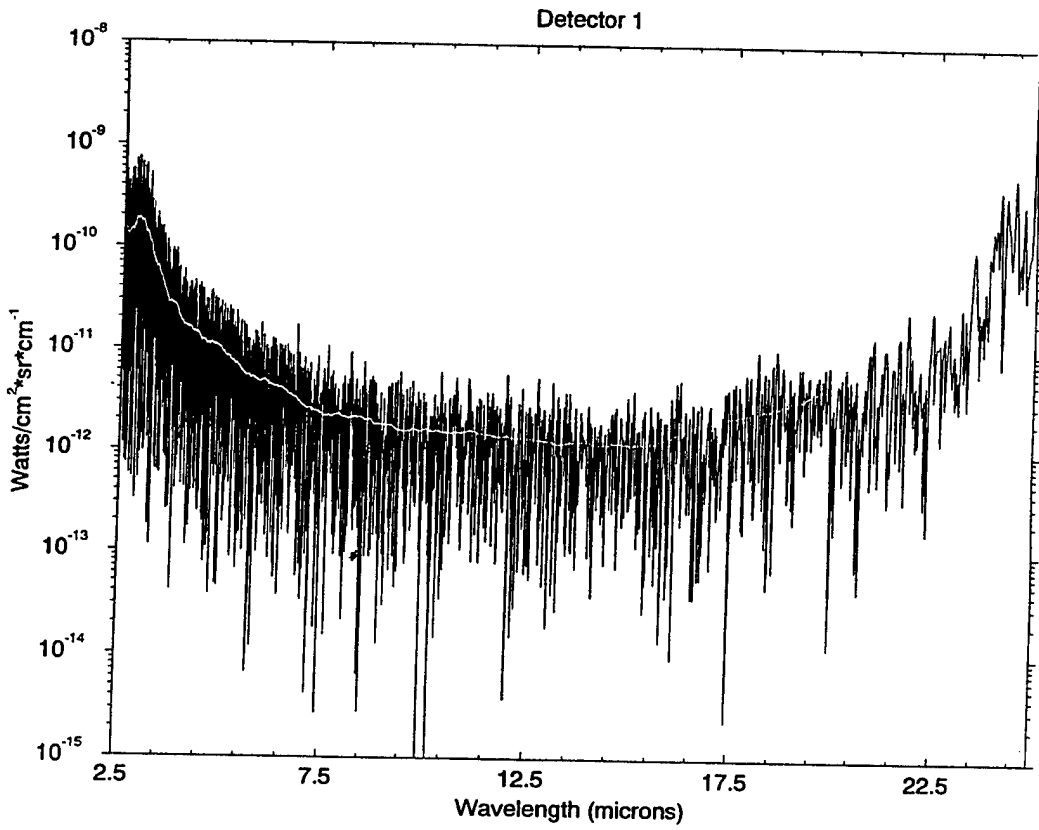
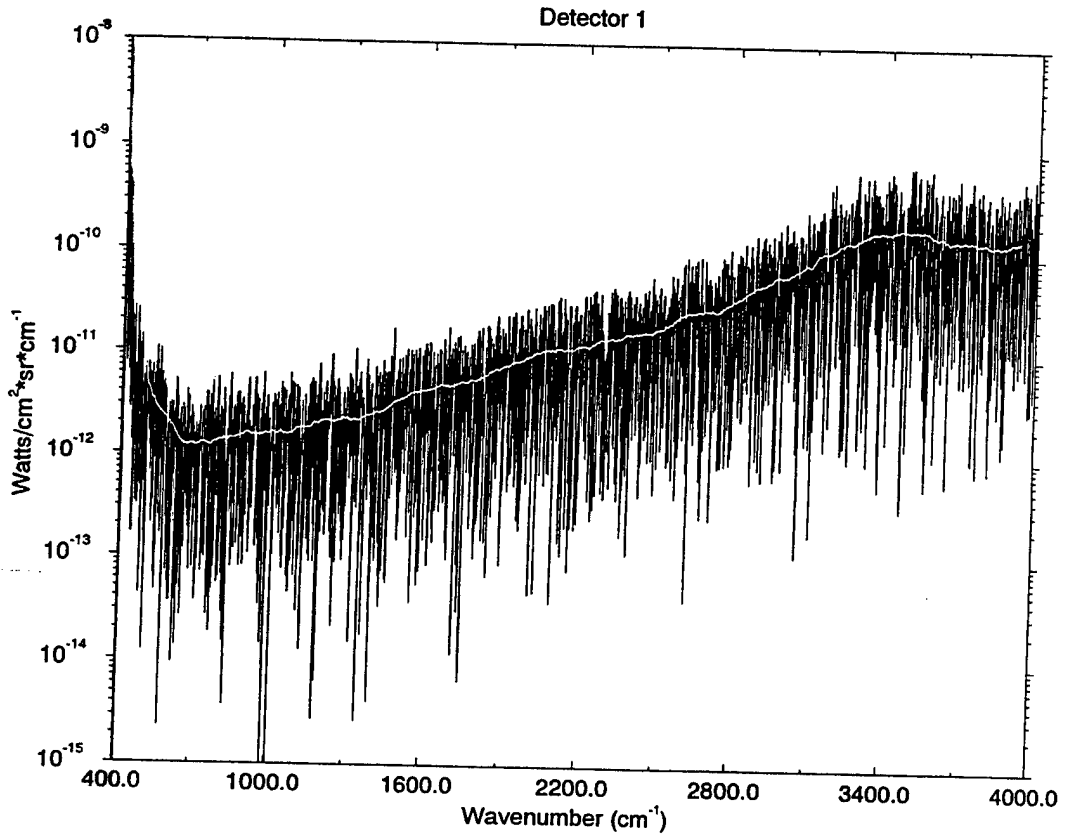


Figure 90. Calibrated noise transform and medium curve examples.

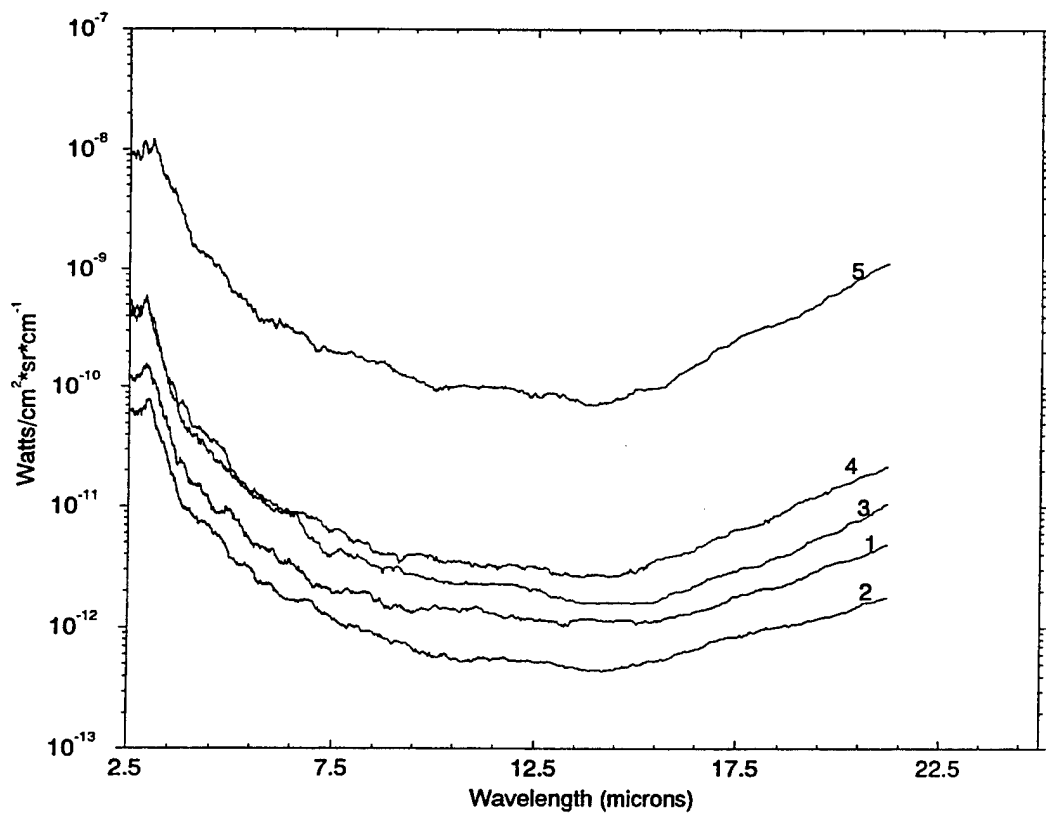
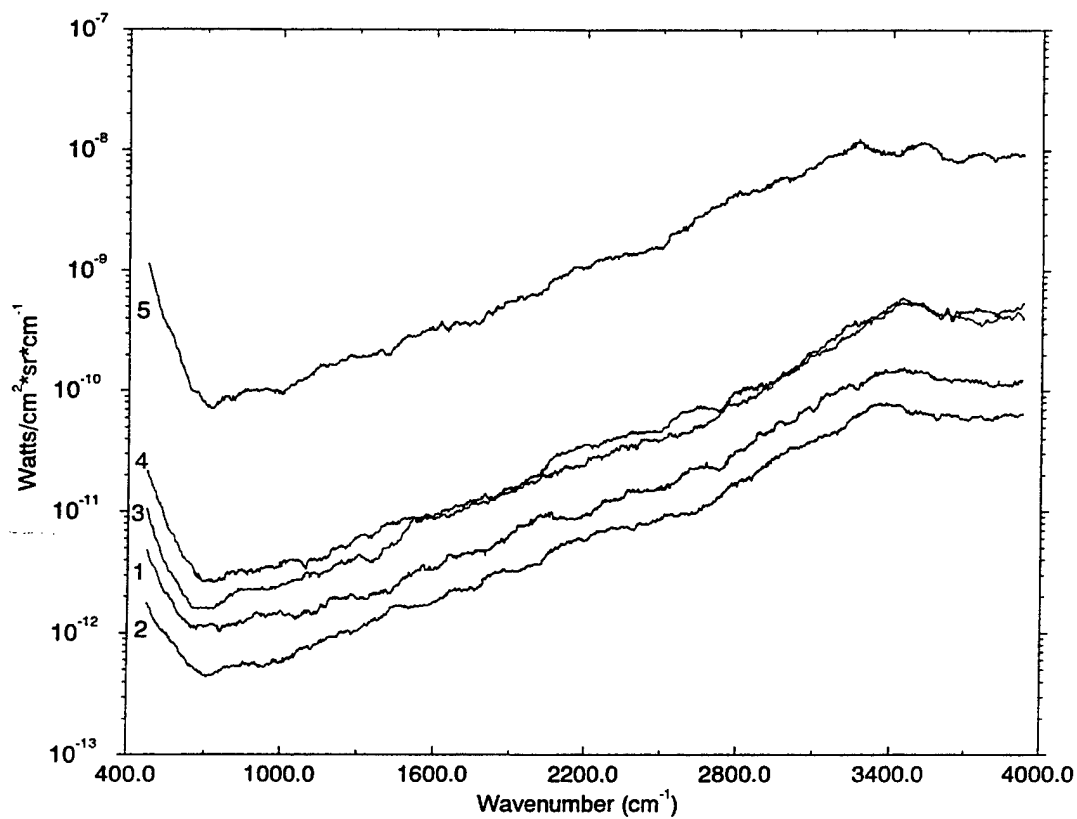


Figure 91. NESR plots for each detector.

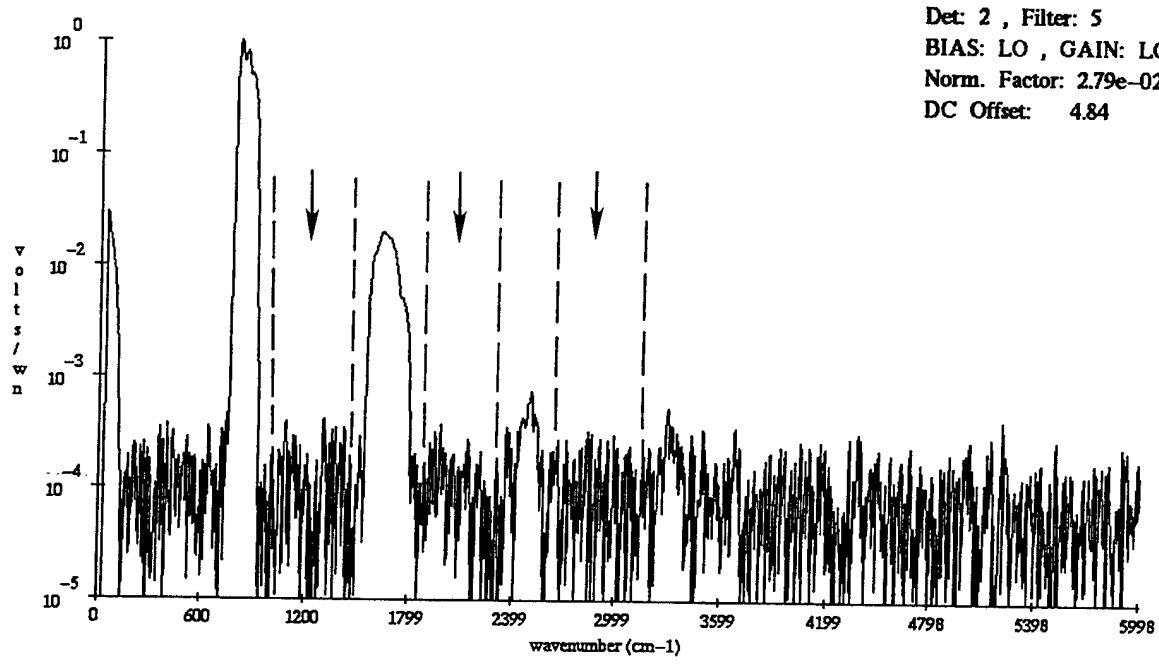


Figure 92. Areas of the spectrum used to calculate the standard deviation of the out-of-band noise, detector 3-2, filter 5 data.

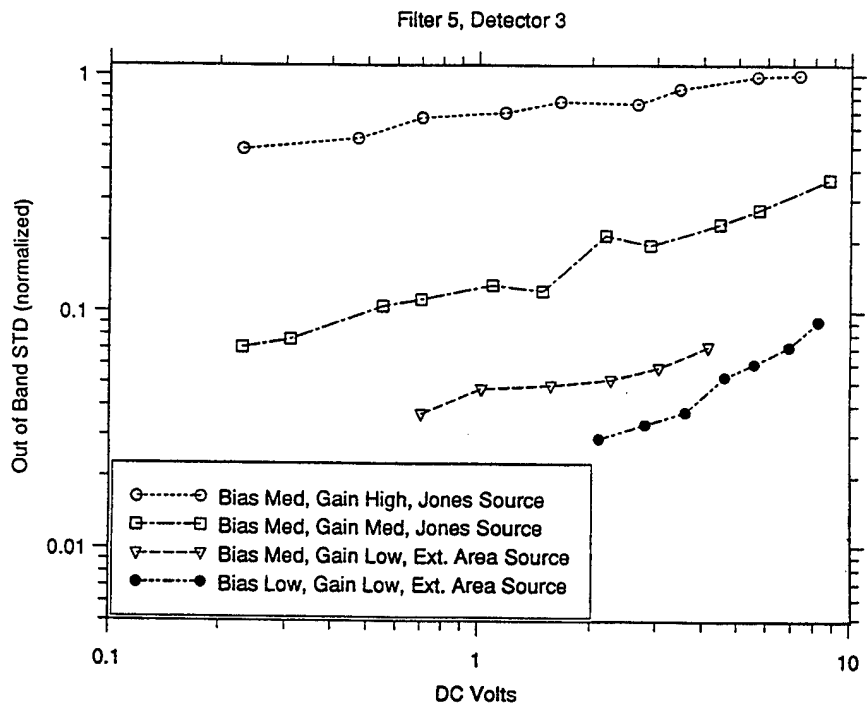
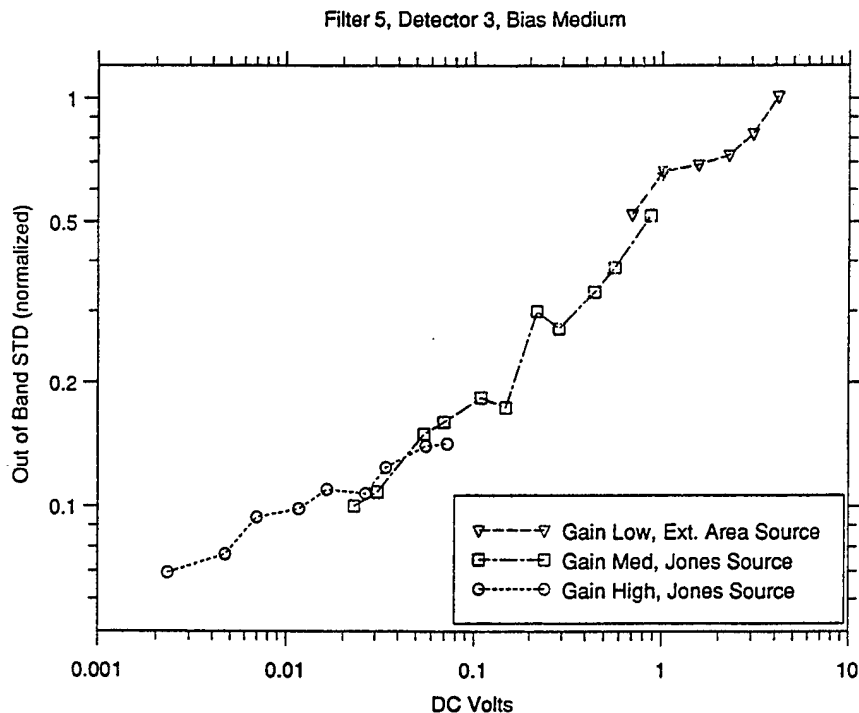


Figure 93. Standard deviation versus flux for the region indicated in Figure 92 (individual range).



**Figure 94. Standard deviation versus flux for the region indicated in Figure 92 -- data adjusted for electronic gain.**

Figure 95 shows the noise versus flux for all detectors in medium bias. All electronic gains were adjusted for in this figure. This clearly indicates a consistently increasing noise level with increased flux and the similarity between channels. The noise level for detector 3-5 is almost an order of magnitude lower due to its lower sensitivity. In order to get the same dc level as the other detectors, detector 3-5 requires a flux level about two orders of magnitude higher. The photon noise is proportional to the square root of the signal. Figure 96 shows the noise versus flux corresponding to low bias. Because of the low gain of detector 3-5, it could not be calibrated in low gain using the Jones source.

The photon noise from the strong emitters in the CIRRIS earthlimb scans is eliminated by narrow bandpass filters, allowing an improved SNR to be applied to the window regions between the emission bands. Despite the low NESR of the interferometer detectors, the signal to noise ratio in any given scene will seldom exceed 1000/1 because of photon noise.

#### 4.2.4.1.4 Interferometer Calibration Light Leak Analysis

Under normal operating conditions and during dark noise offset measurements, detectors 3-1 and 3-2 have relatively large dark offsets (dc). The dc offset voltage of these detectors has a drift that is thought to be a light leak from the focal plane heaters. Since this signal is not modulated by the interferometer, it is only evident as a drifting dc offset in several detectors and at frequencies that transform below the detector cutoff ( $400 \text{ cm}^{-1}$ ). The result of this light leak is an

increased NESR (raised noise floor-same sensitivity) of the interferometer for detectors 3-1 and 3-2. Detectors 3-1 and 3-2 do not drop into the high gain medium bias state because of this light leak, limiting the NESR @  $1000 \text{ cm}^{-1}$  to about  $5 \times 10^{-11} \text{ (W/cm}^{-2} \text{ sr cm}^{-1}\text{)}$ . For signals stronger than the minimum sensitivity imposed by this light leak the calibration is not affected.

During calibration another light leak was observed. At that time, CIRRIS personnel could not positively determine whether this was the result of energy radiating out of CIRRIS and being reflected back into the instrument from the calibrator, or whether the energy originated from the calibrator. During the SPIRIT III calibration, the source of this energy was tracked to warm components within the MIC2 calibrator. However, because the signal was modulated by the interferometer, the signal was present in all of the measurements made with the extended source retracted. Calibration personnel investigated its impact on the calibration, and any uncertainties that it added to the CIRRIS measurements. Because this light leak is not observed when the MIC2 extended source is extended, the leak does not affect the absolute calibration of the interferometer or radiometer.

An effort was made to determine whether the light leak was also affecting the extended area source data. Several sets of data were taken while looking at a cold extended area source. These data indicate that no energy was being directed into the interferometer from MIC2 while the extended area source was being used.

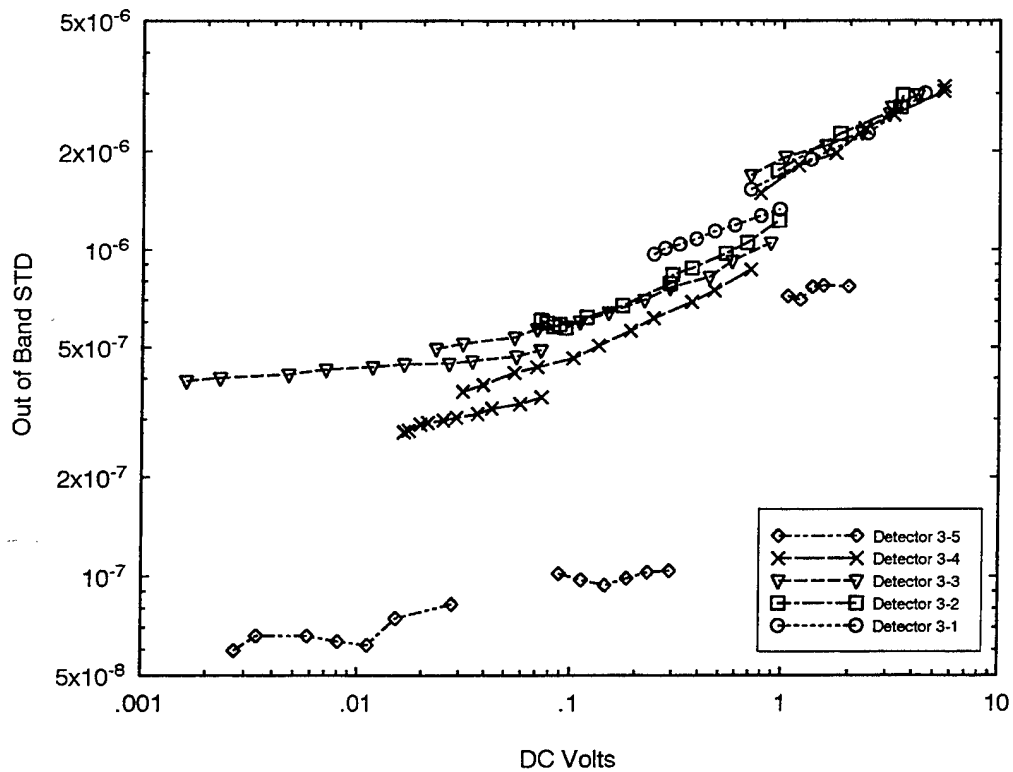


Figure 95. Noise versus flux for all interferometer detectors, medium bias.

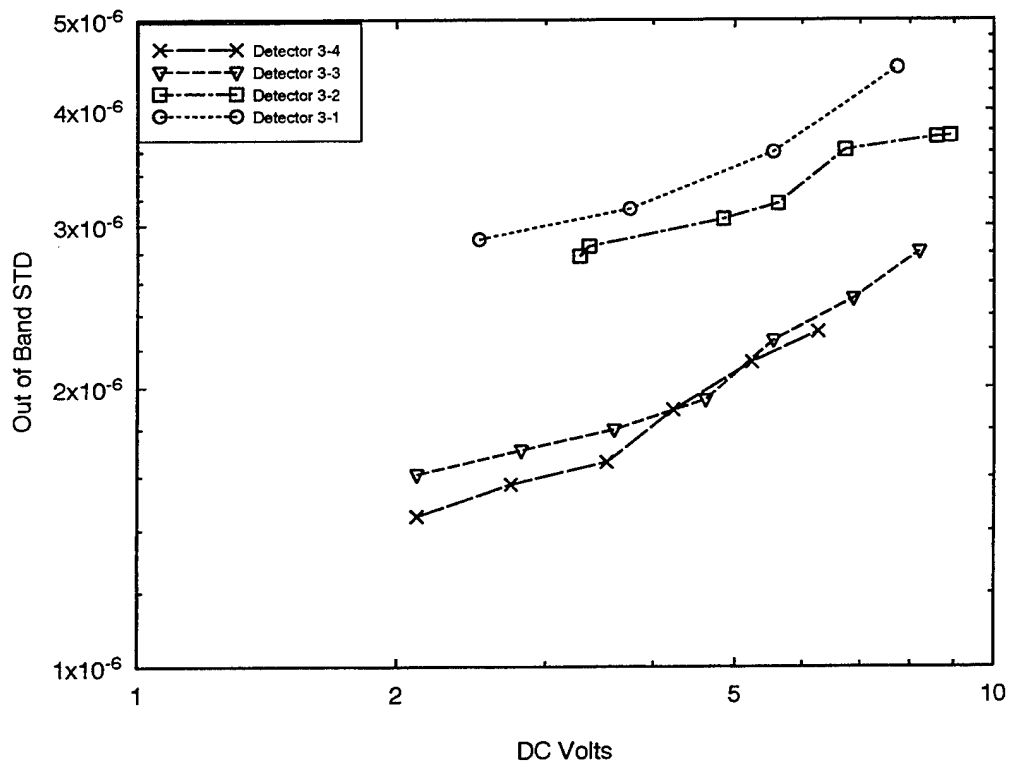


Figure 96. Noise versus flux for interferometer detectors, low bias.

Because the light does not enter CIRGIS with the extended source deployed, the only effect of the leak would be in the development of the RSR curves. To evaluate the effect of this light leak on the RSR calibration, data were taken for detectors 3-1 and 3-2 with the interferometer filter 0 in place, the calibrator aperture closed, and the scatter plate in place. Filter 0 is actually no filter, allowing all wavelengths to enter. Shutting the aperture eliminates external energy from entering the calibrator. Extending the scatter plate places a known, full aperture surface in the CIRGIS field of view. The results are compared to the reference interferogram data for filter 0, detectors 3-1 and 3-2. The reference interferogram data for this filter/detector condition were taken with the scatter plate in place. The light leak has a spectral signature corresponding to a 80 K blackbody.

Each interferogram was transformed using both the IDAS processing software and the ARC processing software. The transforms were then imported into RS1 tables so that the data could be analyzed. Figure 97 shows (a) the transforms of the reference interferograms, (b) the light leak corresponding to a small 80 K grey body, and (c & d) a corrected curve which is the reference transform with the light leak transform subtracted on a point-by-point basis for detector 2. These figures show that the light leak error in the RSR is below 1% above  $700 \text{ cm}^{-1}$ . This error is expected to be evident in the filter 0 and filter 6 data. The leak was not measured using filter 6, but since filter 6 is a long pass filter, the size of the error is expected to be similar to that measured in filter 0 in the  $400 - 500 \text{ cm}^{-1}$  region. Because of the reference interferogram method used to calculate the RSRs, correcting this error in OPUS is not easy and has not been implemented.

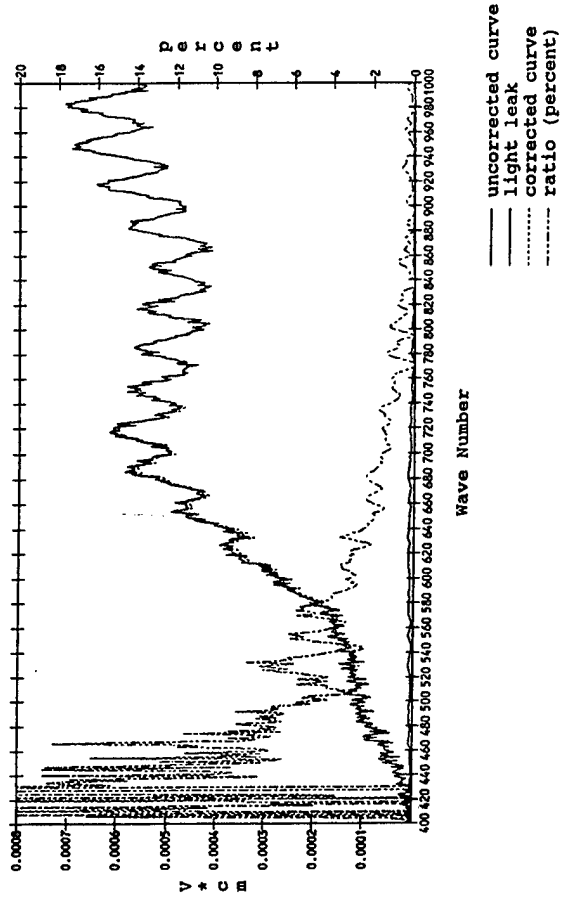
Tables 25 and 26 are subsets of the data tables. Column 0 of both tables lists the RS1 table name containing the data and indicates the process used to perform the transform and the detector number. Table 25 is a comparison of the relative response data at the wavenumber where the light leak spectrum is at its maximum. Column 1 indicates the wave number where the maximum was found. The reference spectrum value at the same wave number is in column 3 and the percent difference is found in column 4. This indicates that at approximately  $686 \text{ cm}^{-1}$  for detector 3-1 and approximately  $632 \text{ cm}^{-1}$  for detector 3-2 the error is around 2%.

Table 26 shows the maximum value of the reference spectrum for each process in column 3. This table is a comparison of the relative response data at the wavenumber where the reference spectrum is at its maximum. The value of the light leak spectrum at the same wavenumber is listed in column 2. In this case, at  $979 \text{ cm}^{-1}$  and  $968 \text{ cm}^{-1}$  for detectors 3-1 and 3-2 respectively, the error caused by the light leak is around 0.2%.

Detector 2  
Light Leak and Corrected Spectrum  
ARC



Detector 1  
Light Leak Corrected Spectrum



Detector 2  
Light Leak Corrected Spectrum

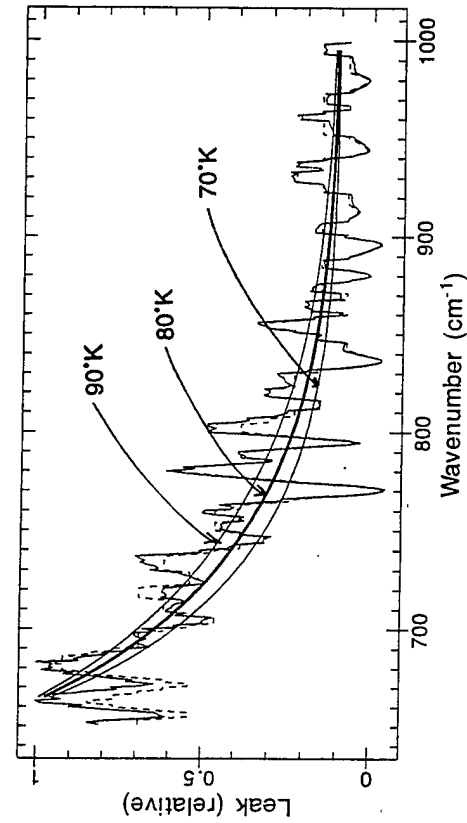
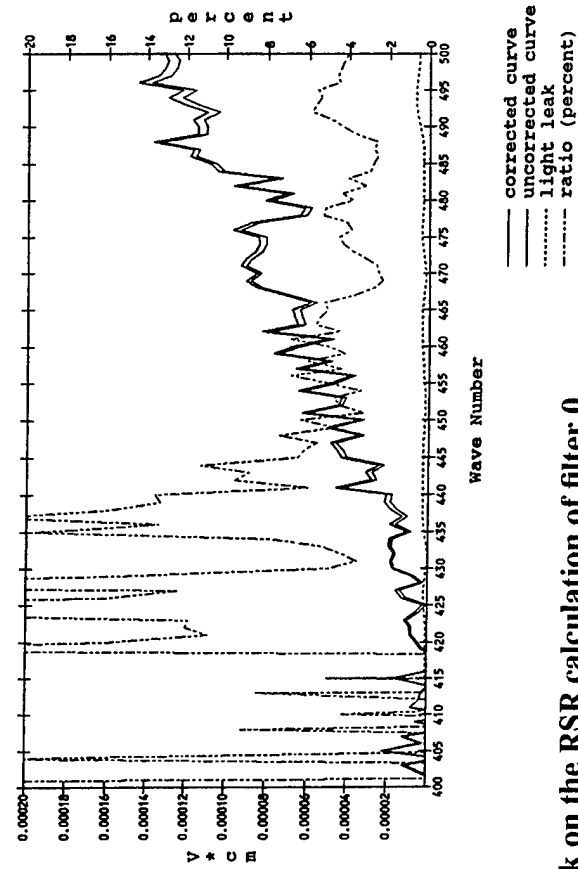


Figure 97. The effect of the MIC2 light leak on the RSR calculation of filter 0.



**Table 25. Relative Response Data at Maximum Light Leak Spectrum**

File	Wavenumber	Maximum (leak)	Reference Value	Percent Difference
ARC1	686.5342	0.091289	4.490003	2.033163
ARC2	632.5371	0.065994	4.064070	1.623851
IDAS1	686.5340	0.000112	0.005810	1.925990
IDAS2	632.5370	0.000084	0.003610	2.339298

**Table 26. Maximum Value of the Reference Spectrum**

File	Wavenumber	Leak Value	Maximum (Reference)	Percent Difference
ARC1	979.6611	0.009569	5.338156	0.179257
ARC2	968.0903	0.010851	6.020116	0.180251
IDAS1	983.5180	0.000015	0.006922	0.213232
IDAS2	983.5180	0.000014	0.006922	0.196345

As a result of these studies, SDL/USU personnel concluded that the throughput of the light leak present during calibration was relatively small, accounting for approximately 2% of the flux at the maximum flux peak of the light leak spectrum and 0.2% of the flux at the maximum flux peak of the reference signal using the scatter source. This could contribute a small amount to the uncertainty in long wavelength measurements. The effect of this light leak on the filter 6 and filter 0 RSRs is shown in Figure 97.

#### 4.2.5 Interferometer Processing Software Verification/Comparison

The spectral frequency, relative spectral responsivity and absolute responsivity calibration measurements used in the OPUS software were processed using software provided by Atmospheric Radiation Consultants, Inc. (ARC). However, all of the CIRRIS interferometer ground test data were processed with the Interferometer Data Acquisition System (IDAS) software, developed by SDL. As part of the calibration process, SDL/USU personnel performed a comparison between the two software packages to verify that the resultant measurements were similar.

##### 4.2.5.1 Frequency (Wavelength) Verification

Unlike a prism or grating spectrometer, an interferometer does not require frequency calibration. The CIRRIS interferometer sampling is controlled by a 632.992 nm laser which is passed through the same optical path as the IR light. The interferogram of laser light is a sine wave which peaks for each 632.992 nm of optical path length difference. Given evenly spaced data around and across the point of zero path length difference, the only thing that can affect the accu-

racy of the frequency data is an error in the transform process. To determine how accurately each of the two processing methods calculated the frequency of a particular feature in the spectrum, a calibration interferogram containing the interferometer output from a Helium-Neon laser with a wavelength of  $3.391\mu\text{m}$  was processed. The purpose was to determine which, if either, of the processes placed the laser emission line correctly in the spectrum. The results of each transform method are shown in Figure 98.

Both systems transform the laser line at the same location, when its sampling wavelength is properly represented ( $632.992\text{ nm}$ ). CIRRIS wavelength resolution was also verified by inserting a methane absorption cell in the path between the high temperature blackbody and MIC2. Figure 99 shows the comparison between two of the  $\text{CH}_4$  absorption lines measured by CIRRIS and line location predicted by FASCOD3 using the HITRAN92 database.

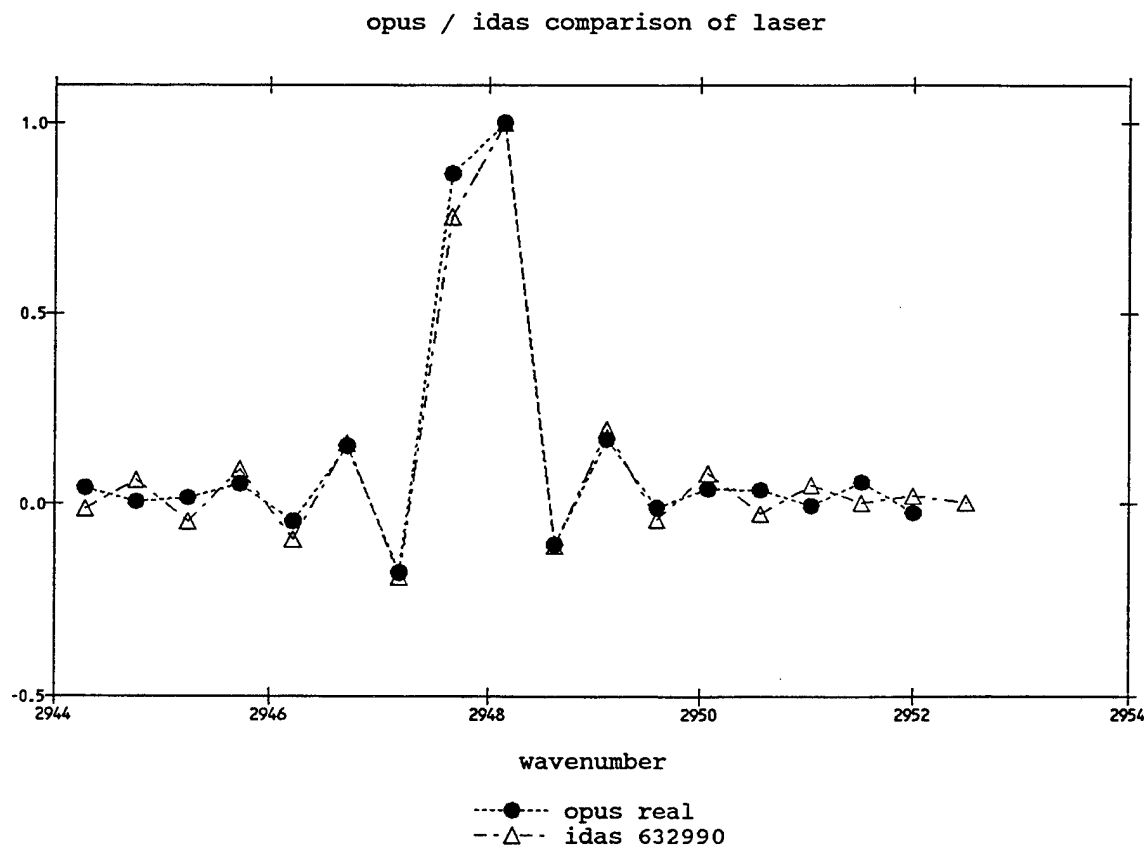


**Figure 98.** Comparison of the ARC and IDAS software transforming the  $3.391\text{ laser line (}2948.12\text{ cm}^{-1}\text{ in vacuum)}$ .

methane absorption cell (300 torr)

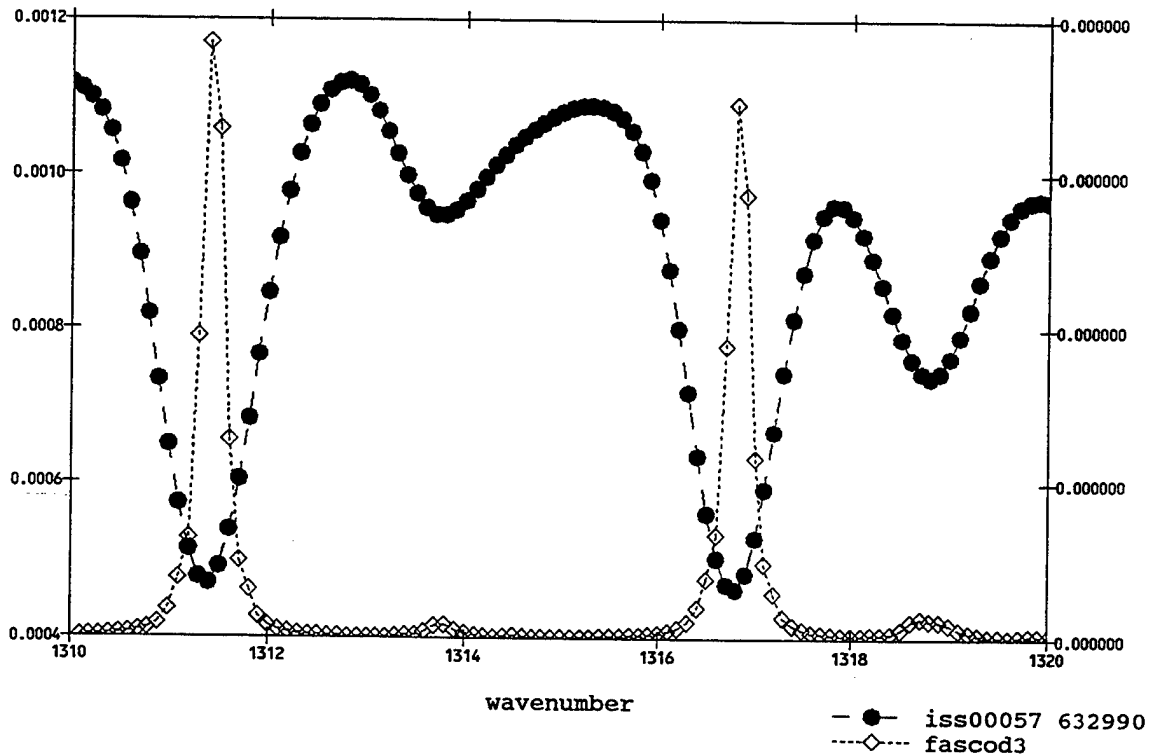
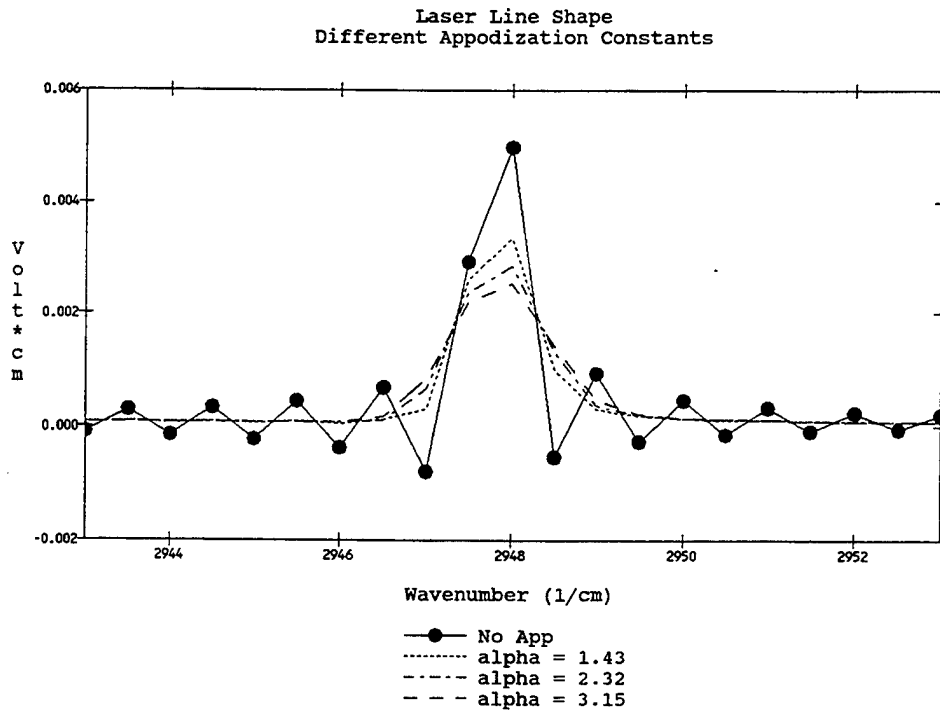


Figure 99. Comparison of CIRRIS absorption cell measurements and FASCOD3 predicted line shape.

#### 4.2.5.2 Spectral Line Shape

The spectral resolving power of an interferometer is established by the path length difference, which in turn is established by the moving mirror. While this can be established theoretically, it can also be demonstrated using the laser data shown in Section 4.2.5.1. Spectral line shape is determined by the apodization level applied in the transform process. The CIRRIS interferometer should have an unapodized optical full line width at first zero of approximately  $1 \text{ cm}^{-1}$ . Figure 100 shows the line shape developed by the ARC software at each of the options available. The CIRRIS interferometer has a physical mirror travel of 5.360 mm on the long side, providing an optical path difference (OPD) of 1.072 cm. The laser vacuum wavelength is  $632.992 \times 10^{-7} \text{ cm}$  and the A/D converter samples on every positive zero crossing. The formula for calculating the theoretical line width at the full width, first zero point is  $1/\text{OPD}$ . Therefore, CIRRIS should provide a full width, first zero resolution of  $1/1.072$  or  $0.933 \text{ cm}^{-1}$ . Figure 100 shows that CIRRIS resolves the laser line with about a  $1.4 \text{ cm}^{-1}$  full width first zero shape with apodization turned off, and the line is broadened when apodization is applied. The apodization levels set in Figure 100 correspond to OPUS default values of  $\alpha = 2, 2.5, 3.5$  ( $\text{dB} = -46, -57, -82$ ). Note that with a 16 K transform, data points in the transform are only reported at  $0.5 \text{ cm}^{-1}$  resolution.

The CIRRIS line shape can also be demonstrated using flight data. Figure 101 shows an OPUS transformed rotational water band collected at a tangent height of  $4840 \text{ cm}^{-1}$  and its model using FASCOD3-HITRAN92 with a resolution of  $0.05 \text{ cm}^{-1}$ . The data were collected using detector 3-2 at tangent height of 38 km. The band resolves with a half width of  $0.7 \text{ cm}^{-1}$  and a full width first zero of  $1.4 \text{ cm}^{-1}$ .



**Figure 100.** CIRRIS 1A unapodized line shape and line shape with various Kaiser-Bessel apodizations. Line is from a 3.391  $\mu\text{m}$  laser flooding detector 3-2.

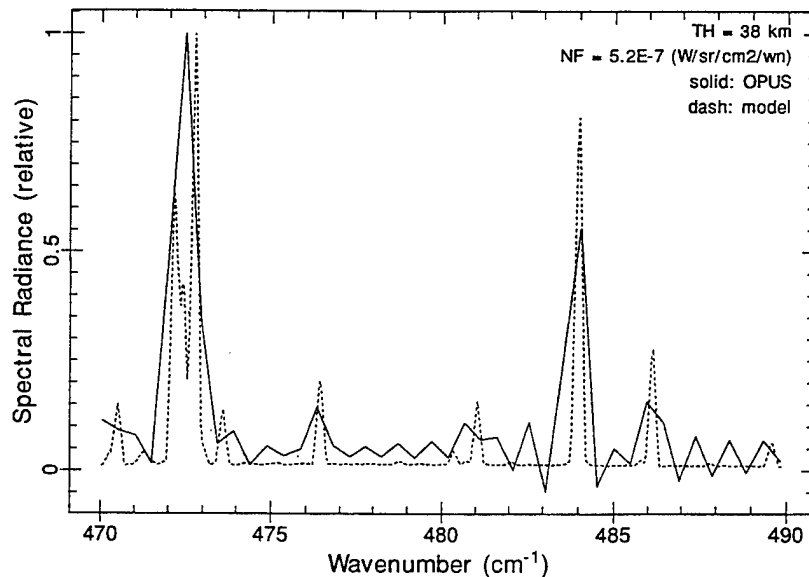


**Figure 101.** Demonstration of the CIRRIS 1A line shape of detector 3-2 using rotational water at 884  $\text{cm}^{-1}$  collected at a tangent height of 34 km. Model is FASCOD3-HITRAN 92 at 0.05  $\text{cm}$  resolution.

The theoretical line position determined by an interferometer assumes that the light being measured follows the same path as the laser beam which provides the sampling frequency. In a real interferometer with off axis detectors, measured light takes a slightly longer path and is transformed at a slightly longer path length. This effect is evident for detector 2, which is supposed to be centered on the optical axis, but is large enough to show some wavelength dispersion. Figure 102 shows the wavelength dispersion that occurs when a 3.391  $\mu\text{m}$  laser is focused on the center and four corners of detector 3-2. The left (vignetted) side of the detector shifts the peak by about  $1 \text{ cm}^{-1}$ , and the right (object space) side shifts it by less than  $0.5 \text{ cm}^{-1}$ . The net result is that resolution on detector 3-2 is about  $1.4 \text{ cm}^{-1}$  instead of the theoretical  $0.933 \text{ cm}^{-1}$ . This is explained by the fact that not all of the energy falls on the centerline of the detector, reducing its resolving capability.

Figure 103 shows the spectral dispersion of a line fracture (NO Q branch @  $1876 \text{ cm}^{-1}$ ) collected during flight where all four detectors responded to the fracture. The net spectral shift for the four detectors is shown in the figure. The shift from 3-2 to 3-1, 3-3 and 3-4 are about 0.9, 1.0, and  $0.6 \text{ cm}^{-1}$ , respectively. When making spectral comparisons between detectors, these offsets should be included.

Laser Line Resolution  
 Detector 2  
 Various Positions in Object Space

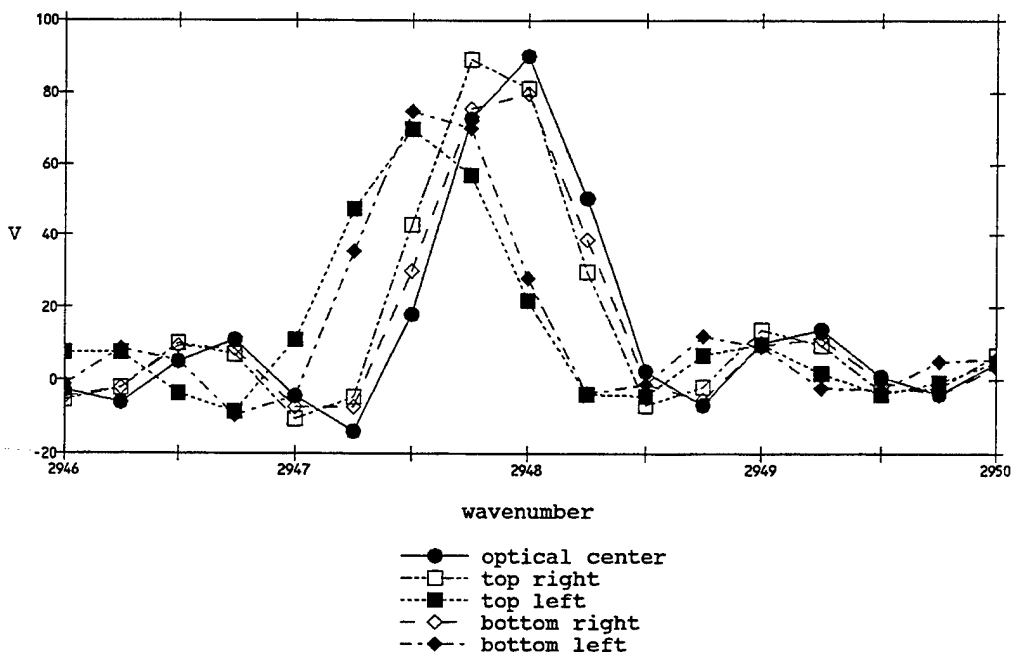


Figure 102. Wavelength dispersion of a 3.391 laser focused on the center and four corners of interferometer detector 3-2.

Detector to Detector Comparison  
 Flight Data  
 Time: 01/12:57:01

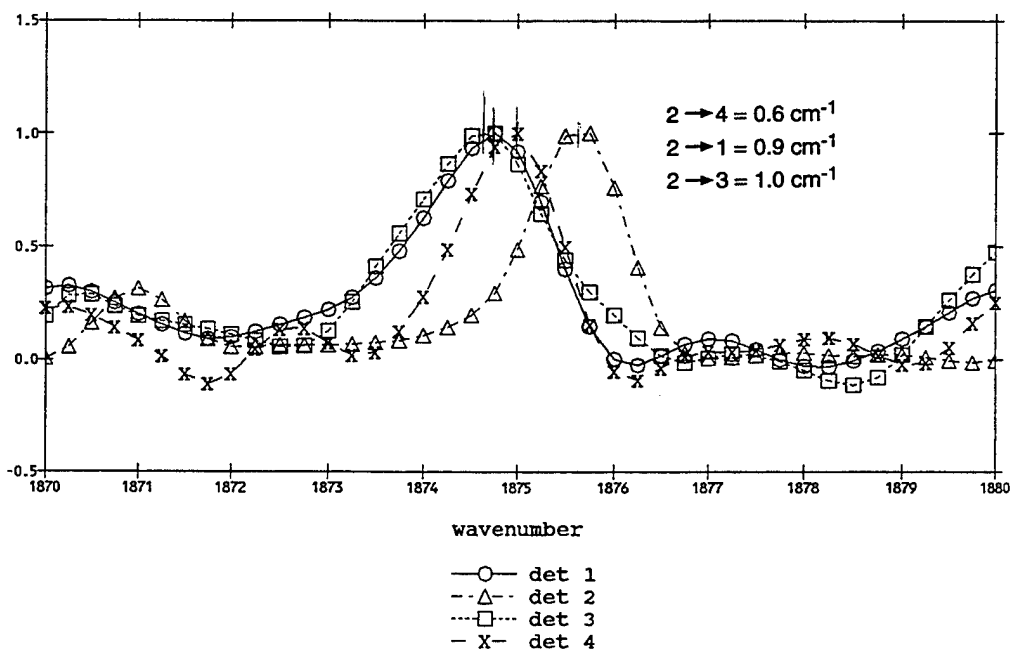


Figure 103. Spectral line dispersion between the central (detector 3-2) and off-axis detectors of CIRIS 1A.

## 5. ANCILLARY SENSORS CALIBRATION

### 5.1 PHOTOMETERS

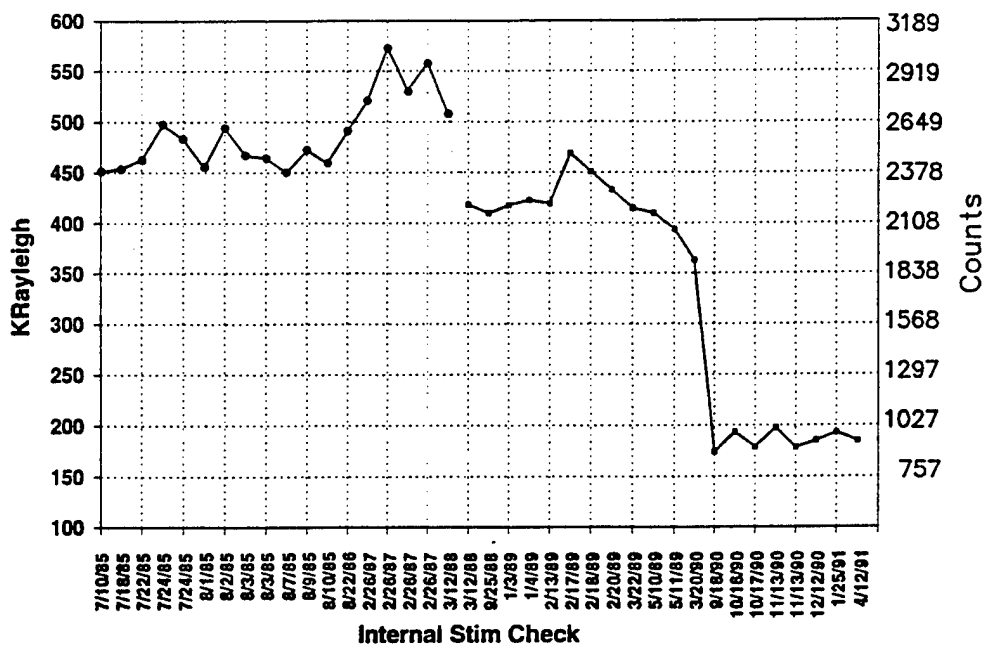
CIRRIS 1A housed two co-aligned, baffled, photon counting photometers with narrow bandpass filters at 3914Å and 5577Å to measure emissions from  $N_2^+$  and atomic oxygen. The two photometers were identical except for the optical filter. Each photometer incorporated a sun sensor that automatically shut down the photometer when the sun entered the 40° field of view of the sun sensor.

The original photometer calibration was performed in 1985, and their operation was tracked throughout 1985, 1986, and 1987. They were then recalibrated in March 1988 because of the delay following the shuttle Challenger accident. SDL personnel continued monitoring the photometers' output with the new calibration throughout the engineering calibration, functional testing, space simulation testing, and integration testing at both LMSC and KSC.

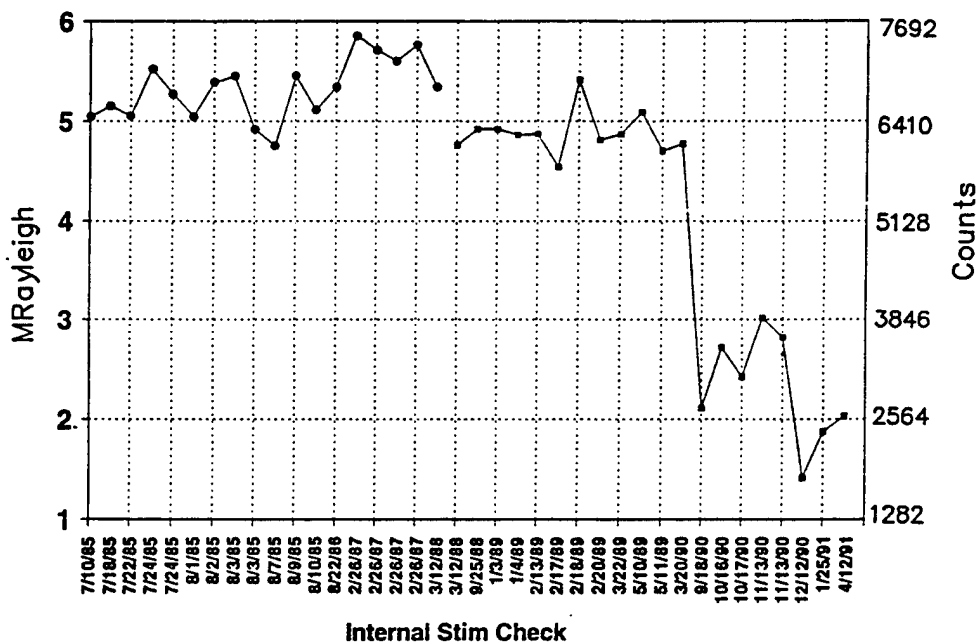
During the initial photometer tracking tests, the photometers' response to the internal stimulator was observed during power ON checks. The photometers housed a stimulator light emitting diode (LED) that was turned on for approximately ten seconds upon power ON. The LED stimulated the photometer photocathode and produced a count, indicating that the signal processing wiring was in place and the data collection hardware was functioning properly, which was actually the main objective of the test. The tracked photometer output was then taken as the peak count or kiloRayleigh value displayed on the command and monitor panel (CMP).

Although the initial photometer tracking tests provided an output response value, it was somewhat subjective because the peak value was taken visually from the CMP, which was updated approximately once per second. Therefore, in March 1990, SDL incorporated a more formal and precise method of recording the photometer output response values. This test was incorporated into the Health Check, and consisted of capturing part of the ten second pulse during ancillary power ON with the CIRRIS 1A interferometer data analysis system (IDAS), and determining the mean and standard deviation of the data. The radiometer data analysis system (RDAS) collected photometer housekeeping data.

Figure 104 shows the photometer stimulator tracking history from the initial calibration in 1985 to launch. In general, this history indicates a general degradation of the amplitude response of the photometer tube (counts) of both photometers until September 1990, when a 50% decrease in response was observed for both photometers. Investigation revealed no electrical or mechanical problems. Therefore, SDL and PL personnel agreed that the lower readings resulted from a decrease in the photometers' sensitivity. After the significant drop in stim response observed on 9/18/90, an additional test using a diffuse incandescent lamp source was initiated to monitor the responsivity of the photometers. In this test, the photometers were exposed to increasing lamp current and the resulting response was recorded. This test was incorporated into the health check. Figure 105 shows the resulting photometer response versus current. In general, the photometers tracked well throughout subsequent tests and indicated that further degradation was not occurring. The stimulator tracking was also stable throughout this period for each instrument.



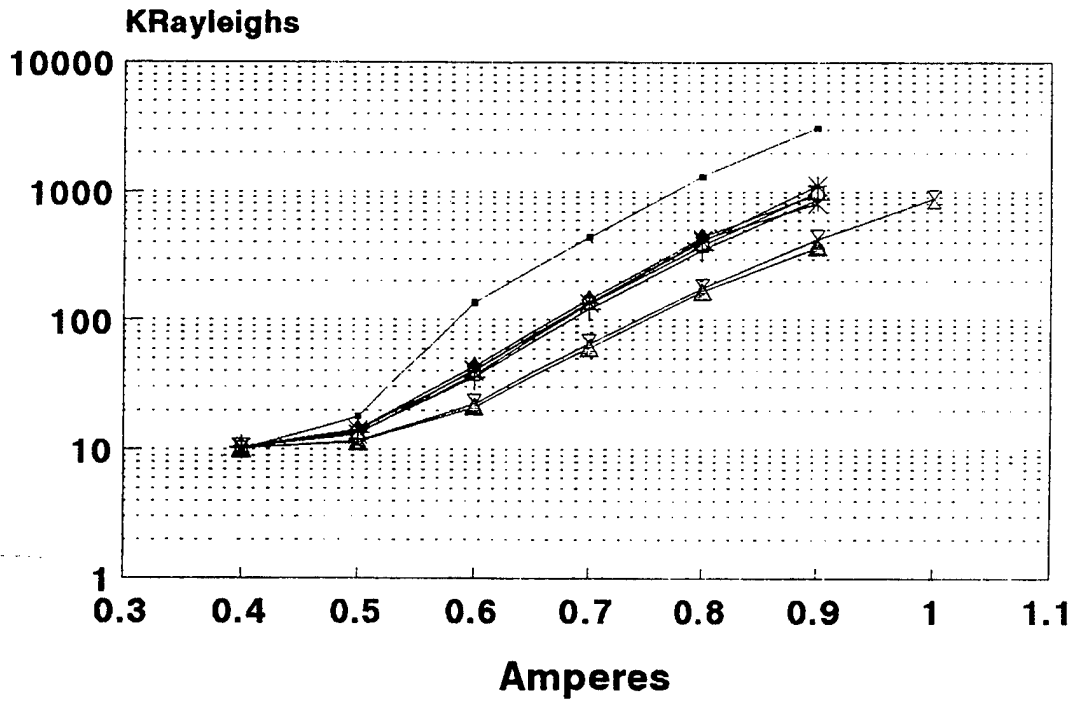
Photometer #1 - 5577Å



Photometer #2 - 3914Å

Figure 104. Photometer stimulator tracking history from initial calibration to launch.

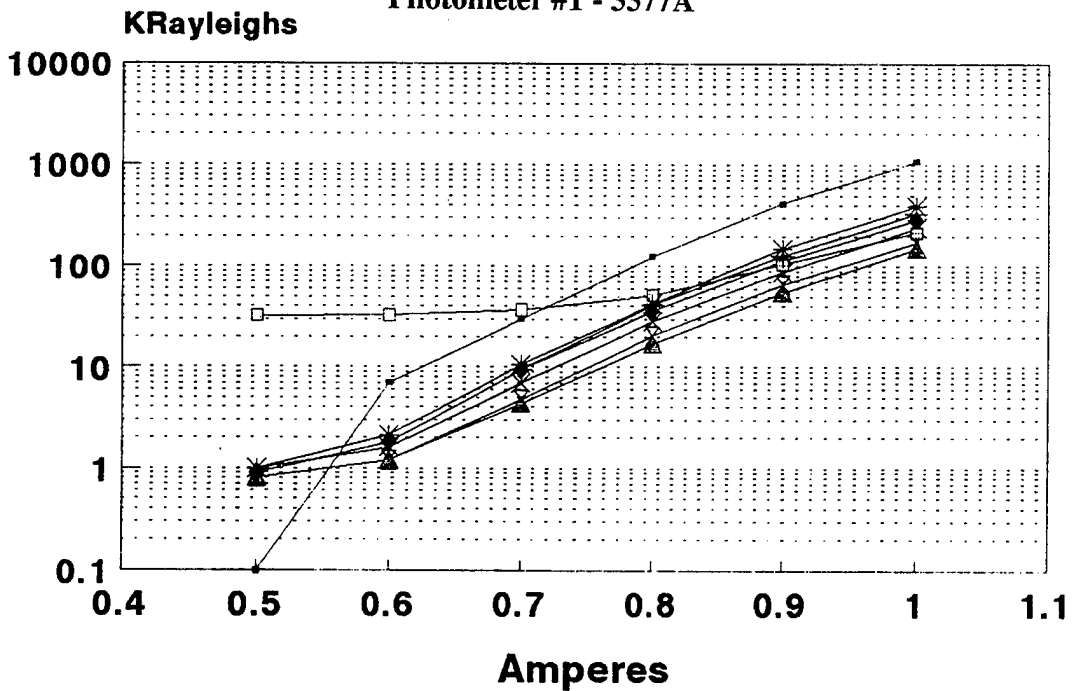




→ Ref + 17OCT90 \* 13NOV90 □ 11DEC90 × 25JAN91 ◆ 11APR91 ▲ 11JUN91 ⚗ 25SEP91

Diffuse Lamp Source Check

Photometer #1 - 5577Å



→ Ref + 17OCT90 \* 13NOV90 □ 11DEC90 × 25JAN91 ◆ 11APR91 ▲ 11JUN91 ⚗ 25SEP91

Diffuse Lamp Source Check

Photometer #2 - 3914Å

Figure 105. CIRRIS 1A photometer response versus lamp current.

During the flight, the photometers were exposed to extremely high light levels which further degraded their photomultiplier tubes. These high light levels resulted from solar scattering from the atmosphere during daylight portions of the orbit. The photometers were occasionally exposed to 15-20 minutes of small scattering angles when the C-1A viewing angle looked back toward the sun side of the orbit. In these conditions, the light levels became so great that the photometer counters could not reset between pulses and the outputs dropped to zero. During the following dark period, the photometers would tend to recover slightly, but succeeding high light exposure continued to reduce the number of counts observed at each initial stim reading. Figure 106 shows the stim response during the flight and at the post flight calibration.

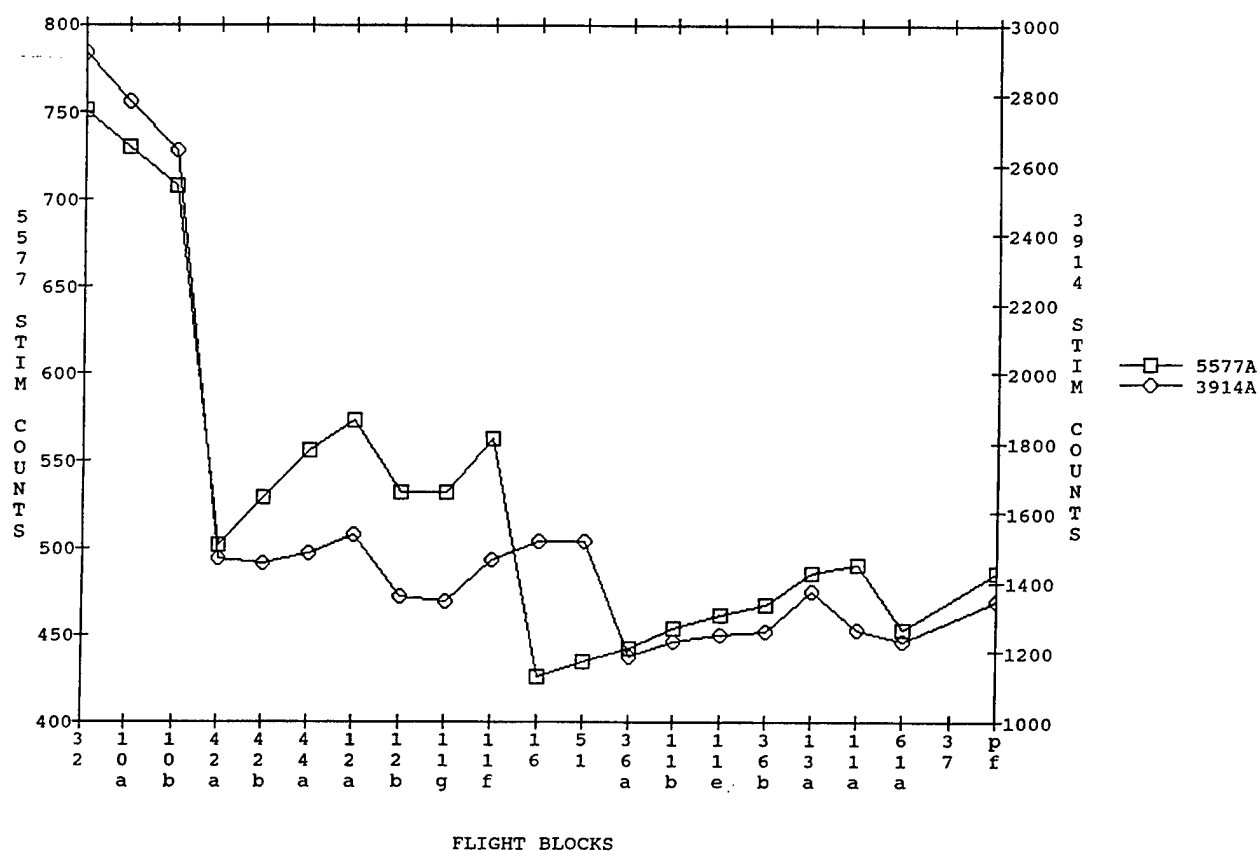


Figure 106. Stim history during flight and at the post flight calibration (pf).

### 5.1.1 Photometer Radiance Calibration

To calibrate the photometers, each photometer was exposed to a NIST traceable calibrated lamp. The lamp was at sufficient distance that it appeared as a near point source to the photometer. Photometer output was collected on a logic analyzer using the photometer internal clock (50.18 Hz). The counts were then scaled to the DFE clock rate (183.3 Hz). This scaling was confirmed by collecting data on both the logic analyzer and C-1A DFE using the diffuse light source. The highest point in the calibration was adjusted by varying the distance between the photometer and

the light source. Through put at that distance was calculated using geometric and filter transmission information. Lower points on the calibration curve were established by stacking calibrated neutral density filters between the light source and the photometer. The filters are calibrated at each wavelength by the manufacturer. The same filter set was used for all of the calibrations. Between the pre and post flight measurements, the calibration lamp burned out and was replaced. Both lamps were purchased with NIST traceable calibrations and performed consistently on photometer PCP3-1.

The post flight calibration showed that the C-1A photometers had lost about 90% of their sensitivity between the preflight 1988 calibration and the post flight calibration. The validity of the calibrations, and the fact that the damage to the flight tubes was due to operational exposures to excessive light levels is evident by the fact that the calibration of the flight spare photometer did not change during the period 1988-1993. Photometer calibration summaries are shown in Tables 27 through 30. The consistency of the "spare" photometer is evident in the tables, along with the decreases in PCP3-2 (3914Å) and PCP3-3 (5577Å) units. The data for the July 1991 calibrations of PCP3-2 and 3 are shown in Figure 107, along with a linear fit to the data. The continued degradation of PCP3-2 and 3 between the 1991 and 1993 calibrations is due to high light exposures between the calibration used to confirm the lock up in the counting circuit observed when the photometers were exposed to extremely bright light sources.

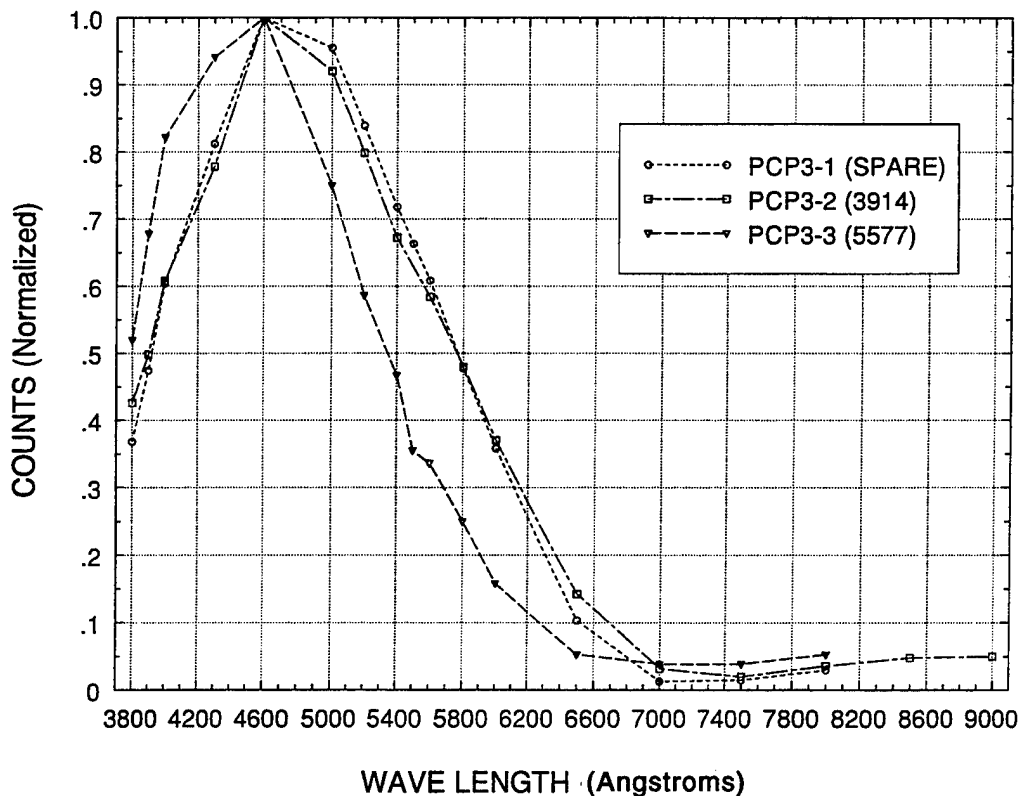


Figure 107. Normalized spectral response for the three CIRRIS 1A photometers measured post flight.

**Table 27. Calibration Data for Photometer PCP 3-1, Flight Spare with 3911.Å Filter**

16 March 1988 Stim response distance from lamp = 10' 1130 counts = 582 kR		22 July 1991 Stim response distance from lamp = 10' 1132 counts =		15 September 1993 Stim response distance from lamp = 10' 1151 counts =	
Rayleighs	Counts	Rayleighs	Counts	Rayleighs	Counts
2.08E + 6	3874	1.72E + 6	3495	1.72E + 6	4107
1.05E + 6	2105	8.87E + 5	1924	8.87E + 5	2187
6.80E + 5	1312	5.59E + 5	1214	5.59E + 5	1439
3.59E + 5	708	3.11E + 5	617	3.11E + 5	773
2.24E + 05	435	2.02E + 5	380	2.02E + 5	450
1.20E + 05	235	1.11E + 5	220	1.11E + 5	253
7.98E + 04	154	7.50E + 4	147	7.50E + 4	157
4.19E + 04	85	4.09E + 4	80	4.09E + 4	94
2.34E + 04	33	1.69E + 4	30	1.69E + 4	33
		3.33E + 3	7	3.33E + 3	8
Dark noise = 1 count		Dark noise = 1 count		Dark noise = 1 count	

**Table 28. Calibration Data for Photometer PCP 3-1, Flight Spare with 5580Å Filter**

16 March 1988 Stim response = 1130 counts = 825 kR		22 July 1991 (not calibrated with 5580Å filter)		17 September 1993 Stim response = 1151 counts =	
Rayleighs	Counts			Rayleighs	Counts
3.95E + 6	5460			3.89E + 6	5893
2.00E + 6	2889			2.45E + 6	3742
1.29E + 6	1771			1.37E + 6	2002
6.82E + 5	934			8.86E + 5	1110
4.27E + 5	598			4.88E + 5	629
2.27E + 5	227			3.30E + 5	417
1.52E + 5	185			1.79E + 5	221
7.96E + 4	96			7.44E + 4	108
				2.86E + 4	42
				5.67E + 3	10
				3.44E + 3	6

**Table 29. Calibration Data for Photometer PCP 3-2, 3914Å Filter**

16 March 1988 Distance from lamp = 10', Stim response: 6098 counts = 4756 kR		23 July 1991 Distance from lamp = 9', Stim response: 1569 counts = 6760 kR		30 September 1993 Distance from lamp = 6.0', Stim response: 996 counts =	
Rayleighs	Counts	Rayleighs	Counts	Rayleighs	Counts
2.41E + 6	3041	2.45E + 6	562	5.52E + 6	643
1.22E + 6	1602	1.27E + 6	301	2.85E + 6	311
7.88E + 5	10/9	7.99E + 5	196	1.80E + 6	203
4.16E + 5	540	4.45E + 5	108	1.00E + 6	106
2.59E + 5	323	2.88E + 5	60	6.49E + 5	62
1.39E + 5	172	1.59E + 5	35	3.57E + 5	32
9.25E + 4	116	1.07E + 5	22	2.41E + 5	24
4.86E + 4	63	5.84E + 4	13	1.31E + 5	12
2.72E + 4	25	2.42E + 4	05	5.45E + 4	05

**Table 30. Calibration Data for Photometer PCP 3-3, 5577Å Filter**

12 March 1988 Distance from lamp = 15', Stim response: 2208 counts = 418.5 kR		29 July 1991 Distance from lamp = 15', Stim response: 496 counts = 947 kR		29 September 1993 Distance from lamp = 10.75', Stim response: 160 counts =	
Rayleighs	Counts	Rayleighs	Counts	Rayleighs	Counts
2.35E + 6	11564	3.92E + 6	2232	7.63E + 6	1270
1.52E + 6	8399	2.03E + 6	1121	3.94E + 6	600
8.02E + 5	4366	1.28E + 6	656	2.48E + 6	349
5.02E + 5	2837	7.11E + 5	348	1.38E + 6	174
2.67E + 5	1289	4.61E + 5	184	8.98E + 5	90
1.78E + 5	844	2.54E + 5	102	4.94E + 5	45
9.36E + 4	437	1.71E + 5	68	3.34E + 5	30
5.24E + 4	223	9.34E + 4	37	1.82E + 5	16
Dark noise = 1 count		2.08E + 4	10	7.54E + 4	9
		7.60E + 3	04		

Because of the significant changes in the response of the tubes to the power up stims during the flight, a calibration coefficient was calculated for each block using the stim pulses. While the stims were originally designed only to verify proper operation of the photometer readout circuits, the stims have been shown to be stable light sources and reliable transfer standards. Table 31 shows the block number, pulse height, and photometer sensitivity during each block, based on the post flight (July 1991) calibration. The response is assumed to be linear and without an offset. The photometer calibration applies only to eclipse (night) portions of each orbit.

The postflight calibration shown in Tables 29, 30, and 31 suggest an inconsistency in this approach to photometer calibration. If the post flight stim-based adjustment approach is applied to the preflight (March 1988) calibration data, the stim brightness in PCP3-2 and 3 appear to increase by factors of 42% (4756 to 6760 kR) and 126% (418.5 to 947 kR), respectively. Since 19 September 1990, photometer sensitivity has been tracked by both the internal stim and the external light source. These two systems tracked the sensitivity changes consistently, indicating that the change in stim sensitivity occurred before this date. This appears to confirm the use of the stim sources as a block-by-block calibrator, using the post flight calibration.

### 5.1.2 Photometer Spectral Sensitivity

To verify the use of the stims as calibration sources, tube spectral sensitivity and temperature stability were examined. The power-on stim in each of the photometers is located behind the filter and light is reflected from the cavity into the tube. The diode consists of a HPIN6094 (green) LED. The peak of the LED emission is at 5650Å. This emission is very close to the measured wavelength of the 5577Å filter, but is far removed from the 3914Å band. Because PCP3-1 response has not shown any change, it was used for a reference in the spectral responsivity test.

The spectral response test was conducted by removing the filter from each of the photometers and illuminating the tube with the calibration lamp through a monochromator. The monochromator calibration was verified by resolving the line spectra of a standard mercury lamp. The normalized lamp response for all three photometer tubes is shown in Figure 107. The normalizing factors for each of the curves is also shown in the figure. While the two flight tubes have changed spectral sensitivity, the change is not sufficient to explain changes in the apparent stim brightness observed between the preflight and post flight calibrations.

**Table 31. Photometer Sensitivity During Flight Blocks**

Block		Pulse Time	5577 kRayleigh	5577 Counts	Sensitivity	3914 kRayleigh	3914 Counts	Sensitivity
1	Pre-Cal	n/a	418.5	2208	0.189538	4756	6098	0.779928
2	PC32	11:30:40	947.0	751	1.260985	6760	2922	2.313484
3	10a	20:20:48	947.0	730	1.297260	6760	2782	2.429907
4	10b	23:29:28	947.0	708	1.337571	6760	2643	2.557700
5	42a	27:47:36	947.0	502	1.886454	6760	1471	4.595513
6	42b	29:17:16	947.0	529	1.790170	6760	1459	4.633310
7	44a		947.0	556	1.703237	6760	1487	4.546066
8	12a	36:36:39	947.0	573	1.652705	6760	1541	4.386762
9	12b	48:36:00	947.0	532	1.780075	6760	1360	4.970588
10	11g	39:36:16	947.0	532	1.780075	6760	1346	5.022288
11	11f	44:04:50	947.0	563	1.682060	6760	1468	4.604905
12	16_	46:59:07	947.0	426	2.223005	6760	1519	4.450296
13	51_		947.0	435	2.177011	6760	1520	4.447368
14	36a	50:30:38	947.0	442	2.142534	6760	1187	5.695029
15	11b	53:02:40	947.0	454	2.085903	6760	1233	5.482563
16	11E No pulse		947.0	462	2.049784	6760	1250	5.408000
17	36b	56:32:40	947.0	467	2.027837	6760	1262	5.356577
18	13a	59:01:11	947.0	486	1.948560	6760	1377	4.909223
19	11a	60:31:11	947.0	490	1.932653	6760	1264	5.348101
20	61a	62:27:10	947.0	453	2.090508	6760	1232	5.487013
21	37 No pulse		947.0			6760		
22	pf		947.0	486	1.948560	6760	1346	5.022288
23	post-cal		947.0	496	1.909274	6760	1569	4.308477

### 5.1.3 Photometer Temperature Response

Two tests were made to determine the response of the photometers to the changes in temperature during flight. The measured temperature profile for the two photometers during flight are shown in Figure 108. The temperature response of the tube-stim combination over the temperature range observed during the flight is shown in Figure 109. Over the 40°F to 85°F temperature range, the stim pulse counts were reduced by a factor of 0.7 for both the 3914Å and 5577Å photometers. During the tests, both photometers occasionally reported a higher output signal (+12%), and that these higher pulses were consistent in their increased valve and temperature response. The cause of these larger pulse counts is not known. The increased count level occurs more often in the 3914Å photometer.

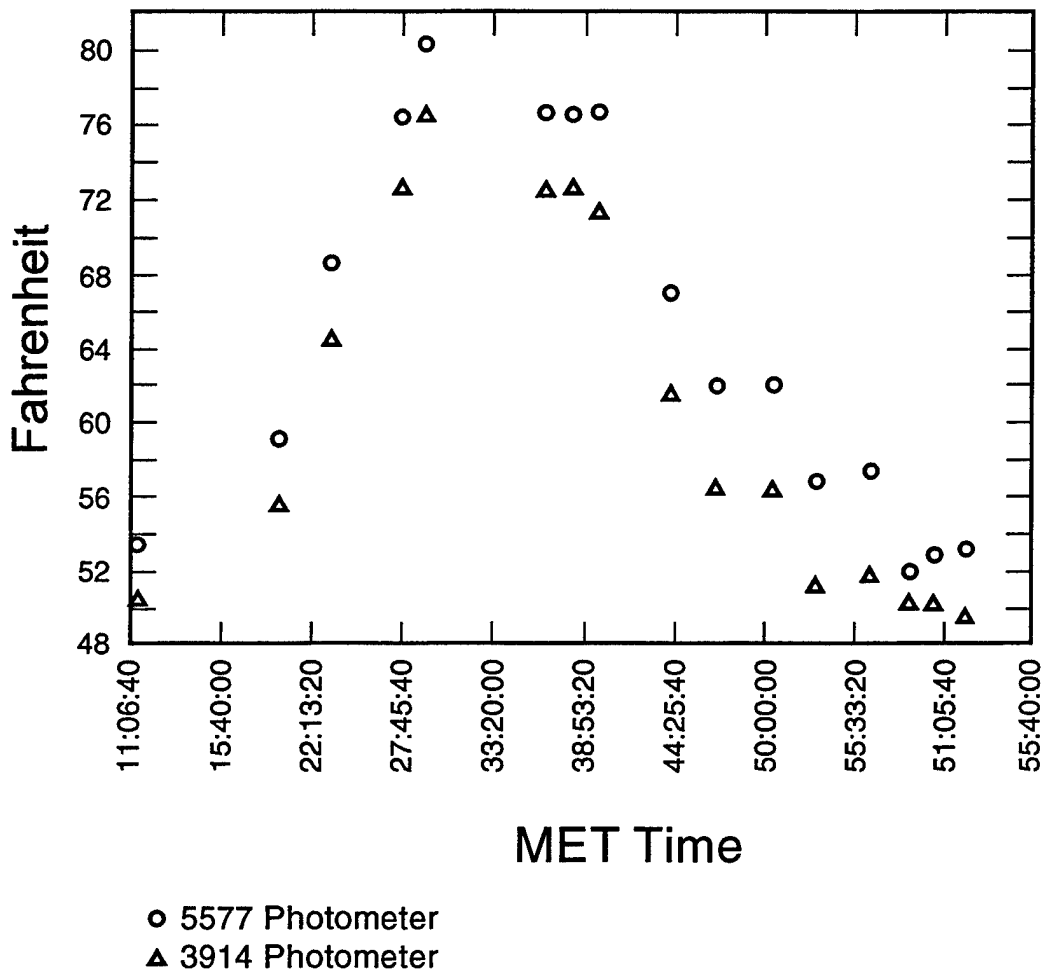
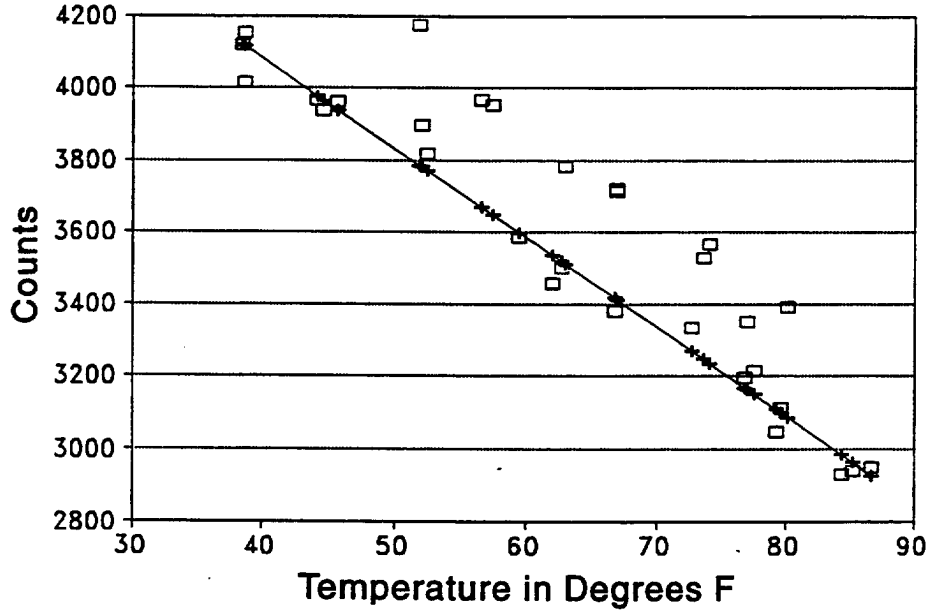


Figure 108. Photometer temperatures during flight.



### MIDDLE VALUES OF 3914A

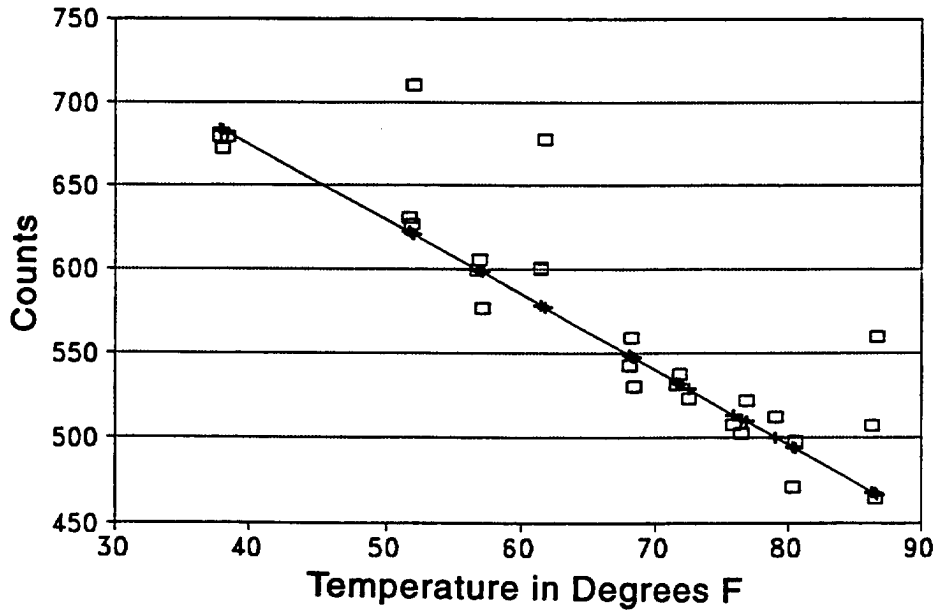
$$Y = -24.7087 * X + 5066.927$$



(a)

### MIDDLE VALUES OF 5577A

$$Y = -4.4519 * X + 852.1952$$



(b)

Figure 109. Photometer stim temperature response curve.

To confirm that the temperature response was due to the tube response and not the stimulator, the temperature response tests were re-run, including not only a measurement of the stim at each temperature, but also the external diffuse lamp source. The results of this test are shown in Figure 110. These data show that most of the change in sensitivity is due to the tube. Between 50°F and 80°F, the reduction in counts to the external lamp source is  $\frac{620 - 525}{620} = 15$  versus  $\frac{780 - 670}{780} = 14\%$  for the stim. Based on these data, we conclude that the stim sensitivity data shown in Table 31 are reliable estimates of the photometer sensitivity during the night portions of the mission block.

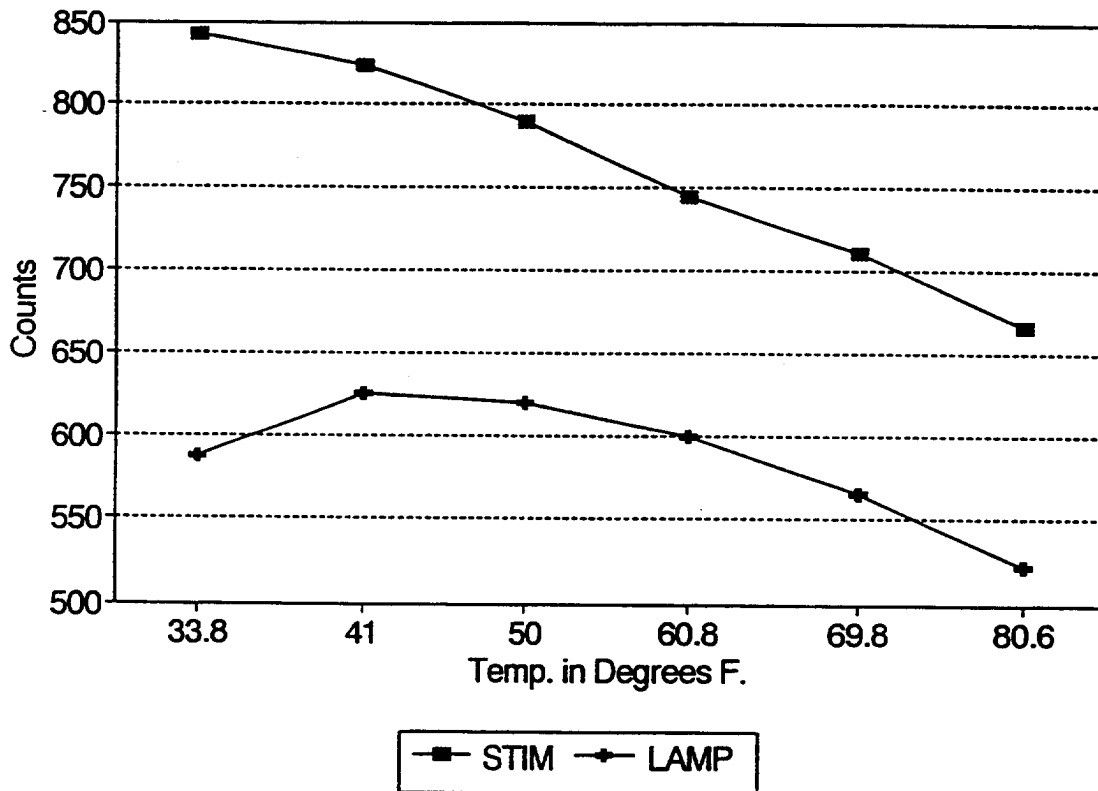


Figure 110. Temperature response of the photometer PCP3-3 5577Å to internal stim and an external chamber light source.

## 5.2 CELESTIAL ASPECT SENSOR (CAS)

The CAS camera provided 16-mm images of star fields at precisely known times during the flight. These images were digitized to provide precise pointing angles. The CAS was mounted at a 45° angle to the telescope line of site and was calibrated from analysis of actual star photographs. The CAS was reworked after the Challenger postponement to improve the fiducial mark system that is used to precisely register the film at each shot. An example photograph is shown in Figure 111.

### 5.3 HORIZON SENSOR

The horizon sensor was used to detect the displacement of the CIRRIS 1A instrument above the 40 km CO<sub>2</sub> layer. The sensor swept out a 45° cone with respect to the telescope line of sight and fed back tangent height information to the CIRRIS 1A controller for use during some of the automatic data acquisition modes. Information from the horizon sensor was also available to the payload specialists controlling CIRRIS 1A on their command and monitor panel. The horizon sensor test fixture was replaced with an improved fixture during the time delays after the Challenger disaster. The new horizon sensor remained stable throughout the entire period of testing and during flight.

### 5.4 LOW-LIGHT-LEVEL TELEVISION CAMERAS (LLTV)

The CIRRIS 1A LLTV cameras are coaligned with the main telescope and are the primary means of pointing the instrument at visible targets. The cameras have two different fields of view, a wide field of view (WFOV) (20° x 15°) on the acquisition camera and a narrow field of view (NFOV) (3.5° x 2.5°) on the pointing camera. The NFOV camera has reticles which outline the view of each detector. The WFOV camera has a reticle for selecting specific tangent heights. Each camera contains an auto-iris and electronic gain control for high light protection. These cameras are new and have passed their shake, thermal, and low-light calibration, and orbiter compatibility tests.

Appendix 2 includes a report by Miranda Laboratories entitled "Characterization of the CIRRIS 1A LLTV Systems." This report describes one approach to derive absolute source radiance from the LLTV output signals.

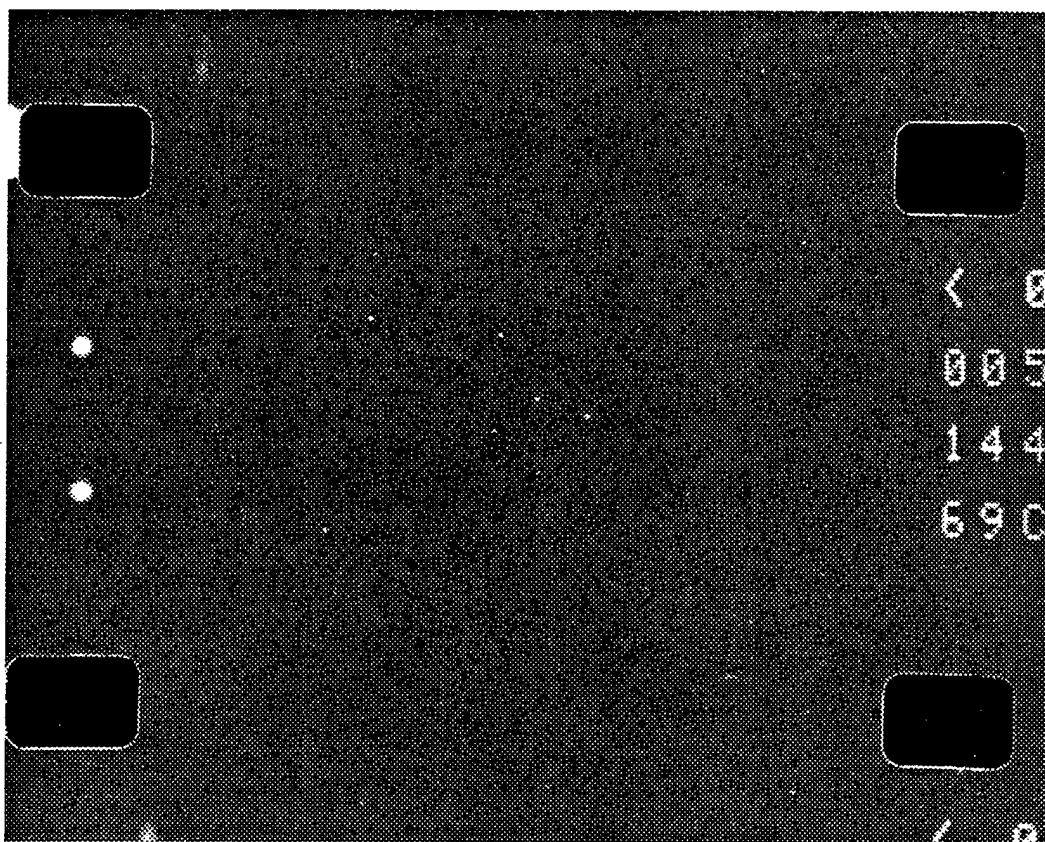


**Figure 111.** A photograph taken with the CIRRIS 1A celestial aspect sensor camera. The camera fiducials are the two larger dots on the left edge of the film.

## 5.5 TAPE RECORDERS

Calibration personnel compared the flight data in the OPUS 9-file format for the two sets of optical disks obtained from tape recorder 1 (TR1) and tape recorder 2 (TR2). This consisted of a bit-by-bit comparison of 15- to 25-minute blocks of radiometer and interferometer data extracted from some of the CIRRIS 1A measurement blocks that were recorded at the beginning, middle, and end of the mission to include the different combinations of TR1 and TR2 recording speeds. Eight measurement blocks were partially compared for a total of 530 MBytes or about 15% of the recorded flight data. Most of the differences between the two sets of data were found at the beginning and end of the measurement blocks, where the timing is off by one or two seconds. This could be attributed to the tape engagement and disengagement as the tape recorders were started and stopped. When the tape recorders were restarted, the data were not recorded where they had left off when they were stopped. The data gaps that were previously found in some of the blocks obtained from TR1 were also discovered in TR2. These gaps were actually 1 or 2 seconds longer in TR2. During the comparison process, a gap in the TR2 interferometer data was found that was not in TR1; this gap was not found in the TR2 interferometer data which would indicate that the data were lost during the tape duplication process. Only three bit

errors were found for the samples taken. This results in a bit error rate of 1 out of every  $1.4 \times 10^9$  bits.

Overall, the TR1 data appear to be better than that of TR2. After doing the comparison it is recommended that the OPUS data base should not be modified since it already uses the TR1 data.

## 5.6 DFE-2 FLIGHT ANOMALY

During the flight of CIRRIS 1A, DFE-2 quit operating while the system was powered up via bus A or PDC-1. Flight procedures switched the system to bus B or PDC-2 and everything worked fine and the mission continued in this manner.

After the post flight calibration effort, SDL investigated the problem and found the +28 volt fuse in PCD-1 had blown. The fuse (F6 on D4-1583) is a 5 amp fuse and DFE -2 pulls 1.2 amps. There is a safety factor of a little over 4 in the design and that should have been more than adequate. There is some concern over derating the fuse due to thermal considerations because of operation in a vacuum. However, if the fuse has almost any amount of heat sinking, then the temperature rise due to operation in a vacuum is not applicable. The actual derating value to use is therefore an engineering decision.

There is one other possible concern over the  $I^2$ \*Time rating of fuses. The theory is that given enough time, any fuse will blow with any level of current through it, no matter how low the current (the integration of time making up for any  $I^2$  level). However, this theory obviously can't be extrapolated to any limit or all wires would eventually disintegrate. SDL has contacted two engineers at Littlefuse Inc. who said that unless the fuse is running close to its rated level, the  $I^2$ \* Time plays no factor in causing the fuse to blow no matter how long the fuse is in use.

The fuse was replaced and the system powered up and everything checked out.

## 6. CALIBRATION EVALUATION

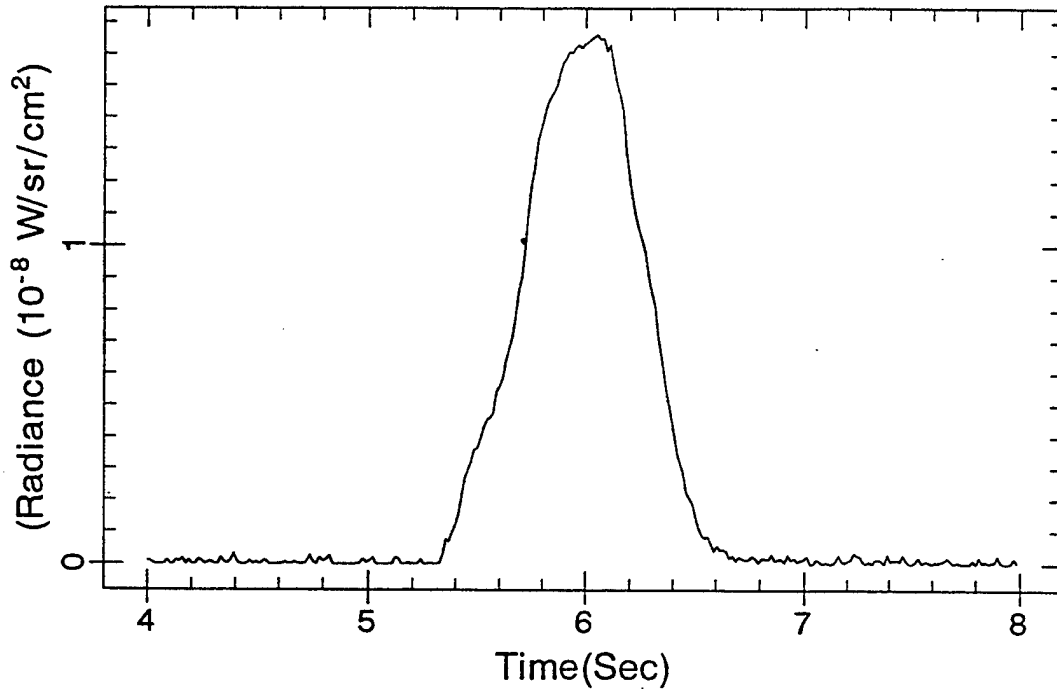
### 6.1 CALIBRATION EVALUATION

This section reviews the current understanding of the accuracy of the CIRRIS 1A calibration and discusses the remaining questions currently being resolved during the on-going flight data analysis.

#### 6.1.1 Radiometer Calibration

To improve flight data comparison from various infrared sensors, the Department of Defense (DoD) has selected a set of stars for sensors to view to standardize the sensors' calibration. The DoD encourages each program to view these stars during the sensor's lifetime. The CIRRIS program complied with this request and the measurements from these standard stars were compared with infrared emittance values determined by other investigators (IRAS) to verify the CIRRIS radiometer calibration.

During flight, CIRRIS made measurements against three infrared emitting stars, Alpha Booties, Alpha Sco, and Alpha Centary. Figure 112 shows the response of D1-6 when the star Alpha Sco crossed the detector in the delta y direction (3 mrad). The radiometer-measured peak radiance was  $1.83\text{E-}8 \text{ W/cm}^2 \text{ sr}$ . Using the measured solid angle of D1-6 (Table 5), this value is converted to a measured irradiance of  $3.12\text{E-}14 \text{ W/cm}^2$ . The IRAS integrated irradiance for this star in the bandpass of CIRRIS filter 0 was about  $3.27\text{E-}14 \text{ W/cm}^2$ , using standard (white) radiometer calibration. Thus, the irradiance measured by the CIRRIS radiometer is within about 5% of the value measured by IRAS. If the actual spectral emittance of the star is used, the radiometer-measured value would be higher, and the two values would be within a smaller percentage. Similar measurements made against Alpha Booties with radiometer filter 1 also calculate to within about 95% of the IRAS value. From these measurements, we conclude that the radiometer absolute calibration is accurate to within 5% of the best stellar measurement standard available.



C1A RAD Filter 0 = 8.37-18.0  $\mu\text{m}$  [RAD det #1-6]  
 The max radiance = 1.86E-8 (W/sr/cm<sup>2</sup>)

The measurement of IRAS of Alpha Scorpio:  
 Irrad = 3.27E-14 (W/cm<sup>2</sup>)  
 Radiance = 1.918E-08 (W/cm<sup>2</sup>/sr) [using FOV 1.705E-6 sr]  
 Error = 4.65%

Figure 112. The radiometer response to a crossing of Alpha Sco.

## 6.1.2 Interferometer Calibration

Most of the interferometer calibration data have been successfully used in state-of-the-art models of line spectral position and other aspects. The medium bias mode calibration of D3-1 to D3-4 shows an absolute calibration to within a few percent of the star-verified radiometer calibration. The calibration of these detectors for low bias and for D3-5 shows larger offsets and some spectral inconsistencies, which are discussed in this section.

### 6.1.2.1 Intersensor Absolute Calibration Difference

To determine its accuracy, the interferometer spectral and absolute calibration data were compared with data collected by other sensors and with the CIRRIS radiometer. Most of the higher atmosphere data agreed with theory and compared favorably with the data from the other sensors. However, the lower atmosphere data showed some discrepancies, which were manifested as differences in absolute radiance. This discrepancy is obvious in the comparison of the radiometer-derived radiance and the interferometer integrated spectral radiance. In a vertical scan of the earthlimb this comparison can be made over the entire dynamic range of both instruments.

The fields of view of the radiometer and interferometer detectors are shown in Figure 65. This figure shows that D3-3 and D3-4 have about the same vertical integration as the largest radiometer detectors, D1-3 is at about the same height as D3-3, and D1-4 and D3-4 share a similar vertical view. The radiometer fields of view are offset horizontally by about 4 mr. This offset allows some differences between simultaneous measurements, but provides informative trends through the radiance range. During the mission, vertical scans were taken with all of the radiometer and interferometer filter pairs.

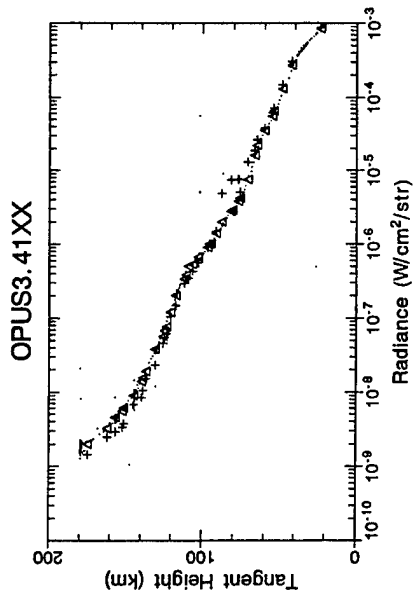
Figure 113 shows a comparison of the OPUS processed radiometer radiance and the interferometer radiometer-bandpass-frequency integrated spectral radiance for each radiometer filter. The comparison shows the radiances reported for tangent heights about 15 km to 160 km. In this figure, the dots are the individual data points reported by OPUS, the deltas are the average of the radiometer data points that fell within the interferometer field of view at the specific tangent height where an interferometer scan was made, and the (+)s are the integrated spectral radiances collected by the interferometer.

Figure 114 shows the data in Figure 113 plotted as radiometer versus interferometer. With this configuration, a perfect match would place all data on the 1-1 line. Three types of trends are shown in the individual filter responses. Filters 1, 3, 5, 6 and 7 show linear relationships across the whole dynamic range. However, different bias offsets are seen across the various filters, ranging from about 15 to 25% for all the filters except filter 6, which is about 50%. Filter 0, however, shows a changing bias with tangent height (radiance). From the noise level at about  $10^{-9}$  to the mid-radiance level ( $\sim 10^{-6}$ ), the radiometer values are slightly above the 1-1 relationship. At higher radiance levels, however, the interferometer values are larger. Data for filter 2 are not shown in this fashion because of the large jump at the lower altitude (higher radiance) levels (Figure 113 (c)). The cause of this jump is shown in Figure 120 (b).

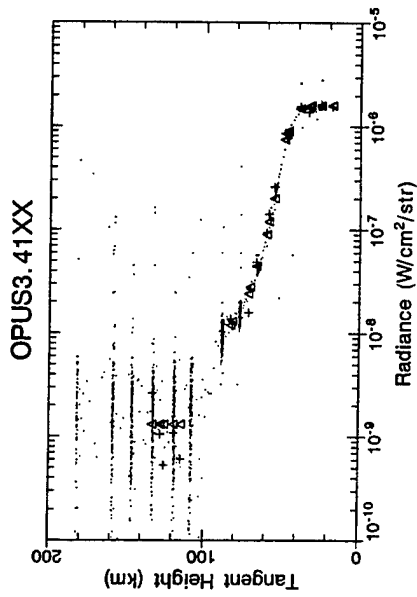
Because these plots contain data collected by multiple interferometer detectors and bias levels, the details of these radiometer-interferometer calibration shifts are not immediately evident. To determine if the interferometer gain calibration contributes to the filter-to-filter variation problem, the filter 7 response of each of the interferometer detectors was plotted with the gain stage showing as a different symbol. Figure 115 shows an example of this analysis for D3-4, which clearly shows that gain correction does not contribute to the problem.

The radiometer response to stellar illumination was only verified for two filters; therefore, some of the filter-to-filter variation probably still resides in the radiometer. The linear intercomparison observed for most of the filter bandpass regions indicates a multiplicative factor. An example would be an error in our measurement of the radiometer RSR bandpass which would not properly account for some of the energy from a spectrally flat source. The large differences between the in situ measured RSR of the radiometer filters and those provided by the manufacturer may be somewhat troublesome and could be an area that could be re-examined in the radiometer calibration. However, we believe that some of the variation also comes from the interferometer calibration.

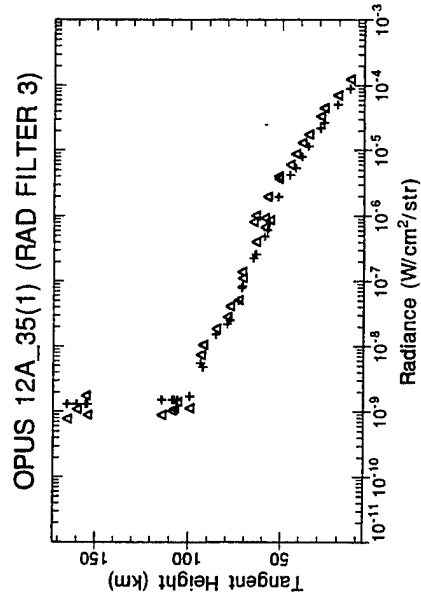
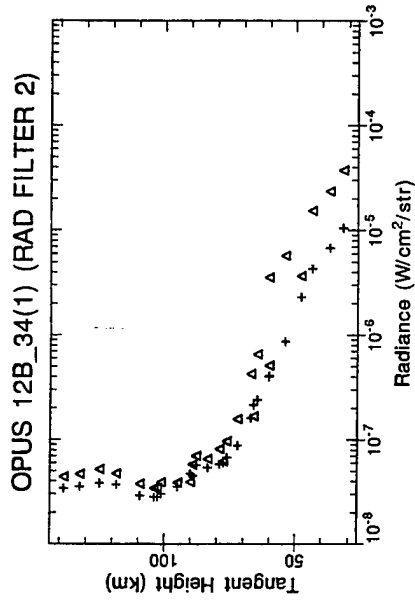




points: RAD filter 0 (555-1195  $cm^{-1}$ ), det.=1-3L  
 $\Delta$ : RAD data at same TH point of IRF data  
 $+$ : IRF filter 0, integrated in the same region of RAD, with R=1.00.

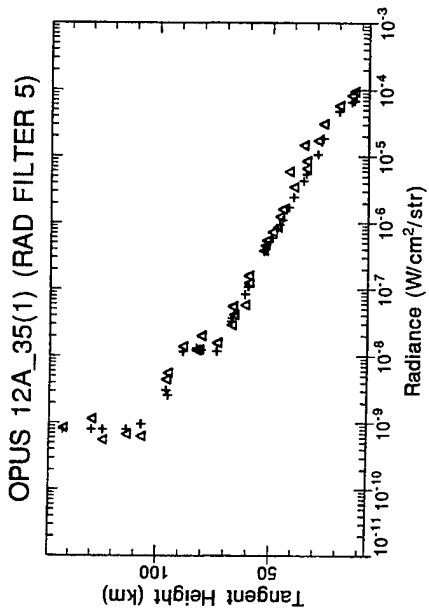


points: RAD filter 1 (2207-2450  $cm^{-1}$ ), det.=1-3L  
 $\Delta$ : RAD data at same TH point of IRF data  
 $+$ : IRF filter 1, integrated in the same region of RAD, with R=0.90.

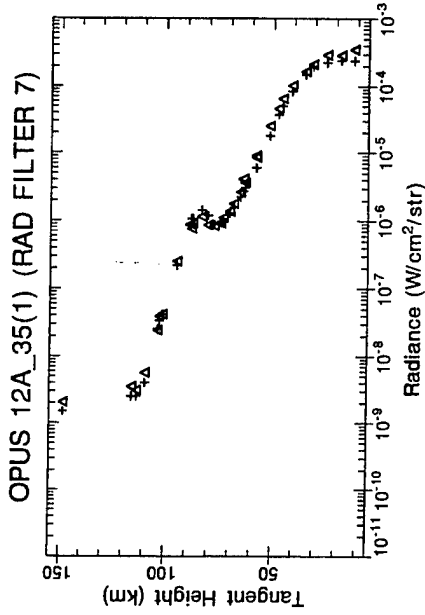


$+$ : radiometer filter 3 = 1120-1692  $cm^{-1}$ , det.=1-3L  
 $\Delta$ : Interferometer filter 3, integrated in the same region of radiometer.

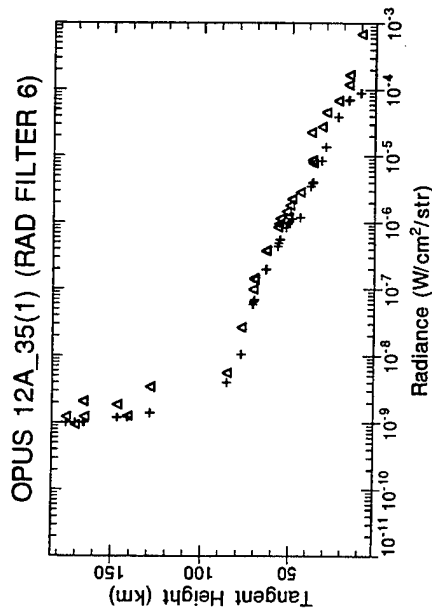
Figure 113. A comparison of the interferometer and radiometer radiance data for a vertical limb scan from about 15 km to 160 km tangent height.



+: radiometer filter 5 = 775-909  $\text{cm}^{-1}$ , det. = 1-3L  
 $\Delta$ : interferometer filter 5, integrated in the same region as radiometer.

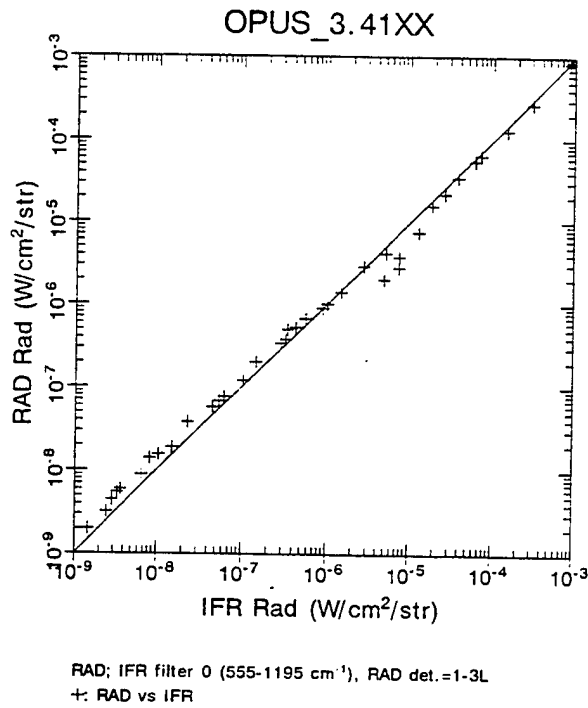


+: radiometer filter 7 = 840-1251  $\text{cm}^{-1}$ , det. = 1-3L  
 $\Delta$ : interferometer filter 7, integrated in the same region of radiometer.

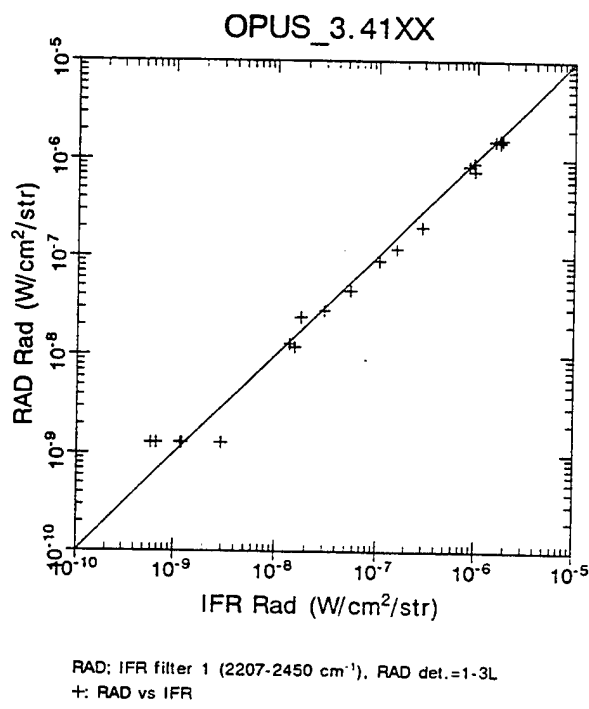


+: radiometer filter 6 = 420-565  $\text{cm}^{-1}$ , det. = 1-3L  
 $\Delta$ : interferometer filter 6, integrated in the same region as radiometer.

**Figure 113 (cont).** A comparison of the interferometer and radiometer radiance data for a vertical limb scan from about 15 km to 160 km tangent height.

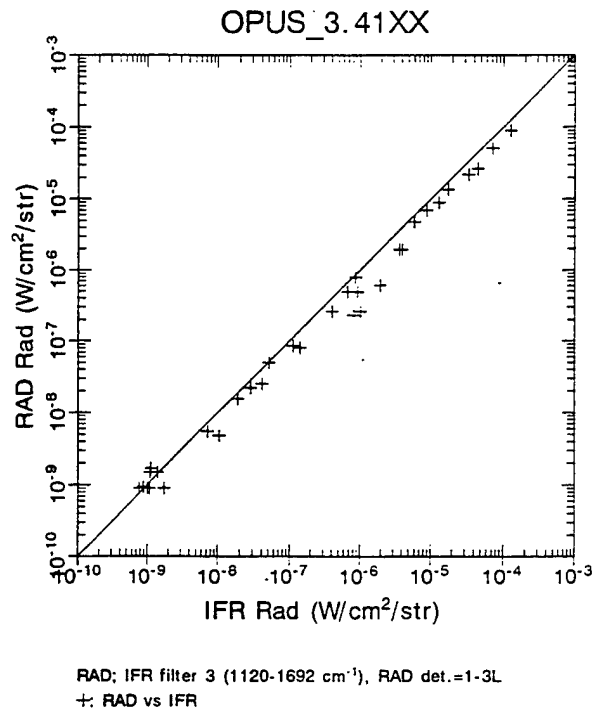


A

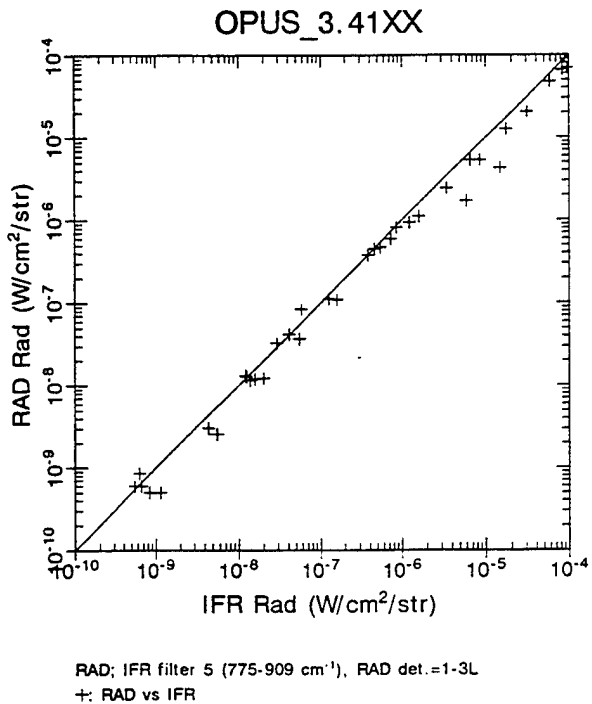


B

**Figure 114. A comparison of the interferometer and radiometer radiance data for a vertical limb scan from about 15 km to 160 km tangent height.**



C



D

**Figure 114 (cont).** A comparison of the interferometer and radiometer radiance data for a vertical limb scan from about 15 km to 160 km tangent height.

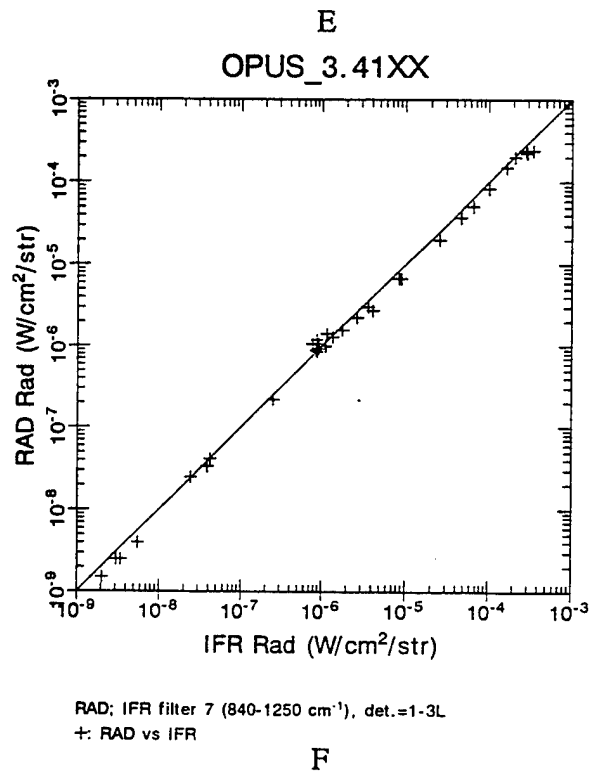
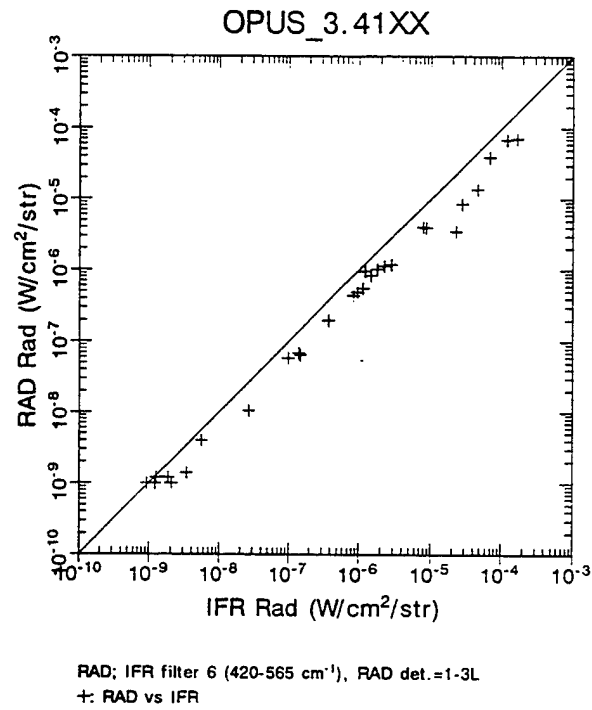


**Figure 114 (cont).** A comparison of the interferometer and radiometer radiance data for a vertical limb scan from about 15 km to 160 km tangent height.

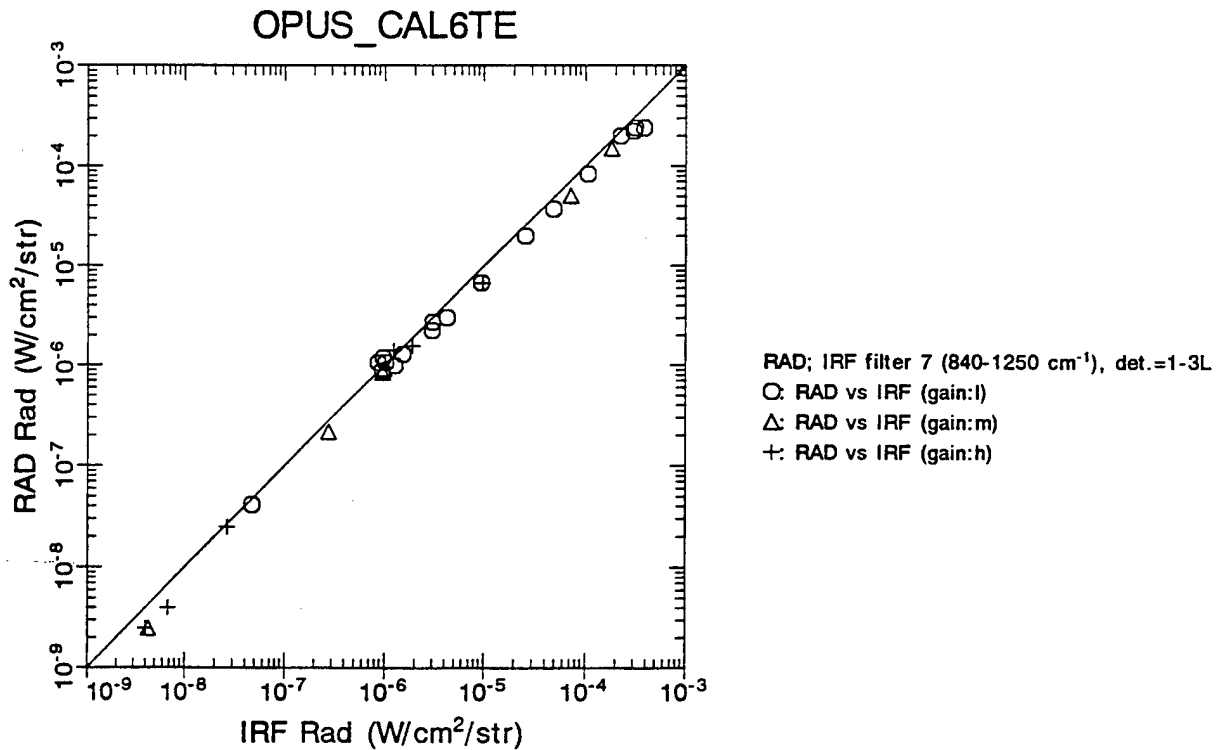


**Figure 115. Verification of interferometer gain linearity as a function of radiometer change in radiance.**

### 6.1.2.2 Interferometer Spectra versus Blackbody Response

Because the radiometer response to the reference stars compared favorably to the expected response, the interferometer calibration was more closely examined. The interferometer data provide two checks on calibration accuracy because the interferometer processing software can provide both the integrated absolute radiance and the spectral shape. These variables can then be compared with the theoretical values expected from the calibration blackbody temperatures. To determine the reliability of the interferometer calibration, some of the original calibration interferograms were input back into OPUS and their spectral shape was plotted against the theoretical shape of a blackbody at the temperature reported by the calibration equipment. This test was performed for each filter and detector at a high, medium, and low dc value for each bias mode.

At the lower radiance levels, where D3-1 to D3-4 were in the medium bias mode, the absolute radiances from the two radiance curves (measured and theoretical) agree almost exactly. Figure 116 shows the results of a middle dc level interferogram for each filter for D3-4 for the medium bias mode. These results are typical of the other detectors. These figures show obvious noise in the RSR curves for filters 1 and 2. The figures also show that the curves agree for filters 3, 5 and 7, while filter 6 shows a significant deviation in the RSR below about  $450 \text{ cm}^{-1}$ , which is probably caused by the light leak in MIC2 at these wavelengths. This deviation could explain a significant portion of the extra offset in the filter 6, interferometer-radiometer curve. It can be concluded from these data that the interferometer medium bias data are accurate, especially at the lower radiance levels. This agrees with the response of the CIRRIS flight data analysts who have used use medium bias data. At the low and medium radiance levels, the theoretical (Planck) curve and that reported by OPUS are identical for all filters, except filter 6.

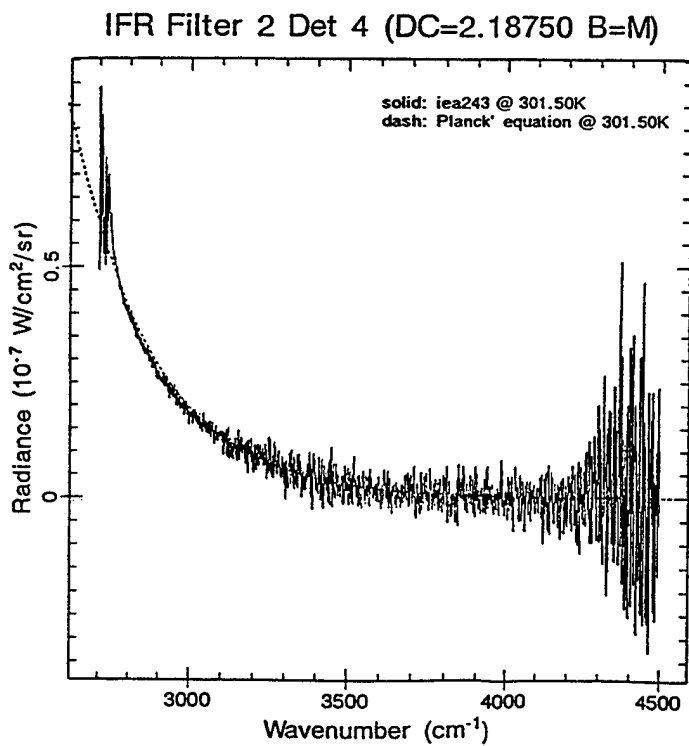
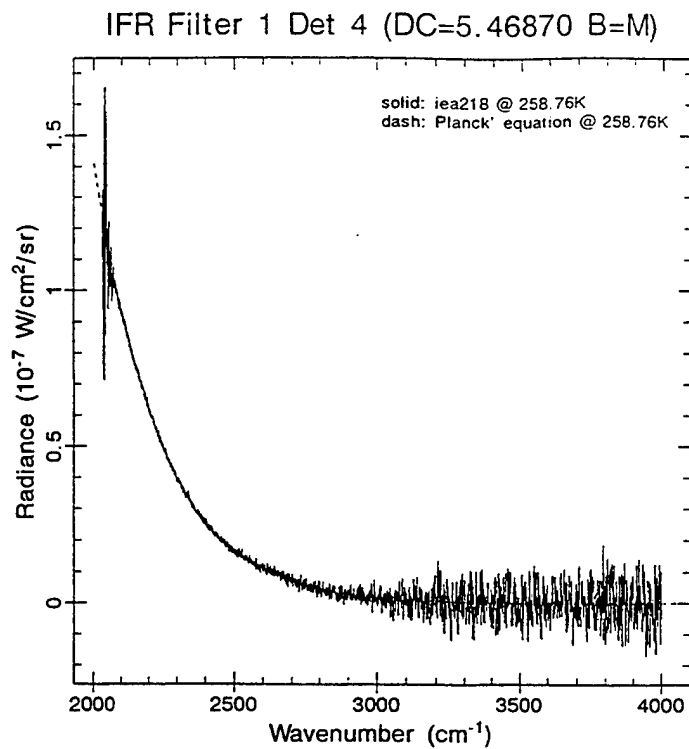
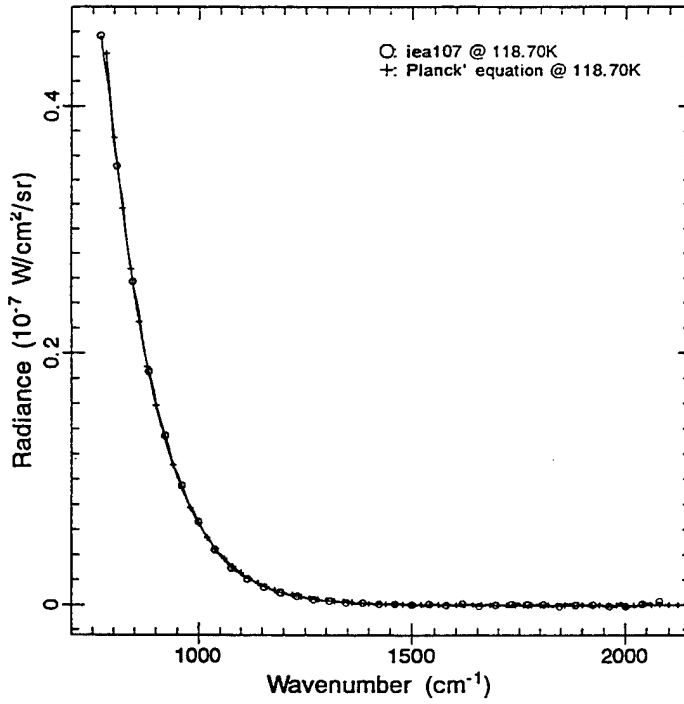


**Figure 116. Examples of middle level dc calibration spectra for D3-4, medium bias mode, compared with the theoretical spectra.**

IFR Filter 3 Det 4 (DC=0.85940 B=M)



IFR Filter 5 Det 4 (DC=3.20312 B=M)

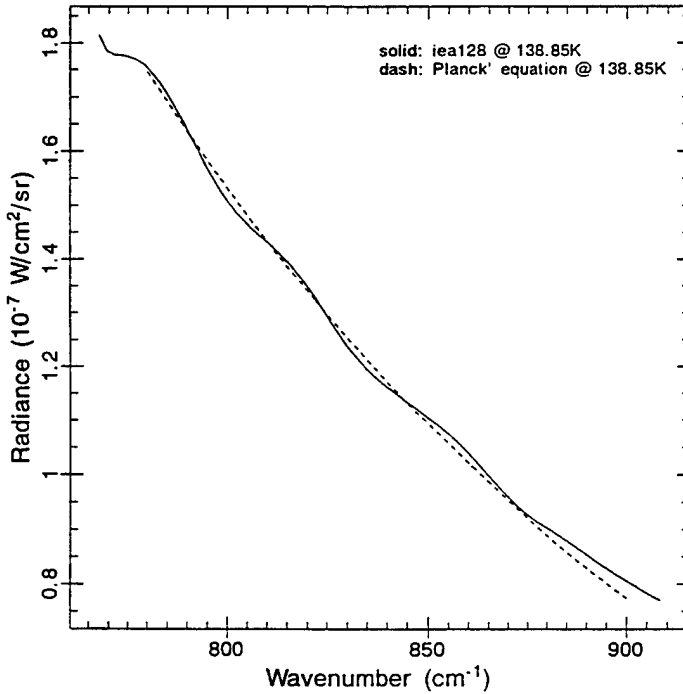
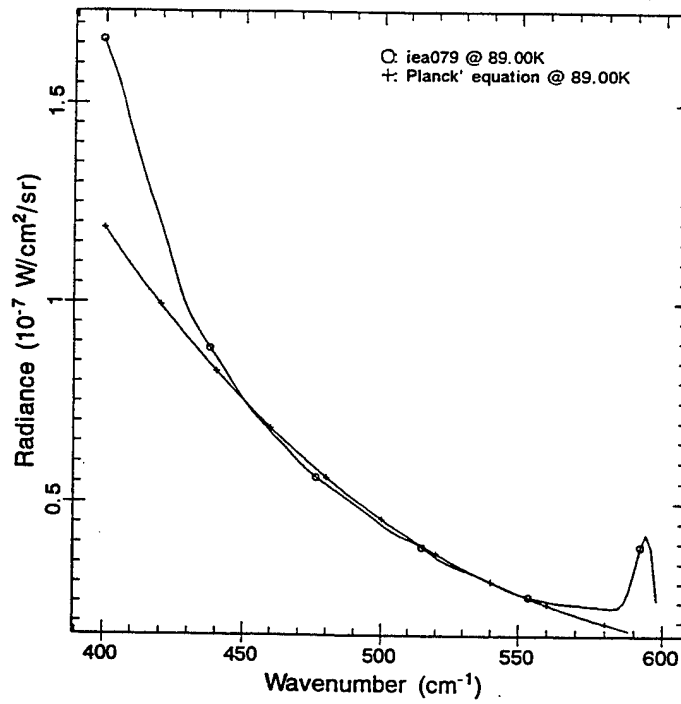


Figure 116 (cont). Examples of middle level dc calibration spectra for D3-4, medium bias mode, compared with the theoretical spectra.



IFR Filter 6 Det 4 (DC=0.78130 B=M)



IFR Filter 7 Det 4 (DC=1.32810 B=M)

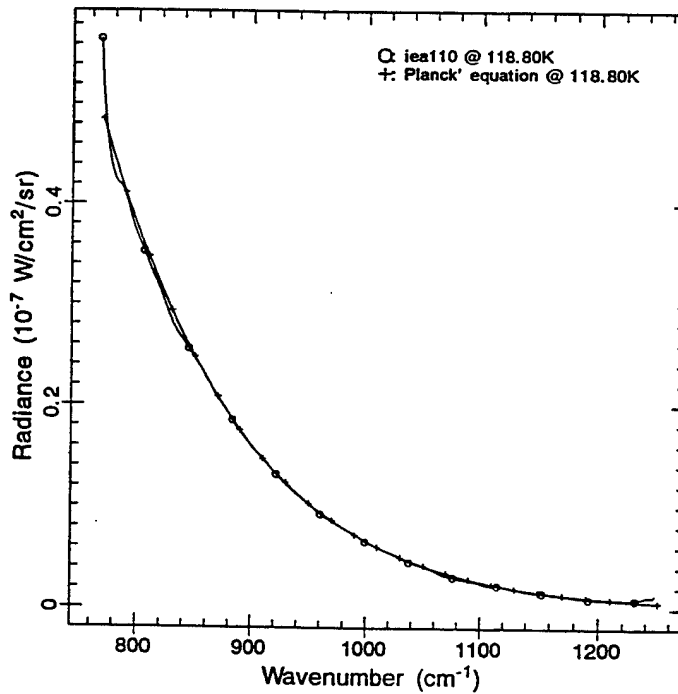


Figure 116 (cont). Examples of middle level dc calibration spectra for D3-4, medium bias mode, compared with the theoretical spectra.

The low bias OPUS spectra for each detector and filter were then plotted against their theoretical blackbody curves. In addition, the curves were plotted for the medium bias spectra for D3-5. These plots revealed significant differences. Figure 117 shows that the two curves deviate at higher radiance (dc) values for some of the filters. Only the reported spectra and the theoretical curve for filter 1 agree at all temperatures for low and medium bias.

Figure 118 shows the medium bias results for D3-5. The OPUS-derived calibration interferogram in this figure shows three small problems. The curves show both an offset (temperature) error, an error in the slope of the RSR curve, and uncompensated channel spectra. Because of the low sensitivity of D3-5, the RSR curve had to be collected using a source configuration that added additional channel spectra (see Figure 68). The theoretical curve for 269.09 K averages the peaks and valleys of the channels at about  $825 \text{ cm}^{-1}$ , but cuts below the curve at about  $1000 \text{ cm}^{-1}$ . Reducing the magnitude of the theoretical curve by 0.92 brings the OPUS-derived curve down to the average at  $1000 \text{ cm}^{-1}$ . Some of this offset could be due to extra energy in the RSR due to the MIC2 light leak, but at this temperature only a small part of the extra slope would come from this feature. The error resulting from this feature is about  $\pm 4\%$ . The extra offset added to the 1-1 comparison by the D3-5 low bias calibration is shown in Figure 119.

Figure 120 shows examples of the low bias data for interferometer filters 1 and 3. Filter 1 shows a near perfect match to the theoretical curve, while the filter 3 curve shows a significant deviation of the curves above about  $1500 \text{ cm}^{-1}$ . This deviation results in the large jump in the inter-comparison curve for radiometer filter 2 above about  $10^{-7}$  (Figure 113). The theoretical blackbody versus OPUS-derived comparison curve for filter 3 shows a good fit for a temperature 2 K warmer than that reported. At about 1600 K, noise in the RSR is improperly rectified and turned into an increase in the RSR that causes the curves to separate.

During the calibration, a nonlinearity correction was developed for the low bias data. A version of OPUS using this correction was developed and tested. The results of this correction on the reported versus theoretical spectral radiance is shown in Figure 121. At the lowest temperature, the reported temperature appears to be too large. This difference increases with temperature (radiance). The reason for this inconsistent correction is under investigation. The use of the medium bias RSR with this correction in OPUS could contribute to the problem.

The effect of these errors in the interferometer low bias calibration implementation on the results computed for radiances collected lower in the atmosphere is shown in Figure 122. This figure compares an ozone profile collected by CIRRS with measured values reported by other investigators using other methods. The gas concentrations developed using uncorrected radiance data from filter 7 are about 15% too large. A similar response is seen when radiances from filter 3 are used, but the bias is about 25%. When the low bias data for these filters is reduced by these factors, the CIRRS data for the stratosphere agrees with that collected by other experiments. Table 32 shows the radiance coefficients developed by SDL to be applied to the low altitude interferometer data to bring the integrated radiance data to the same level as reported for the same scene by the radiometer. These coefficients have been verified against CFC,  $\text{HNO}_3$ , and other gases.

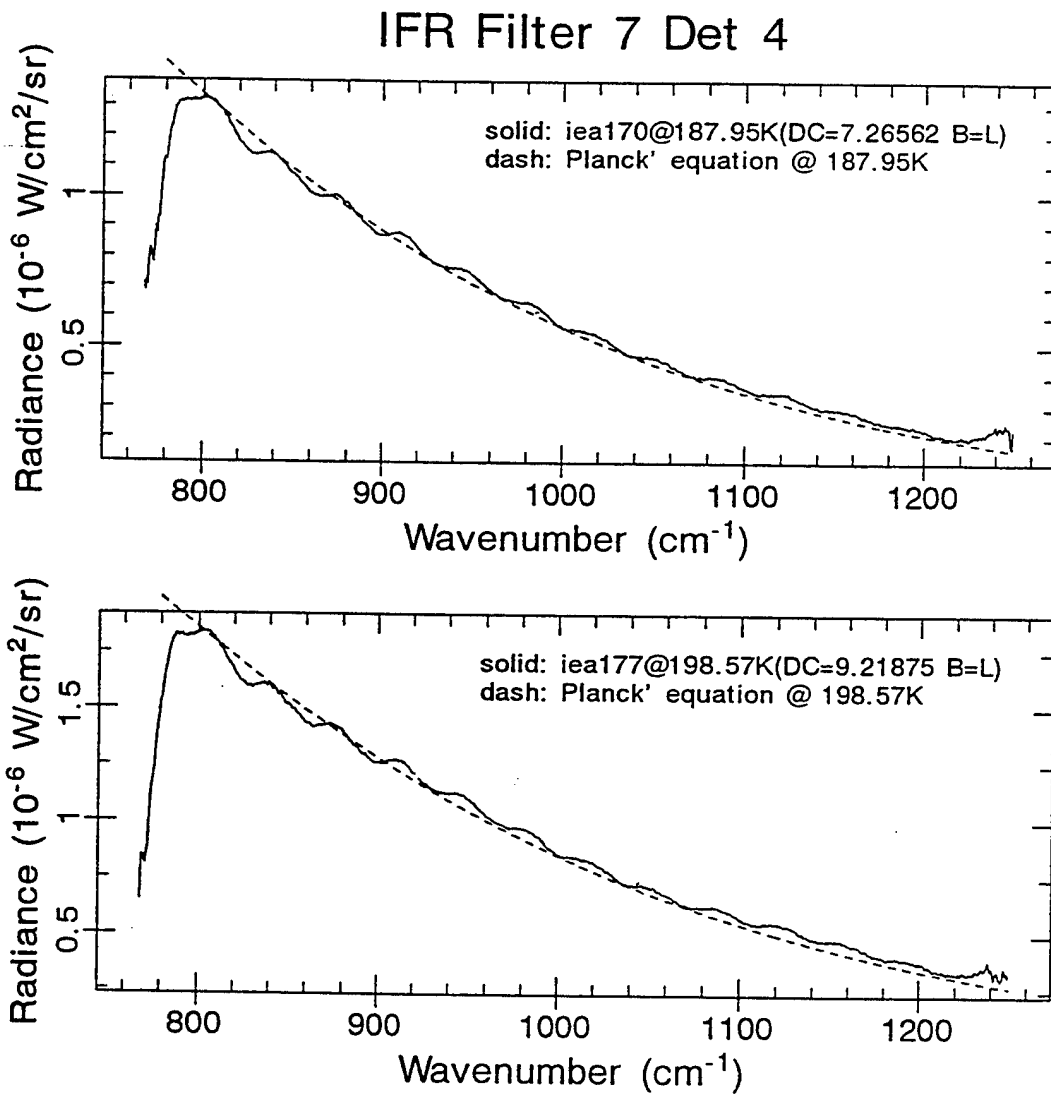


Figure 117. Two examples of comparisons of calibration spectra compared with theoretical spectra for D3-4, filter 7, low bias.

## IFR Filter 7 Det 5

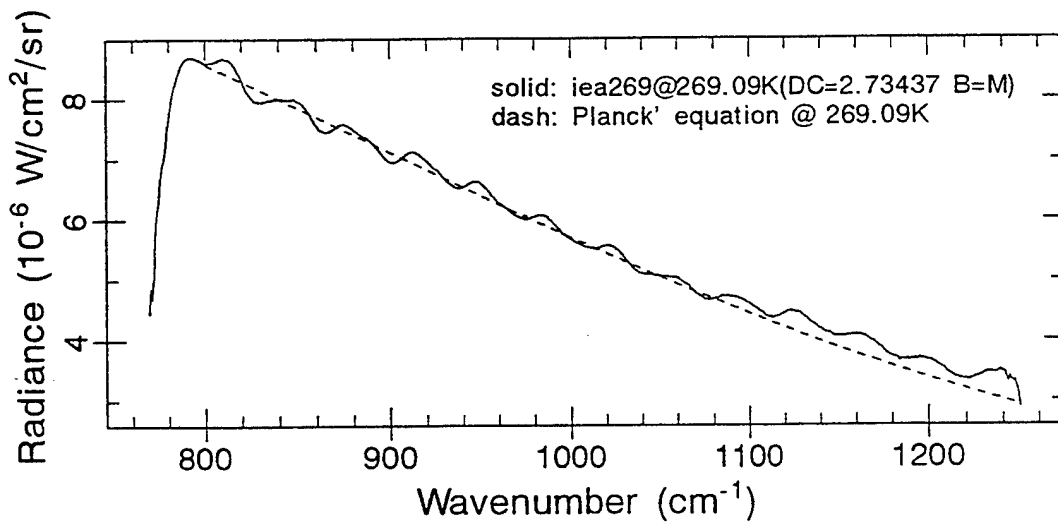
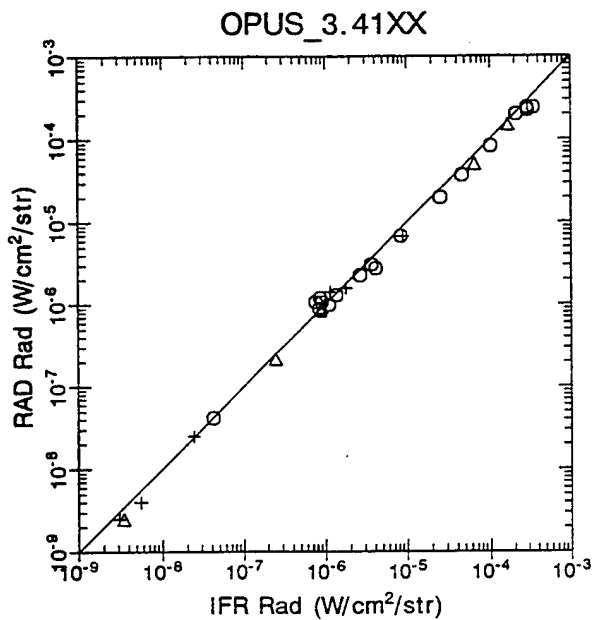


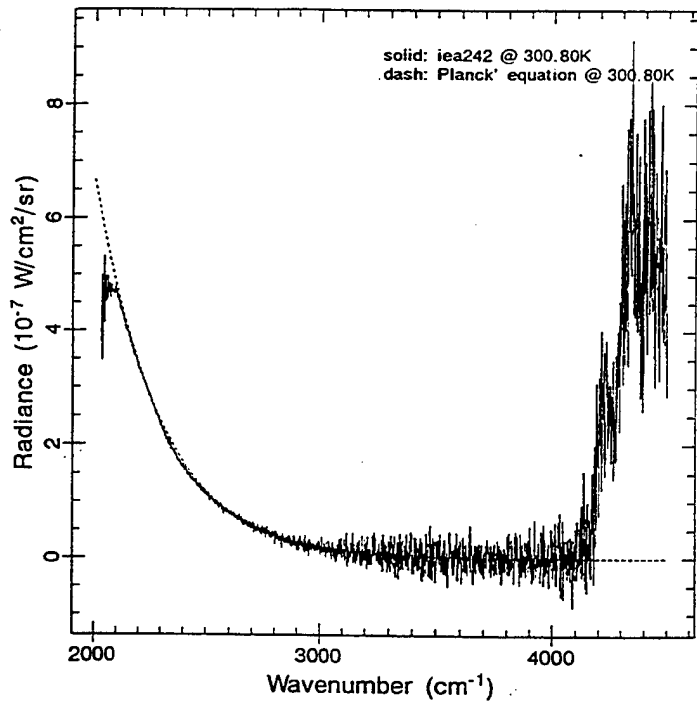
Figure 118. A comparison of calibration spectra and theory for detector 5, medium bias.



RAD; IFR filter 7 (840-1250 cm<sup>-1</sup>), RAD det.=1-3L  
 O: RAD vs IFR (gain:l)  
 Δ: RAD vs IFR (gain:m)  
 +: RAD vs IFR (gain:h)

Figure 119. The effect of interferometer gain on the radiometer-interferometer relationship.

IFR Filter 1 Det 4 (DC=1.48440 B=L)



IFR Filter 3 Det 3 (DC=3.9063; B=L)

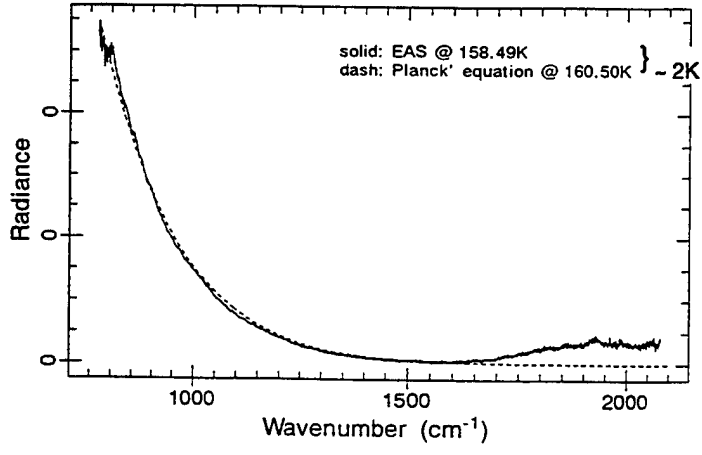
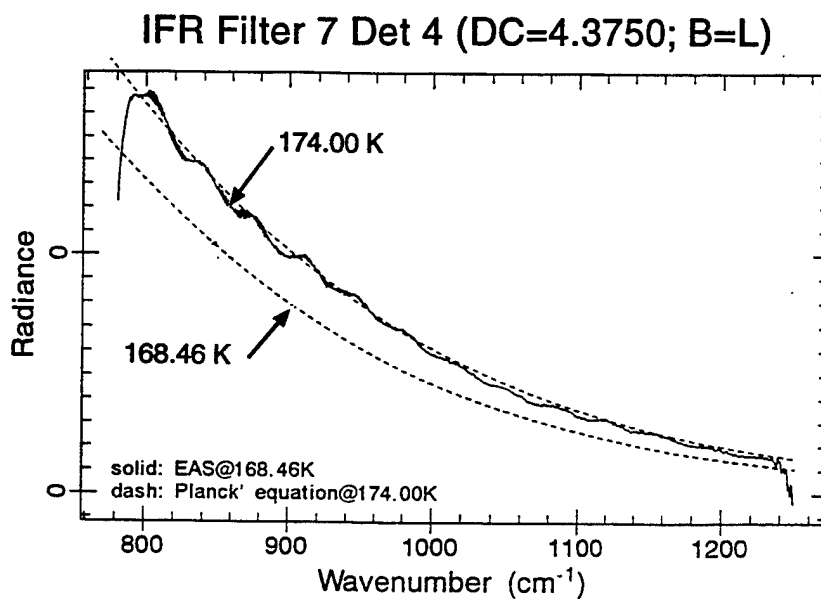
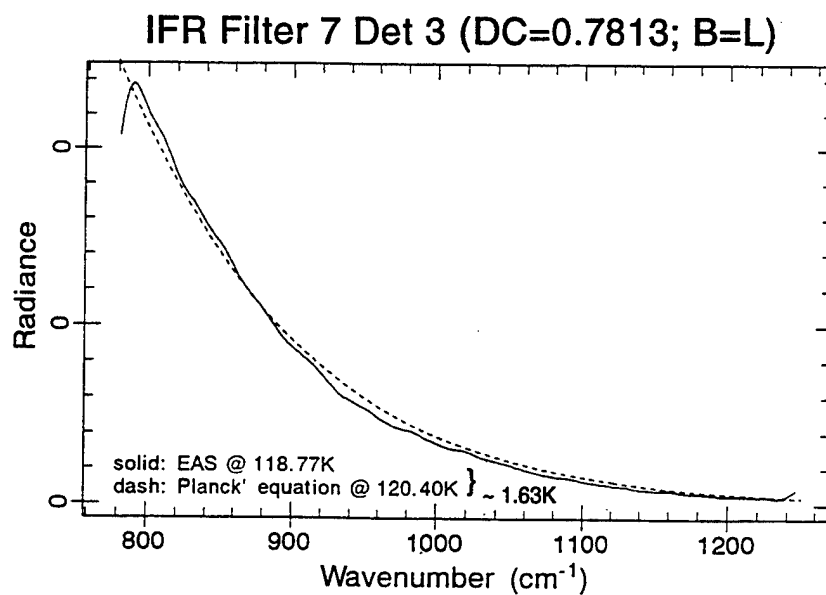


Figure 120. Two examples of the comparison of the calibration spectra with the theoretical shape for low bias.



**Figure 121. Two examples of the large differences in the calibration and theoretical spectra generated by OPUS when the nonlinearity correction was tested.**

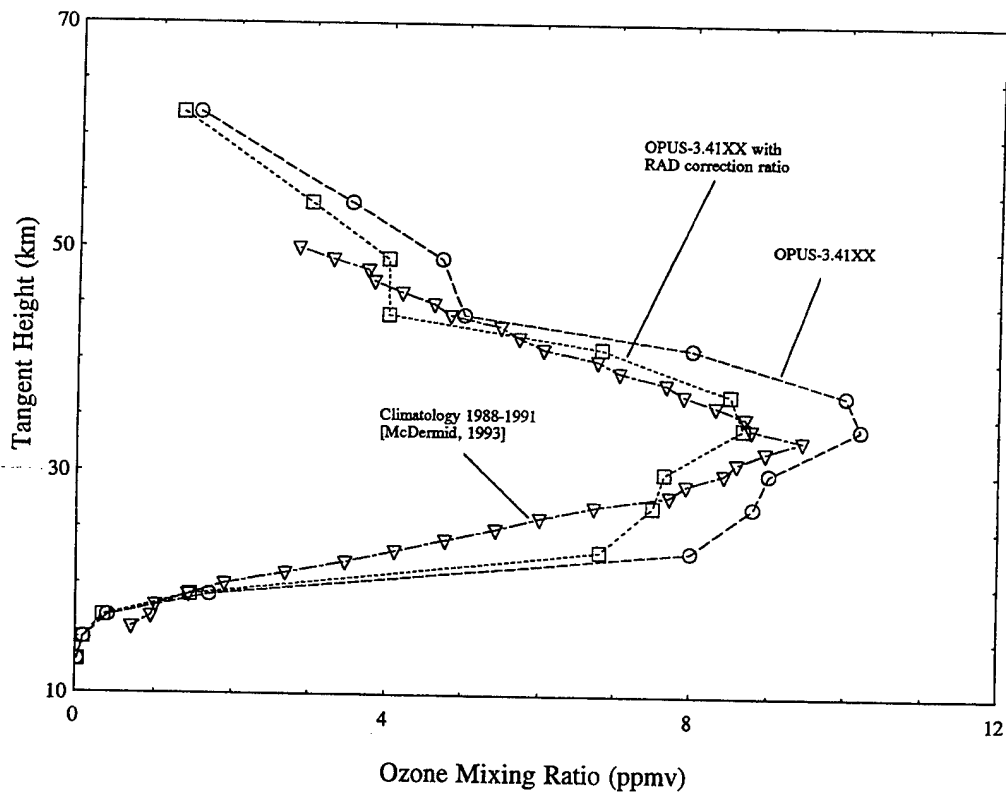


Figure 122. CIRRIS data (filter 7) of ozone profile comparison with climatology.

Table 32. Radiometer and Interferometer Comparisons for Filter Pairs

Radiometer Filter	Integration Region (cm <sup>-1</sup> )	Interferometer Filter	Coefficient Multiplication Factor
0	555.0 - 1195.0	0	1.00
1	2207.0 - 2450.0	1	0.90
FP2	2700.0 - 3700.0	2	NA
3	1119.8 - 1692.1	3	0.75
5	775.0 - 909.00	5	0.80
6	420.0 - 565.00	6	0.50
7	840.0 - 1251.0	7	0.85

### 6.1.3 Radiometer and Interferometer Calibration Accuracy

Based on the analysis described in this section and current experience with the CIRRIIS flight data, the following conclusions can be made about the accuracy of the main instrument calibrations.

#### 6.1.3.1 Radiometer

The results of the analysis of the irradiance calculations as returned by OPUS of the star crossings using data from both filter 0 (8.37 - 18  $\mu\text{m}$ ) and filter 1 (4.08 - 4.48  $\mu\text{m}$ ) indicate that the radiometer calibration may be about 5% lower than the irradiance values being reported by IRAS. This information is based on a white spectral content assumption in OPUS and a paper integration of the spectra of the stellar irradiance data from IRAS. This analysis continues to be refined. The Alpha Centary measurement in Block 42B is not currently included in the analysis. The track of this star is along the Y axis of the array and may not have been completely on the radiometer detectors. The values reported by filters 0 and 1 are within a few tenths of a percent of each other, and are both about 4.6% low. How well the intercalibration of the other filters holds cannot be judged, but the intercomparison with the interferometer would suggest that filter-to-filter variation in the radiometer calibration is within  $\pm 5\%$  of each other. The calibration of filter 6 is probably not as precise, and no uncertainty values have been ascribed to it.

#### 6.1.3.2 Interferometer

No interferometer data have been successfully reduced against the stellar sources; therefore, to judge the interferometer calibration, spectral consistency checks of the calibration data, earth limb analysis, and comparison with the radiometer outputs must be made. The analysis described in this section indicates that the interferometer calibration in medium bias is self consistent within about  $\pm 10\%$  for all detectors and filters except for filter 6 and interferometer detector 5. The low bias and D3-5 calibrations have several problems that continue to be analyzed and would widen the uncertainty bounds on data collected. We believe that the uncertainty of data reported by OPUS for these conditions may be too large by 15 to 20% for the short and middle filters and as much as 25% for filter 6. Filter 3 data in low bias should not be used for wavenumbers above about 1600  $\text{cm}^{-1}$  because of the improper handling of the RSR noise. The low bias offset coefficients provided in this report should bring the low bias and detector 5 data back to within the same error bounds as reported for the radiometer and for the medium bias data.

The capability to analyze long wavelength ( $>20 \mu\text{m}$ ) calibration data needs improvement. Analysis of the calibration intercomparison between the radiometer and interferometer shows about a 50% difference in the absolute calibrations for data collected using filter 6. The MIC2 light leak and the uncertainty of the Bomem calibration at wavelengths longer than 20  $\mu\text{m}$  are the prime sources of error in this wavelength region. Additional analysis could reduce the uncertainty in this filter band.



#### 6.1.4 Ancillary Sensors

The photometers were the only ancillary sensors subjected to a post flight calibration. Repeated, significant damage to the photometers during flight caused a significant calibration problem because the sensitivity level appeared to change with each block. During post flight calibration, the stim flash at the beginning of each block was used to establish a sensitivity level for that block. Since most blocks began in the dark and ended in daylight, the damage to the tube as a result of exposure to earthshine occurred after all dark measurements had been completed.

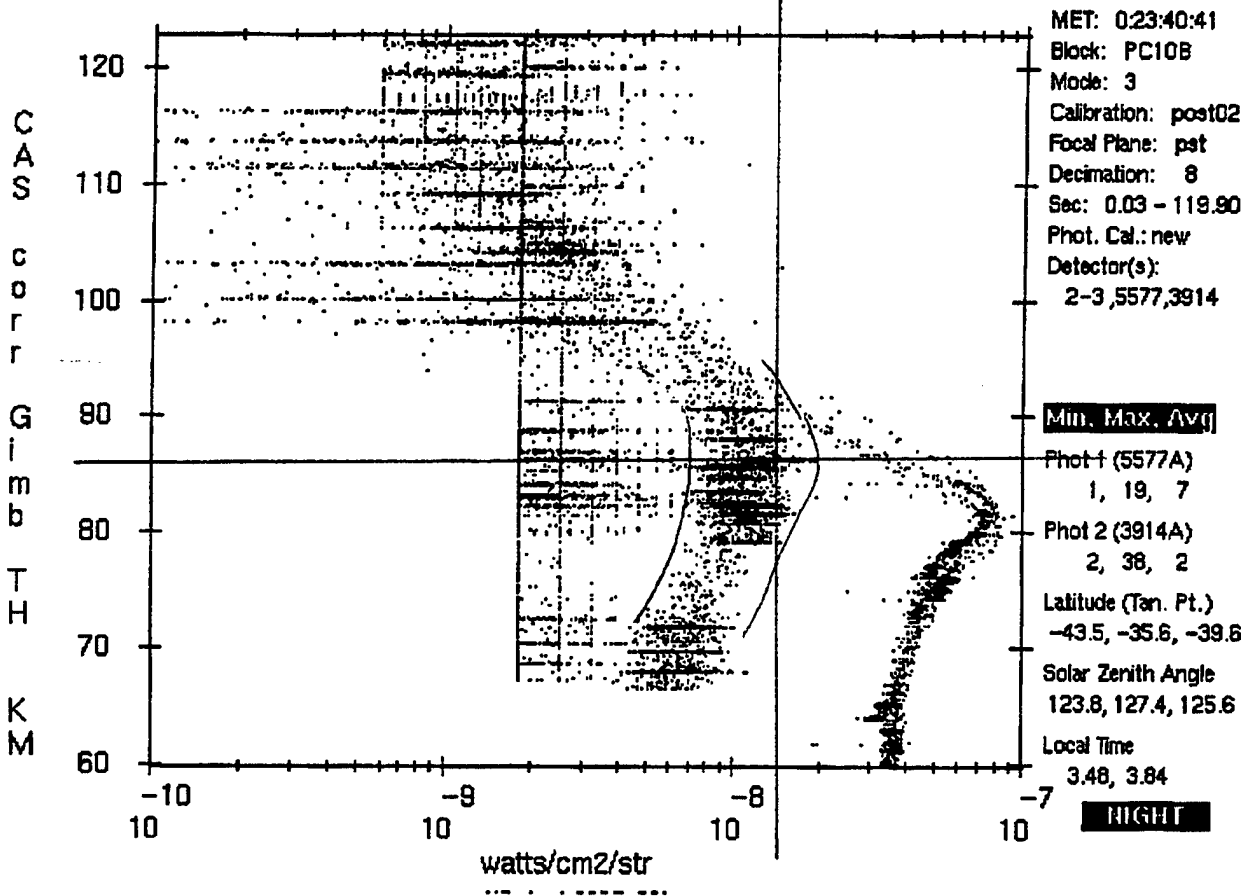
An attempt was made to verify the stability of the stim adjustment of the post flight calibration by studying the photometer readings recorded when CIRRIS was staring in the region of the air glow layer at about 90 km. In this region, the 5517Å photometer should be stimulated and the 3914Å photometer should show no response when aurora are not present. The results of this study are shown in Table 33. In the crossings examined, only 5 show low levels of energy recorded by the 3914Å photometer. Aurora or moonshine eliminate the use of the other crossings. Three of the air glow crossings occur in Block 10B at the beginning of the flight, while the other two occur in Block 11F near the middle of the mission and Block 11A near the end of the measurements. The measurements for Blocks 10B and 11A are shown in Figures 123 and 124, respectively.

While the number of photometer measurements of the air glow layer in truly dark conditions is low, the available measurements provide a good indication that our calibration assumptions are correct. The Block 10B readings are 12.8, 12.9 and 12.0 kR for a mean of 12.6, with a standard deviation of 0.49 kR. The readings from Blocks 11F and 11A are 12.0 and 12.2 kR, falling well within the scatter of the block 10B data. This study verifies that the calibration adjustment scheme developed using the flight stim pulses is consistent with the flight measurement data.

**Table 33. A Comparison of Photometric Responses to Air Glow Layer (89 km) Crossing Through the Mission. (Measurements with 3914 levels greater than about 2 kR have significant moonshine or auroral contamination.)**

Block	Measurement time	3914Å (counts)	kR	5577Å (counts)
10 A	0:20:38:08-16	---	8.7	15.17 Seg. Fault
10 A	0:20:43:26-36	---	14.2	24.7 Seg. Fault
10 B	0:23:40:41-42:46	.22	12.8	11.286
10 B	0:23:44:30-36	24.4 mom	16.3	26.286
10 B	0:23:38:18-39.25	.33	12.9	17.96
10 B	0:23:39:08-39.27	.31	12.0	21.30
12 A	01:12:56:31-42	4.93	13.5	17.02
12 A	01:12:59:40-51	4.53	14.0	17.53
12 A	01:13:02:33-46	4.98	19.0	25.15
12 A	01:13:05:42-54	4.49	14.8	19.03
12 B	01:14:27:17-29	6.0	25	27.40
12 B	01:14:30:11-24	8.05	29.0	35.86
12 B	01:14:33:20-30	7.11	39.3	49.33
12 B	01:14:36:26-38	5.05	29.5	34.84
11 F	1:20:29:16-45	1.44	12:0	13.88
11 A	2.12:58:19-44	0.58	12:2	12.76
11 G	01:15:54:06-24	3.63	16.4	20.40

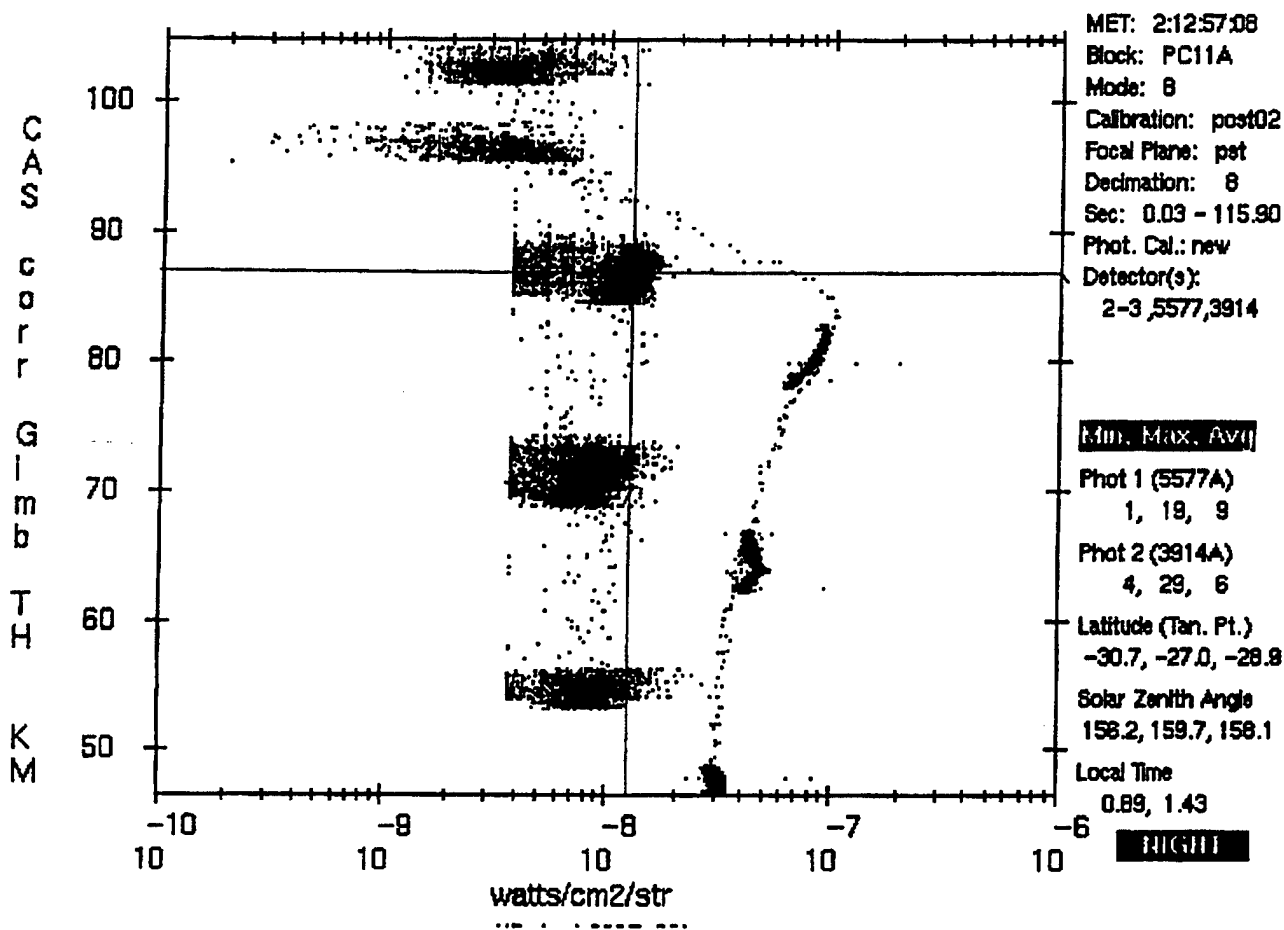
Coordinates: 1.383E-08, 8.613E+01



Date/Time: 06-Jul-93, 14:24  
OPUS Version # 3.41xx  
PTG/CAL/HKG/FPL: 008/004/001/pst

Figure 123. 5577 Photometer response to air glow layer at about 85 km in block 10B near the early part of the mission.

# CIRRIS 1A PRELIMINARY DATA



Date/Time: 28-Jun-94, 20:08  
 OPUS Version # 3.41xx  
 PTG/CAL/HKG/FPL: 008/004/001/pst

Figure 124. 5577 Photometer response to air glow layer at about 85 km in block 11A near the end of the mission.

## REFERENCES

- Ahmadjian, M., R. M. Nadile, J. O. Wise, and B. Bartschi, CIRRIS 1A Space Shuttle Experiment, *Journal of Spacecraft and Rockets*, 27, 6, pp. 669-674, Nov - Dec 1990.
- Bartschi, B., J. C. Kemp, D. A. Burt, G. D. Allred, and L. J. Zollinger, Applying an Interferometer Spectrometer Aboard the Space Shuttle with a Payload Specialist in the Control Loop, *Proceedings of SPIE*, Vol. 787, May 1987.
- CIRRIS 1A Engineering Calibration Interim Report, SDL/USU, SDL/89-034, May 1989.
- CIRRIS 1A Final Engineering Calibration Report, SDL/USU, SDL/91-056, April 1991.
- CIRRIS 1A Post Flight Calibration Test Plan, SDL/USU, SDL/91-011, June 1991.
- CIRRIS 1A Post Flight Calibration Interim Report, SDL/USU, SDL/92-004, January 1992.
- Elwell, J.D., and J.C. Kemp, SPIRIT II Interferometer and Radiometer PCM Encoder Format Specifications, SDL/USU, SDL/90-056A, May 1991.
- Jacobsen, L., and S. Sargent, Calibration of a Helium-cooled Infrared Spatial Radiometer and Grating Spectrometer, *Proceedings of SPIE*, Vol. 1340, pp. 217-228, July 1990.
- Jacobsen, L., Statistical Approach to Calibrating Focal Plane Arrays Based on Nominal Detectors, *Proceedings of the 2<sup>nd</sup> Annual SDL/USU Symposium on Cryogenic Infrared Radiometric Sensor Calibration*, September 18-20, 1991.
- Kemp, J., E.R. Huppi, and M. Madigan, Measurements of High Out-of-Band Filter Rejection Characteristics, *Proceedings of SPIE*, Vol. 1112, pp. 433-441, 1989.
- Russell, R.W., G.M. Boyd, S.C. Chapman, J.E. Cox, D.J. Edelson, L.M. Friesen, J.A. Hackwell, A.M. Kishi, D.K. Lynch, C.J. Rice, and G.S. Rossano, Infrared Detector Array Test Program for the Kuiper Infrared Technology Experiment (KITE) Final Report, Space Sciences Laboratory, The Aerospace Corporation, April 1987.
- SPIRIT II Infrared Sensor Calibration Test Plan, SDL/USU, SDL/89-026A, February 1991.
- Wyatt, C.L., *Radiometric Calibration: Theory and Methods*, Academic Press, New York, 1978.
- Wyatt, C.L., and L. Jacobsen, CIRRIS 1A Final Calibration Test Report, Appendices A, B, and C, SDL/USU, CSE/87-039, April 1987.
- Wyatt, C.L., L. Jacobsen, and A. Steed, Portable Compact Multifunction IR Calibrator, *Proceedings of SPIE*, Vol. 940, pp. 63-72, 1988.
- Wyatt, C.L., An Engineering Calibration of CIRRIS 1A, CSE/86-011, January 1989. Wyatt, C. L., "Sources of Error in Radiometric and Spectrometric Measurements," SDL/USU, SDL/90-060-II, September 1991.

Wyatt, C.L., "Acceptance Test Data and Algorithms for Predicting SPIRIT III Radiometric Performance," SDL/USU, SDL/92-048, June 1992.

Yap, B.K., CIRRIS Radiometer Postflight Calibration Final Report, Yap Analytics, Inc., June 1992.

Zachor, A.S., Software for Processing CIRRIS Interferometer Data, August, 1992.

**APPENDIX 1**

**CIRRS 1A PROGRAM SUMMARY**

# CIRRIS 1A PROGRAM SUMMARY

## INTRODUCTION

The Cryogenic Infrared Radiance Instrumentation for Shuttle (CIRRIS 1A) instrument, launched on the shuttle Discovery (STS-39) on 28 April 1991, was developed to characterize the phenomenology and dynamics of upper atmospheric processes. Primary sponsors for the CIRRIS mission were the Geophysics Directorate of the United States Air Force Phillips Laboratory and the Strategic Defense Organization of the Department of Defense.

CIRRIS is a state of the art, cryogenically cooled instrument designed to collect simultaneous high resolution spectral and spatial measurements of the upper atmosphere and space objects. The instrument was designed, constructed, calibrated, and tested by the Space Dynamics Laboratory at Utah State University (SDL/USU), and features two primary infrared sensors: a high resolution Michelson interferometer and a dual-channel radiometer. The sensors share the collection optics of a high off-axis-rejection telescope. The telescope has a 30.48-cm diameter, D-shaped aperture with an image quality of 0.5 mrad on axis, optical efficiency of 60%, and out-of-field-of-view rejection of  $1 \times 10^{-10}$  at  $2.5^\circ$ . The optics, detectors, and preamplifiers are cooled with helium to temperatures of 12 K to maximize instrument sensitivity to faint infrared sources. Two photometers, two low light level television (LLLTV) cameras, a 16-mm film camera celestial aspect sensor (CAS), and an infrared horizon sensor are coaligned on the outside of the telescope heat exchanger. The entire assembly is mounted on a two-axis gimbal system to provide pointing and scanning capability. The entire payload mass is 2045 kg. During flight, all of the sensor and housekeeping data were redundantly recorded on tape recorders for post flight reduction and analysis. Figure 1 is a drawing of the CIRRIS in measurement position with the shuttle in gravity gradient mode, showing the scan capabilities of the gimballed sensor.

The primary objective of the CIRRIS mission was to obtain simultaneous spectral and spatial measurements of infrared atmospheric emissions in the spectral region between 2.5 and 25  $\mu\text{m}$  over altitudes ranging from the earth's surface to 260 km. Figure 2 shows a current U.S. Air Force radiance model of atmospheric airglow emissions in this spectral range at a tangent height of 100 km. The emission plot of a cold satellite target is superimposed on this trace. This figure shows significant emission peaks at 5.3  $\mu\text{m}$  (NO), 10  $\mu\text{m}$  ( $\text{O}_3$ ), and 15  $\mu\text{m}$  ( $\text{CO}_2$ ). The airglow emissions are much stronger than the superimposed satellite emissions except in narrow areas or windows between strong atmospheric bands. The goal of the CIRRIS experiment was to precisely define the extent of these spectral windows, including: (1) optimum wavelengths of atmospheric windows for detecting cold body targets, (2) background radiance levels in the window regions, (3) spatial structure (clutter) of the background in terms of power spectral densities, and (4) variabilities of earthlimb emissions as a function of day/night and geomagnetic activity.



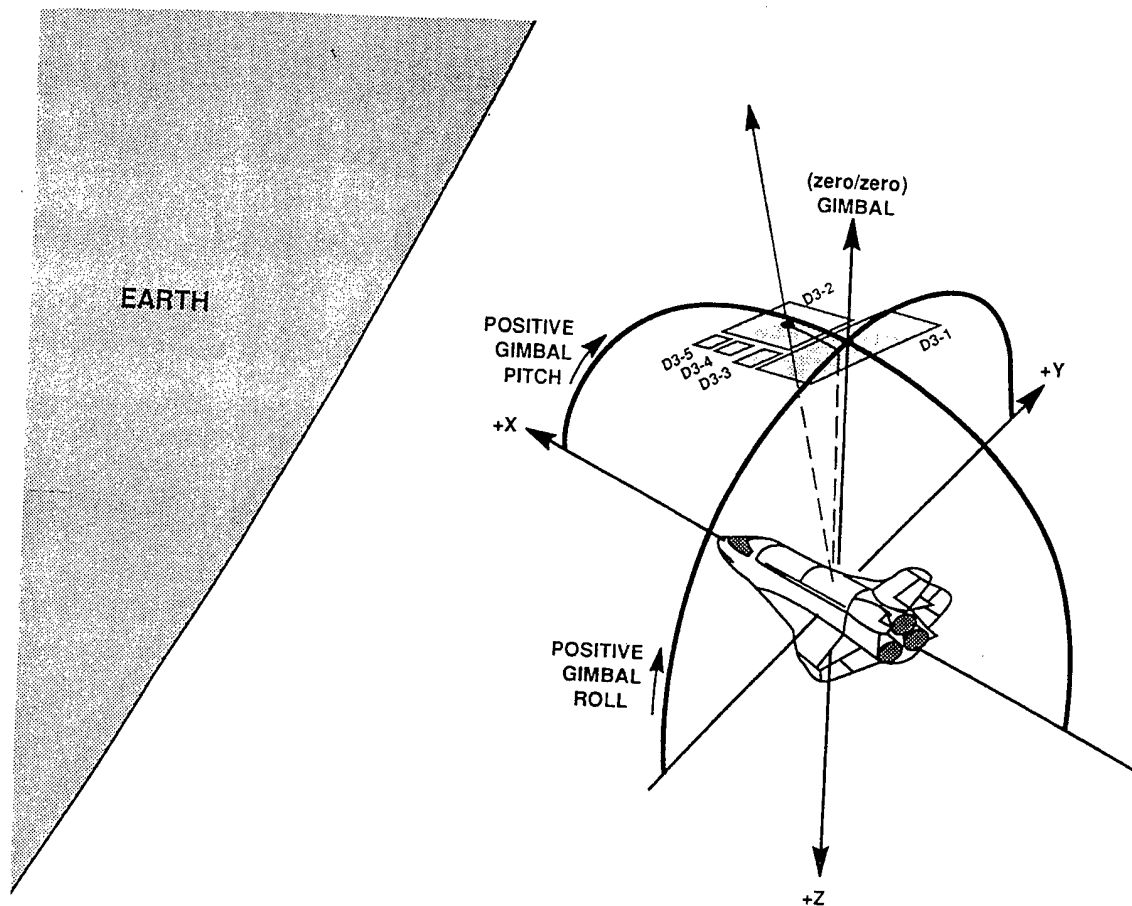


**Figure 1. A drawing of the shuttle Discovery in gravity gradient data collection mode, indicating the CIRRIS interferometer field of view.**

Exceptional data were obtained during the STS-39 mission, and analysis shows that all primary sensors performed well. This mission provided data to characterize background conditions, including target signatures and emissions produced by atomic and molecular species in the earth's upper atmosphere. The main observation targets were earthlimb airglow, celestial targets, and auroral emissions. Data obtained from this experiment will help refine knowledge of the background radiance and structure of atmospheric infrared emissions, and will be used to update and validate U.S. Air Force atmospheric models used in the design of operational systems.

A complete ground calibration of the primary and ancillary sensors was performed to verify the instrument design and to create algorithms necessary for post flight data reduction. The wide spectral range of the CIRRIS mission put special requirements on the sensor calibration. The calibration had to accurately cover a dynamic range approaching nine orders of magnitude over a wide spectral range, for two instruments with fundamentally different principles of operation.

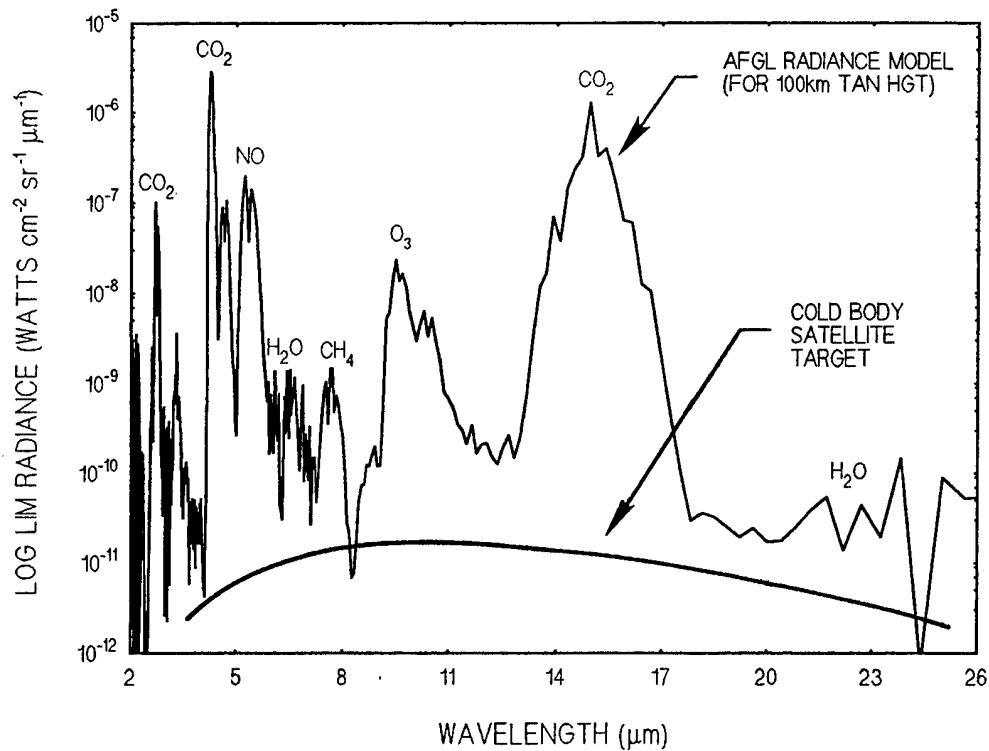


**Figure 2. Air Force earthlimb model of atmospheric infrared emissions compared with a theoretical 300 K, 1-m<sup>2</sup> blackbody target.**

The CIRRIS sensor underwent an engineering evaluation before flight and a full calibration after the mission. The infrared calibration was conducted using a multifunction infrared calibration source (MIC2) designed by SDL/USU. MIC2 contains extended, Jones, scatter, and point source functions within a single vacuum shell. A complete description of MIC2 is in "SPIRIT II Infrared Sensor Calibration Test Report, Volumes 1 and 2" (SDL/92-021). The CIRRIS photometers were calibrated using a National Institute of Standards and Technology (NIST) calibrated light source and a series of calibrated neutral density filters. The horizon sensor was calibrated at the manufacturer, and the LLLTV systems and the CAS did not require calibration. Alignment of the main sensors and the subsystems was measured on the ground using a precision theodolite system, and was verified in flight using star crossings. An overview of the calibration procedures and results is provided in this summary.

## PRIMARY SENSOR CALIBRATION

### Primary Sensor Description

The primary sensors of the CIRRIS instrument are a multi-band spectral radiometer and a high-resolution Michelson interferometer. Detailed descriptions of the sensors are found in Bartschi et al. (1987) and Ahmadjian et al. (1990). Table 1 lists the primary sensor design specifications.

The CIRRIS radiometer contains two focal plane arrays (FPA) whose images are overlapped by the use of a dichroic beamsplitter. The focal plane arrays include a 9-element arsenic-doped silicon (Si:As) array (FP1) and a 5-element bismuth-doped silicon (Si:Bi) array (FP2). These arrays are coaligned with the interferometer focal plane. The 9-element FPA is located behind an 8-element filter wheel, and the 5-element FPA is housed behind a 2.95  $\mu\text{m}$  (2.5 - 3.4  $\mu\text{m}$  band width) fixed filter. The 2.95  $\mu\text{m}$  filter acts as a constant reference channel for comparison with the eight selectable bandpass filters. A combination of detector sizes, bias levels, and signal conditioning electronics makes the radiometer sensitive over a wide dynamic range; it is capable of measuring zodiacal light, earthlimb emissions, and hard-earth emissions. Figure 3 shows the flight configuration and angular fields of view of the detectors for the radiometer and interferometer FPAs.

The Michelson interferometer is a flex pivot design with three selectable scan lengths that provide spectral resolutions of 1, 4, and 8  $\text{cm}^{-1}$  with moving mirror scan times of 9.7, 2.7, and 1.5 sec, respectively. The spectral sensitivity of the interferometer is 4000 - 400  $\text{cm}^{-1}$ . The interferometer focal plane array is an impurity band conduction (IBC) type arsenic-doped silicon (Si:As) array (FP3) with five, various-sized detector elements to allow a wide range of measurement scenarios and resolutions. The focal plane optics are Ritchey-Chretien  $f/1.6$ . An 8-element filter wheel is used to reduce photon noise in selected bandpasses by minimizing out-of-band radiation, as shown in Figure 4. This figure also shows the correlation of the bandpass regions of the radiometer and interferometer. An auto-alignment mechanism is built into the interferometer. This mechanism would have allowed on-orbit alignment of the interferometer optics if they had become misaligned due to forces encountered during launch. This feature was not exercised.

The radiometer and interferometer were calibrated during the same cold cycles, but separately. Radiometric and interferometer data were not collected simultaneously.

### Radiometer Calibration

The radiometer calibration measured sensor point source response, spectral response, and absolute response. Because of known dielectric relaxation effects (DRE) in the bulk silicon detectors, individual response equations were fit to each detector range, and a linearity calibration was not performed. The positions of the interferometer and radiometer focal planes with respect to each other and to the interferometer field stop were mapped.

Table 1. CIRRIIS 1A Sensor Specifications

Parameter	Interferometer	Radiometer
Detectors	5-element IBC FPA	9-element Si:As FPA 5-element Si:Bi FPA
Optical filters	8 selectable	7 selectable, 1 fixed
Noise Equivalent Spectral Radiance (NESR)	$7.8 \times 10^{-13} \text{ W cm}^{-2} \text{ sr}^{-1} \text{ cm}^{-1}$ at $700 \text{ cm}^{-1}$	
Noise Equivalent Radiance (NER)	---	$7 \times 10^{-11} \text{ W cm}^{-2} \text{ sr}^{-1}$
Dynamic range	A to D: $6.5536 \times 10^4$  Feedback resistor difference between channel 5 and other channels: $3 \times 10^2$ Electronic gain: $1 \times 10^2$ 2 bias levels: $3 \times 10^0$ Ratio of det areas: $1.597 \times 10^1$  TOTAL: $9.42 \times 10^{10}$	A to D: $6.5536 \times 10^4$  Feedback resistor difference: $1 \times 10^0$ Electronic gain: $1 \times 10^2$ 3 bias levels: $1 \times 10^2$ Ratio of det areas: $2.4 \times 10^1$  TOTAL: $1.57 \times 10^{10}$
Field of view	$.93^\circ \times 1.5^\circ$	$1.2^\circ \times 0.2^\circ$
Aperture	$161 \text{ cm}^2$	$182 \text{ cm}^2$
Chopper	---	Tuned fork at 84.6 Hz

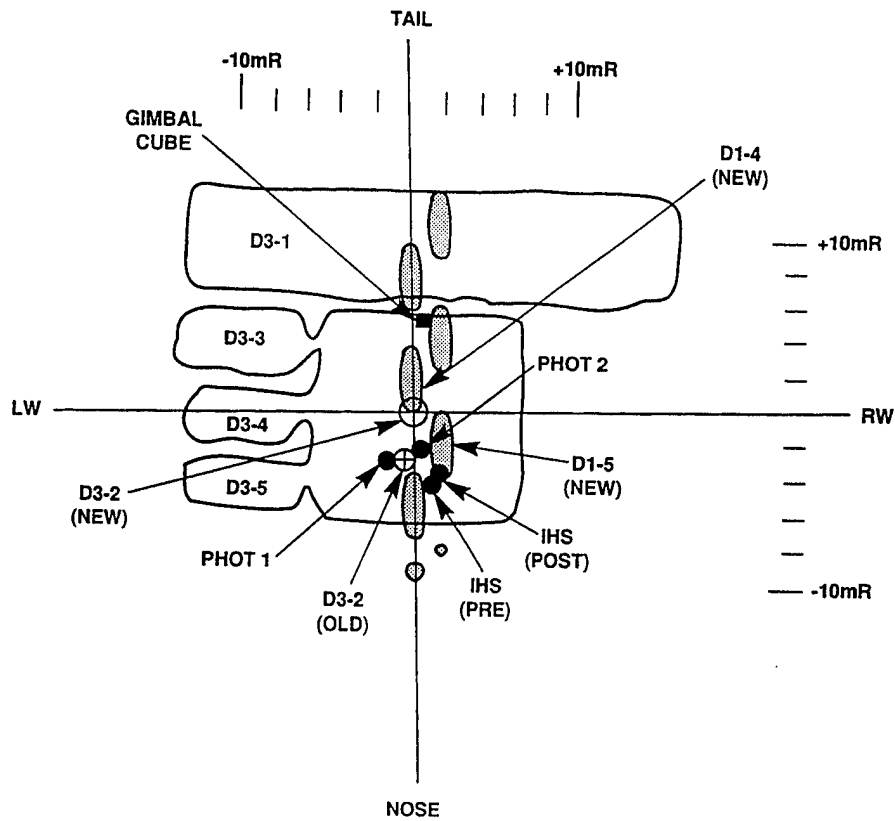


Figure 3. Measured flight radiometer and interferometer focal plane coalignment, along with ancillary sensors, at the 30% response level (provided by Boston College and Miranda Laboratories).

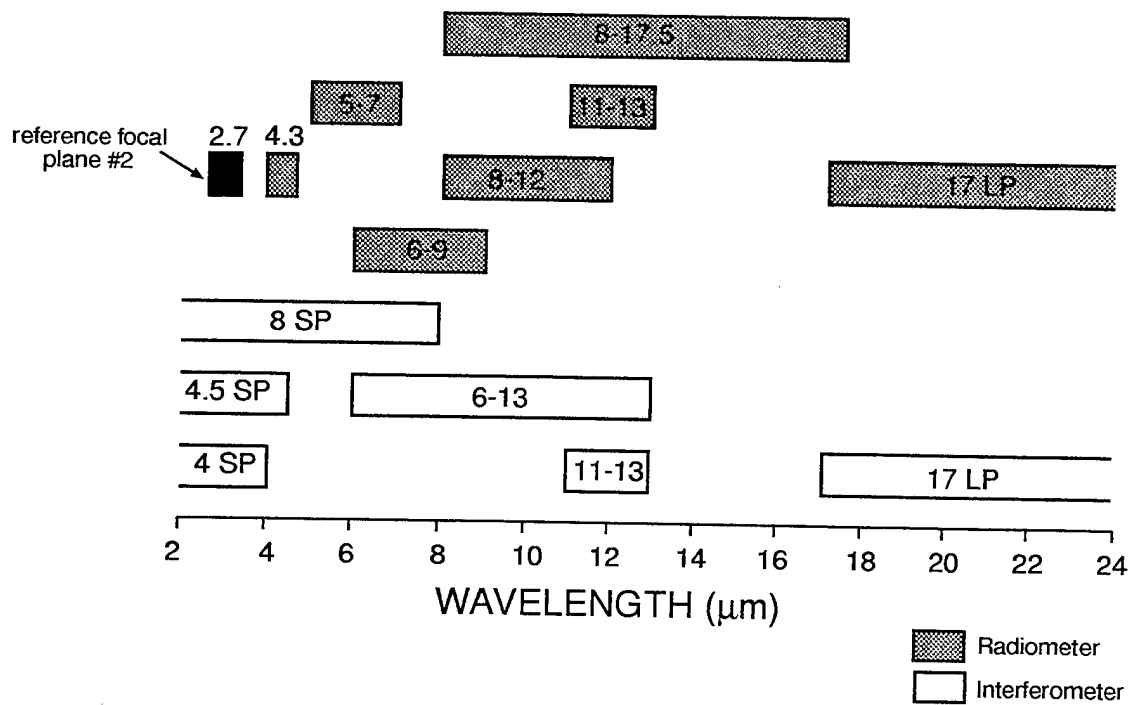


Figure 4. Radiometer and interferometer filter bandpasses.

## Point Source Spatial Response

The point response calibration measures the shape of the radiometer spatial response, effective field-of-view solid angles, detector modulation transfer function (MTF), and any glints or scatter locations. The focal planes were mapped seven times. Short (2.5 - 4.3  $\mu\text{m}$ ) and long (17 - 25  $\mu\text{m}$ ) wavelength maps were made of the entire field of view at  $0.1 \times 0.25$  mrad ( $X \times Y$ , respectively) using a 40  $\mu\text{rad}$  point. The area around the smallest detectors was mapped at  $0.05 \times 0.5$  mrad steps at short, middle, and long wavelengths. Maps of the detector response regions were developed and contoured. The detector field of view and solid angle responses were found to be uniform and to agree with design specifications. The response of each detector's surface was uniform to within 0.7 of the peak.

Much of the time devoted to the point source calibration was used to quantify the vignetting of the right side of the telescope's field of view. The reduction of the effective collecting aperture of the vignetted detectors was verified. This vignetting reduced the throughput to the odd detectors of FP1 and the even detectors of FP2 by about 50%. The more severe vignetting of FP2 had required the gain of D2-2 (detector 2 on focal plane array 2) to be increased by a factor of 15. The gain and noise of this channel were quantified. Focal plane 2 has a field of view about 0.5 mrad to the right and 0.3 mrad lower than the designed overlap of FP1, as shown in Figure 3. No scatter sources or detector-to-detector crosstalk greater than 0.1% of the peak response of any detector were found. The MTF of each detector was measured and plotted. Each was found to be within the measurement error of the convolution of the detector size with the 0.5 mrad design blur circle of the telescope.

## Relative Spectral Response

The effective relative spectral response (RSR) of each filter bandpass was quantified in situ. Spectrally coded radiation from a Bomem Model 100 interferometer was fed into MIC2 and focused on D1-6. The output of D1-6 was fed back into the Bomem to complete the interferometer. In-band response was measured using an open aperture in the MIC2 filter slide. The effective RSR of each filter with D1-6 is shown in Figure 5. The figure also shows the spectra of a primary emitter measured in that filter region by the interferometer during the CIRRIS flight. The RSR of each filter was peak normalized to 1. In OPUS (Optical Physics User System), the computer aided data display and analysis system developed to analyze the CIRRIS flight data, a "white radiation" multiplication factor was applied. These efficiency factors are presented in Table 2. Out-of-band rejection was measured by blocking the bandpass of the CIRRIS filter using a second filter in the MIC2 slide. This allowed the full gain of the CIRRIS radiometer to be used to determine any leaks in the filter blocking region exposed by the bandpass of the MIC2 filter. Two minor, predicted leaks were measured in the blocking regions measured. All of the filter out-of-band rejection ratios were found to be greater than  $5 \times 10^{-6}$ .

# FILTER RSR and OPUS SPECTRA

(dash: filter rsr; solid: opus spectrum)

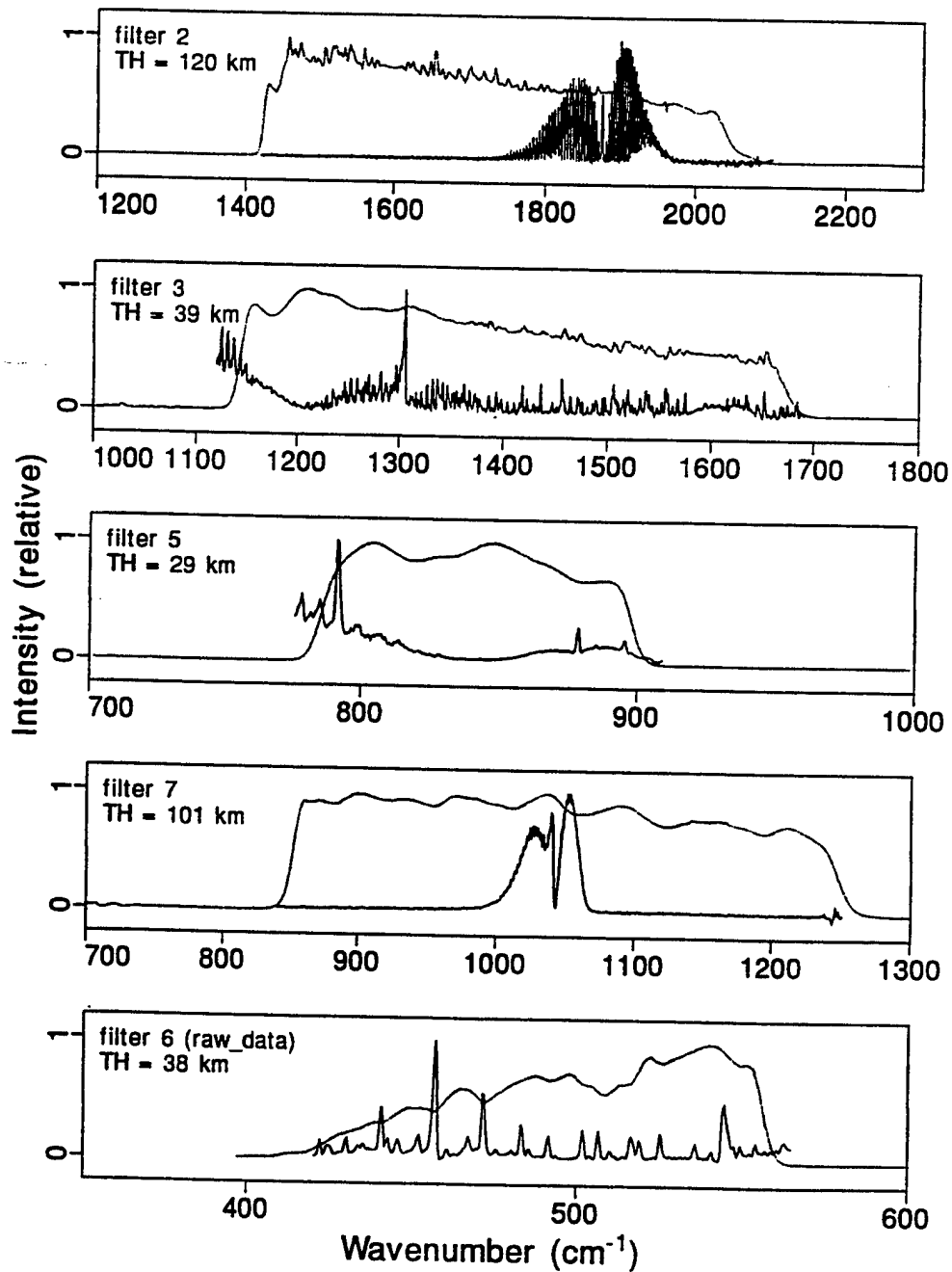


Figure 5. A comparison of the CIRRIS filter RSR and typical atmospheric spectra in each band.

**Table 2. Constants Used in OPUS**

Filter	Filter Efficiency	Multiplier
0	0.588	1.70068
1	0.828	1.20773
2	0.638	1.5674
3	0.675	1.48148
5	0.799	1.25156
6	0.599	1.66945
7	0.822	1.216545
FP2		

### **Radiometric Response**

To meet the wide dynamic range requirements, the CIRRIIS radiometer was designed with two electronic gain and three bias gain ranges. Both the  $\times 1$  and  $\times 100$  electronic gain channels are connected to the output of the detectors. The bias gain of the detectors in each bias group is automatically adjusted when the key detector of that group reaches a specified output voltage. The radiometer detectors are grouped in four bias groups. Bias gain is reduced when the ac peak voltage of the key detector reaches 7.2 volts and increases again when the peak is reduced to 1.2 volts. This scheme gives the radiometer four ranges: high gain - high bias, low gain - high bias, low gain - medium bias, and low gain - low bias. Each range was carefully calibrated using the various sources of MIC2. The gain of the  $\times 100$  channel was measured electronically and radiometrically and was found to be within 0.5% of the design value. The measured value is used in the OPUS data reduction software.

Because of the observed DRE in the two high bias ranges of the bulk silicon detectors, single linearized response equations were not developed for each channel. Instead, individual response equations were developed for each electronic and bias gain for each filter. The DRE observed in the extended source response equations was verified using an independent small signal response analysis. Most of the absolute response data points were collected using the full aperture extended source in MIC2. For the short wavelength filters, the upper portion of the range was developed using the MIC2 point source configuration. The relation between the dc-restored voltage and the absolute flux were curve fit using a  $1/Y^2$  weighting. Standard error of the fit was in the range of  $10^{-4}$  for all of the low gain ranges and  $10^{-2}$  for the high gain channel. The fit equation was then multiplied by a "radiation whitening" factor that adjusts the peak-normalized RSR to one that assumes that measured radiation has a flat spectral response. The dynamic range in each filter band is shown in Table 3 for D1-6 and Table 4 for D2-3.



**Table 3. Bandpass, Noise Equivalent Response, Maximum Calibrated Response and Maximum Flight Measurement for D1-6.**

Parameter	Filter							
	0	1	2	3	4	5	6	7
Actual Filter Bandpass ( $\mu\text{m}$ )	8.4-17.5	4.1-4.5	4.9-7.0	6.0-8.7	NA	11.1-12.7	>18.0	8.0-11.7
NEP ( $\text{w}/\text{cm}^2/\text{sr}$ )	7.2E-11	5.5E-10	2.5E-10	1.7E-10	NA	9.1E-11	4.7E-11	8.9E-11
Max. Calibration ( $\text{w}/\text{cm}^2/\text{sr}$ )	2.0E-4	6.0E-5	9.0E-4	8.0E-4	NA	5.0E-4	3.0E-4	3.0E-4
Maximum Flight Measurement ( $\text{w}/\text{cm}^2/\text{sr}$ )	3.8E-4	5.1E-6	3.3E-6	3.5E-4	NA	5.2E-4	3.1E-4	2.4E-4

**Table 4. NEP, Maximum Calibrated Response and Maximum Flight Measurements.**

Parameter	Detector				
	2-1	2-2	2-3	2-4	2-5
NEP ( $\text{w}/\text{cm}^2/\text{sr}$ )	1.5E-9	1.5E-9	2.0E-9	1.3E-8	9.3E-9
Max. Calibration Response ( $\text{w}/\text{cm}^2/\text{sr}$ )	1.5E-2	4.0E-2	3.0E-2	4.0E-2	5.0E-2
Maximum Flight Measurement ( $\text{w}/\text{cm}^2/\text{sr}$ )	3.0E-7	4.0E-7	2.0E-6	2.4E-6	2.4E-6

The noise parameters of each radiometer channel were quantified by collecting 8 seconds of detector output with the input blocked by filter wheel position 4. The standard deviation of the measurement (dark noise) and the offset (mean) were tracked from the time of the engineering evaluation through the flight and final calibration. The noise level was stable throughout the period. The noise level as a function of input flux was measured by quantifying the standard deviation of the sensor output at each of the flux levels during the extended source calibration. An example of this response is shown in Figure 6.

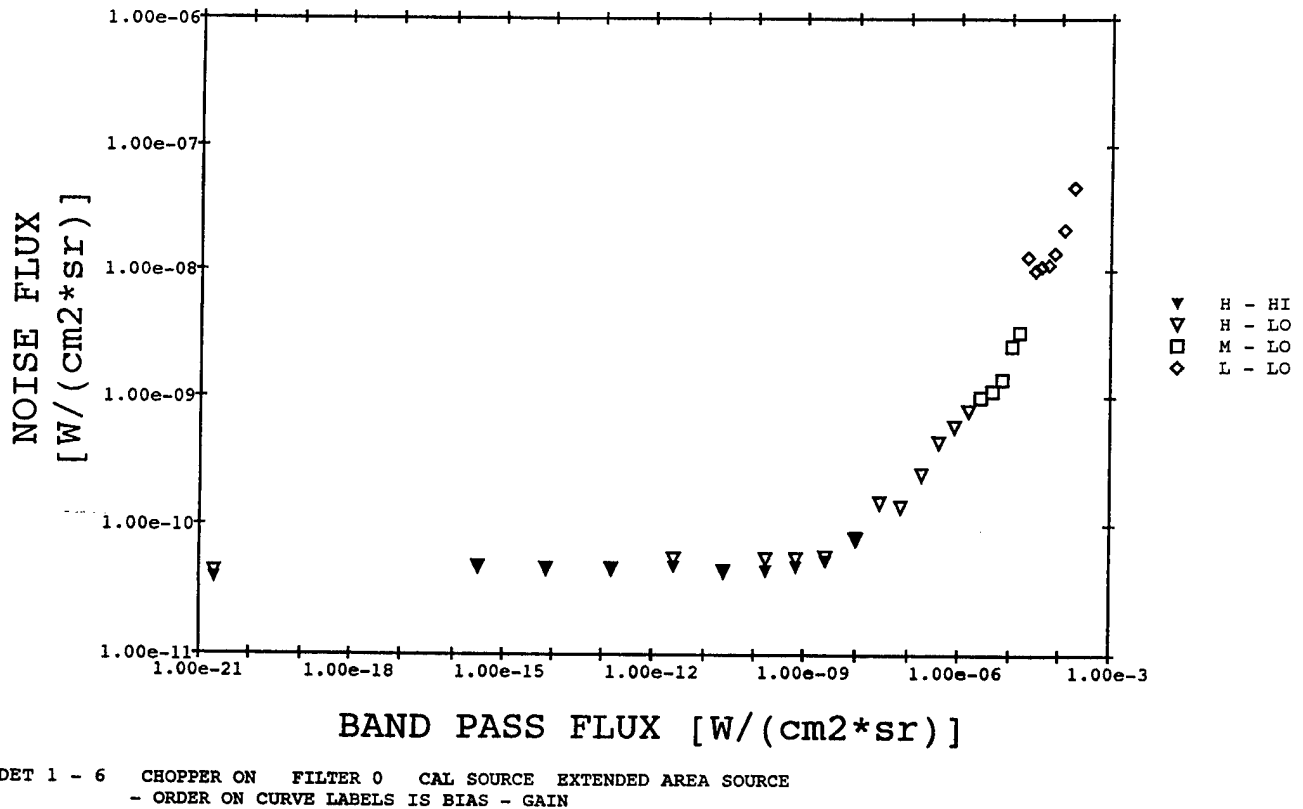


**Figure 6. Noise flux versus bandpass flux for radiometer detector 1-6, filter 0.**

The dark noise and offset of each detector were measured at the start of each calibration measurement section. The dark offset measured at the beginning of each section was subtracted from that day's measurement. A long-wavelength light leak was measured in filters 6 and 0 when the MIC2 aperture was closed. The measured energy was assumed to be a collimator artifact and the extra offset (the difference between filter 4 (blank) and the closed aperture position in filter 6) was subtracted from the source response of these two filters. This assumption was later confirmed during the SPIRIT III calibration by the discovery that MIC2 had several warm surfaces that could have been viewed by CIRRIS.

### **Interferometer Calibration**

The interferometer calibration produced a map of the point source response of each detector, the relative spectral response of each filter passband for each detector, and the absolute response of each detector in each passband. The point response mapping also provided a map of the telescope field stop with respect to the interferometer detectors. This linkage was used to align the ancillary sensors with the detectors of the primary sensors. The point source response map showed no signal response outside the detector outlines.

## Relative Spectral Responsivity

The relative spectral response (RSR) of each filter band quantifies the throughput efficiency radiation at each different wavelength, both within and outside its spectral passband. The RSR of each CIRRIS detector was measured using a 1300 K blackbody source. The source emittance was strongly attenuated to keep the detectors from saturating. Sixty to seventy scans were co-added to provide RSR curves with as low signal-to-noise ratios (SNR) as possible. A low SNR is critical for this measurement because during the calibration of each flight measurement, the spectra are divided point by point by the RSR to adjust for wavelength dependent response. Noise in the RSR function adds directly to the measurement. The effectiveness of the co-adding techniques in noise reduction can be seen in Figure 7 where the second harmonic is clearly visible due to the reduction in the noise floor when 61 scans have been co-added.

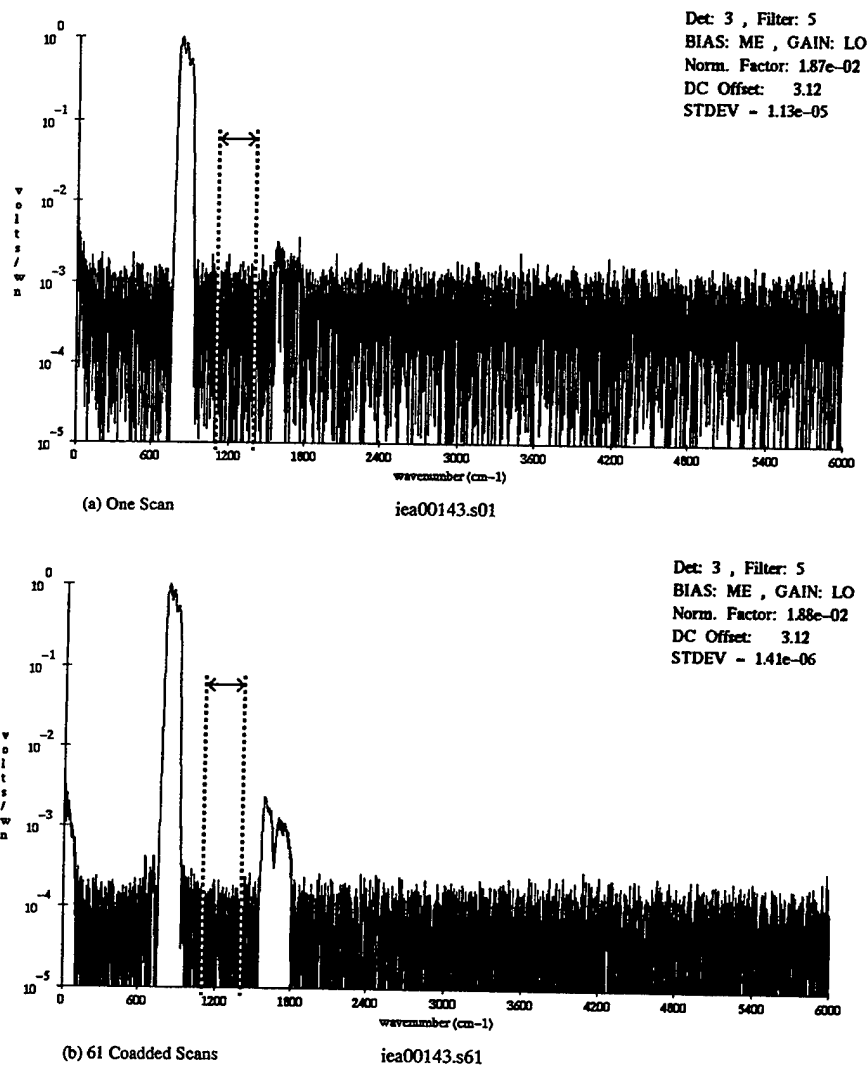


Figure 7. Example of coadding to increase signal-to-noise ratio.

The high temperature (1300 K) blackbody was used in developing the RSR curves so that the resulting spectral emission had significant energy in the shorter wavelength regions (2-5  $\mu\text{m}$ ). However, filter 1 (2.5-4.9  $\mu\text{m}$ ) was sufficiently broad that energy in the 4-5  $\mu\text{m}$  range saturated the detector while significant noise remained in the 2-3  $\mu\text{m}$  region. To improve the calibration of the 2-3  $\mu\text{m}$  region, an additional long wavelength blocker was used in a second set of measurements in the calibration of this filter to remove the 3.5-5  $\mu\text{m}$  radiation. The RSR for the whole filter was developed by combining the spectra from both sets of scans. Despite the use of this double measurement technique, the RSR data for wavelengths shorter than about 3  $\mu\text{m}$  in the open filter (0) and in filter 1 have significantly more noise in the 2.5-3  $\mu\text{m}$  region than at longer wavelengths.

The high energy density of the 1300 K source was reduced by use of a small aperture in MIC2, or by using the Jones or scatter source mirror configurations. RSR data sets varied significantly with the source (mirror) configuration, with both the Jones and scatter source configurations showing more channel spectra than the small aperture configuration. An example of the various observed RSR responses is shown in Figure 8. When possible (most filter and detector configurations), the RSR data used in the CIRRIS data analysis were collected using the collimator (point source) configuration.

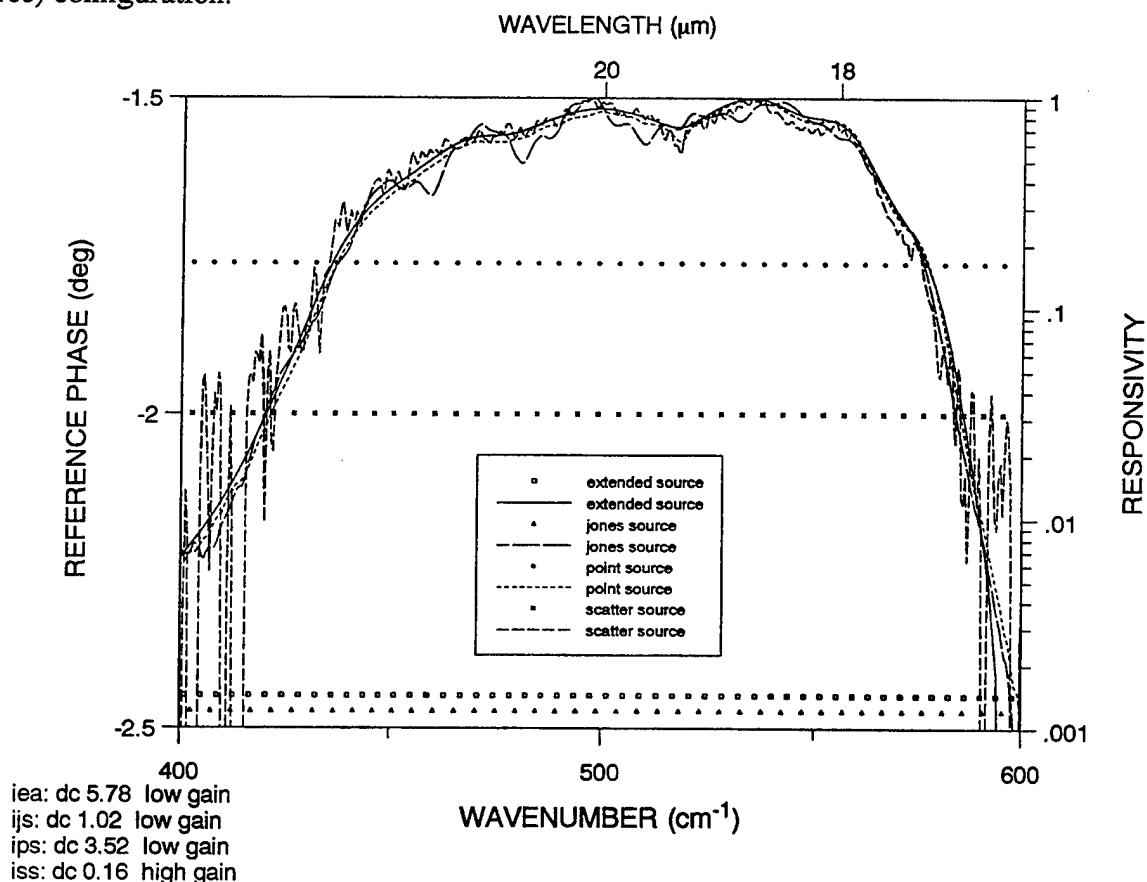


Figure 8. Relative spectral response curves obtained with each of the four sources for detector 3-3, filter 6.

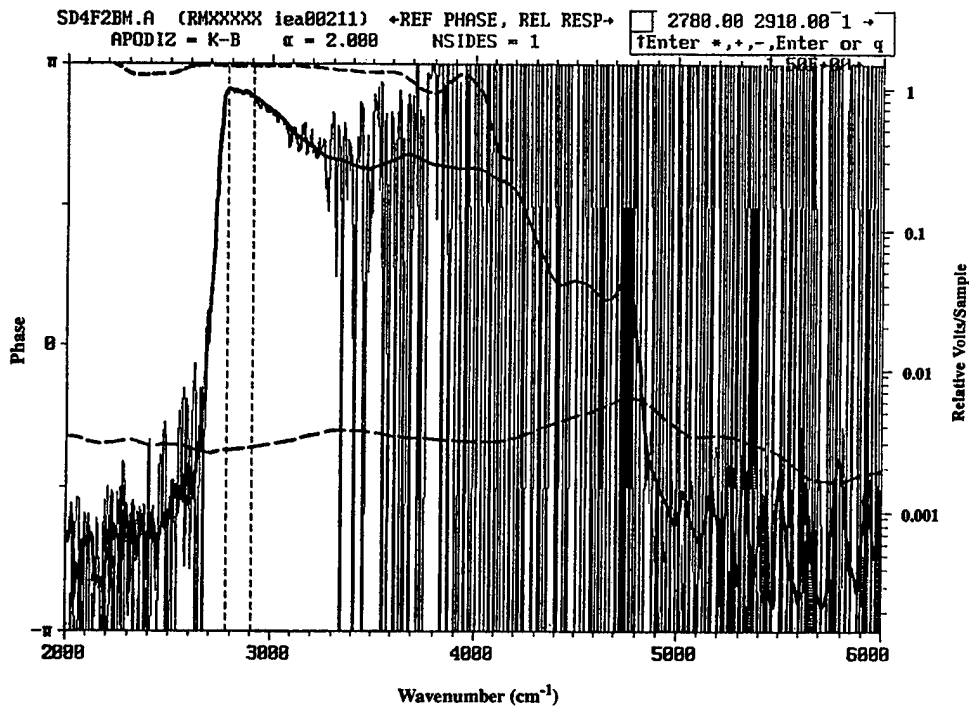
The CIRRIS interferometer used two detector bias voltages in flight: low (0.1 volts) and medium (1.0 volts). The low bias voltage provided a detector response about 1/3 less than the medium bias mode, extending the dynamic range of the sensor. However, the low bias also showed significantly more detector nonlinearity than data collected using medium bias. Because of the significant difference and out-of-band noise added by this nonlinearity, existing versions of OPUS use medium bias RSR (reference interferograms) for both high and low bias ranges. Although a nonlinearity correction routine was developed, the absolute response developed by test versions of OPUS using this correction were increased by about 15% over values developed without the correction. This large response may be due to the use of the medium bias RSR in the test version of OPUS and this effect would probably be eliminated if the low bias RSR data were added to the software. Some problems remain in the low bias calibration as applied in OPUS (Section 6.1.2.2).

### **Absolute Response Measurements**

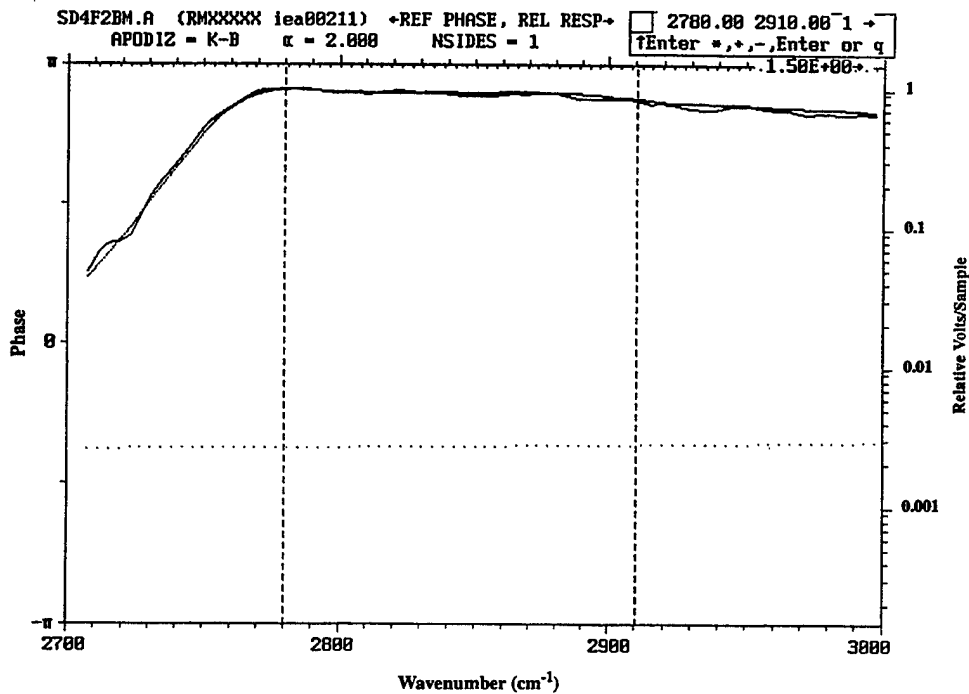
The absolute responsivity calibration determines the absolute radiance level assigned to the peak of each spectrum after it has been corrected for RSR. The absolute responsivity coefficients for the CIRRIS interferometer were developed using a full aperture, unattenuated blackbody source located inside of MIC2. Extended source temperatures used in the CIRRIS absolute responsivity coefficient development ranged from 47 to 300 K.

A range of absolute coefficients for each filter and detector was collected by heating the extended area source inside MIC2 to a given temperature, and then collecting multiple scans with each unsaturated filter/detector combination. Data were collected at 5 to 10 K temperature steps in two sessions. Data for filters 0, 3, 5 and 7 were collected using short scans over the temperature range of 44 to 150 K. Data for filters 1, 2 and 4 were collected at a later time, using long scans and a temperature range of 90 to 300 K. These temperature ranges allowed characterization of the detectors from near noise limits to full saturation.

The absolute coefficient was derived from these scans by overlaying the low temperature, absolute-calibrated spectra over the RSR curve for that detector, bias, and filter. The ratio of the two curves in the lowest noise region of the low temperature spectra was used to develop the required ratio. Figure 9 shows an example of this procedure for filter 2, including the entire overlay of the extended source file on the RSR of filter 2, and an expanded view of the integrated region. All files for filter 2 were integrated over this same region. An example of the absolute coefficient data for detectors D3-3 and D3-4 is shown in Figure 10. This figure shows some slope (change in absolute coefficient with increasing DC level) as the radiant flux increased. These curves are not smoothly monotonic, especially in the low bias data, which showed no consistent pattern. Coefficients for filters 4, 2, 1, 6, and 0 were multiplied by 150, 30, 10, 3, and 0.5, respectively, to bring the values into a similar range for comparison.



(a)



(b) Blowup of the integrated region

Figure 9. The overlay of the measured, extended source file at 248 K on the RSR of filter 2.

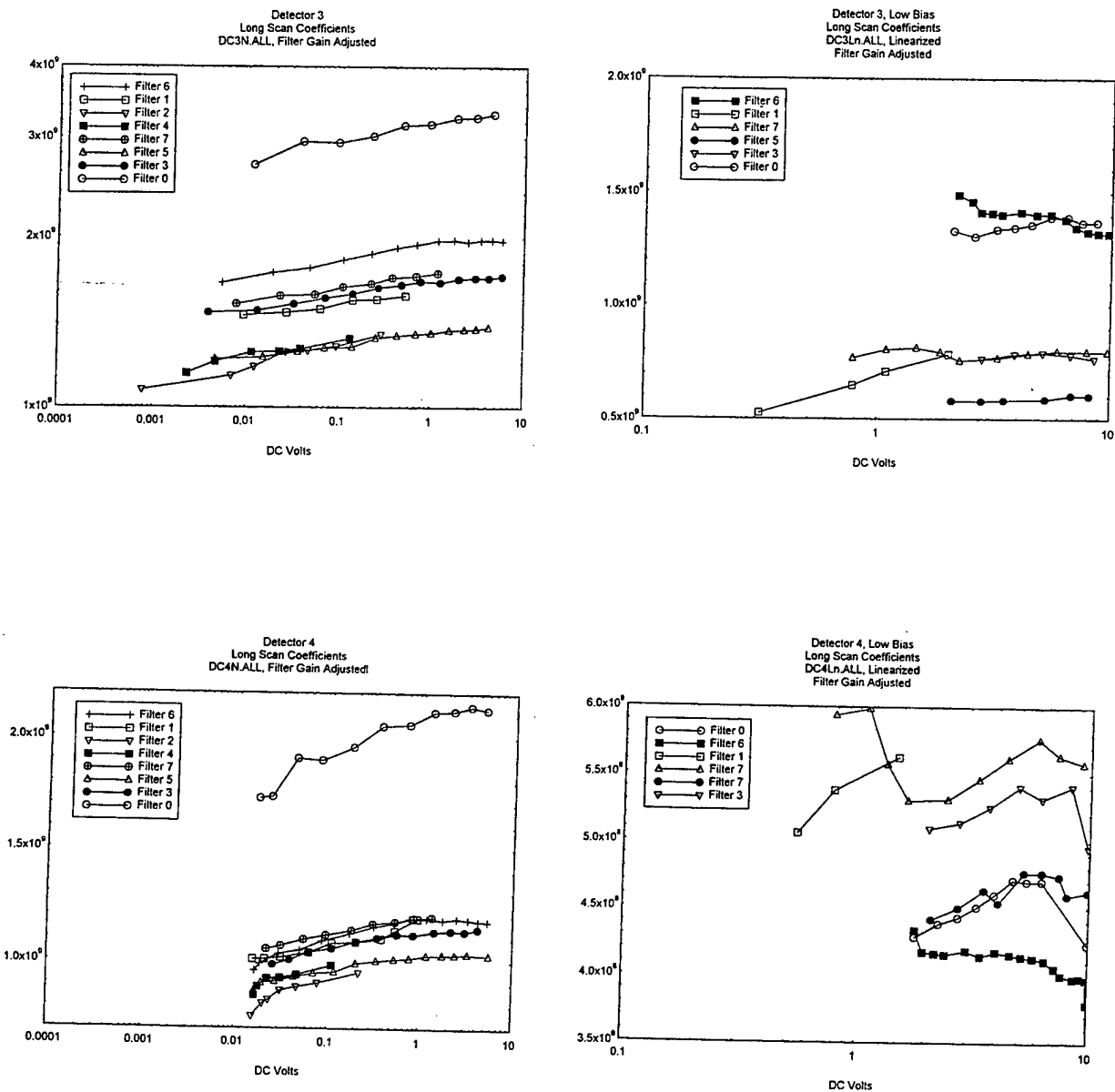


Figure 10. Filter adjusted long scan curves showing the similar slopes to all the medium bias data for each detector.

Three approaches were studied in the application of the absolute calibration data. Published versions of OPUS use a simple linear interpolation between the data points, based on the flight inter-

ferogram dc level. This approach preserves all of the structure observed in the absolute calibration curves. To determine if this structure was actually noise that should be eliminated, linear curves were fit to the absolute data and a version of OPUS using these curve fits for the absolute calibration was developed. When applied to flight data, the smoothed absolute calibration curves produced results with larger scatter than the data using linear interpolations. Based on this study, it was concluded that the structure observed in the absolute calibration data represented real instrument response variations.

Data for filters 1, 2 and 4 were collected at a different time than the other filters. During this second collection, scans were repeated at two temperatures for filters 5 and 7. The comparison of the absolute coefficients between the two calibrations for D3-3 is shown in Figure 11. The four data points from the second data collection event are circled in the figure. The repeatability of the four data points when compared with those collected in the earlier collection should provide some indication of the absolute precision of the interferometer absolute calibration. The absolute coefficients collected during the second data take are 3 to 8 percent greater and show less slope than those collected initially. The reason for this discrepancy could not be determined.

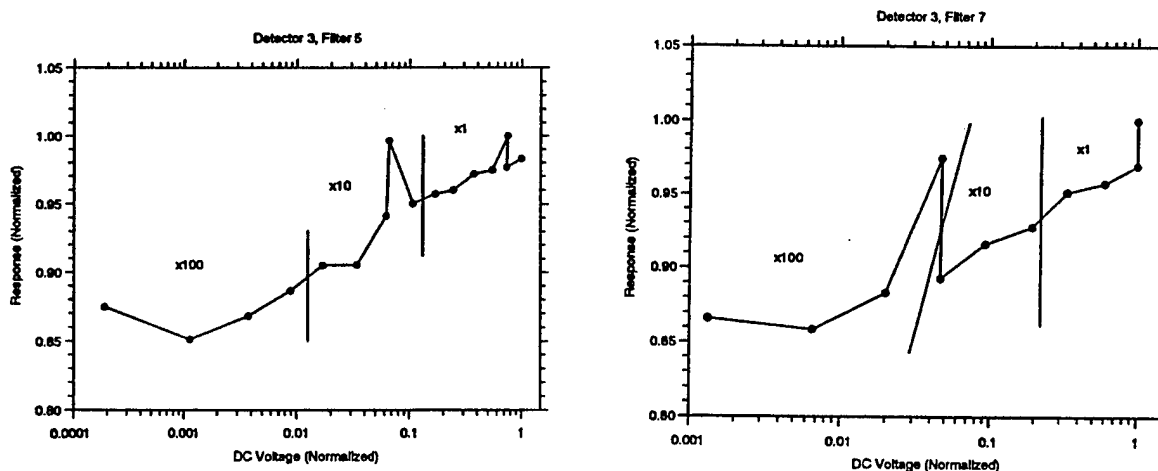


Figure 11. Normalized absolute response data for interferometer detector 3, medium bias (raw data).

### Linearity Correction

The low bias mode of the CIRRIS detectors introduced significant nonlinearity into the system. A method was developed to remove this nonlinearity. However, when the nonlinearity correction



was applied in the current version of OPUS, the absolute-calibrations of the flight spectra were increased by about 10%. This increased the difference between the radiometer- and interferometer-determined radiances at low altitudes and was assumed to be an error. This discrepancy could be due to the use of medium bias RSR interferograms in both low and high bias data in the OPUS system. Further examination of the problems associated with correcting nonlinear data is required.

### **Noise Response**

The short term repeatability and noise levels of the CIRRIS interferometer were examined by comparing the scan-to-scan variability of the RSR data set and the noise levels of the absolute data sets. The interferometer was found to be extremely stable when collecting a series of scans. For example, D3-3 showed a variation in standard deviation between scans of only 0.00036 volts x sample for 25 long scans. The measured NESR curves for each detector are shown in Figure 12. The effect of photon noise on out-of-band standard deviation was measured using the extended source data. The noise level increased about 1 order between the NESR level and saturation. This noise level is assumed to be 'white', and to apply across the entire frequency range.

### **Line shape verification**

With the interferometer spectrometer, line shape should only be a function of the number of points in the transform and the apodization. The CIRRIS line shape and position were verified using a laser line at 3.391  $\mu\text{m}$ . Spectral line position was also verified using the laser data. The off-center detectors, D3-1, D3-3 and D3-4, were found to be long wavelength shifted by 0.9, 1.0, and 0.6  $\text{cm}^{-1}$ , respectively. This is a known artifact in off-axis response and is due to the longer path of light to these detectors.

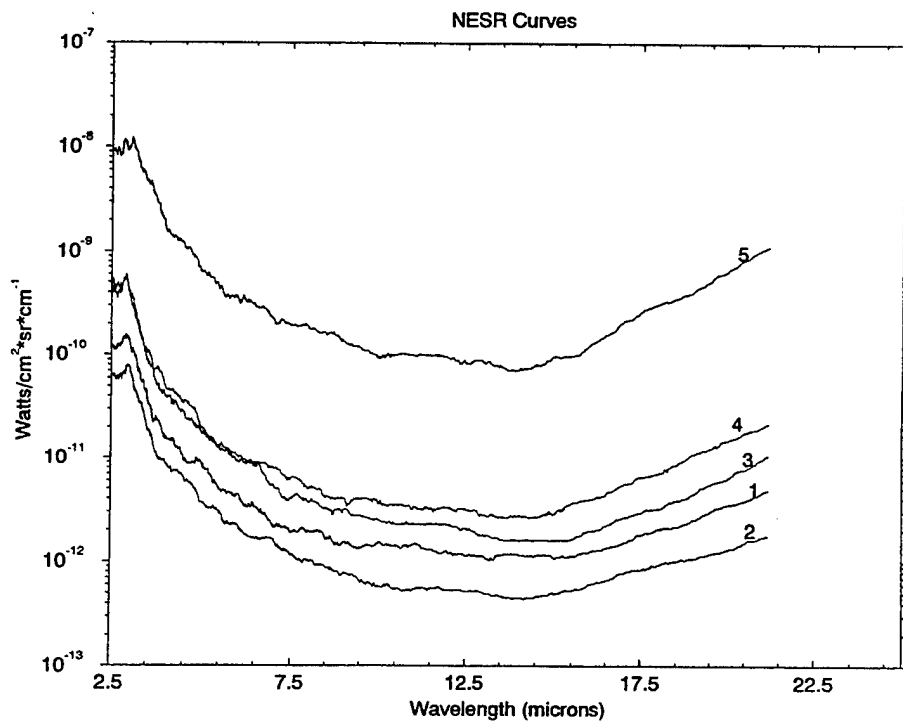
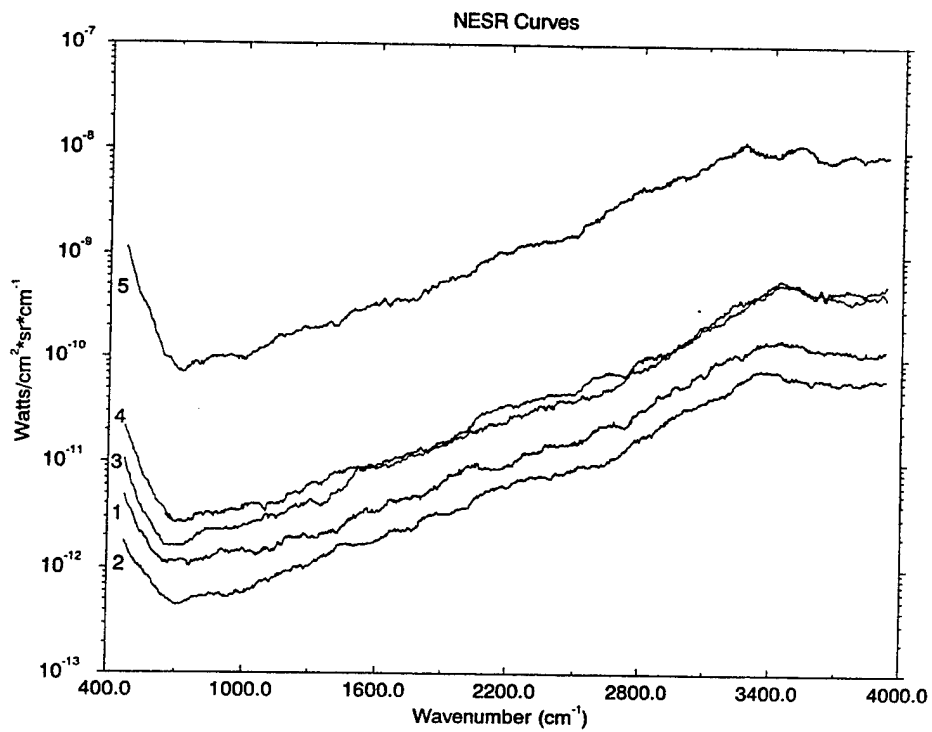


Figure 12. NESR plots for each interferometer detector plotted as a function of wavenumber and wavelength.

## ANCILLARY INSTRUMENT CALIBRATION

All of the CIRRIS ancillary instruments were coaligned with the primary sensor line of sight by reference to a windowed alignment mirror. The mirror was visible from the exterior of the sensor, and its position was surveyed with respect to the field stop. Figure 13 shows the fields of view for all the sensors.

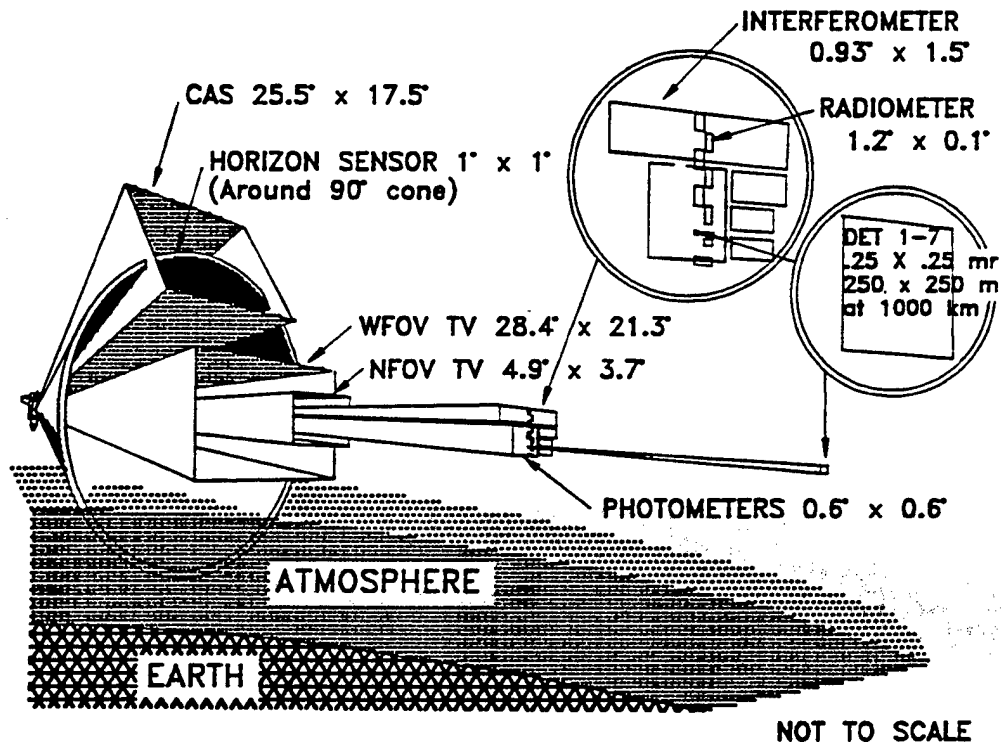


Figure 13. Fields of view for CIRRIS 1A infrared and ancillary sensors.

### Photometers

The externally mounted photometers are bandpass filtered to detect visible and ultraviolet radiation at 5577Å and 3914Å. The 5577Å photometer acts as both an auroral and an airglow monitor for atomic oxygen  $^1S\text{-}^1D$  emission. The 3914Å channel monitors the nitrogen ion ( $N_2^+$ ) (0-0) band that serves as a monitor for electron deposition into the upper atmosphere, such as in an auroral event. Each photometer incorporates a sun sensor that automatically shuts down the photometer when the sun enters the 40° field of view of the sun sensor, the restricted field of view for the infrared telescope. During flight, the photometers were exposed to sufficiently bright earthshine and solar forward scattering to saturate the photomultiplier tube counters and damage the photo cathodes. Tube sensitivity decreased by about a factor of 10 during the flight. A relative calibration for each measurement block was established post flight using the photometer internal stimulator that was recorded at the beginning of all but two of the measurement sequences. The photometers were calibrated using a NIST traceable light source and calibrated neutral density filters. Spectral sensitivity of the photometer tubes was measured using the cali-

bration light source and a monochromator. Temperature response of the tubes and the internal stim sources were determined over the flight temperature range.

### **Low-Light-Level Televisions (LLTV)**

Two LLTVs are coaligned with the telescope to assist the shuttle crew members in pointing the CIRRIS instrument at visible targets of interest. The acquisition camera has a wide-angle field of view ( $20^\circ \times 15^\circ$ ) and the pointing camera has a narrow field of view ( $3.5^\circ \times 2.5^\circ$ ), slightly larger than the total field of view of the interferometer and radiometer. During flight operations, the crew was able to select one of the camera outputs for display on the orbiter aft flight deck closed circuit television screens. They used the display to point the sensor using a joystick controller. Because the LLTVs contained automatic apertures and gain circuits that were not recorded, no absolute calibration could be made of their output.

### **Horizon Sensor**

The horizon sensor detects the displacement of the CIRRIS instrument above the 40-km  $\text{CO}_2$  layer. By sensing pitch and yaw angles relative to this emission source, the horizon sensor provided the crew with real time data on sensor pitch and yaw. The gimbal controller also received these data in certain scan modes, where it was important to maintain a constant pitch angle with respect to the horizon. The horizon sensor was not recalibrated after flight, but comparison with the CAS showed that the horizon sensor performed within specifications.

### **Celestial Aspect Sensor (CAS)**

The CAS is a 16-mm film camera mounted such that its field of view is  $45^\circ$  from that of the telescope. In this orientation, it recorded the star field while CIRRIS collected earthlimb data. Post flight data reduction of the film, in conjunction with the orbiter ephemeris information, was used to determine where the instrument was pointing with greater precision than was possible with the horizon sensor. Analysis of the CAS data allowed pointing solutions to 0.25 mrad, which is the resolution of the smallest detector.

### **Pointing System**

The pointing system is a two-axis system that rotates the CIRRIS sensor in the orbiter pitch and roll planes in response to commands from either the CIRRIS avionics, the orbiter aft flight deck command and monitor panel, or the crew-held joystick, as various mission modes require. Main system elements include the gimbal frames proper, drive and brake elements, and control electronics. The gimbal proper consists of two nested structural frames. The outer frame is rigidly attached to the shuttle experiment support system (ESS) at four points. An inner frame is suspended from the fore and aft beams of the outer frame. The inner frame rotates about an axis parallel to the orbiter's roll axis, and enables the instrument to sweep through an angle of  $\pm 38^\circ$  from top dead center in the roll plane. The CIRRIS instrument itself is suspended from the inner frame about an axis parallel to the orbiter's pitch axis through a sweep of  $+6^\circ$  (aft) to  $-24.5^\circ$  (forward) from top dead center in the pitch plane.

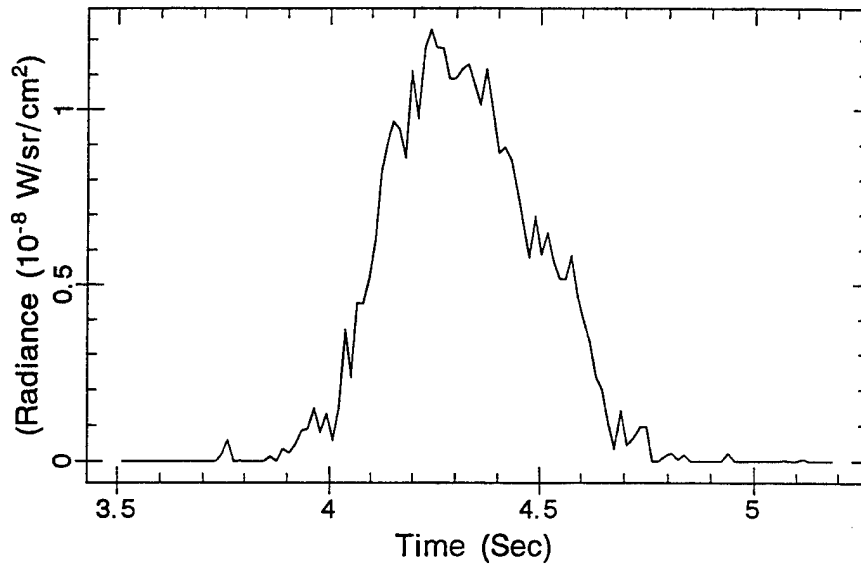
The gimbal controller directed and monitored all gimbal operations in response from the CIRRIS avionics or commands from the aft flight deck. Two identical drive brake modules, responding to commands from the gimbal system controller, moved the sensor through various scan patterns. In addition to the driving torque motor, each module contains a 16-bit optical shaft encoder to provide position information, a tachometer to measure rotation rate, and a fail-safe brake. The outputs of the pointing system were bench marked using the CAS data. Data between the CAS measurement points were assigned tangent altitudes based on orbiter attitude and pointing system output data. These data allowed pointing solutions to  $\pm 0.25$  mrad ( $\pm 0.75$  km at maximum limb radii).

## SUMMARY

The radiometer calibration measured sensor point source response, spectral response, and absolute response. Individual response equations were fit to each detector range. The interferometer calibration produced a map of the point source response of each detector, the relative spectral response of each filter passband for each detector, and the absolute response of each detector in each passband. The results show that the CIRRIS interferometer has met all specifications for resolution and spectral accuracy. The positions of the interferometer and radiometer focal planes with respect to each other and to the interferometer field stop were mapped and verified using flight data.

Because the main CIRRIS calibration occurred after flight, the opportunity existed to verify the general accuracy of the calibration using the flight data. Through this approach, several problems have been identified in the interferometer and radiometer absolute calibrations, and attempts to resolve them are being made.

The radiometer absolute calibration was verified by examining star crossing data collected by individual radiometer detectors. Since the radiometer detectors are sufficiently small and sensitive to see individual stars, comparisons between CIRRIS and other sensors are possible. CIRRIS viewed three infrared stars, Alpha Bo, Alpha Sco, and Alpha Centary. The response of the radiometer to a crossing of Alpha Bo is shown in Figure 14. The CIRRIS measurement of this star peaks at  $1.205\text{E-}14$  W  $\text{cm}^{-2}$ , which is within 4.65% of the value reported by IRAS (infrared astronomy satellite) for this star. From this and other CIRRIS celestial observations we conclude that the radiometer absolute calibration is within 5% of the standards used by other space and ground-based celestial observation systems.

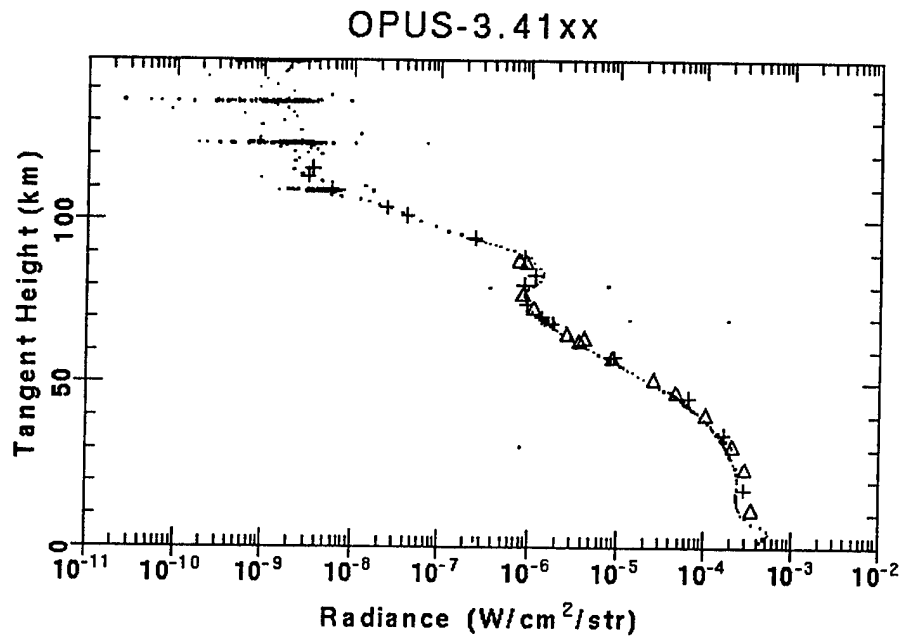


C1A RAD Filter 1 = 4.08-4.48  $\mu\text{m}$  [RAD det #1-6]  
 The max radiance = 1.23E-8 (W/sr/cm<sup>2</sup>)

The calculation of Regridded spectrum of Alpha Boo:  
 Irrad = 1.205E-14 (W/cm<sup>2</sup>)  
 Radiance = 1.29E-08 ((W/cm<sup>2</sup>/sr) [using FOV 1.705E-6 sr]  
 Error = 4.65%

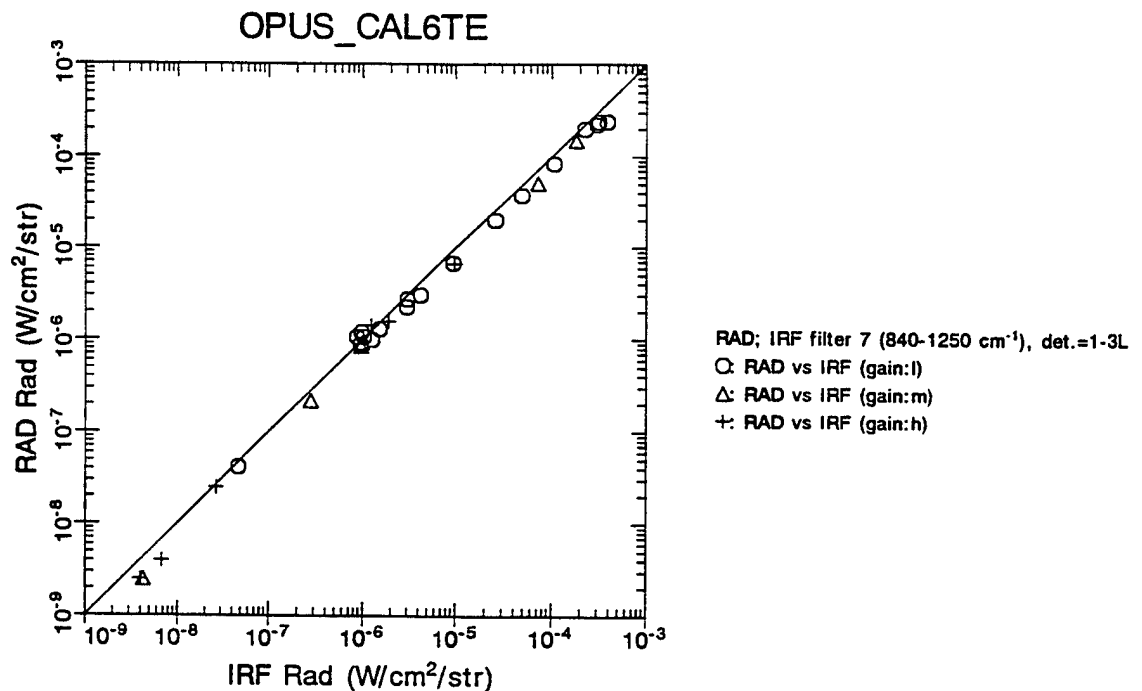
**Figure 14. The response of the radiometer to a crossing of Alpha Boo.**

The major question remaining in the calibration is the discrepancy between the wavenumber integrated spectral radiance reported by OPUS for the interferometer and the radiance reported for the same passband from the radiometer. An example of the difference is shown in Figure 15. Figure 15a shows a comparison of the interferometer and radiometer radiance data for a vertical scan of the limb from about 15 km to 160 km tangent height. Since the radiometer and interferometer share the aperture of the telescope, they are observing essentially the same target. The larger size of the interferometer detectors modifies this somewhat. The dots in Figure 15a are the individual radiometer data points reported by OPUS. The deltas are the interferometer data collected in low bias, but using the OPUS medium bias RSR correction. These data are about 15% larger than the radiometer values at the same height. The '+' symbols are the integrated spectral radiance of the interferometer at that height using interferometer filter 7. The lowest four '+' symbols were made using detector 5 data. At tangent heights between 50 km and 125 km, the radiometer and interferometer medium bias calibrations have good agreement. At the noise level of the systems, the two are about equal, but at the highest radiance levels (lowest tangent heights) the integrated interferometer values are all larger than the radiometer averages. Figure 15b shows a direct comparison of the interferometer and radiometer data for filter 7. The medium bias data for the low radiance regions (50 - 125 km) lie directly on the 1-1 line. Interferometer data at the lowest radiance levels fall a little higher, but this is due to improper averaging of the spectra noise in the transform. At the lowest tangent heights, both the interferometer medium bias detector 5 data and the low bias detector 4 data show absolute values that are about 0.15% too large. Calibrations for these conditions were collected with the extended source at its highest temperature, and may require additional temperature correction. Section 6.1.2.2 provides more details on the cause of this offset.



points: RAD filter 7 ( $840-1250\text{ cm}^{-1}$ ), det.=1-3L  
 $\Delta$ : B-L; IRF filter 7, integrated in the same region of RAD  
 $+$ : B-M; IRF filter 7, integrated in the same region of RAD

a. A comparison of the interferometer and radiometer radiance data for a vertical scan of the limb from about 15 km to 160 km tangent height.



RAD; IRF filter 7 ( $840-1250\text{ cm}^{-1}$ ), det.=1-3L  
 $\circ$ : RAD vs IRF (gain:l)  
 $\Delta$ : RAD vs IRF (gain:m)  
 $+$ : RAD vs IRF (gain:h)

b. Direct comparison of interferometer and radiometer data.

Figure 15. Example of OPUS data showing the discrepancy between the radiometer and interferometer spectral radiance data.

Table 5 shows the radiometer and interferometer comparisons for most of the filter pairs. The coefficient necessary to shift the low bias interferometer radiance to match the radiometer is shown for each filter, along with the region of integration used for the interferometer. This coefficient varies from 1 to 0.5. Additional effort is being directed toward improving the low bias calibration and understanding the processing problems being experienced by the existing OPUS software. Blackbody data from the calibration of each instrument have been inserted into the OPUS software to verify its functionality. Both the radiometer and interferometer OPUS processing return proper radiances for the reported blackbody temperatures in the medium bias mode, but they diverge for the low bias data. Investigation into this difference continues.

Comparisons of the concentrations of the green house gases O<sub>3</sub>, CHC11, CFC12, and HNO<sub>3</sub> developed by integrating the CIRRIS limb spectra also indicate that the interferometer absolute calibration in the low bias mode is too large by the factor indicated in Table 5. Based on these two pieces of evidence, we recommend that the absolute coefficient data be modified by the amount indicated. Additional effort in this area will help to reduce the uncertainty surrounding the low bias calibration data.

**Table 5. Radiometer and Interferometer Comparisons for the Interferometer Low Bias Calibration Region for Filter Pairs.**

Radiometer Filter	Integration Region (cm <sup>-1</sup> )	Interferometer Filter	Coefficient Multiplication Factor
0	555.0 - 1195.0	0	1.00
1	2207.0 - 2450.0	1	0.90
FP2	2700.0 - 3700.0	2	NA
3	1119.8 - 1692.1	3	0.75
5	775.0 - 909.00	5	0.80
6	420.0 - 565.00	6	0.50
7	840.0 - 1251.0	7	0.85



**APPENDIX 2**

**CHARACTERIZATION OF THE CIRRIS 1A LLLTV SYSTEMS**

CHARACTERIZATION OF THE CIRRIS 1A LLLTV SYSTEMS

By

H. A. Miranda, Jr.

May 1992

Work performed under  
Subcontract No. C801020  
Amendment No. 5  
Task 1.6

MIRANDA LABORATORIES  
74 Loomis Street  
Bedford, MA 01730

## 1. INTRODUCTION

The work reported here was prompted by the conjecture that the LLLTV cameras are subject to the simultaneous action of three separate AGC systems. Owing to the lack of information regarding the design philosophy governing the coordination of these separate systems in the feedback control loop, it had hitherto been widely believed that any attempt to characterize the response of these systems in a meaningful manner would be fraught with difficulties. This judgment arose from the inability to extract the requisite design information from the vendor's representatives. Thus the program philosophy had resigned itself to the limitation whereby only qualitative information would be derived from these sensors.

However, an approach was developed by the author which offered the prospect of deriving absolute source radiance from the output signals over at least the lower portion of the dynamic range. This approach, which is described briefly in the next section, proved to be successful beyond our original expectations, as is shown in the results presented in Section 4 below. This means that the data management effort can be directed accordingly to include this newly enhanced capability, should the nature of the flight data warrant.

It is particularly noteworthy in this regard to realize that the resolution data reported here, (i.e., spot-size of a simulated star image), is extremely useful in deriving a reliable INFLIGHT radiant calibration of both cameras by using selected star images, as discussed below.

## 2. DISCUSSION OF THE APPROACH ADOPTED

The three separate AGC systems to be unraveled are: 1) a mechanical auto-iris, and 2) electronic circuitry, (both of which act in some coordinated fashion to maintain the output signal level within acceptable signal processing limits), together with 3) high-voltage control circuitry protecting the image intensifier cathode against excessive long-period illumination levels. That these three subsystems are undoubtedly coupled to one another in a manner designed to prevent the phenomenon of "motorboating", was a prime ingredient in the approach developed here, as is discussed next.

Arguing from first principles, it was reasoned by the author that the LLLTV's could not have exhibited the observed repeatable consistency over a wide range of background conditions without the existence of a hierarchy of cooperative AGC subsystem functions incorporated into the overall system design. Based upon this logic, it was then presumed that the hierarchical separation was very likely to have been manifested in the frequency domain, with the high-voltage AGC acting at the highest frequency regime, the electronic circuitry at the mid range frequencies, and the auto-iris at the lowest. Suitable filters in the feedback network would then route the sensed background level signals to the appropriate control destination circuitry, using the rise time of the changing background levels as the discriminant.

Finally, because the sensed instantaneous background level is unidimensional, (i.e., represented by a single voltage), it was further reasoned that it is very likely proportional to the spatial integral of the illumination over the entire sensor area. From this it followed that the presence of an

additional point of illumination within the field of view, even though relatively intense, would probably affect the integral only minimally.

On the basis of the above arguments, it was thought possible to use an extended source as a means of stimulating the feedback system network, while simultaneously utilizing a point source as a means of measuring the change in gain resulting from the action of the AGC as it responds to the extended source level, (which change is manifested as the opposite change in the point source amplitude). An experimental apparatus was assembled embodying these concepts; and several series of measurements were performed to derive the desired information. The results were gratifying; and the end product of this effort will be a useful adjunct to the extraction of quantitative information from the LLLTV flight data.

This investigation has been necessarily limited. As such, it restricts itself to the low end of the system response.

### 3. DESCRIPTION OF THE APPARATUS USED

The key element of the experimental setup assembled for this investigation is a 200 mm collimator lens having a flat field of about 45 mm diameter in its focal plane. (This translates into a full angle of about 12 degrees in object space.) The focal plane of the collimator is fitted with a plate having a 25 mm hole centered about the optical axis. Onto this plate was fixed a sheet of white bond paper with a small circular hole ( $\approx 2$  mm diam.) through which was passed a He Ne laser beam focused in the plane of the paper. When illuminated with a known radiant flux, the paper provided an extended source of calibrated illumination at the entrance aperture of the LLLTV under investigation, of about 6 degree full angle. Means were provided for varying both the extended source and the point source independently.

The apparatus was used in the following manner:

1. The point source intensity was adjusted, (using filters) so as to provide a peak signal near the saturation level
2. The value of this level was measured on the oscilloscope screen.
3. Without changing the point source intensity, an extended source background illumination, provided by an LED (at 590 nm), was increased, (using the LED current as a measure of the illumination level).
4. At each selected illumination level, the point source peak signal level was determined, the relative change of this signal being a measure of the gain reduction.

Finally, special pains were taken to ensure that the point source adequately simulated a star image in the focal plane of the LLLTV under test. This permitted a separate determination of the spot size for both the NFTV and the WFTV cameras. Although the data reported here relate to the spare unit, this parameter is not likely to be significantly different in the flight units. The reason for this is that: 1) the lens is the dominant factor in this regard, and 2) tight tolerances are usually applied to spot size in lens fabrication. With this item of information at hand, the output signal level for any given (unsaturated) star image of known brightness is linked to the entrance

aperture illumination from that star, (by spreading the illumination over the known spot size in the detector plane), to derive accurate in-flight calibrations. These data may be compared with the laboratory data derived from the present investigation.

A schematic of the apparatus is shown in Figure 1.

#### 4. EXPERIMENTAL RESULTS

The data for both the WFTV and the NFTV were collected in the same manner separately. Since only a single spare CCD camera is in existence, this was used for both "systems", (each with its own respective spare lens). The following video system specifications are taken from vendor data for the Xybion ISS-255 RI camera:

Item	Vertical	Horizontal	Comments
CCD format	6.6 mm	8.8 mm	
Pixel size (nominal)	13 $\mu\text{m}$	11 $\mu\text{m}$	Center/center spacing
Number of CCD pixels	493	768	Total
	484	756	Usable
Video "resolution"	480 lines	533 lines	

#### 4.1 Widefield TV Camera

##### 4.1.1 Point-source spot size

A 25 mm focal length lens formed the wide field-of-view. The vendor data listed above was used to calculate the object-space angular dimensions of video resolution, as follows:

$$\text{VERTICAL: } \frac{(6.6) (484/493)}{(480) (25)} = 0.535 \text{ milliradian}$$

$$\text{HORIZONTAL: } \frac{(8.8) (756/768)}{(533) (25)} = 0.650 \text{ milliradian}$$

(It should be noted here that the inherent accuracy of angular pointing derived from star image processing is somewhat better than the line "resolution", for reasons beyond the scope of this discussion.)

The "point source" image spot size, (FWHM), for this system was found to be 65  $\mu\text{m}$ , (the full diameter being 83  $\mu\text{m}$ ). The resulting angular diameters are 2.56, (FWHM) and 3.32 mr, respectively.

This point source was observed by the TV camera; and by using an oscilloscope, it was possible to identify its location in the TV field on a given horizontal raster line, as shown schematically in Figure 2. This depicts the voltage excursion of one entire line, (i.e., between two adjacent sync pulses, in between which are contained all of the pertinent data). Shown in the figure is the extended source background level, (on both sides of the small central circular region depicted by the lower signal level, which is associated with the hole in the paper). At the center of the latter is the laser spot signal.

As the LED current is increased, the extended background level rises accordingly, and is observed on the oscilloscope screen. Up to a certain point, the laser spot signal, (i.e., the difference between the central depressed level and the peak), remains constant. As the LED background level is raised beyond this point, the laser spot signal begins to decrease. The raw data used for the material presented here are taken directly from these point source oscilloscope voltages.

#### 4.1.2 Radiant calibration

As mentioned in the introductory section, the data presented here pertain to extended sources. Limitations of a programmatic nature precluded a thorough examination of all laboratory data for the purpose of deriving point source calibration. Should future circumstances permit, the data can be revisited to develop this information.

Owing to the low light levels involved, it was necessary to employ a special imaging photomultiplier system at the ML facility which permits the measurement of low-level light from a diffuse source located at any remote distance issuing from a well-defined area selectable by the user. It was possible using this device to determine the radiance of scattered LED light issuing from a circular region of background source as small as 0.26" diameter. The region selected for this observation was situated at a point close to the small circular opening through which the laser "point" source light passed, (but did not include the opening).

By comparing the response of the imaging photometer with that of a calibrated UDT detector (using an appropriate set of ND filters to attenuate the LED light when observed by the PMT, the radiance (i.e., brightness) level of diffuse paper used as the extended source of background light was measured over a range of LED currents spanning that value at which the laser spot signal began to decrease.

#### 4.1.3 Extended-source AGC response

As noted earlier, the effort reported here has focused on the lowest levels, (i.e., from the noise level up to and somewhat beyond the point at which the low-frequency AGC begins to actuate the system gain change). Although funding limitations did not permit examining the full range, (i.e., to include the point at which the mechanical iris system begins to be actuated), this could be performed at a later time, should conditions warrant.

The raw data are shown in Figure 3. This clearly reveals the point at which the AGC begins to actuate, which occurs at an LED current of about 5.5 mA. Calibration of the diffuse radiance that is associated with this driving current yields the desired end result.

The lower curve, which depicts a run performed with an extra filter, provides an indication of the quality of the data.

The following facts have emerged from this investigation:

- The AGC actuation level lies at  $2.1 \times 10^{-9}$  W/ster-cm<sup>2</sup>
- The LLLTV output is linear from the noise level out to this value
- At twice this value, the gain is reduced by a factor of two; and at three times this value, the gain is reduced by a factor of about 3-4.

## 4.2 Narrowfield TV Camera

### 4.2.1 Point-source spot size

The linear spot size is virtually identical to that of the WFTV, (namely, 65 microns diameter FW @ HM). In terms of object space, this translates to a smaller value of 0.87 milliradian.

### 4.2.2 Extended-source AGC response

The raw data are shown in Figure 4. In this instance the AGC actuation occurs at 0.87 nanowatts per cm<sup>2</sup>-ster. This indicates a sensitivity of about 2.4 times that of the Widefield system. It should be recalled, however, that the NFTV sensitivity is reduced by a factor of 2, due to the presence of a baffle chamber that preempts half of the usable aperture. It follows therefore that the NFTV sensitivity is about 20% greater than that of the WFTV.

## 5. CONCLUSIONS AND RECOMMENDATIONS

A technique has been developed for the purpose of providing a laboratory calibration and characterization of the LLLTV's. In conjunction with special ancillary apparatus at the facilities of Miranda Laboratories, meaningful data have been collected with the spare WF and NFTV systems which permits the extraction of useful radiant emission from the flight data, on the presumption that the spare units are similar to the flight units with regard to those parameters affecting the overall system sensitivity.

The investigation was restricted to the low end of the system dynamic range. However, it has been demonstrated that the means are available for covering the full extent of the system response.

In the event that the CIRRIS 1A payload should be reflown on some future mission, it is recommended that a characterization of the full dynamic range be performed with the flight hardware as part of the refurbishment effort in preparation for the reflight.

Parenthetically, it is also recommended that measures be taken to ensure that internal stability problems discovered during postflight data reduction, be addressed and corrected as part of such refurbishment.

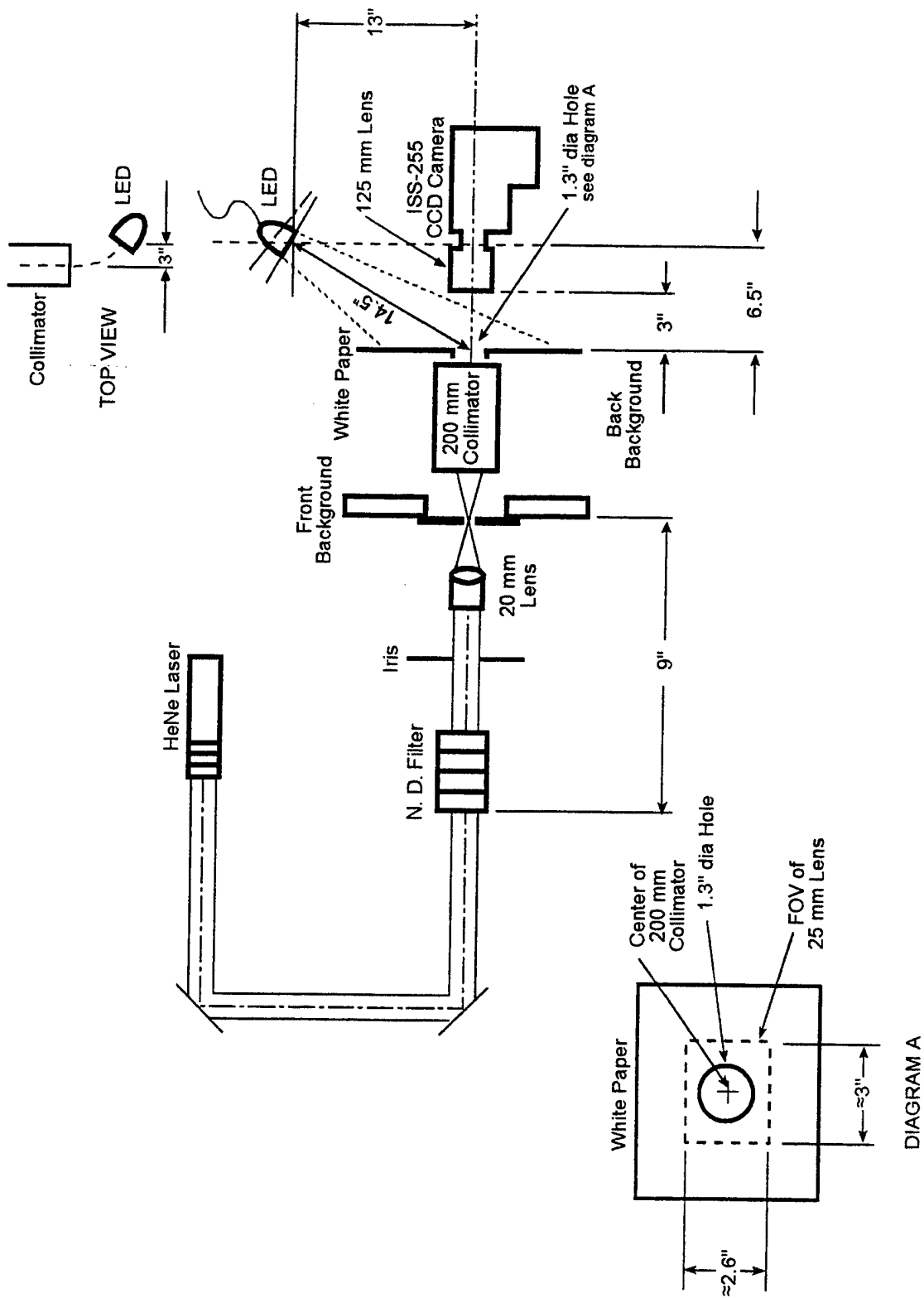


Figure 1. Schematic of the Experimental Apparatus used for Testing.



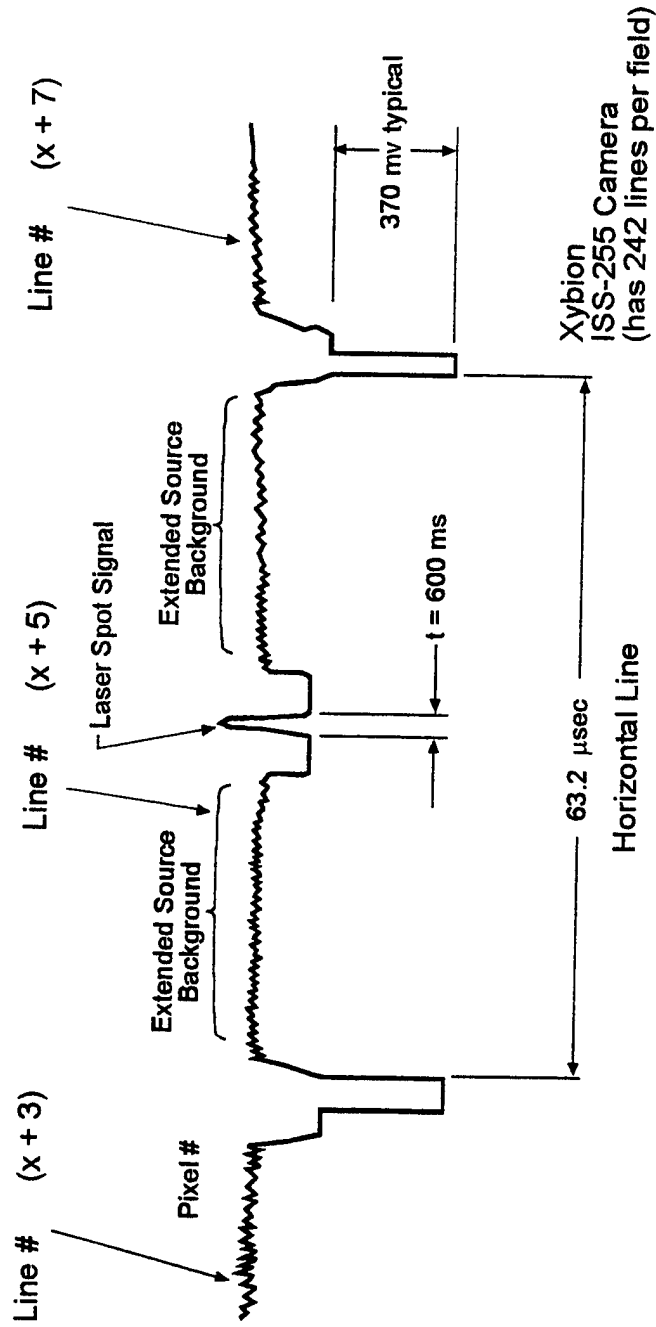


Figure 2. Typical Oscilloscope Trace of a Single Horizontal TV Raster Line.

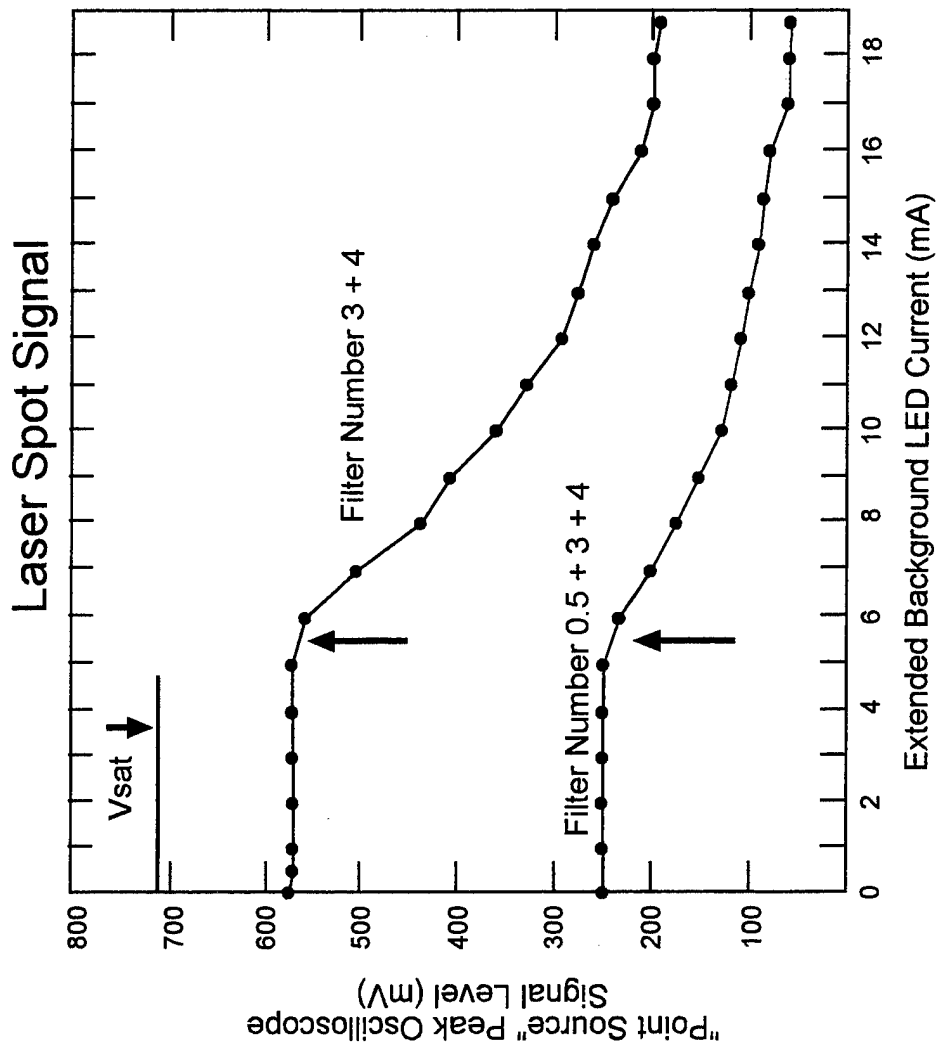


Figure 3. AGC Response Curves for the 25 mm Lens.

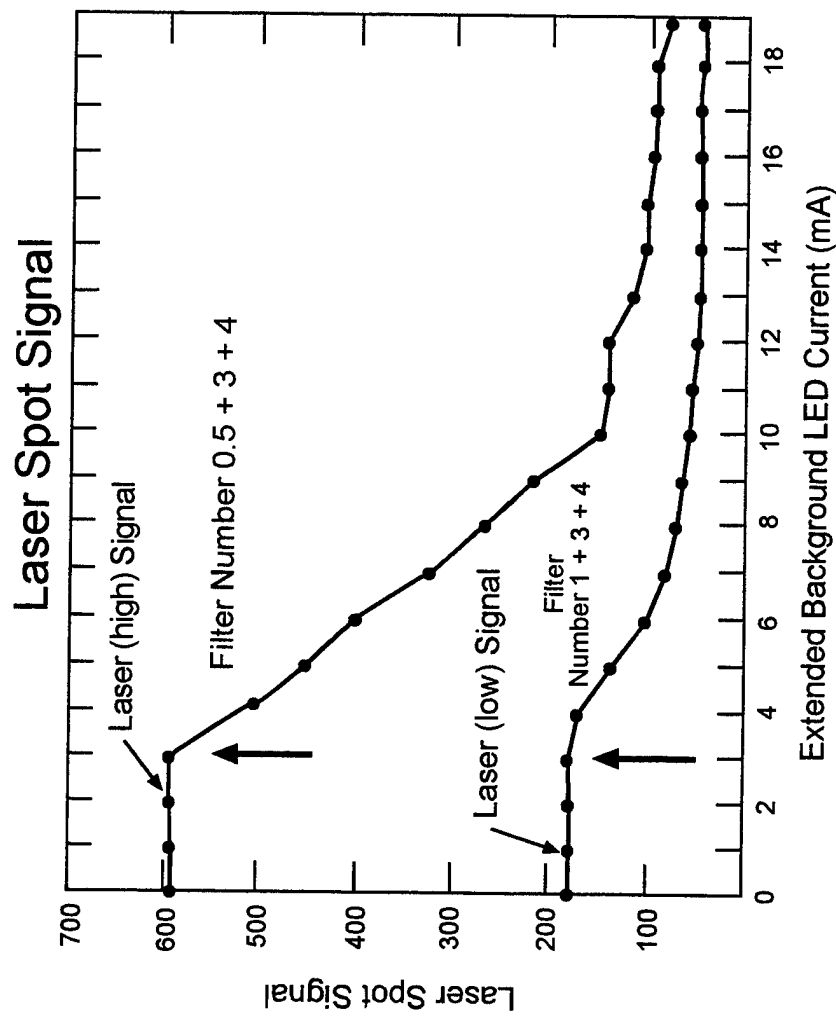


Figure 4. AGC Response Curves for the 75 mm Lens.